

Copyright Undertaking

This thesis is protected by copyright, with all rights reserved.

By reading and using the thesis, the reader understands and agrees to the following terms:

- 1. The reader will abide by the rules and legal ordinances governing copyright regarding the use of the thesis.
- 2. The reader will use the thesis for the purpose of research or private study only and not for distribution or further reproduction or any other purpose.
- 3. The reader agrees to indemnify and hold the University harmless from and against any loss, damage, cost, liability or expenses arising from copyright infringement or unauthorized usage.

IMPORTANT

If you have reasons to believe that any materials in this thesis are deemed not suitable to be distributed in this form, or a copyright owner having difficulty with the material being included in our database, please contact lbsys@polyu.edu.hk providing details. The Library will look into your claim and consider taking remedial action upon receipt of the written requests.

DEVELOPMENT OF SUSTAINABLE AND COMFORTABLE POLY(LACTIC ACID) MATTRESS SURFACE FABRICS WITH INTEGRATED CAPACITANCE SENSORS FOR SLEEP MONITORING

JU ZIXIN

PhD
The Hong Kong Polytechnic University
2025

The Hong Kong Polytechnic University School of Fashion and Textiles

Development of Sustainable and Comfortable Poly(lactic acid) Mattress Surface Fabrics with Integrated Capacitance Sensors for Sleep Monitoring

Ju Zixin

A thesis submitted in partial fulfilment of the requirements for the degree of Doctor of Philosophy

December 2024

CERTIFICATE OF ORIGINALITY

Ju Zixin

| I hereby declare that this thesis is my own work and that, to the best of my knowledge |
|--|
| and belief, it reproduces no material previously published or written, nor material that |
| has been accepted for the award of any other degree or diploma, except where due |
| acknowledgement has been made in the text. |
| |
| |
| |
| |
| |
| |
| (Signed) |
| |
| |

(Name of student)

To My Loved Ones

For Their Constant Love and Support

Abstract

Sleep is essential for maintaining health and promoting brain function and immune strength, while insufficient sleep increases the risks of illness and early mortality. Improving sleep quality has become a major research focus, with efforts centered on optimizing environmental factors like mattress comfort and employing advanced technologies such as integrated sensors for behavioral data collection. Among these, mattress surface fabrics are attracting growing attention for their ability to simultaneously enhance the contact environment through improved comfort and enable real-time sleep behavior monitoring via embedded sensing technologies. However, traditional mattress surface fabrics, typically made from commonly used synthetic fibers that lack sustainability or natural fibers that are prone to bacterial growth, raise significant concerns regarding environmental impact and hygiene. Poly(lactic acid) (PLA) emerges as an ideal alternative material due to its renewable origins, biodegradability, antibacterial properties, and excellent mechanical performance. Despite its potential, the application of PLA in mattress surface fabrics remains unexplored.

To address this gap, this study aims to design and fabricate a PLA-based smart mattress surface fabric that combines enhanced comfort with integrated sleep monitoring functionality. The research begins with producing crimped PLA filaments in four linear densities (150D, 450D, 600D, and 900D) using the knit-de-knit technique. Through a comprehensive evaluation of their crimped and tensile properties, optimal heat-setting conditions of 120°C for 90 s were determined, and predictive models for these properties were established. The optimized crimped PLA filaments exhibit excellent crimped and tensile properties, making them highly suitable as inlaid filaments in mattress surface fabrics.

Subsequently, crimped PLA filaments were utilized to produce PLA weft-knitted inlaid

fabrics for mattress surface applications. The effects of connection rate, stitching pattern shape, and yarn types on the physical and comfort properties of these fabrics were systematically investigated, along with their durability. The findings reveal that increasing the connection rate enhances fabric air and water vapor permeabilities while reducing thermal insulation and compression energy absorption. Stitching pattern shape also plays a critical role, with triangular patterns promoting air permeability, hexagonal patterns leading to greater thickness loss, and rhombic patterns absorbing more compression energy. Additionally, fabrics made with crimped PLA inlaid filaments exhibit superior comfort properties, reduced thickness loss, and higher compression energy absorption. Compared to PET fabrics, these PLA fabrics display improved water vapor permeability and comparable overall comfort, pilling, and abrasion resistance, highlighting their potential as sustainable materials for mattress applications.

To achieve sensing functionality, this study further integrated conductive yarns into PLA weft-knitted inlaid fabrics, developing a PLA-based textile capacitive pressure sensor (TCPS) through the intarsia knitting technique. The improved TCPS exhibits a sensitivity range of 1.73-0.09 kPa⁻¹ within 0-15 kPa, along with stable capacitive responses under varying compressive pressures (1–15 kPa) and rates (5–20 mm/min). Moreover, it maintains consistent performance even after five washings and 5000 compression cycles, emphasizing its durability. Building on this, a PLA smart mattress surface fabric integrating a 4 × 4 matrix of 16 TCPS units was seamlessly fabricated. Supported by a wireless data acquisition system, this fabric records capacitance changes across each TCPS, enabling real-time monitoring of sleep behaviors such as getting into and out of bed, lying flat, and lying on the side. To analyze the recorded capacitance data, a one-dimensional convolutional neural network (1D-CNN) was developed, achieving 100% accuracy in classifying sleep behaviors and 80-100% accuracy in identifying seven participants. In conclusion, this study successfully develops a sustainable, comfortable, and intelligent PLA-based mattress surface fabric, providing a reliable technical foundation for advanced sleep monitoring applications.

List of Publications

Published Journal Papers:

- 1. **Ju Z**, Dong S, Lau W, Liu Y, Hu H. Comfort properties of PLA/cotton multilayered quilted fabrics[J]. Textile Research Journal. 2024;95(7–8):728–747.
- 2. **Ju Z**, Yang Y, Fei B, Hu H. Enhancing dyeability of sustainable polylactic acid fabrics through cross-sectional modification of filaments[J]. Textile Research Journal. 2025.
- 3. Dong S, **Ju Z**, Yao P, Liu Y, Xu B, Hu H. Flexible and freely cuttable fleecy triboelectric fabrics for ultra-high scalability in self-powered sensing applications[J]. Applied Materials Today, 2025, 42: 102569.
- 4. Yang Y, **Ju Z**, Tam PY, Hua T, Hu H. Sustainable profiled poly (lactic acid) multifilaments with high moisture management performance for textiles[J]. Textile Research Journal, 2022, 92(21–22): 4298–4312.
- 5. Dong S, Yao P, **Ju Z**, Sheng Y, Xu B, Liu Y, Hu H. Conductive chenille yarn-based triboelectric carpet fabrics with enhanced flexibility and comfort for smart home monitoring[J]. Materials Today Energy, 2024, 41: 101527.

Journal Papers in Preparation:

1. **Ju Z**, Lau W, Hu H. Sustainable crimped poly(lactic acid) filaments – Part I: fabrication and process optimization [J]. In preparation for submission.

- 2. **Ju Z**, Lau W, Hu H. Sustainable crimped poly(lactic acid) filaments Part II: application in weft-knitted inlaid fabrics and performance evaluation [J]. In preparation for submission.
- 3. **Ju Z**, Dong S, Liu Y, Hu H. Poly(lactic acid)-based smart mattress surface fabrics for real-time sleep monitoring [J]. In preparation for submission.

Granted Patents:

- 1. Hu H, **Ju Z**, Yang Y, Tam P. Moisture-absorbing and sweat-wicking multilayer poly(lactic acid) knitted fabric and its preparation method [P]. Invention Patent, China, CN114086304A. Granted: 2022-02-25.
- 2. Hu H, **Ju Z**, Dong S, Lau W. Poly(lactic acid) knitted fabric for mattress applications [P]. Utility Model Patent, China, CN221775464U. Granted: 2024-09-27.
- 3. Wang X, Dong S, **Ju Z**, Xiong Y. Double air layer fabric and its fabrication method [P]. Invention Patent, China, CN114737306B. Granted: 2023-07-07.

Acknowledgements

I would like to express my heartfelt gratitude to my chief supervisor, Prof. Hong Hu, for his insightful guidance and invaluable advice throughout my academic research. His mentorship has been an honor, and I am deeply grateful for the knowledge, inspiration, and support he has generously provided.

My sincere thanks go to my co-supervisor, Prof. Yanping Liu, for his precise guidance in structuring this dissertation and for his thoughtful advice regarding my future development. I am equally grateful to my co-supervisor, Prof. Bin Fei, for his critical feedback and expert recommendations on my experimental design, which were essential to the success of this study.

I am also grateful to Dr. Chou Jinyun and the technical team, including Mr. Tiu Calvin, Dr. Hui Kevin, Dr. Lam Ling, Mr. Ng Shui Wing, Dr. Lee Samuel, and Mr. Sze Marco, for their patience and prompt assistance during the experimental phase. Their expertise and support were essential to the completion of this work.

My heartfelt appreciation extends to my friends and colleagues for their encouragement, companionship, and support, especially Dong Shanshan, Tian Xiao, Kwan Mei Ying, Xia Gang, Yao Pengpeng, Yang Yadie, Jin Liang, Tam Po Ying, Kwai Hing Tang, Lau Wing Hei, Tu Yuecheng, and many others whose names are not listed here. Their presence enriched my time at PolyU and made this journey meaningful and memorable.

I would like to express my deepest gratitude to my husband, Wang Jinchao, for his constant support and encouragement, which gave me the strength to persevere. My sincere thanks also go to my parents and my brother, Ju Bohan, for their unconditional love and continuous encouragement, which inspired me throughout this journey.

Finally, I extend my deepest appreciation to the Hong Kong Innovation and Technology Commission, HKRITA, and Mr. Wang Jingfeng for their financial support of my PhD research through project ITP/030/21TP. These contributions have been invaluable in facilitating this research.

Table of Contents

| Abstract | I |
|---|------|
| List of Publications | III |
| Acknowledgements | V |
| Table of Contents | VII |
| List of Figures | XI |
| List of Tables | XVII |
| List of Abbreviations | XIX |
| Chapter 1 Introduction | 1 |
| 1.1 Background | 1 |
| 1.2 Objectives | 3 |
| 1.3 Methodology | 4 |
| 1.4 Research significance | 7 |
| 1.5 Thesis outline | 8 |
| Chapter 2 Literature Review | 10 |
| 2.1 Introduction | 10 |
| 2.2 Sleep process and promotion | 10 |
| 2.2.1 Stages of sleep | 10 |
| 2.2.2 Effects of sleep deprivation | 12 |
| 2.2.3 Approaches to improve sleep | 13 |
| 2.3 Mattress surface fabrics | 16 |
| 2.3.1 Definition | 16 |
| 2.3.2 Classification and fabrication | 17 |
| 2.3.3 Materials and their limitations | 24 |
| 2.3.4 The potential of PLA for mattress surface fabrics | 26 |
| 2.4 Research on mattress surface fabrics | 28 |
| 2.4.1 Enhancing comfort | 28 |
| 2.4.2 Integrating sleep monitoring technologies | 32 |

| 2.5 Conclusions | 37 |
|--|----|
| Chapter 3 Fabrication of Crimped PLA Filaments | 39 |
| 3.1 Introduction | 39 |
| 3.2 Materials and methods | 40 |
| 3.2.1 Materials | 40 |
| 3.2.2 Fabrication | 40 |
| 3.3 Property evaluation | 43 |
| 3.3.1 Differential scanning calorimetry | 43 |
| 3.3.2 Crimped properties | 43 |
| 3.3.3 Tensile properties | 45 |
| 3.3.4 Morphologies | 45 |
| 3.3.5 X-ray diffraction | 45 |
| 3.3.6 Statistical analysis | 46 |
| 3.4 Results and discussion | 46 |
| 3.4.1 DSC Analysis | 46 |
| 3.4.2 Crimped properties | 47 |
| 3.4.3 Tensile properties | 55 |
| 3.4.4 Production process optimization | 60 |
| 3.4.5 Micromorphology and crystallization analysis | 62 |
| 3.5 Conclusions | 66 |
| Chapter 4 Design and Fabrication of PLA Weft-Knitted Inlaid Fabric | 69 |
| 4.1 Introduction | 69 |
| 4.2 Materials and methods | 70 |
| 4.2.1 Materials | 70 |
| 4.2.2 Fabric production | 71 |
| 4.3 Property evaluation | 75 |
| 4.3.1 Physical properties | 76 |
| 4.3.2 Air permeability | 76 |
| 4.3.3 Water vapor permeability | 76 |

| 4.3.4 Thermal insulation | 77 |
|--|----------------|
| 4.3.5 Compression durability | 77 |
| 4.3.6 Pilling and abrasion resistance tests | 79 |
| 4.3.7 Statistical analysis | 79 |
| 4.4 Results and discussion | 80 |
| 4.4.1 Physical properties | 80 |
| 4.4.2 Air permeability | 84 |
| 4.4.3 Water vapor permeability | 86 |
| 4.4.4 Thermal insulation | 88 |
| 4.4.5 Compression durability | 90 |
| 4.4.6 Pilling and abrasion resistance | 97 |
| 4.5 Conclusions | 98 |
| Chapter 5 Development of PLA Textile Capacitive Pressure Sensor | 101 |
| 5.1 Introduction | 101 |
| 5.2 Fabrication and working principle of the TCPS | 102 |
| 5.2.1 Materials | 102 |
| 5.2.2 Structure and fabrication | 103 |
| 5.2.3 Modeling and working principle of the TCPS | 106 |
| 5.3 Property evaluation | 109 |
| 5.3.1 Physical properties | 109 |
| 5.3.2 Sensing performance | 110 |
| 5.3.3 Comfort properties | 112 |
| 5.4 Results and discussion | 112 |
| 5.4.1 Effect of structural parameters | 112 |
| 5.4.2 Sensing performance of the TCPS | 114 |
| 5.4.3 Comfort performance of the TCPS | 119 |
| 5.5 Conclusions | 122 |
| Chapter 6 Development of PLA Smart Mattress Surface Fabrics for Ro | eal-Time Sleep |
| Monitoring | 124 |

| 6.1 Introduction | 124 |
|--|-----|
| 6.2 Design and fabrication | 124 |
| 6.3 Development of capacitance data acquisition system | 126 |
| 6.4 Sleep behavior data collection | 128 |
| 6.5 Sleep behavior analysis through deep learning | 129 |
| 6.6 Results and discussion | 131 |
| 6.6.1 Getting into bed | 131 |
| 6.6.2 Getting out of bed | 134 |
| 6.6.3 Lying flat | 136 |
| 6.6.4 Lying on the left | 138 |
| 6.6.5 Lying on the right | 140 |
| 6.6.6 1D-CNN for sleep behavior and individual recognition | 142 |
| 6.7 Conclusions. | 143 |
| Chapter 7 Conclusions and Future Work | 145 |
| 7.1 Conclusions. | 145 |
| 7.1.1 Fabrication of crimped PLA filaments | 145 |
| 7.1.2 Fabrication of PLA weft-knitted inlaid fabric | 145 |
| 7.1.3 Development of PLA-based TCPS | 146 |
| 7.1.4 Development of PLA smart mattress surface fabrics | 146 |
| 7.2 Limitations and future research directions | 147 |
| 7.2.1 Optimization of materials and structures | 147 |
| 7.2.2 Enhancing sensitivity and monitoring precision | 148 |
| 7.2.3 Algorithm optimization and system portability | 148 |
| 7.2.4 Durability and practicality enhancement | 148 |
| References | 150 |

List of Figures

| Figure 1.1 Flowchart of the overall methodology5 |
|---|
| Figure 2.1 Overview of the PSG: (a) monitoring sensors; (b) typical PSG output [84]. |
| 15 |
| Figure 2.2 Structure of typical mattress types: (a) spring; (b) latex; (c) foam and spring; |
| (d) hybrid17 |
| Figure 2.3 Functionality of mattress surface fabrics |
| Figure 2.4 Jacquard loom: (a) full view of the machine; (b) formation of woven fabric. |
| 18 |
| Figure 2.5 Woven mattress surface fabrics: (a) face structure and warp cross-section of |
| a double honeycomb fabric; (b) back structure and weft cross-section of a double |
| honeycomb fabric [12]; (c) front side of a jacquard woven fabric; (d) back side of |
| a jacquard woven fabric [13]. |
| Figure 2.6 Quilted mattress surface fabrics: surface (a) and cross-section (b) images of |
| fabric produced by sewing; surface (c) and cross-section (d) images of fabric |
| produced by ultrasonic quilting20 |
| Figure 2.7 Different knitting methods: (a) weft knitting; (b) warp knitting [16]21 |
| Figure 2.8 Warp knitting machine: (a) full view of the machine; (b) yarn arrangement; |
| (c) formation of warp-knitted fabric |
| Figure 2.9 Warp-knitted spacer fabric: (a) surface; (b) cross-section |
| Figure 2.10 Weft-knitted machines and fabrics: (a) electronic double jacquard circular |
| knitting machine; (b) dial and cylinder needles; (c) computerized flat knitting |
| machine; (d) surface of weft-knitted inlaid fabric; (e) cross-section of weft-knitted |
| inlaid fabric. |
| Figure 2.11 Methods for producing crimped yarns: (a) false-twist; (b) stuffer-box; (c) |
| gear; (d) knit-de-knit; (e) bi-component composite spinning; (f) asymmetrical |
| quenching |
| Figure 2.12 Conversion of lactic acid to poly(lactic acid) |

| Figure 2.13 Lifecycle of PLA. |
|---|
| Figure 2.14 The patient turn system: (a) the bedside liquid-crystal display; (b) the |
| flexible sensor mattress cover [11]. |
| Figure 2.15 Smart mattress cover system: (a) physical setup; (b) neural network |
| framework; (c) classification results [54]. |
| Figure 2.16 The mattress system: (a) signal-sensing electrode structure; (b) mattress |
| schematic; (c) scatter plot of RRI correlation; (d) scatter plot of JJI correlation [55] |
| Figure 2.17 Smart mattress topper system: (a) the active ECG electrode; (b) the smar |
| mattress topper; (c) the control unit [56] |
| Figure 3.1 The knitting and heat-setting processes of crimped PLA filaments41 |
| Figure 3.2 Images of knitted PLA fabric: (a) 150D PLA fabric; (b) 450D PLA fabric |
| (c) 600D PLA fabric; (d) 900D PLA fabric |
| Figure 3.3 DSC curves for the 150D PLA filament. |
| Figure 3.4 Effect of the dry heat-treated temperature and time on the crimp number of |
| crimped PLA filaments: (a) 150D; (b) 450D; (c) 600D; (d) 900D49 |
| Figure 3.5 Effect of the dry heat-treated temperature and time on the crimp ratio o |
| crimped PLA filaments: (a) 150D; (b) 450D; (c) 600D; (d) 900D52 |
| Figure 3.6 Effect of the dry heat-treated temperature and time on the crimp elastic ratio |
| of crimped PLA filaments: (a) 150D; (b) 450D; (c) 600D; (d) 900D54 |
| Figure 3.7 Effect of the dry heat-treated temperature and time on the tenacity of crimped |
| PLA filaments: (a) 150D; (b) 450D; (c) 600D; (d) 900D |
| Figure 3.8 Effect of the dry heat-treated temperature and time on the elongation of |
| crimped PLA filaments: (a) 150D; (b) 450D; (c) 600D; (d) 900D59 |
| Figure 3.9 The designed machines: (a) circular knitting machine; (b) de-knit winding |
| machine61 |
| Figure 3.10 The digital photos of bobbins and corresponding microscopic images of the |
| crimped PLA filaments produced under optimal dry heat-setting conditions: (a |
| and (e) 150D; (b) and (f) 450D; (e) and (g) 600D; (d) and (h) 900D62 |

| Figure 3.11 The longitudinal morphologies of 150D crimped PLA filaments under |
|---|
| different heat-setting conditions: (a)–(e) 80°C for 20–120 s; (f)–(j) 100°C for 20– |
| 120 s; (k)–(o) 120°C for 20–120 s; (p)–(t) 140°C for 20–120 s; (u)–(y) 160°C for |
| 20–120 s |
| Figure 3.12 The XRD patterns and crystallinity of 150D crimped PLA filaments treated |
| with different heat-setting conditions: (a) 80°C; (b) 100°C; (c) 120°C; (d) 140°C; |
| (e) 160°C; (f) crystallinity66 |
| Figure 4.1 The schematic illustration of the fabric structure71 |
| Figure 4.2 Designed stitching patterns of weft-knitted inlaid fabrics: (a) pattern A; (b) |
| pattern B; (c) pattern C; (d) pattern D; (e) pattern E |
| Figure 4.3 The knitting process of weft-knitted inlaid fabric: (a) the designed stitching |
| pattern B; (b) the circular knitting machine used; (c) the knitting process for a |
| knitting cycle74 |
| Figure 4.4 The upper layer, lower layer, and cross-section of fabricated weft-knitted |
| inlaid fabrics: (a) fabric A-600C; (b) fabric B-600C; (c) fabric C-600C; (d) fabric |
| D-600C; (e) fabric E-600C; (f) fabric B-450C; (g) fabric B-900C; (h) fabric B- |
| 450N; (i) fabric B-600N; (j) fabric B-900N; (k) fabric B-600C-S; (l) fabric B- |
| 600T-P |
| Figure 4.5 The Instron 5566 testing machine: (a) the primary testing components; (b) |
| the compression platen |
| Figure 4.6. Effects of fabric structural parameters and yarn types on course density, |
| wale density, GSM, and thickness: (a) and (b) effect of connection rate (Pattern A: |
| 6.34%, B: 9.29%, C: 12.86%); (c) and (d) effect of stitching pattern shape (Pattern |
| B: rhombus, D: triangle, E: hexagon); (e) and (f) effect of inlaid yarn type and |
| linear density (C = crimped PLA, N = normal PLA); (g) and (h) effect of surface |
| yarn type (S = PLA staple, P = PET filament)81 |
| Figure 4.7 Effects of fabric structural parameters and yarn types on air resistance: (a) |
| effect of connection rate (Pattern A: 6.34%, B: 9.29%, C: 12.86%); (b) effect of |
| stitching pattern shape (Pattern B: rhombus, D: triangle, E: hexagon); (c) effect of |

| inlaid yarn type and linear density (C = crimped PLA, N = normal PLA); (d) effectively |
|--|
| of surface yarn type (S = PLA staple, P = PET filament) |
| Figure 4.8 Effects of fabric structural parameters and yarn types on WVTR: (a) effects |
| of connection rate (Pattern A: 6.34%, B: 9.29%, C: 12.86%); (b) effect of stitchin |
| pattern shape (Pattern B: rhombus, D: triangle, E: hexagon); (c) effect of inlain |
| yarn type and linear density (C = crimped PLA, N = normal PLA); (d) effect of |
| surface yarn type (S = PLA staple, P = PET filament) |
| Figure 4.9 Effects of fabric structural parameters and yarn types on keeping warmt |
| ratio: (a) effect of connection rate (Pattern A: 6.34%, B: 9.29%, C: 12.86%); (b) |
| effect of stitching pattern shape (Pattern B: rhombus, D: triangle, E: hexagon); (o |
| effect of inlaid yarn type and linear density (C = crimped PLA, N = normal PLA |
| (d) effect of surface yarn type (S = PLA staple, P = PET filament)8 |
| Figure 4.10 Compression stress-strain curves of weft-knitted inlaid fabrics: (a) fabric |
| A-600C; (b) fabric B-600C; (c) fabric C-600C; (d) fabric D-600C; (e) fabric B |
| 600C; (f) fabric B-450C; (g) fabric B-900C; (h) fabric B-450N; (i) fabric B-600N |
| (j) fabric B-900N; (k) fabric B-600C-S; (l) fabric B-600T-P9 |
| Figure 4.11 Effects of fabric structural parameters and yarn types on thickness loss: (a |
| effect of connection rate (Pattern A: 6.34%, B: 9.29%, C: 12.86%); (b) effect of |
| stitching pattern shape (Pattern B: rhombus, D: triangle, E: hexagon); (c) effect of |
| inlaid yarn type and linear density (C = crimped PLA, N = normal PLA); (d) effectively |
| of surface yarn type (S = PLA staple, P = PET filament) |
| Figure 4.12 Effects of fabric structural parameters and yarn types on energy absorption |
| (a) effect of connection rate (Pattern A: 6.34%, B: 9.29%, C: 12.86%); (b) effect |
| of stitching pattern shape (Pattern B: rhombus, D: triangle, E: hexagon); (c) effective |
| of inlaid yarn type and linear density (C = crimped PLA, N = normal PLA); (c |
| effect of surface yarn type (S = PLA staple, P = PET filament)9 |
| Figure 5.1 Structure and fabrication of the TCPS fabric: (a) schematic diagram of the |
| entire TCPS fabric and a magnified cross-section of the integrated TCPS; (b) the |
| designed pattern and computerized flat-knitting machine used for fabrication; (|

| silver-coated nylon conductive yarn; (d) yellow PLA filament; (e) white PLA |
|---|
| filament; (f) crimped PLA filament |
| Figure 5.2 The upper and lower layers of TCPS fabrics: (a) fabric 1; (b) fabric 2; (c) |
| fabric 3; (d) fabric 4; (e) fabric 5; (f) fabric 6; (g) fabric 7105 |
| Figure 5.3 Working principle of the TCPS |
| Figure 5.4 Experimental setup for measuring the capacitance of the TCPS during |
| compression |
| Figure 5.5 $\Delta C/C_0$ of TCPS under single compression: (a) schematic diagram of the |
| TCPS; (b) effect of conductive yarns; (c) effect of inlaid filaments; (d) effect of |
| electrode wales (m) and courses (n) |
| Figure 5.6 Sensitivity of the TCPS across different compressive pressure ranges 115 |
| Figure 5.7 $\Delta C/C_0$ of the TCPS under different compression conditions: (a) varying |
| compressive pressures (1, 3, 6, 9, 12, and 15 kPa); (b) varying compression rates |
| (5, 10, 15, and 20 mm/min) |
| Figure 5.8 $\Delta C/C_0$ of the TCPS after different washing cycles |
| Figure 5.9 Response and recovery times of the TCPS under a vertical pressure of 1.07 |
| kPa |
| Figure 5.10 Repeatability of the TCPS over 5000 compression cycles |
| Figure 5.11 Morphology of commercial mattress surface fabric for comparison: (a) |
| fabric a; (b) fabric b; (c) fabric c; (d) fabric d; (e) fabric e120 |
| Figure 5.12 Comparison of comfort properties between the TCPS fabric and |
| commercial mattress surface fabrics (fabrics a-e): (a) keeping warmth ratio; (b) |
| air resistance; (c) water vapor transmission rate (WVTR); (d) compressional |
| linearity (LC); (e) compressional energy (WC); (f) compressional recoverability |
| (RC) |
| Figure 6.1 Design and fabrication of the PLA smart mattress surface fabric: (a) key |
| stress regions; (b) fabric design; (c) computerized flat-knitting machine used; (d) |
| produced fabric with 16 integrated TCPS units |
| Figure 6.2 Illustration of the capacitance data acquisition system: (a) measurement |

| flowchart; (b) diagram of the PCap01-AD chip; (c) hardware module; (d) |
|---|
| visualization interfaces |
| Figure 6.3 Architecture of the 1D-CNN model for sleep behavior analysis and |
| individual identification |
| Figure 6.4 Dynamic capacitance variation during the getting-into-bed process: (a) |
| schematic of a volunteer preparing to get into bed; (b)–(h) heat maps for volunteers |
| 1–7 |
| Figure 6.5 Dynamic capacitance variation during the getting-out-of-bed process: (a) |
| schematic of a volunteer preparing to get out of bed; (b)-(h) heat maps for |
| volunteers 1–7 |
| Figure 6.6 Dynamic capacitance variation during the lying-flat process: (a) schematic |
| of a volunteer lying flat; (b)–(h) heat maps for volunteers 1–7137 |
| Figure 6.7 Dynamic capacitance variation during the left-side-lying process: (a) |
| schematic of a volunteer lying on the left side; (b)–(h) heat maps for volunteers 1– |
| 7 |
| Figure 6.8 Dynamic capacitance variation during the right-side-lying process: (a) |
| schematic of a volunteer lying on the right side; (b)–(h) heat maps for volunteers |
| 1–7 |
| Figure 6.9 Training performance and classification results of the 1D-CNN model: (a) |
| training curve for five-behavior classification; (b) confusion matrix for five- |
| behavior classification; (c) training curve for seven-individual classification; (d) |
| confusion matrix for seven-individual classification |

List of Tables

| Table 2.1 Physiological changes during NREM and REM sleep stages [67-69] | 12 |
|--|------|
| Table 3.1 Technical specifications of normal PLA filaments | 40 |
| Table 3.2 Details of knitted PLA fabrics | 42 |
| Table 3.3 Conditions for dry heat-setting | 42 |
| Table 3.4 Two-way ANOVA results for the crimp number of PLA filaments | 50 |
| Table 3.5 Regression models and R ² values for filament crimp number | 50 |
| Table 3.6 Two-way ANOVA results for the crimp ratio of PLA filaments | 52 |
| Table 3.7 Regression models and R ² values for filament crimp ratio | 53 |
| Table 3.8 Two-way ANOVA results for the crimp elastic ratio of PLA filaments | 54 |
| Table 3.9 Regression models and R^2 values for filament crimp elastic ratio | 55 |
| Table 3.10 Two-way ANOVA results for the tenacity of PLA filaments | 57 |
| Table 3.11 Regression models and R ² values for filament tenacity | 57 |
| Table 3.12 Two-way ANOVA results for the elongation of PLA filaments | 59 |
| Table 3.13 Regression models and R^2 values for filament elongation | 60 |
| Table 3.14 Properties of crimped PLA filaments produced under optimal dry ho | eat- |
| setting conditions | 62 |
| Table 4.1 Technical details of filaments | 71 |
| Table 4.2 Technical details of PLA staple yarn | 71 |
| Table 4.3 Details of the designed stitching patterns | 72 |
| Table 4.4 Production details of weft-knitted inlaid fabrics | 74 |
| Table 4.5 ANOVA results for physical properties of weft-knitted inlaid fabrics | 82 |
| Table 4.6 ANOVA results for air resistance of weft-knitted inlaid fabrics | 85 |
| Table 4.7 ANOVA results for WVTR of weft-knitted inlaid fabrics | 87 |
| Table 4.8 ANOVA results for keeping warmth ratio of weft-knitted inlaid fabrics | 89 |
| Table 4.9 The pilling degree and abrasion resistance cycles of weft-knitted inlaid fab | rics |
| | 98 |
| Table 5.1 Technical details of 150D PLA filaments | 102 |

| Table 5.2 Technical details of silver-coated nylon conductive yarns | 103 |
|--|---------|
| Table 5.3 Production details of TCPS fabrics | 105 |
| Table 5.4 Technical specifications of TCPS fabrics | 106 |
| Table 5.5 Physical properties of the TCPS fabric and commercial mattress | surface |
| fabrics | 120 |

List of Abbreviations

1D-CNN One-dimensional convolutional neural network

ANOVA Analysis of variance

BCG Ballistocardiogram

CBT-I Cognitive behavioral therapy for insomnia

CSV Comma-separated values

DSC Differential scanning calorimetry

ECG Electrocardiogram

EEG Electroencephalogram

GSM Grams per square meter

LC Compressional linearity

LCD Liquid crystal display

MCU Microcontroller unit

NREM Non-rapid eye movement

PCMs Phase change materials

PET Polyethylene terephthalate

PLA Poly(lactic acid)

PSG Polysomnography

RC Compressional recoverability

ReLU Rectified linear unit

REM Rapid eye movement

SEM Scanning electron microscopy

SPI Serial peripheral interface

SWS Slow wave sleep

 T_c Crystallization temperature

TCPS Textile capacitive pressure sensor

 T_g Glass transition temperature

 T_m Crystalline melting point

UART Universal asynchronous receiver-transmitter

WC Compressional energy

WVTR Water vapor transmission rate

XRD X-ray diffraction

Chapter 1 Introduction

1.1 Background

Sleep is a fundamental physiological need essential for achieving optimal health [1, 2]. It plays a vital role in supporting biological functions, including the restoration of brain energy stores, the regulation of hormone secretion, and the enhancement of immune system performance [3, 4]. Conversely, chronic insomnia poses significant health risks, notably increasing the likelihood of depression, inflammatory disorders, infectious diseases, and even mortality [5, 6]. Recognizing the critical impact of sleep, recent years have seen an increased focus on promoting sleep quality through strategies such as environmental optimization [7, 8] and the adoption of smart monitoring technologies [9]. These approaches have gained popularity due to their simplicity and reduced reliance on self-discipline or complex therapeutic interventions. Mattress surface fabrics emerge as a key solution that enhances both strategies simultaneously. They can not only improve sleep quality by optimizing the body-mattress contact environment [10] but also enable real-time monitoring of sleep behaviors through embedded sensing technologies, offering valuable insights for further sleep optimization [11]. Therefore, the development of mattress surface fabrics with enhanced comfort and monitoring capabilities is critical for better sleep health.

Mattress surface fabrics are categorized into three primary types based on their manufacturing techniques: woven, multilayer quilted, and knitted fabrics [12-15]. Woven fabrics, however, require a complex and time-consuming warp preparation process, often resulting in production challenges [16]. Similarly, the fabrication of multilayer quilted fabrics is complicated, as each layer must be produced separately and then stitched together [14]. In contrast, weft-knitted inlaid fabrics, a multilayer fabric produced in a single step using weft-knitted technology, have become the preferred choice for mattress surface fabrics due to their versatile patterns, superior softness, and high production efficiency [13, 17]. These fabrics typically consist of three layers: an

upper layer, a middle layer, and a lower layer [18, 19]. The upper and lower layers can be made from various materials, including natural and synthetic yarns [13, 20-25]. Commonly used natural fibers are prone to bacterial growth, raising hygiene concerns, whereas conventional synthetic fibers, derived from petroleum, are non-degradable and contribute to environmental issues. The middle layer of weft-knitted inlaid fabrics is typically inserted with bulky textured filaments, which significantly influence the fabric's physical properties and overall comfort. Various techniques have been developed to produce these textured filaments, including false-twist [26], stuffer-box, gear crimping [27], knit-de-knit [28], and melt spinning [29-34]. Among these, the knit-de-knit technology is notable for its economical production, adjustable crimp shapes, and consistent crimp patterns. However, like most other techniques, the filaments produced using this method are predominantly made from unsustainable polyethylene terephthalate (PET) [35].

The limitations of conventional natural and synthetic fibers emphasize the need for alternative materials that effectively balance functionality and environmental sustainability. Poly(lactic acid) (PLA), a renewable and biodegradable polymer, offers a promising solution. PLA is derived from 100% annually renewable sources such as corn, cassava, sugarcane, and sugar beet, and it can be fully composted at the end of its lifecycle [36-38]. As the only biobased and biodegradable polymer suitable for large-scale melt-spinning into textile fibers with desirable mechanical properties, PLA provides an attractive alternative to traditional fibers in textile applications [38, 39]. Additionally, PLA fibers exhibit low flammability, good antibacterial properties, and weather resistance, making them particularly well-suited for mattress surface fabrics [40-52]. However, there is a lack of research on the comfort properties of weft-knitted inlaid fabrics made from sustainable PLA materials, which limits their widespread use in textiles. Furthermore, no studies have been conducted on textured PLA filaments, further restricting the potential of PLA-based mattress surface fabrics. Therefore, the development of bulky textured PLA filaments and their integration into sustainable

weft-knitted inlaid fabrics is crucial for expanding the use of PLA in mattress surface fabrics.

Sleep monitoring is another crucial aspect of mattress surface fabric research, offering valuable insights through the long-term tracking of human sleep behaviors. Such data can facilitate the development of healthier sleep habits, ultimately enhancing overall sleep quality [9]. A variety of studies have focused on smart mattress surface fabrics designed to monitor different sleep states, such as body pressure distribution [11], sleep posture and position [53, 54], electrocardiogram (ECG), and ballistocardiogram (BCG) signals [55, 56], and respiratory rate [57]. However, all of these fabrics require the additional embedding of sensors or electrodes, making the manufacturing process more complex, while potentially causing discomfort and requiring more maintenance [11, 53-57]. Therefore, in addition to ensuring sustainability and comfort, there is a rising demand for more efficient and cost-effective methods to fabricate smart mattress surface fabrics.

1.2 Objectives

In view of the above, this study aimed to enhance human sleep quality by utilizing PLA materials to design and fabricate sustainable and comfortable mattress surface fabrics with integrated sleep monitoring functionality. The specific objectives of this study are as follows:

- (1) To design and produce crimped PLA filaments with varying linear densities using knit-de-knit technology, establish regression prediction models to correlate heat-setting parameters with their crimped and tensile properties, and optimize these parameters to achieve superior overall performance.
- (2) To develop comfortable and durable PLA weft-knitted inlaid fabrics for mattress surface, systematically investigating the effects of knitting parameters and material

types on their physical, comfort, and compression performance.

- (3) To manufacture PLA-based textile capacitive pressure sensor (TCPS) by integrating conductive yarns into PLA weft-knitted inlaid fabrics through a single-step knitting process, investigate structural parameters to achieve superior sensing performance, and comprehensively evaluate their sensing properties and comfort to ensure durability and suitability for long-term use in mattress surface applications.
- (4) To fabricate PLA smart mattress fabrics with an integrated TCPS matrix, design hardware, and software systems to record and analyze capacitance data during individual sleep, and employ machine learning for precise behavior classification and individual identification, ultimately achieving efficient wireless sleep monitoring.

With the successful completion of this study, bulky PLA filaments with superior crimped and tensile properties will be produced, and PLA smart mattress surface fabrics with excellent comfort and sleep monitoring capabilities will be developed. These advancements are expected to improve individual sleep quality while promoting the use of sustainable PLA materials in the textile industry.

1.3 Methodology

To achieve the objectives outlined in this study, a comprehensive investigation was conducted on the development of bulky crimped PLA filaments and their application in sustainable and comfortable mattress surface fabrics with integrated sleep monitoring capabilities. The specific research methodology employed in this study is presented in the flowchart shown in Figure 1.1.

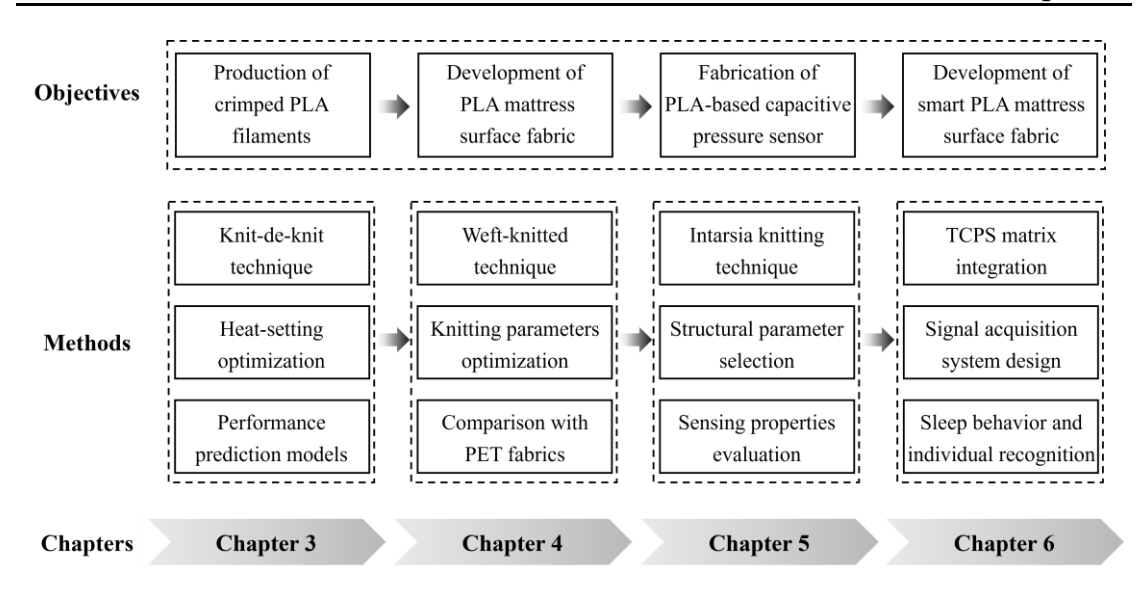


Figure 1.1 Flowchart of the overall methodology.

To produce bulky and textured PLA filaments while ensuring knittability, the production process and properties of crimped PLA filaments using the knit-de-knit technique were systematically investigated. PLA filaments with varying linear densities (150D, 450D, 600D, and 900D) were initially knitted into plain fabrics and subsequently subjected to dry heat-setting under controlled temperature (80°C to 160°C) and time (20 s to 120 s) conditions. After heat-setting, the fabrics were unraveled to obtain crimped PLA filaments. Standard testing methods were used to measure their crimped properties (crimp number, crimp ratio, and crimp elastic ratio) and tensile properties (tenacity and elongation). The significance of the relationship between heatsetting parameters and filament properties was analyzed through a two-way analysis of variance (ANOVA), while regression analysis was applied to establish performance prediction models. Based on the optimized heat-setting conditions, a specialized circular knitting machine and a de-knit winding machine were developed to enhance the efficiency of crimped PLA filaments production. Finally, microstructural changes and crystallinity of 150D PLA filaments under different heat-setting conditions were examined using scanning electron microscopy (SEM) and X-ray diffraction (XRD) to reveal the intrinsic mechanisms governing their crimped and tensile properties.

To develop sustainable, comfortable, and durable PLA weft-knitted inlaid fabrics for

mattress surface applications, this study employed weft knitting techniques to fabricate PLA fabrics and investigated the influence of structural parameters on their properties. Optimized 450D, 600D, and 900D crimped PLA filaments were selected as middle inlaid yarns, while 150D PLA filaments and 32 Ne PLA staple yarns were used as surface yarns, with commercially available PET yarns included for comparison. The fabrics were produced using a UCC548 electronic double jacquard circular knitting machine, with key parameters such as connection rates, shapes of stitching patterns, and types of inlaid and surface yarns carefully controlled. The resulting fabrics were subjected to comprehensive testing to assess their physical properties and comfort performance, including air permeability, water vapor permeability, and thermal insulation, with the results analyzed using ANOVA statistical methods. Furthermore, compression durability, pilling, and abrasion resistance were evaluated to validate their suitability for practical applications.

To develop high-performance PLA-based TCPS, this study utilized the intarsia knitting technique to integrate conductive yarns into PLA weft-knitted inlaid fabrics and explored the effects of structural parameters on their sensing performance. The structure and knitting parameters for the TCPS were first designed using the SDS-ONE Apex3 system and then transferred to an SVR123SP computerized flat knitting machine for production. During this process, the conductive yarns, inlaid filaments, and the arrangement of electrode wales and courses were precisely controlled to effectively form various designed sensor structures. The capacitive performance of the TCPS was evaluated under uniform compression conditions using an Instron 5566 tester and a TH2830 LCR meter, identifying the sensor configuration with improved performance. Based on that, the capacitive response and dynamic properties of the enhanced TCPS were characterized under varying pressure loads, compression rates, and repeated washing and loading cycles. Furthermore, key comfort properties, including air permeability, water vapor permeability, thermal insulation, and compression performance, of the selected TCPS fabric were evaluated and compared with those of

commercial mattress surface fabrics to verify its suitability for both comfort and smart mattress applications.

To achieve precise sleep monitoring, this study developed PLA smart mattress surface fabrics integrated with a 4 × 4 matrix of 16 TCPS units, produced using the intarsia knitting technique with previously improved TCPS knitting parameters. The smart fabric was also designed using the SDS-ONE Apex3 system and fabricated on the SVR123SP computerized flat knitting machine. Additionally, a signal acquisition system was developed for the produced smart fabric, featuring an STM32 microcontroller as the core control unit and a PCAP01 capacitance detection module for real-time data collection from each TCPS unit. The collected data were wirelessly transmitted via Bluetooth to a computer interface for visualization and analysis. Based on this integrated platform, the capacitance data for five typical sleep behaviors in seven volunteers were recorded and analyzed. Furthermore, a one-dimensional convolutional neural network (1D-CNN) was applied to classify the recorded sleep behaviors and recognize individual participants, exploring the potential of PLA-based smart mattress surfaces for advanced sleep monitoring and personalized health management.

1.4 Research significance

The primary contribution of this study lies in the comprehensive investigation of textured PLA filaments and their application in sustainable and comfortable mattress surface fabrics with integrated sleep monitoring functions. Bulky crimped PLA filaments were successfully produced using the knit-de-knit technique, and regression models were developed to correlate heat-setting parameters with the crimped and tensile properties of PLA filaments. This achievement not only enhances the predictability and precise regulation of PLA material properties but also broadens the application potential of renewable materials in high-performance textiles.

Moreover, this study successfully produced comfortable and durable PLA mattress

surface fabrics by utilizing crimped PLA filaments. It systematically analyzed the effects of knitting parameters and yarn types on the physical properties, comfort performance, and durability of these fabrics, addressing a significant research gap in the development of PLA-based functional bedding materials. The findings offer valuable theoretical guidance and practical insights for the development of advanced eco-friendly bedding.

Furthermore, this study successfully introduced the conductive yarn into PLA weft-knitted inlaid fabric to produce TCPS with excellent sensing and comfort properties. Building on this achievement, PLA smart mattress surface fabric with an integrated TCPS matrix was further fabricated through a single-step fabrication process using intarsia knitting technology. Supported by wireless data acquisition, real-time signal processing, and a 1D-CNN deep learning model, the PLA smart fabric can accurately monitor sleep behaviors and identify both behaviors and individuals. By seamlessly combining sustainable materials with intelligent functionalities, this study represents a meaningful advancement in the development of eco-friendly smart home products, contributing to the realization of sustainable and intelligent innovations.

1.5 Thesis outline

Chapter 2 provides a comprehensive review of the achievements and limitations of previous studies in relevant disciplines, offering a thorough understanding of the research background. This review identifies key research gaps, defines the research objectives, and highlights the significance of developing sustainable and comfortable PLA mattress surface fabrics with integrated sleep monitoring functionality.

Chapter 3 focuses on the production of crimped PLA filaments using the knit-de-knit technique. It details the optimization of heat-setting parameters to enhance crimped and tensile properties and the establishment of performance prediction models based on these parameters. Additionally, advancements in machinery for more efficient crimped

filament production are introduced.

Chapter 4 investigates the development of PLA weft-knitted inlaid fabrics for mattress surface applications. It explains the effects of knitting parameters and yarn types on the physical and comfort properties of the fabrics, supported by statistical analysis. Additionally, their compression durability, pilling resistance, and abrasion resistance are evaluated. All properties of the PLA fabrics are compared with those of the PET mattress surface fabrics.

Chapter 5 details the fabrication of the TCPS by integrating conductive yarns into PLA weft-knitted fabrics through a single-step intarsia knitting process. It focuses on investigating structural parameters to enhance the TCPS's capacitive performance and comprehensively evaluates its sensing behavior under varying conditions as well as overall comfort properties.

Chapter 6 focuses on the development of PLA smart mattress surface fabrics integrated with a TCPS matrix for sleep monitoring. It covers the design and fabrication of the PLA smart fabric and the development of a real-time capacitance data acquisition system, which facilitates the recording and analysis of five typical sleep behaviors from seven volunteers. Furthermore, it introduces a 1D-CNN deep learning model to classify these sleep behaviors and identify individual participants.

Chapter 7 summarizes the study's conclusions, contributions, and limitations and provides recommendations for future research.

Chapter 2 Literature Review

2.1 Introduction

This chapter provides a comprehensive review of the literature relevant to the objectives of this study. It begins by providing an overview of the sleep process and its promotion, with a focus on sleep stages, the effects of sleep deprivation, and the current approaches for improving sleep quality. Following this, attention is directed to mattress surface fabrics, emphasizing their critical role in supporting the sleep process. This section explores the definition, classification, fabrication, and commonly used materials for mattress surface fabrics, as well as the limitations associated with these materials. Additionally, the potential of poly(lactic acid) (PLA) as a sustainable and effective alternative for mattress surface fabrics is explored. The chapter also reviews prior studies aimed at enhancing the comfort of mattress surface fabrics and incorporating sleep monitoring technologies into them to promote sleep quality. Finally, it concludes by summarizing the existing literature and identifying key research gaps related to the primary objectives of this study.

2.2 Sleep process and promotion

2.2.1 Stages of sleep

Sleep is an essential biological necessity for all humans, closely associated with various physiological functions, including the restoration of the body, brain, and neurocognitive systems [58]. It is classified into two distinct types: non-rapid eye movement (NREM) sleep and rapid eye movement (REM) sleep, with NREM sleep further divided into three stages: N1, N2, and N3 [59]. A typical night of sleep consists of four to five cycles, each lasting approximately 90 to 110 minutes and generally progressing through the sequence of N1, N2, N3, N2, and REM [59]. Throughout the sleep process, individuals transition between NREM and REM multiple times. Each stage is characterized by specific physiological changes, including variations in brain wave patterns, eye

movements, and muscle tone, which collectively support the restoration and recovery of the body and brain [2].

The N1 stage, the lightest stage of sleep, marks the beginning of a gradual decrease in brain wave activity, eye movements, heart rate, and respiratory functions. This stage typically lasts approximately 1 to 5 minutes, accounting for 5% of the total sleep duration, and is easily disrupted by external noises [60]. Stage N2, a deeper stage of sleep, is characterized by a continued decline in heart rate and body temperature, along with two distinct brain activities: sleep spindles and K-complexes [60]. Sleep spindles are brief bursts of thalamocortical activity at 11–16 Hz frequencies, lasting 0.5–3 s and recurring every 3-6 s, and are associated with enhanced learning and memory performance [61, 62]. K-complexes, long delta waves lasting approximately one second, are crucial for maintaining sleep stability and supporting memory consolidation [63]. Stage N2 generally lasts 10 to 25 minutes during the first sleep cycle and gradually extends with each subsequent cycle, ultimately constituting 45–55% of the total sleep duration [64]. The N3 stage, also known as slow wave sleep (SWS), is the deepest stage of NREM sleep. It is particularly difficult to awaken individuals during this stage, which typically occurs in the first third of the night and accounts for 15–20% of the total sleep period [65]. N3 is essential for physiological restoration, including tissue repair and regeneration, bone and muscle growth, and immune system enhancement [60].

The final REM stage, often described as a restless stage of sleep, is closely associated with dreaming. During REM sleep, the individual's eyes move rapidly beneath closed eyelids, and the electroencephalogram (EEG) resembles that of an awake state [60]. The first REM cycle typically begins around 90 minutes after falling asleep, with subsequent REM cycles increasing in duration, eventually comprising 20–25% of the total sleep duration [60, 66]. A summary of the physiological changes occurring during NREM and REM sleep stages is presented in Table 2.1.

Table 2.1 Physiological changes during NREM and REM sleep stages [67-69]

| Physiological Process | During NREM | During REM | |
|--------------------------|--|----------------------------------|--|
| Eye movement | Slow | Rapid | |
| Vital signs | Steady | Fluctuating | |
| EEG | Spindles, V-waves, K-complexes, slow waves | Low voltage | |
| Dream | Uncommon | Frequent | |
| | | Increases in motor and sensory | |
| Brain activity | Reduces from wakefulness | regions, while other regions are | |
| | | compared to NREM | |
| Heart rate | Slows compared to wakefulness | Rises and fluctuates compared to | |
| Healt late | Slows compared to wakefulliess | NREM | |
| Blood pressure | Reduces from wakefulness | Rises (up to 30%) and fluctuates | |
| Blood pressure | Reduces from wakerumess | from NREM | |
| Sympathetic | Reduces compared to wakefulness | Rises considerably compared to | |
| nerve activity | | wakefulness | |
| Muscle tone | Similar to wakefulness | Absent | |
| Blood flow to | Reduces from wakefulness | Rises compared to NREM, | |
| the brain | reduces from wakerumess | depending on the brain area | |
| | | Rises and varies compared to | |
| Respiration | Reduces from wakefulness | NREM; may show short stops in | |
| | | breathing | |
| Airway | Rises from wakefulness | Rises and fluctuates compared to | |
| resistance | Rises from wakefulness | wakefulness | |
| | Decayleted at a legger set point | Unregulated; no shivering or | |
| Body | Regulated at a lower set point | sweating; drifts towards the | |
| temperature | compared to wakefulness; shivering | temperature of the surrounding | |
| | occurs at lower temperatures | environment | |
| Sexual arousal | Occurs occasionally | More frequent than during NREM | |

2.2.2 Effects of sleep deprivation

The intricate physiological processes occurring across the stages of sleep underscore its

fundamental role in maintaining both physical and mental health. However, when the natural progression of these stages is disrupted or sleep becomes insufficient, the resulting deprivation can lead to profound adverse effects on overall health [1, 2]. For healthy adults, the short-term consequences of sleep deprivation include heightened stress levels, physical discomfort, diminished quality of life, and impairments in memory and behavior. Over the long term, chronic sleep deprivation significantly elevates the risk of developing severe health conditions, including obesity, depression, cardiovascular and cerebrovascular diseases, diabetes, hypertension, kidney disease, cancer, and even premature mortality [5, 6, 70-73].

Despite the critical role of sleep in overall health, sleep-related problems have emerged as a growing global public health concern, partly driven by the accelerating pace of modern life. Recent studies reveal that 65% of individuals in the United States report experiencing sleep problems, along with 43.2% in the Netherlands [74], 31% in Western Europe, and 23% in Japan [75]. A wide range of factors contributes to insufficient sleep, including family responsibilities, excessive work demands, challenges in maintaining work-life balance, mental health issues, physical activity levels, sleep disorders, and other underlying medical conditions [73, 76].

2.2.3 Approaches to improve sleep

The importance of improving sleep quality is receiving increasing attention, with various approaches developed to enhance sleep, including lifestyle modifications [77-79], therapeutic interventions [80, 81], environmental optimization [7, 8], and smart monitoring technologies [9]. Lifestyle interventions help regulate the biological clock and promote relaxation through consistent sleep schedules [77], moderate exercise (e.g., deep breathing, yoga, and meditation) [78], and consuming sleep-promoting foods, such as fresh fruits and vegetables rich in tryptophan and B vitamins [79]. Although these methods are safe, they require sustained commitment and self-discipline, and their effects are generally mild and vary among individuals. In contrast, therapeutic

interventions, including psychological treatments like cognitive behavioral therapy for insomnia (CBT-I) [80] and pharmacological aids such as benzodiazepines or melatonin [81], are widely recognized for their effectiveness in improving sleep [82]. However, psychological interventions require long-term commitment and professional guidance, while prolonged use of pharmacological treatments poses risks such as dependence and adverse side effects.

Environmental optimization strategies, which enhance sleep quality by improving the external physical environment, are gaining increasing popularity due to their simplicity and lower reliance on self-discipline or complex treatments. These strategies include using blackout curtains, maintaining temperatures between 17–28°C, controlling humidity at 40–60%, and ensuring good air quality, all of which effectively enhance sleep depth and continuity [7]. While optimizing the overall room environment is important, attention to individual contact experiences through a well-designed bedding system is equally essential. Within the bedding system, the comfort of the mattress surface fabric plays a critical role, as it is the component of the mattress in closest contact with the human body [8]. During sleep, the body generates heat and releases moisture through the skin as part of metabolic processes [10]. A comfortable mattress surface fabric helps regulate the physiological skin microclimate, thereby promoting better sleep quality.

In addition, advancements in intelligent technologies have driven the development of smart sleep monitoring systems, which enhance sleep quality by providing scientific feedback based on sleep parameters analysis [9]. These technologies can be classified into direct and indirect contact methods. Direct contact methods include polysomnography (PSG, Figures 2.1(a) and (b)) [83-85] and wearable devices such as headbands [86], wristbands [87, 88], and smartwatches [89]. While PSG offers comprehensive and detailed data, it is costly and uncomfortable. Although more affordable, wearable devices require mandatory use, which can result in discomfort and

a sense of burden. Indirect contact methods include environmental monitoring technologies (e.g., Wi-Fi and radar) [90, 91], smartphone apps [92-94], under-mattress sensors (e.g., piezoelectric and capacitive sensors) [95, 96], and smart mattress surface fabrics [11, 53-57]. However, environmental monitoring technologies are easily influenced by external factors such as light, noise, and temperature, while smartphone apps raise privacy concerns. Under-mattress sensors, placed beneath the mattress, may experience accuracy issues due to mattress thickness, material, and movement. In comparison, smart mattress fabrics with embedded sensors provide more precise data, greater convenience, and minimal interference, making them a promising and effective solution for sleep monitoring.

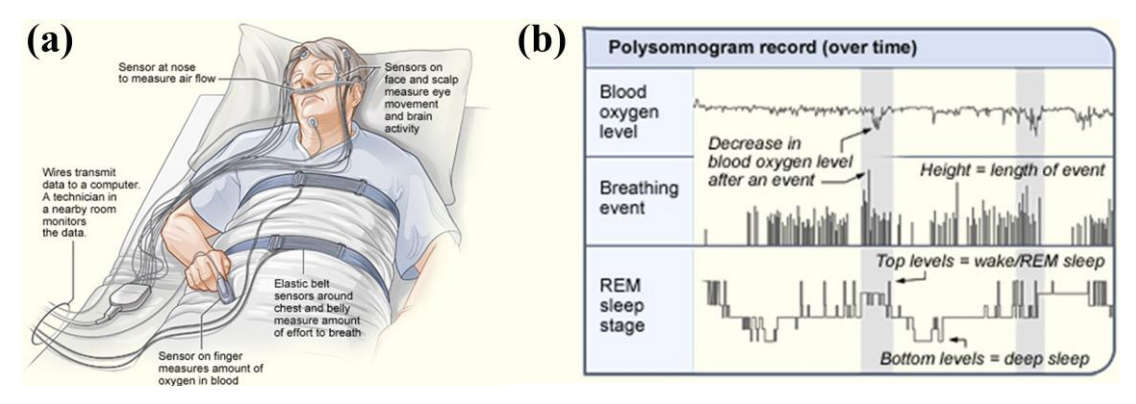


Figure 2.1 Overview of the PSG: (a) monitoring sensors; (b) typical PSG output [84].

An effective approach to enhance sleep quality involves combining multiple strategies, particularly by simultaneously optimizing the sleep environment and incorporating smart monitoring technologies. Mattress surface fabrics play a pivotal role in this process, as they seamlessly integrate both aspects. An ideal mattress surface fabric should not only provide users with exceptional comfort but also possess the ability to monitor and deliver real-time feedback on sleep states, thereby facilitating comprehensive regulation and enhancement of sleep quality. Furthermore, the mattress surface fabric is an essential component of the mattress, whereas other sleep improvement methods typically require additional devices, thus increasing complexity. Therefore, conducting in-depth research and developing high-performance mattress

surface fabrics is crucial for creating a comfortable and intelligent sleep environment. The following section will review the definition, manufacturing technologies, and common materials of mattress surface fabrics, establishing a theoretical foundation for further research.

2.3 Mattress surface fabrics

2.3.1 Definition

As the most widely used platform for sleep, mattresses are essential in providing individuals with adequate support and comfort, thereby reducing physical fatigue and promoting deeper sleep. A typical mattress is multilayered, consisting of the foundation, core layer, top layer, and surface fabric, as shown in Figures 2.2(a)–(d) [97, 98]. The foundation provides structural support and extends the mattress's lifespan [98], while the core layer, which determines overall firmness and support distribution, is typically composed of materials such as springs, latex, foam, or hybrids of these [97]. The top layer cushions the body and distributes pressure, often made from materials like foams, gels, wool, and cotton [20]. The surface fabric, also known as mattress ticking, topper, or cover, is the topmost layer positioned closest to the human body. It encases and protects the internal components of the mattress, serving as a barrier against dust, dirt, and moisture (Figure 2.3). Additionally, it significantly contributes to the mattress's aesthetic appeal and overall comfort [99]. Modern mattress covers may also incorporate materials that regulate moisture and temperature, further improving the sleep environment. Therefore, the mattress surface fabric is one of the most crucial components of the mattress, deserving detailed research. The choice of manufacturing methods and materials for the surface fabric significantly impacts its comfort performance and durability, which will be discussed in detail in the following sections.

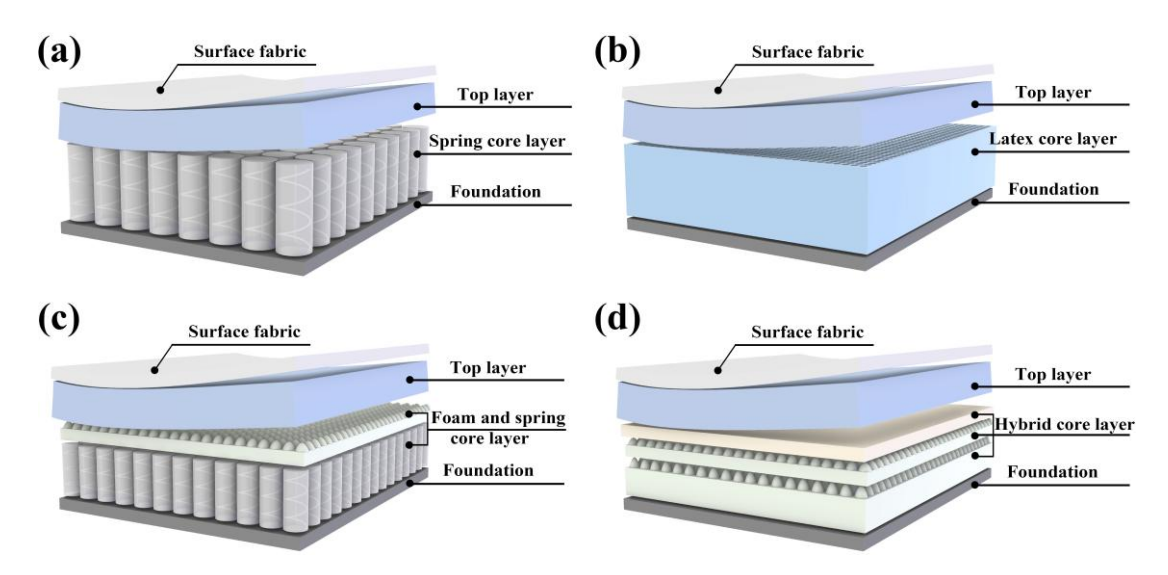


Figure 2.2 Structure of typical mattress types: (a) spring; (b) latex; (c) foam and spring; (d) hybrid.

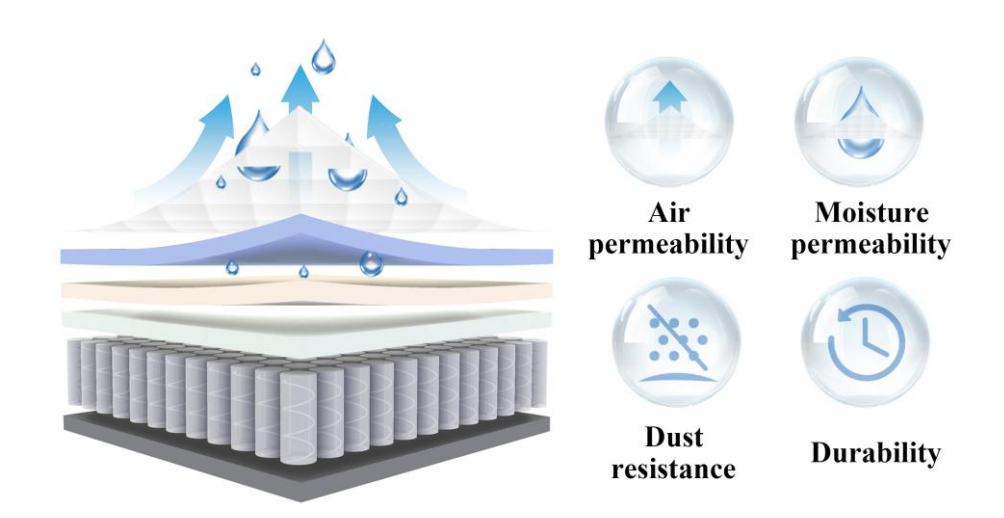


Figure 2.3 Functionality of mattress surface fabrics.

2.3.2 Classification and fabrication

Mattress surface fabrics are classified into three main types based on their manufacturing techniques: woven [12, 13], quilted [14], and knitted fabrics [15]. Woven fabrics are produced by interlacing two perpendicular yarn systems, warp and weft, on a loom, as illustrated in Figures 2.4(a) and (b). This traditional technique provides fabrics with excellent tensile strength and dimensional stability. A notable example is the double honeycomb woven fabric with self-stitching, depicted in Figures 2.5(a) and (b) [12]. Its structure incorporates enclosed air chambers formed by face-to-

face honeycomb pockets, effectively trapping air and enhancing thermal comfort. Another widely used type is the jacquard woven fabric, renowned for its intricate patterns and luxurious aesthetics, which make it a preferred choice for high-end mattresses (Figures 2.5(c) and (d)) [13]. However, the production of woven fabrics is both complex and time-intensive, involving multiple preparatory steps for warp yarns, such as winding, warping, sizing, and drawing-in, and it is prone to challenges like machine stoppages or defects caused by warp faults [16].

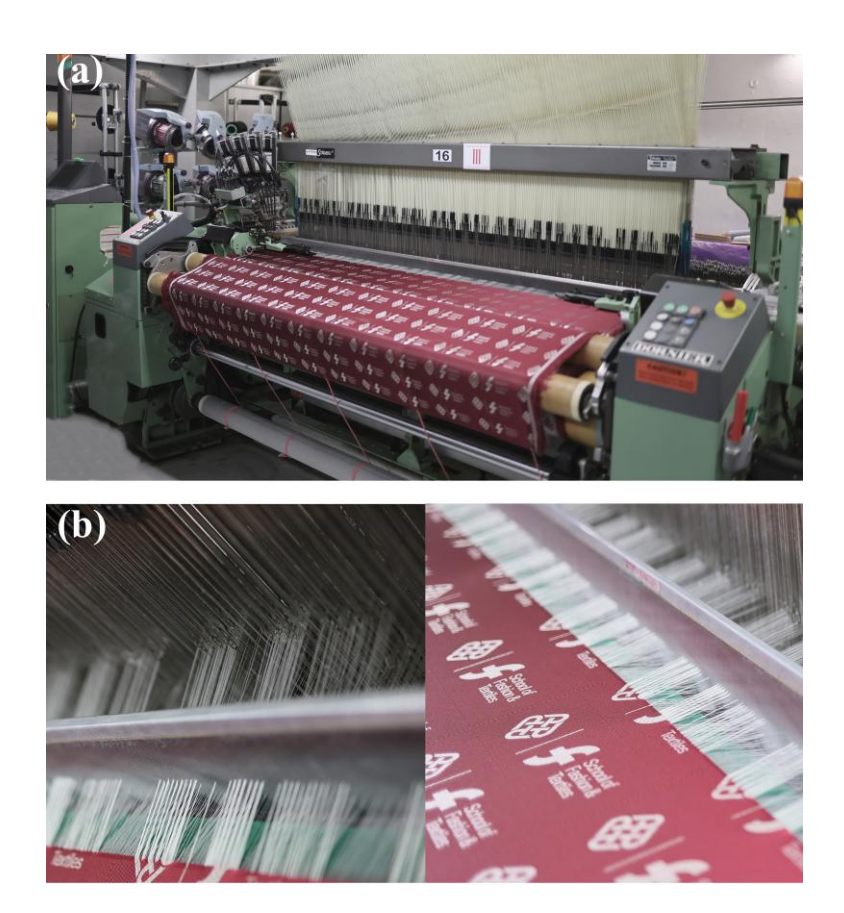


Figure 2.4 Jacquard loom: (a) full view of the machine; (b) formation of woven fabric.

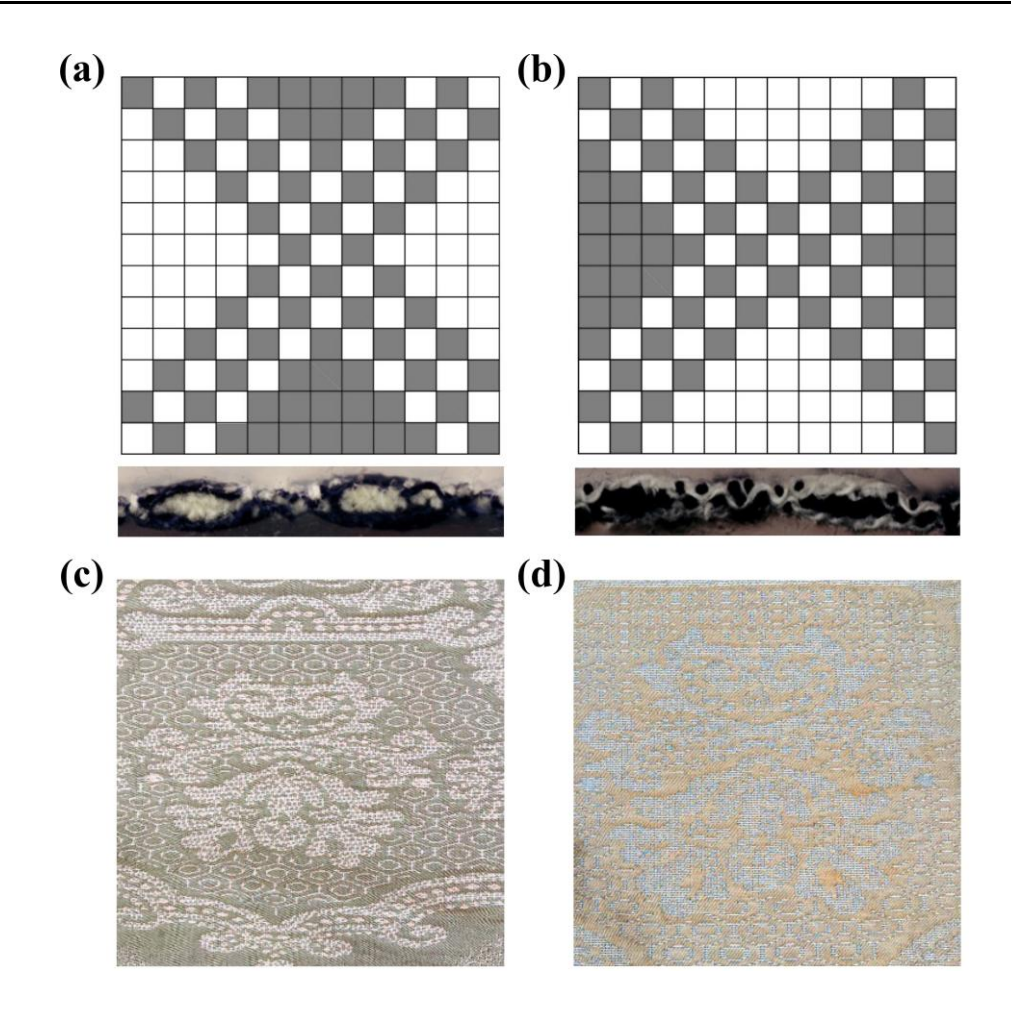


Figure 2.5 Woven mattress surface fabrics: (a) face structure and warp cross-section of a double honeycomb fabric; (b) back structure and weft cross-section of a double honeycomb fabric [12]; (c) front side of a jacquard woven fabric; (d) back side of a jacquard woven fabric [13].

Another widely used type of mattress surface fabric is quilted fabric. These fabrics are constructed by stitching together multiple layers, typically consisting of a top layer, an inner layer, and a bottom layer [14]. The top and bottom layers can comprise woven, knitted, or nonwoven fabrics, while the middle layer generally comprises a nonwoven fiber pad. The stitching process can be carried out using either traditional sewing methods or advanced ultrasonic welding techniques [100]. Figures 2.6(a)–(b) and (c)–(d) depict quilted mattress surface fabrics produced through sewing and ultrasonic quilting, respectively. The performance of quilted fabrics primarily depends on the selection of materials and the configuration of the inner layer, while their aesthetic

appeal is influenced by the stitching pattern [14]. However, their production is relatively complex and time-consuming due to the additional stitching processes involved. Furthermore, the aesthetic appeal of quilted fabrics is often regarded as simplistic, potentially failing to meet the sophisticated design expectations of consumers.

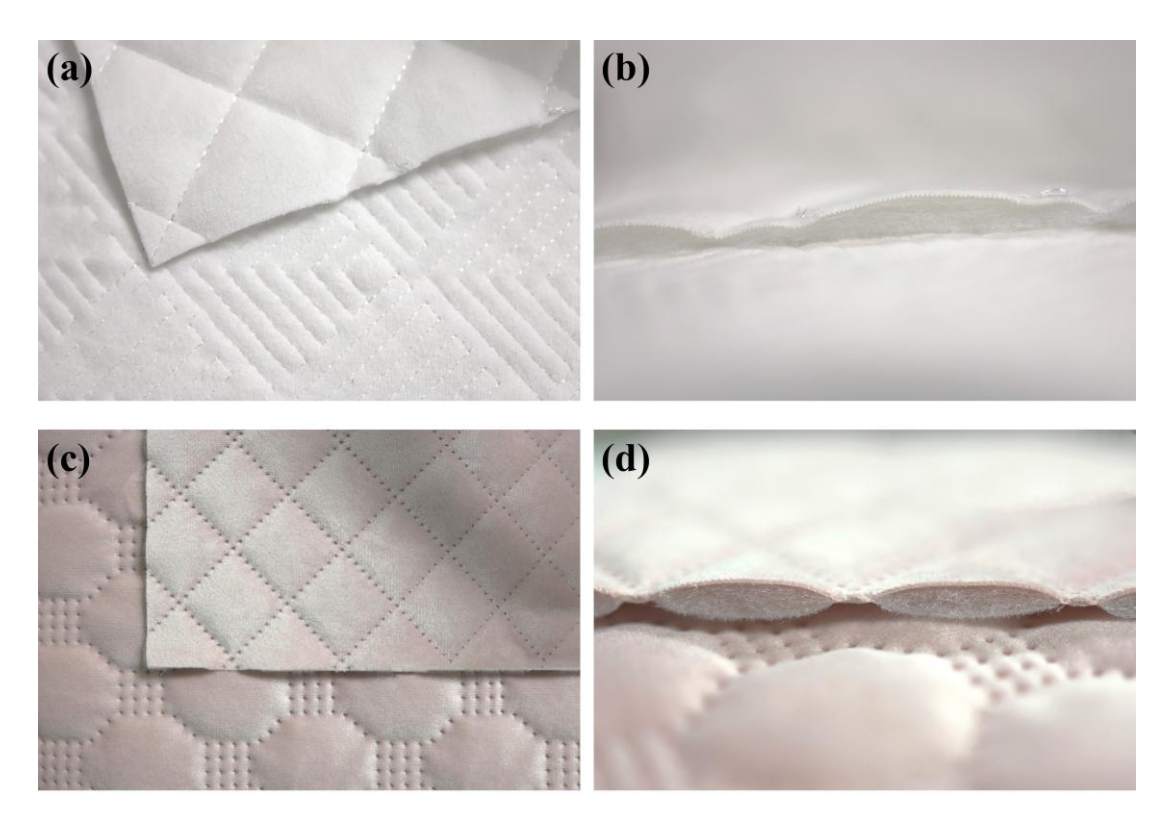


Figure 2.6 Quilted mattress surface fabrics: surface (a) and cross-section (b) images of fabric produced by sewing; surface (c) and cross-section (d) images of fabric produced by ultrasonic quilting.

Compared to woven and quilted fabrics, knitted mattress surface fabrics demonstrate superior production efficiency and simplicity. The manufacturing process for knitted fabric is faster and more economical, requiring minimal yarn preparation and producing fabric in a single step. Knitted fabrics are classified into weft-knitted and warp-knitted fabrics based on the direction of yarn movement during loop formation, as shown in Figures 2.7(a) and (b) [16]. Warp-knitted fabrics are formed vertically, with each row using a separate set of yarns on a warp knitting machine (Figures 2.8(a)–(c)) [17]. While they exhibit excellent structural stability due to their production method, warp-knitted

fabrics lack the extensibility and comfort of weft-knitted fabrics [101]. Consequently, warp-knitted fabrics are not typically used as mattress surface materials but are instead employed as cushioning components within mattresses, such as the warp-knitted spacer fabric illustrated in Figures 2.9(a) and (b) [17].

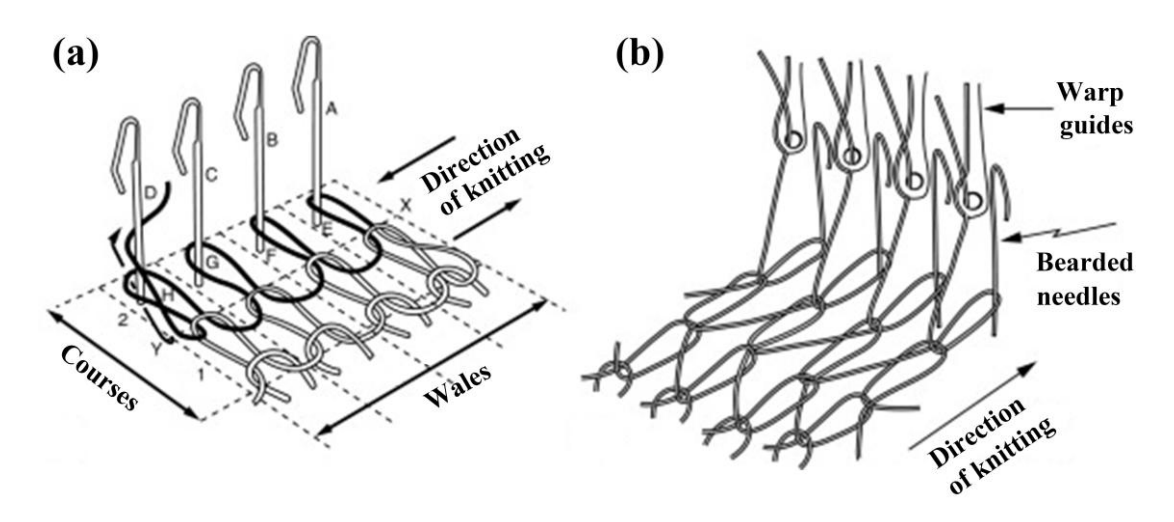


Figure 2.7 Different knitting methods: (a) weft knitting; (b) warp knitting [16].

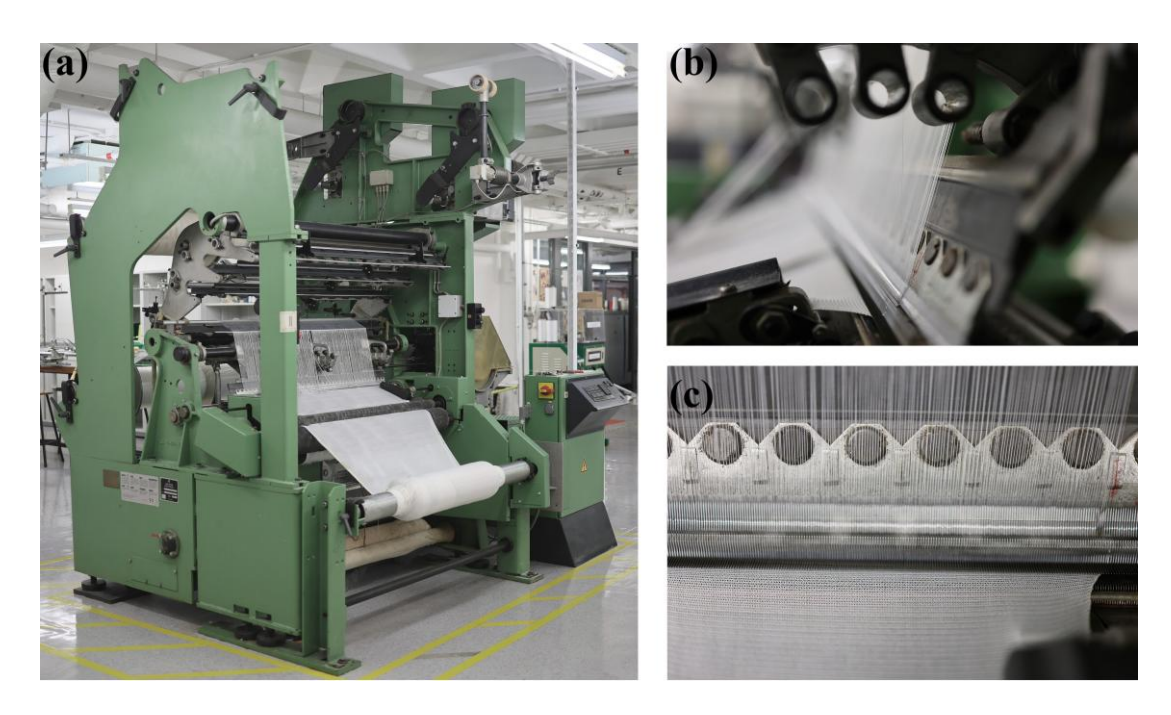


Figure 2.8 Warp knitting machine: (a) full view of the machine; (b) yarn arrangement; (c) formation of warp-knitted fabric.

Chapter 2

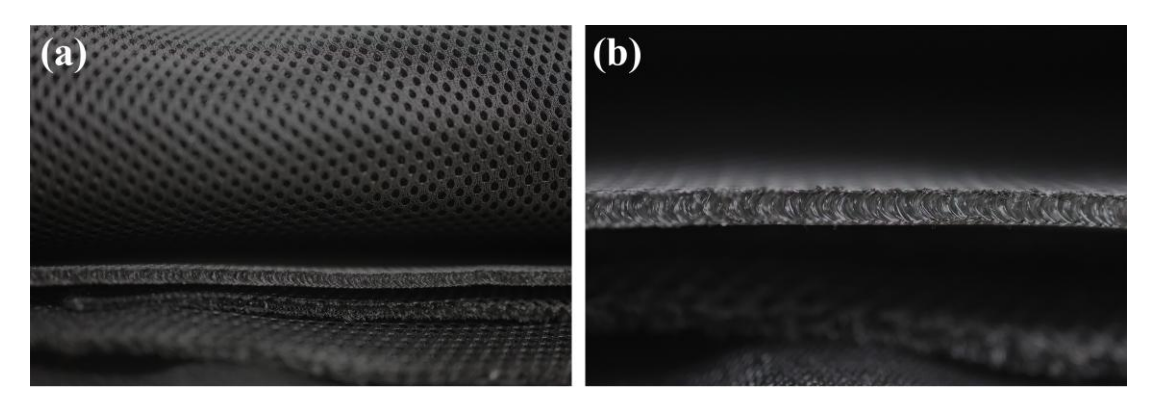


Figure 2.9 Warp-knitted spacer fabric: (a) surface; (b) cross-section.

In contrast, weft-knitted fabrics are formed horizontally, with each row utilizing a single set of yarns on circular or flat knitting machines (Figures 2.10(a)–(e)) [17]. Among these, weft-knitted inlaid fabrics are particularly popular for mattress surface applications. These fabrics are multilayered, consisting of upper, middle, and lower layers, all produced simultaneously in a single step on a weft knitting machine. Additionally, their patterns can be easily modified during production through knitting selection [15, 102]. Weft-knitted fabrics are increasingly preferred in the mattress industry for their customizable patterns, high elasticity, exceptional softness, and efficient production process [13, 17]. These advantages make weft-knitted inlaid fabrics a highly suitable choice for mattress surface material design and innovation, combining functionality with production efficiency. Therefore, the following sections will focus on the materials commonly used in weft-knitted inlaid fabrics and their associated limitations, providing a basis for further material optimization in this study.

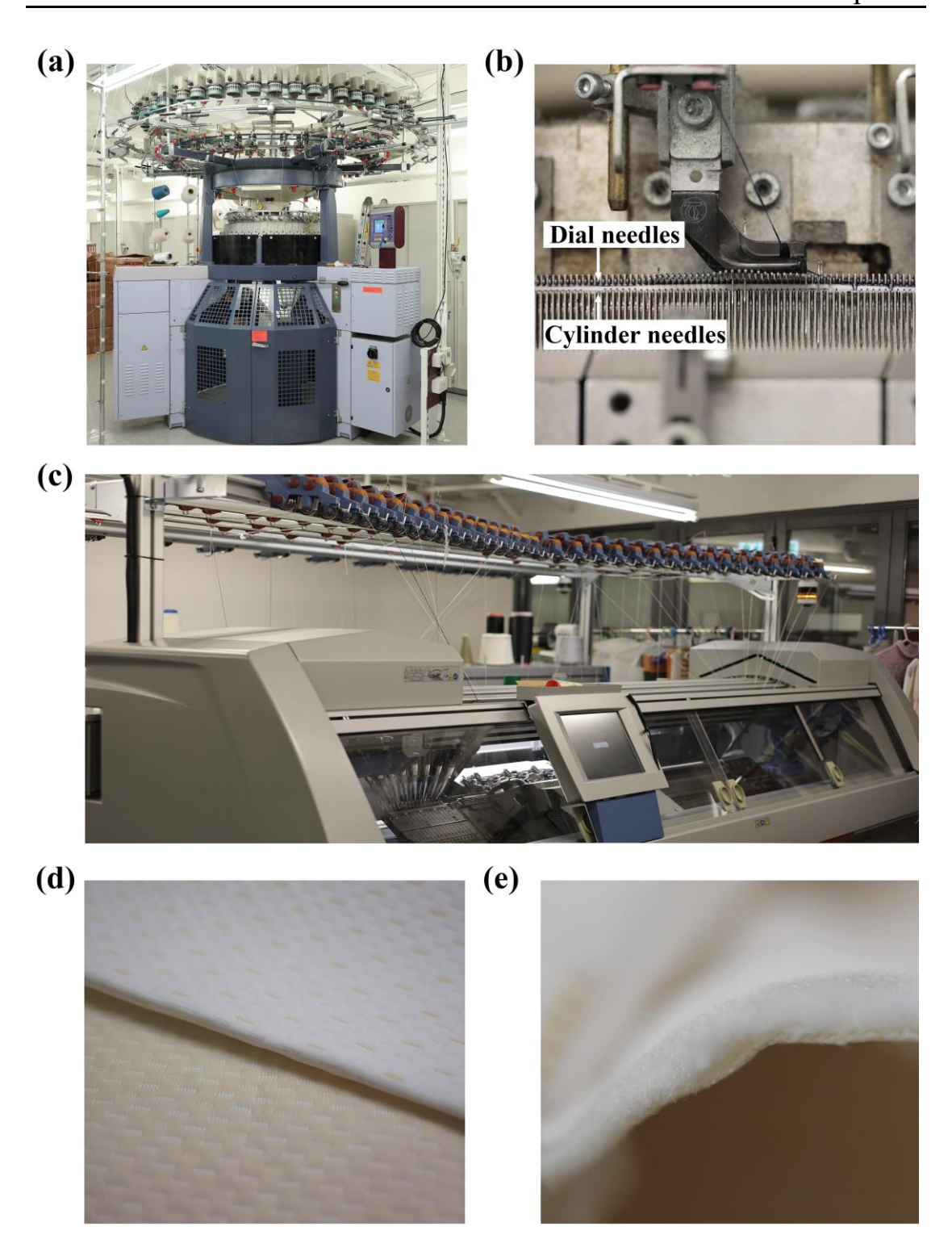


Figure 2.10 Weft-knitted machines and fabrics: (a) electronic double jacquard circular knitting machine; (b) dial and cylinder needles; (c) computerized flat knitting machine; (d) surface of weft-knitted inlaid fabric; (e) cross-section of weft-knitted inlaid fabric.

2.3.3 Materials and their limitations

The upper and lower layers of weft-knitted inlaid fabrics are manufactured from a variety of yarns, including natural yarns (wool, silk, and cotton) [20], synthetic filaments (PET, acrylic, nylon, and rayon) [13, 20-24], and functional filaments (Outlast® and Coolmax®) [25]. Among these, natural yarns are widely utilized due to their inherent comfort and environmental benefits. Wool, for instance, is highly durable and elastic, with excellent moisture absorption and heat insulation properties, making it effective for regulating temperature. However, it is prone to accumulating static electricity and is susceptible to moth damage [20]. Silk provides a smooth texture and high moisture absorbency but offers limited heat insulation. Similarly, cotton is soft and breathable but exhibits poor elasticity, limited heat retention, and vulnerability to mildew, bacteria, and silverfish [20].

Synthetic filaments also play a significant role in mattress fabric applications due to their durability, cost-effectiveness, and ease of maintenance. Acrylic and polyester are lightweight, durable, and resistant to wrinkles and microorganisms. However, their low moisture absorption, tendency to accumulate static charge, and inability to retain heat render them less suitable for certain climates [20]. Nylon, while strong, elastic, and quick-drying, can feel cool and clammy due to its low absorbency [20]. Moreover, the production of these traditional synthetic fibers relies heavily on fossil fuel resources, and their disposal creates significant environmental challenges due to nonbiodegradability and limited recyclability [35, 103]. In contrast, rayon, a regenerated cellulose fiber produced from natural feedstock, offers excellent moisture absorption and softness [23, 24]. Nonetheless, it lacks heat insulation and requires chemicalintensive production processes involving toxic substances, raising concerns regarding human health and environmental impact. Functional fibers, such as Outlast® and Coolmax®, provide temperature regulation and moisture wicking, respectively, significantly enhancing fabric comfort and practicality [25]. Nevertheless, as petroleum-based and non-degradable materials, they also contribute to environmental challenges.

The middle layer of weft-knitted inlaid fabrics for mattress surfaces is typically inserted with bulky textured filaments, which are crucial in determining the comfort properties of the fabric. These filaments can be sourced from both natural and synthetic fibers. Natural crimped fibers, such as wool, are highly effective due to their superior bulkiness and elasticity. However, their high cost and limited availability have driven the development of crimped synthetic filaments, particularly those made from PET [104]. Various methods are employed to produce crimped filaments, including false-twist, stuffer-box, gear crimping, knit-de-knit, bi-component composite spinning, and asymmetrical quenching, as illustrated in Figures 2.11 (a)–(f) [26-34, 105]. False-twist crimping forms crimps by twisting, heat-setting, and untwisting thermoplastic filaments [26], while stuffer-box crimping compresses filaments into a chamber to create sawtooth or looped crimps. Gear crimping utilizes rotating gears for crimp formation through compression [27], and advanced methods like bi-component composite spinning [29-32] and asymmetrical quenching [33, 34] rely on material composition and cooling techniques to achieve crimp structures. Among these techniques, the knitde-knit method is notable for its simplicity and adaptability. This process involves knitting thermoplastic filaments into fabrics, heat-setting them, and subsequently deknitting them to produce crimped filaments with looped shapes [28]. Compared to other methods, knit-de-knit offers economical production, adjustable crimp shapes, and consistent crimp patterns. However, like most others, crimped filaments produced using this technique are predominantly made from PET.

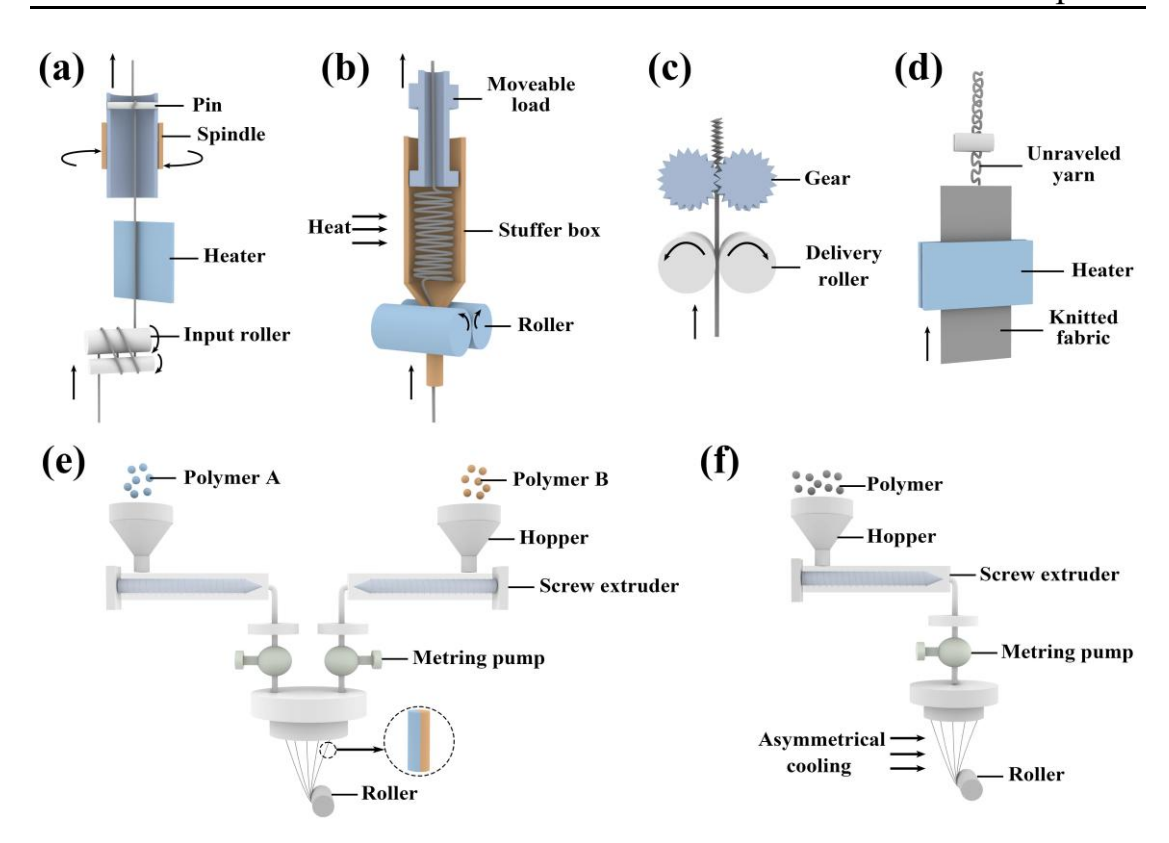


Figure 2.11 Methods for producing crimped yarns: (a) false-twist; (b) stuffer-box; (c) gear; (d) knit-de-knit; (e) bi-component composite spinning; (f) asymmetrical quenching.

Although a wide range of materials is used in mattress surface fabrics, commonly used natural fibers are more susceptible to the growth of microorganisms, such as bacteria and fungi, which can pose health risks. Traditional synthetic filaments, while functional and durable, raise significant sustainability concerns due to their reliance on non-renewable resources and non-biodegradability. These limitations highlight the necessity for alternative materials that balance functionality with environmental sustainability. In this context, PLA, a renewable and biodegradable polymer, emerges as a promising solution. The following section will explore the potential of PLA as a sustainable alternative for weft-knitted inlaid fabrics in mattress surface applications.

2.3.4 The potential of PLA for mattress surface fabrics

PLA is a polymer derived from renewable resources such as corn, cassava, sugarcane, and sugar beet. These raw materials are converted into lactic acid through microbial

fermentation, which is subsequently polymerized into PLA resin. This process is non-toxic, environmentally safe, and allows the final products to biodegrade into carbon dioxide and water [36-38]. In contrast to conventional petroleum-based polymers, PLA is not dependent on fossil fuels, aligning with the principles of sustainable development and the low-carbon economy. The process of converting lactic acid to poly(lactic acid) is depicted in Figure 2.12 [106], while its complete lifecycle, from renewable resources to biodegradable products, is illustrated in Figure 2.13 [107].

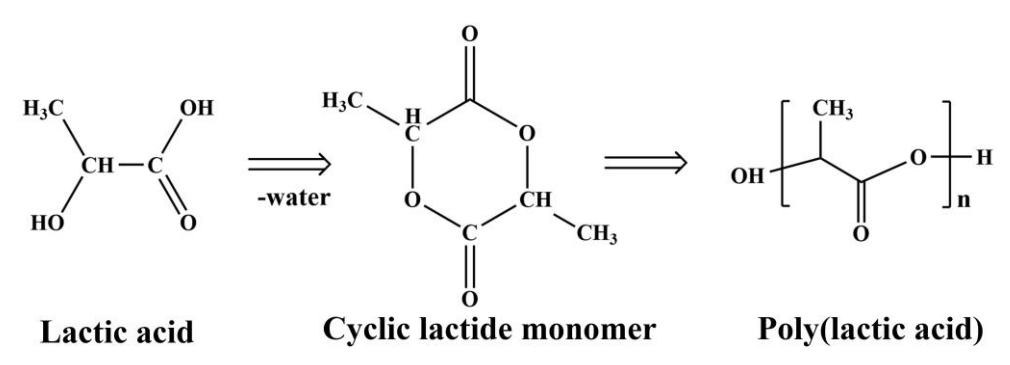


Figure 2.12 Conversion of lactic acid to poly(lactic acid).

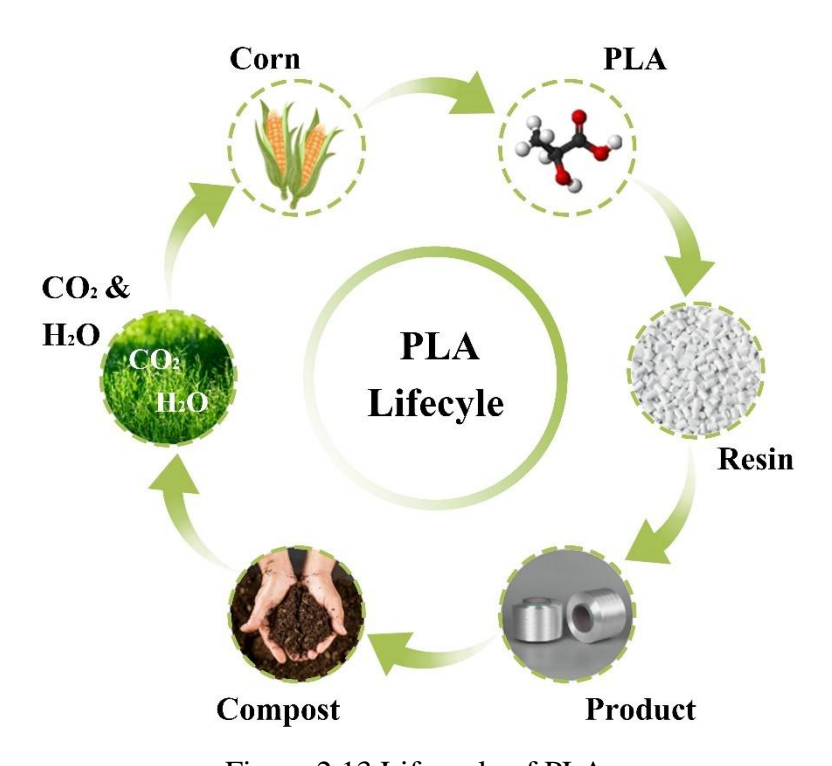


Figure 2.13 Lifecycle of PLA.

PLA is the only biodegradable polymer that can be melt-spun into textile fibers on a

large scale, making it a promising eco-friendly alternative to traditional synthetic fibers [38, 39]. Beyond its environmental benefits, PLA demonstrates excellent mechanical and functional properties, including high strength, thermoplasticity, flame retardancy, antibacterial, UV resistance, and superior processability [40-42] These attributes have enabled PLA to gain significant attention in the textile industry, with extensive research focusing on its fibers, yarns, and fabrics [43-52]. However, despite these advancements, the application of PLA in mattress surface fabrics has not been explored. Additionally, limited attention has been devoted to the development of bulky textured PLA filaments, which are critical for specific textile applications. This limitation hinders the potential use of PLA as inlaid yarns in the middle layer of mattress surface fabrics, highlighting the necessity for further innovation and development in this area.

2.4 Research on mattress surface fabrics

2.4.1 Enhancing comfort

The performance of mattress surface fabrics significantly influences human sleep quality and overall health, making it a key focus of extensive research. An ideal mattress surface fabric should provide sufficient comfort by effectively regulating the exchange of air, heat, and moisture between the body and its surroundings [25]. The primary comfort properties include air permeability, water vapor permeability, and thermal insulation. Air permeability, defined as the ability of a fabric to allow air to pass through, is essential for maintaining comfort in different climates. High air permeability promotes air circulation around the skin, which enhances comfort in hot conditions but can cause discomfort in colder environments by accelerating heat loss. Similarly, adequate water vapor permeability is essential for transferring perspiration and moisture away from the skin, helping to maintain a dry and comfortable sleep environment [108]. Thermal insulation, which governs heat transfer, directly impacts the body's thermal balance and is essential for overall comfort [109]. These properties significantly influence mattress selection and have driven research efforts to optimize air permeability, water vapor permeability, and thermal insulation to improve sleep

quality and maximize user comfort.

Salama et al. [12] investigated the development of a double-layer honeycomb fabric structure featuring self-stitching through a weaving method, aimed at enhancing thermal insulation for bed covers. Their study systematically analyzed the effects of weft density and weft yarn count on the fabric's physical and thermal properties. By employing 24/2Ne yarns for both warp and weft, the researchers directly compared the honeycomb structure and a reversible weft-backed fabric. The results demonstrated that, under optimal conditions, the honeycomb fabric achieved up to 59% higher thermal insulation than the reversible weft-backed fabric. However, the weaving process is quite intricate, and the study focuses only on improving thermal insulation, neglecting other important aspects such as fabric elasticity, hand feel, and aesthetic appeal, which are essential for achieving a more well-rounded fabric performance.

Vlad and Cioca [110] explored the influence of raw materials and weaving patterns on the air permeability of woven mattress surface fabrics. Their research involved creating nine fabric samples with four distinct weave designs: plain weave, 2/2 basket, 4/4 basket, and warp rips. The fabrics were produced using blended yarns made from polyester, cotton, organic cotton, polypropylene, viscose, and bamboo. The findings indicated that warp rips and basket weaves demonstrated superior air permeability. However, the study focuses solely on the air permeability, ignoring other comfort aspects. Despite using diverse yarn types, including natural, synthetic, and functional, each has drawbacks such as environmental concerns, low durability, or suboptimal comfort. Additionally, the labor-intensive warping process and high production costs limit the application of this weaving method.

Shirazi and colleagues [14] studied the functional performance of multi-layered fabrics for mattresses, focusing on comfort-related properties such as thermal transmittance, air permeability, fabric weight, and thickness. The study examined twelve multilayered

fabrics, each composed of a top woven layer (satin or honeycomb weave), a middle polyester nonwoven padding layer (single or double-layer), and a bottom nonwoven layer, all stitched together. The results revealed significant relationships between the structural features and functional properties: increased padding weight improved thermal insulation but reduced air permeability; honeycomb weaves offered higher thermal transmittance compared to satin weaves; and viscose fibers outperformed polyester and cotton in thermal transmittance due to their less uniform cross-sections. However, the complex manufacturing process, requiring separate production and assembly of each layer, poses challenges for large-scale applications.

In addition to woven and multilayered quilted fabrics, weft-knitted fabrics have attracted significant attention for mattress surface applications due to their structural flexibility, softness, and high production efficiency. Onal and Yildirim [25] studied the thermal comfort properties of knitted spacer fabrics incorporating functional fibers such as Outlast® and Coolmax®. Their findings highlighted that fabric design played a crucial role, with open-skin structures demonstrating higher thermal resistance and water vapor permeability than closed-skin designs due to their meshed configuration and increased thickness. Additionally, increasing the composition of Outlast® fibers enhanced thermal absorptivity, creating a cooler sensation. Despite these advantages, functional fibers were applied only to the front face layer of the spacer fabric, with conventional polyester yarns used for binding and reverse layers. The study emphasized the potential of knitted spacer fabrics for temperature regulation, but primarily as cushioning materials rather than as soft mattress surface fabrics.

Terliksiz et al. [111] investigated the comfort properties of double jersey mattress ticking fabrics by assessing their transfer wicking, vertical wicking, and drying rate. The fabrics included cotton, viscose, polyester, and cotton/polyester blends. The results indicated that hydrophilic cotton and viscose fibers exhibited superior transfer wicking, while hydrophobic polyester fabrics demonstrated the fastest drying rates, and

cotton/polyester blends provided the highest vertical wicking performance. In a separate study, Terliksiz et al. [23] evaluated the thermal comfort properties of double-layered mattress ticking fabrics made with cotton, polyester, modal, and viscose fibers on the surface, and thick bulk continuous filaments in the middle layer. The findings highlighted fabric thickness as the most critical factor influencing thermal resistance, air permeability, and water vapor permeability. However, using synthetic fibers poses environmental challenges, and the limited availability of natural fibers emphasizes the importance of developing more sustainable and resource-efficient materials for mattress surface fabric production.

Wan et al. [112] explored the use of polyester yarns modified with coffee carbon particles to produce knitted mattress fabrics, focusing on their antibacterial performance, thermal-wet comfort, pilling, and abrasion properties. The results demonstrated that including coffee carbon particles significantly enhanced the antimicrobial properties of the fabrics. Additionally, the microporous structure of the activated carbon, characterized by its high specific surface area, was found to improve the fabric's moisture management capabilities. However, despite these benefits, the chemical modification process involved is complex, potentially leading to increased production costs and raising concerns about environmental pollution.

Sapancı et al. [113] investigated the development of thermo-regulating knitted mattress fabrics using microcapsules containing phase change materials (PCMs), specifically n-hexadecane and n-octadecane, encapsulated in gum arabic and gelatin shells. The study compared the thermal storage and mechanical properties of these laboratory-produced microcapsules with those of commercially available microcapsules and their blends. The results indicated that the laboratory-produced microcapsules exhibited higher thermal storage capacities than the commercial ones, while the blended microcapsules demonstrated improved thermal performance and more uniform distribution. Furthermore, the microencapsulation process enhanced the bursting strength and

thermal comfort of the fabrics. However, challenges persist, as the performance of PCMs may degrade after repeated washing, and the complexity and cost of the microencapsulation process, along with environmental and health concerns, constrain their long-term viability for textile applications.

2.4.2 Integrating sleep monitoring technologies

Sleep monitoring involves measuring and recording an individual's sleep status and behaviors, serving as a vital tool for identifying and addressing sleep-related issues. With growing awareness of the negative impacts of poor sleep quality on human health, interest in sleep monitoring technologies has risen significantly [84]. Smart mattress surface fabrics have emerged as an innovative and popular solution in this field, gaining attention for their indirect contact, comfort, and user-friendly features. These fabrics monitor body pressure distribution [11], sleep posture and position [53, 54], ECG and BCG signals [55, 56], and respiratory rate [57] by detecting changes in interface pressure between the body and the mattress, as well as utilizing sensors and electrodes embedded within the mattress.

Wong et al. [11] evaluated the ForeSite PTTM pressure-sensing mattress cover system, which was specifically designed to reduce interface pressure and prevent pressure ulcers in hospitalized patients. The system comprised a flexible sensor-embedded mattress cover positioned beneath the bed linen and a bedside liquid crystal display (LCD) monitor that provided real-time visual feedback on pressure distribution (Figures 2.14(a) and (b)). By utilizing a capacitive sensor array, the system continuously monitored interface pressure, enabling healthcare providers to identify pressure points and receive alerts for timely patient repositioning. The study demonstrated that the system effectively reduced interface pressure and enhanced repositioning strategies, thereby contributing to the prevention and management of pressure ulcers. However, its reliance on embedding sensors into a separate mattress cover introduces additional connections and components, potentially compromising user comfort and increasing

the complexity of the system.



Figure 2.14 The patient turn system: (a) the bedside liquid-crystal display; (b) the flexible sensor mattress cover [11].

Pimenta et al. [53] developed an intelligent mattress cover system for continuous monitoring of body position and movement. This system integrated eight bands of conductive yarns into the mattress cover using conventional textile production processes. These conductive yarns functioned as sensors, detecting body movements and pressure changes by their changeable resistance. The bands were connected to an electronic sensor module embedded in the mattress cover, which is responsible for collecting, processing, and filtering the data. The processed information was transmitted wirelessly to a remote server application for analysis and storage. This intelligent mattress cover system demonstrated potential for applications in both home and healthcare settings, offering real-time monitoring to assist caregivers in tracking patient activity and immobility. Despite its effectiveness, the multi-step integration of conductive yarn bands adds significant complexity and maintenance challenges, emphasizing the need for a more efficient single-step manufacturing approach, such as weft knitting technology.

Meier et al. [54] explored the use of neural networks for recognizing patient behaviors using a smart mattress cover equipped with resistive pressure and humidity sensors (Figure 2.15(a)). Their study introduced a machine learning-based framework (Figure 2.15(b)) capable of classifying patient states into three fundamental categories:

unoccupied bed, calm sleep, and active movements. Although the results demonstrated high classification accuracy (Figure 2.15(c)), the recognized behaviors are limited to relatively simple patterns. Furthermore, the research utilized commercially available sensors embedded in the mattress cover, without introducing advancements in fabric design or sensor technology. This lack of hardware development hinders the potential for improved sensor integration, while the simplicity of the machine learning framework limits its ability to identify more complex behaviors.

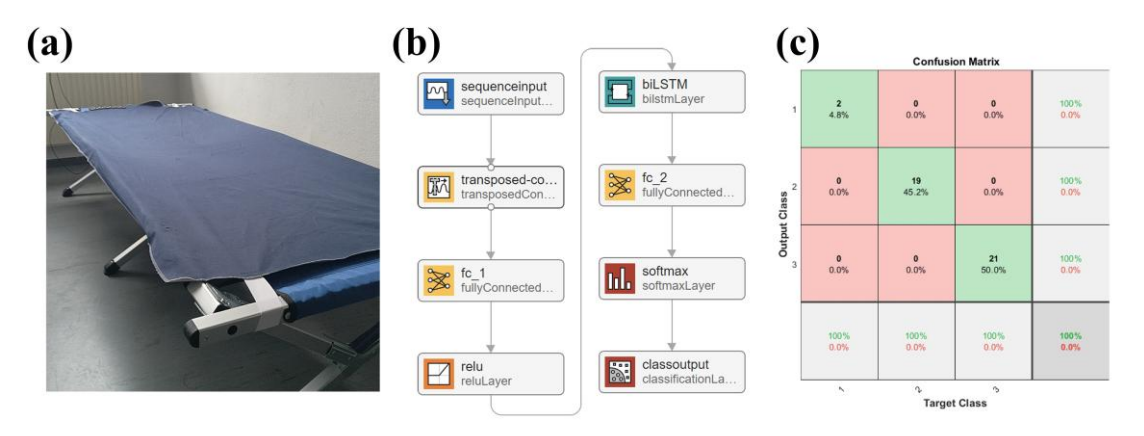


Figure 2.15 Smart mattress cover system: (a) physical setup; (b) neural network framework; (c) classification results [54].

Peng et al. [55] designed a smart mattress capable of measuring ECG and BCG signals through clothing, providing a comfortable and unobtrusive sleep monitoring solution. The mattress incorporated three electrodes made of silver fiber conductive fabric, ensuring user comfort without disturbing sleep (Figures 2.16(a) and (b)). The system also included a signal acquisition module, a data transmission module, and a user interface. To reduce electromagnetic interference, two equipotential shielding layers were placed beneath the signal-sensing electrodes. Experimental results demonstrated the system's effectiveness in measuring ECG and BCG signals through clothing, with high correlation values for R-R intervals (0.988) and J-J intervals (0.963) and minimal error (Figures 2.16(c) and (d)). However, the setup of conductive fabric and equipotential shielding layers adds design complexity, and the limited number of electrodes may restrict the system's ability to detect other sleep states or support more

multifunctional applications.

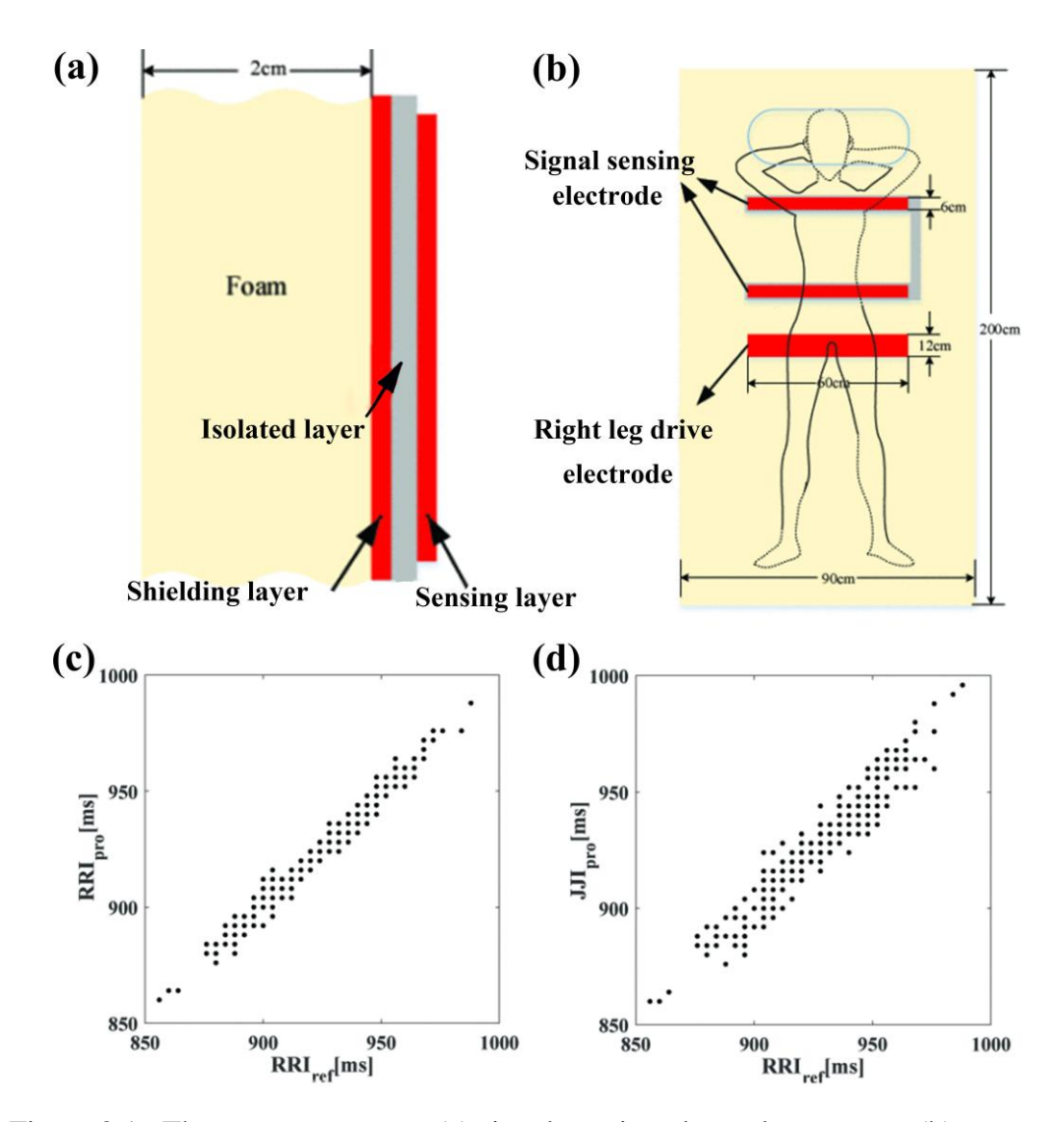


Figure 2.16 The mattress system: (a) signal-sensing electrode structure; (b) mattress schematic; (c) scatter plot of RRI correlation; (d) scatter plot of JJI correlation [55].

Babušiak et al. [56] developed a mattress topper integrated with capacitive textile ECG electrodes for non-contact ECG monitoring. The sensing system included eight active and one reference electrode, all fabricated from electroconductive single jersey fabric with a silver-coated polyamide core. These electrodes, along with a grounded electrode to improve signal quality, were integrated into the mattress topper (Figures 2.17 (a) and (b)). The system also contained a control unit for data acquisition, processing, and USB transmission to a computer, with its connection to the topper shown in Figure 2.17 (c).

Experimental validation confirmed its effectiveness in measuring ECG signals, highlighting its potential for non-contact cardiac monitoring. Nonetheless, the additional embedded components increase fabrication complexity, and the durability of the electrodes during washing remains a notable challenge.

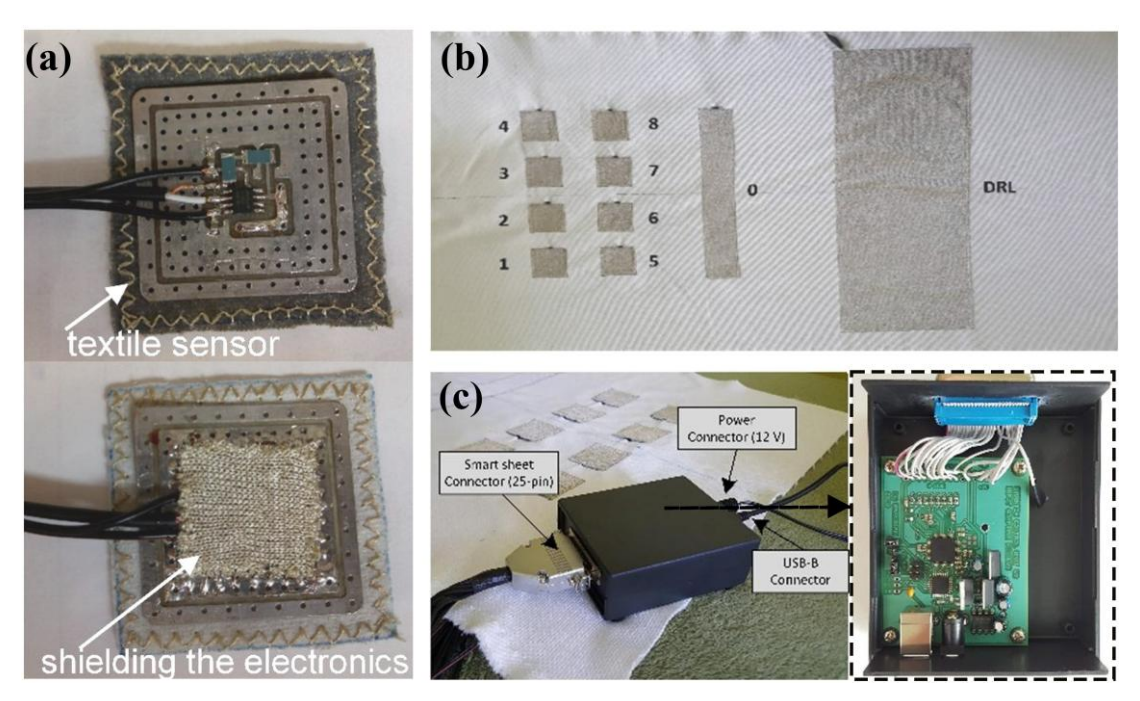


Figure 2.17 Smart mattress topper system: (a) the active ECG electrode; (b) the smart mattress topper; (c) the control unit [56].

Cay and colleagues [57] proposed a smart mattress topper for real-time sleep behavior and respiratory rate monitoring. This system incorporated smart textile pressure sensors made from piezoelectric conductive materials, connected via conductive tapes. These sensors detected subtle pressure changes, such as respiration cycles and changes in sleeping posture. The collected data was initially stored in a comma-separated values (CSV) file and then transmitted to a tablet application via Bluetooth for visualization and further analysis. Despite its potential as an unobtrusive method for sleep monitoring, using conductive tapes for sensor connections raises concerns about mechanical durability, production complexity, and scalability, limiting its practicality for large-scale use.

2.5 Conclusions

This chapter presented a systematic review of the literature relevant to this study, focusing on the sleep process and its promotion methods, the properties of mattress surface fabrics, and the existing related research. The findings emphasize the critical importance of sleep quality for both physiological and psychological health. Enhancing sleep quality requires the combined use of several strategies, particularly optimizing the sleep environment and incorporating advanced monitoring technologies. Mattress surface fabrics are essential in this process, as they influence the body-mattress contact environment, with comfort surface fabrics contributing to improved sleep quality. Furthermore, by integrating sensing technologies, these fabrics enable real-time monitoring of sleep behaviors, providing valuable insights that can further enhance sleep quality.

Currently, multilayered weft-knitted inlaid fabrics are the predominant choice for mattress surface fabrics, but their frequently used raw materials present significant limitations. Commonly used natural fibers are susceptible to bacterial growth, posing hygiene concerns, whereas traditional synthetic fibers are petroleum-based and non-degradable, leading to environmental challenges. In contrast, PLA stands out as a promising alternative due to its bacteriostatic properties, renewable origins, and biodegradable nature. Despite its potential, the application of PLA in mattress surface fabrics remains underexplored. In particular, there is a lack of research on the development of bulky textured PLA filaments and their application in weft-knitted inlaid fabrics to improve both sustainability and comfort.

On the other hand, while sensing technology has introduced smart monitoring to mattress fabrics, current approaches primarily rely on the additional integration of external sensors or electrodes. These methods involve a complex, multi-step manufacturing process that not only increases production costs and maintenance challenges but also potentially compromises the fabric's overall comfort and user

experience. To overcome these challenges, developing a smart mattress surface fabric made from PLA materials and manufactured in a single step using weft knitting technology presents an ideal solution. This proposed fabric would seamlessly integrate comfort and sleep monitoring capabilities. Therefore, this study focuses on the production and optimization of crimped PLA filaments, exploring their application in both comfort-oriented and smart mattress surface fabrics, with the aim of providing sustainable and effective solutions to advance intelligent sleep systems.

Chapter 3 Fabrication of Crimped PLA Filaments

3.1 Introduction

As reviewed in Chapter 2, a critical component of weft-knitted inlaid mattress surface fabrics is the middle layer, which is filled with inlaid filaments. The selection of these inlaid materials is pivotal, as this layer determines the fabric's thickness and mass per unit area, directly influencing properties such as air permeability. Among potential materials, crimped filaments are a preferred choice due to their excellent bulkiness, resilience, and elasticity. These filaments are commonly produced using methods such as false-twist [26], stuffer-box, gear crimping [27], bi-component composite spinning [29-32], and asymmetrical quenching [33, 34]. However, these production techniques face inherent challenges, such as inconsistent crimped morphologies, high complexity, and cost. Moreover, the raw materials predominantly rely on petroleum-based synthetics like PET, raising environmental concerns. In comparison, the knit-de-knit technique offers a cost-effective and convenient approach for producing crimped filaments with regular and uniform crimps [28]. Despite its potential, no research has been conducted on fabricating sustainable crimped PLA filaments using this technology.

This chapter aims to develop crimped PLA filaments efficiently and economically, achieving the desired crimped and tensile properties for application in mattress surface fabrics. It begins by introducing the fabrication process of crimped PLA filaments using the knit-de-knit method, including PLA material selection, knitted structure design, and heat-setting conditions. Property evaluation methods of the crimped PLA filaments are then described. The effects of key production parameters, including heat-setting temperature and time, on the crimped and tensile properties of the filaments are thoroughly analyzed with the support of statistical evaluation. The optimal heat-setting conditions for producing crimped PLA filaments are identified, and prediction models for various filament properties are developed. Production efficiency is further improved by designing and fabricating knit-de-knit machines, and the resulting morphologies and

properties of the optimized crimped PLA filaments are presented. Finally, the micromorphology and crystallinity of 150D crimped PLA filaments under different heat-setting conditions are analyzed to explain the variations in their crimped and tensile properties. This comprehensive investigation provides valuable insights into the production and performance optimization of crimped PLA filaments for advanced textile applications.

3.2 Materials and methods

3.2.1 Materials

Four types of normal PLA filaments with linear densities of 150D, 450D, 600D, and 900D were purchased from Ruomi Technology Co., Ltd. (Qingdao, China) for the production of crimped PLA filaments. Notably, the 450D, 600D, and 900D filaments were formed by merging 3, 4, and 6 strands of 150D PLA filaments, respectively. Table 3.1 provides the detailed technical specifications for these PLA filaments, including linear density measured according to ASTM D1907-01 [114] and tensile properties (tenacity and elongation) tested in accordance with ASTM D2256 [115].

Table 3.1 Technical specifications of normal PLA filaments

| Yarn | Linear density (D) | Tenacity (cN/tex) | Elongation (%) |
|-----------|--------------------|-------------------|----------------|
| 150D PLA | 152.62 | 28.48 | 25.06 |
| 130D PLA | (± 0.12) | $(\pm \ 0.89)$ | $(\pm \ 0.64)$ |
| 450D DI A | 458.15 | 19.41 | 24.16 |
| 450D PLA | (± 1.45) | (± 1.17) | $(\pm \ 0.99)$ |
| 600D DI A | 609.75 | 19.53 | 22.17 |
| 600D PLA | (± 0.31) | $(\pm \ 0.95)$ | (± 0.91) |
| 000D DL A | 905.18 | 17.83 | 23.07 |
| 900D PLA | (± 1.34) | $(\pm \ 0.96)$ | $(\pm \ 0.99)$ |

Note: Standard deviations are given in parentheses.

3.2.2 Fabrication

To efficiently develop crimped PLA filaments with regular and desirable crimped

shapes, this study employed the knit-de-knit technology with normal PLA filaments as the raw material. As shown in Figure 3.1, PLA filaments with different linear densities were first knitted into the fabric using a circular knitting machine, with a tubular jersey stitch chosen to allow easy unraveling. Specifically, a 24-gauge circular knitting machine (HC21K, Wuxi Hongcheng Textile Machinery Electronic Co., Ltd.) was used for knitting 150D PLA filaments, while a 10-gauge machine (QJF95, Hangzhou Qianzhou Knitting Machinery Co., Ltd.) was employed for knitting 450D, 600D, and 900D filaments. The images and technical details of these PLA fabrics are presented in Figures 3.2(a)–(d) and Table 3.2. Fabric properties, including grams per square meter (GSM), thickness, and various densities, were measured according to ASTM D3776-09 [116], ASTM D1777-96 [117], ASTM D3887-96 [118], respectively.

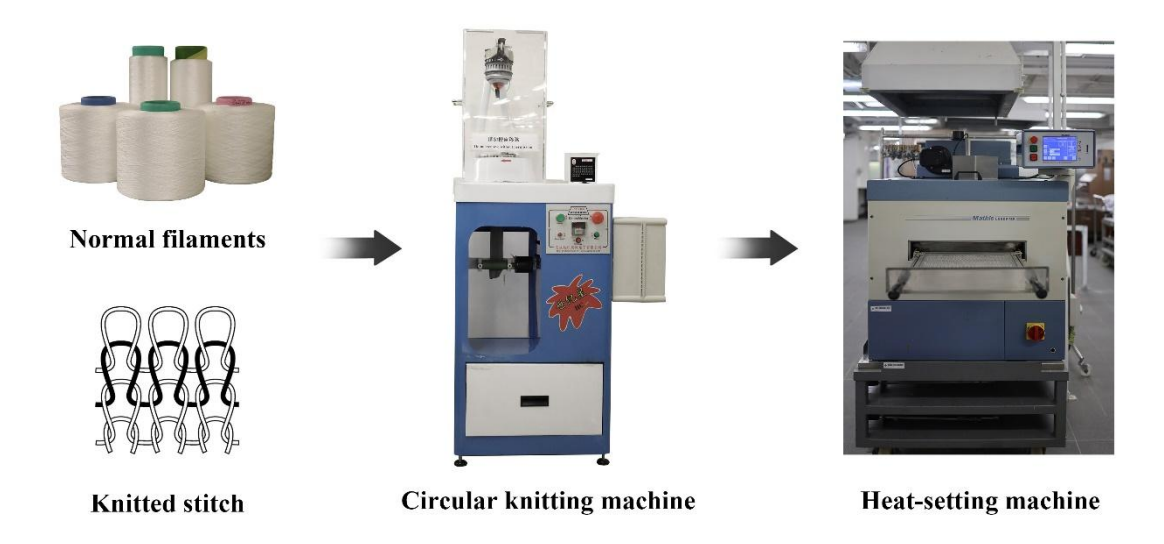


Figure 3.1 The knitting and heat-setting processes of crimped PLA filaments.

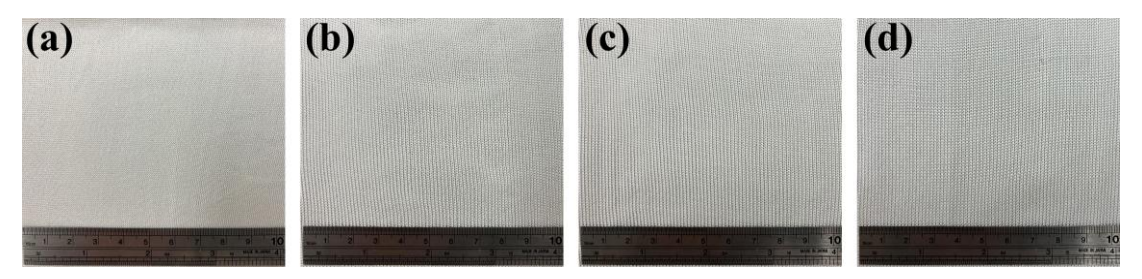


Figure 3.2 Images of knitted PLA fabric: (a) 150D PLA fabric; (b) 450D PLA fabric; (c) 600D PLA fabric; (d) 900D PLA fabric.

Table 3.2 Details of knitted PLA fabrics

| Fabric code | GSM (g/m²) | Thickness (mm) | Stitch density | | |
|-----------------|---------------|----------------|----------------|----------------|--------------------------|
| | | | Course density | Wale density | Stitch density |
| | | | (wales/cm) | (courses/cm) | (loops/cm ²) |
| 150D PLA fabric | 119.86 | 0.57 | 14.17 | 14.17 | 200.88 |
| | (± 1.82) | $(\pm \ 0.01)$ | (± 0.00) | (± 0.32) | (± 4.56) |
| 450D PLA fabric | 199.54 | 0.93 | 7.87 | 9.71 | 76.47 |
| | (± 2.29) | (± 0.02) | $(\pm \ 0.00)$ | (± 0.19) | (± 1.46) |
| 600D PLA fabric | 256.60 | 0.96 | 7.35 | 9.78 | 71.84 |
| | (± 0.98) | (± 0.01) | $(\pm \ 0.19)$ | $(\pm \ 0.09)$ | (± 1.60) |
| 900D PLA fabric | 347.34 | 1.02 | 7.55 | 8.66 | 65.36 |
| | (± 1.84) | (± 0.01) | (± 0.09) | $(\pm \ 0.00)$ | (± 0.80) |

Note: Standard deviations are given in parentheses.

The PLA fabrics were then dry heat-treated to stabilize the crimped structure, using an LTE heat-setting machine (Werner Mathis AG, Switzerland). Wet heat-setting was avoided because PLA is susceptible to hydrolytic degradation when exposed to moisture due to the presence of ester groups in its main chain [42]. During heat-setting, temperature and time are the two primary factors influencing filament properties. Thus, this study focused on optimizing and analyzing these two parameters in detail. The heat-setting temperature was set between 80°C and 160°C, exceeding the glass transition temperature (T_g) of PLA (40–70°C) [119], but remaining below its crystalline melting point (T_m) of 167.2°C [120]. The heat-setting time was ranged from 20 to 120 s. Specific heat-setting conditions are outlined in Table 3.3. After heat treatment, the PLA fabrics were unraveled to obtain crimped filaments with typical knitted-loop shapes for subsequent performance evaluation.

Table 3.3 Conditions for dry heat-setting

| Temperatur (°C) Time (s) | e 80 | 100 | 120 | 140 | 160 |
|--------------------------|-----------|------------|------------|------------|------------|
| 20 | 80°C/20 s | 100°C/20 s | 120°C/20 s | 140°C/20 s | 160°C/20 s |

| 40 | 80°C/40 s | 100°C/40 s | 120°C/40 s | 140°C/40 s | 160°C/40 s |
|-----|------------|-------------|-------------|-------------|-------------|
| 60 | 80°C/60 s | 100°C/60 s | 120°C/60 s | 140°C/60 s | 160°C/60 s |
| 90 | 80°C/90 s | 100°C/90 s | 120°C/90 s | 140°C/90 s | 160°C/90 s |
| 120 | 80°C/120 s | 100°C/120 s | 120°C/120 s | 140°C/120 s | 160°C/120 s |

3.3 Property evaluation

Before performance evaluation, all samples were pre-conditioned for 24 hours under a standard atmosphere of $20 \pm 2^{\circ}$ C and $65 \pm 2\%$ relative humidity, in accordance with ISO 139 standard [121].

3.3.1 Differential scanning calorimetry

Differential scanning calorimetry (DSC) was employed to analyze the thermal properties of PLA filaments using a DSC 8000 (PerkinElmer, USA). Each sample, weighing between 3 to 5 mg, was initially heated from 30°C to 200°C at a heating rate of 10°C/min and held at 200°C for 1 minute. The sample was then cooled back to 30°C at the same rate of 10°C/min. All measurements were conducted under a nitrogen atmosphere with a 20 mL/min flow rate to prevent oxidation or thermal degradation during the analysis.

3.3.2 Crimped properties

The crimped properties, including crimp number, crimp ratio, and crimp elastic ratio, were evaluated following the Chinese National Standard GB/T 14338-2008. For each test, specimens were prepared with a relaxed length of 25 mm. A light load of 0.002 cN/dtex was initially applied, and the filament length was recorded as L_0 . The total number of crimp peaks and valleys (J_{Ai}) within the crimped measured length (L_i) of the specimen was also recorded. The light load was subsequently replaced with a heavy load of 0.050 cN/dtex, and the length of the filament (L_1) was measured once the tension had equilibrated. It was removed after holding the heavy load for 30 s, and the sample was allowed to recover for 2 minutes. The final length (L_2) was then recorded under the

light load. Each type of crimped filament was repeat tested three times.

The crimp number (J_{ni}) refers to the total number of crimps, including both peaks and valleys, within a 25 mm length of the filament. This property influences the friction and cohesion between fibers. The crimp number for each specimen was calculated using Equation (3.1) as follows:

$$J_{ni} = \frac{J_{Ai}}{L_i \times 2} \times 25 \tag{3.1}$$

where L_i is the measured length of the specimen (mm), and J_{Ai} is the total number of crimp peaks and valleys within the measured length L_i of the specimen.

The crimp ratio (J_i) refers to the degree of shortening in the filament after crimping. It is defined as the ratio of the extended length gained by unfolding the crimp wave to the original length of the filament before unfolding [122]. The crimp ratio for each specimen was calculated using Equation (3.2) as follows:

$$J_i = \frac{L_I - L_0}{L_I} \times 100\% \tag{3.2}$$

where L_0 and L_1 are the lengths of the filament under light and heavy loads, respectively (mm).

The crimp elastic ratio (J_{di}) indicates the crimp stability of the filament and was determined using Equation (3.3):

$$J_{di} = \frac{L_1 - L_2}{L_1 - L_0} \times 100\% \tag{3.3}$$

where L_0 and L_1 are the filament lengths under light and heavy loads, respectively (mm),

and L_2 represents the filament length under a light load after removing the heavy load and recovering for 2 minutes (mm).

3.3.3 Tensile properties

The tensile properties, including tenacity and elongation, were measured using a 5566 tensile testing machine (Instron, USA) in accordance with ASTM D2256 [115]. Each specimen was pre-tensioned to 0.5 ± 0.1 cN/tex and clamped at a gauge length of 500 \pm 5 mm, with a tensile speed set to 500 mm/min. A total of 15 specimens for each filament type were tested, and the average values were recorded.

3.3.4 Morphologies

Digital images of the samples were captured using an EOS R8 camera with an RF 35mm f/1.8 lens (Canon, Japan). The surface morphologies of the PLA filaments were observed using an M165C microscope (Leica, Germany). Detailed microscopic surface structures of the PLA filaments were further analyzed with a VEGA3 scanning electron microscope (SEM) (Tescan, Czech Republic). Prior to SEM analysis, the samples were sputter-coated with gold. During the SEM observations, the chamber pressure was maintained below 3.0×10^{-5} torr, and the accelerating voltage was set to 20 kV.

3.3.5 X-ray diffraction

The X-ray diffraction (XRD) analysis was carried out using a D8 Venture X-ray diffractometer (Bruker, Germany), which was equipped with monochromatic Cuk_{α} (λ = 1.5406 Å) radiation and operated at 40 kV and 40 mA. The XRD data were collected across a 2 θ range of 5–60° at a scanning rate of 5°/min. The degree of crystallinity was assessed by deconvoluting the diffraction patterns using Origin 2019 software (OriginLab, USA) and applying a Gaussian function to fit the resolved peaks. The crystallinity (X_c) was then calculated as the ratio of the crystalline peak area to the total diffraction area, as shown in Equation (3.4).

$$X_c = \frac{A_c}{A_a + A_c} \times 100\% \tag{3.4}$$

where X_c is the degree of crystallinity, A_c represents the area of all crystalline peaks, and A_a denotes the area of all amorphous peaks.

3.3.6 Statistical analysis

Statistical analyses were conducted using the Statistical Package for the Social Sciences (SPSS 26.0, SPSS Inc., Chicago, USA) to evaluate the effects of heat-setting temperature and time on the crimped and tensile properties of PLA filaments. A two-way analysis of variance (ANOVA) was performed, with statistical significance set at a P-value ≤ 0.05 . Additionally, polynomial regression analysis was employed in SPSS 26.0 to establish the relationship between each property and the heat-setting conditions.

3.4 Results and discussion

3.4.1 DSC Analysis

The DSC curves of the 150D PLA filament are presented in Figure 3.3, illustrating the typical thermal transitions of the material during heating and cooling. Two primary thermal transitions are observed during the heating process. The first transition occurs at 71.81°C, corresponding to the T_g , which is close to the T_g range reported in the literature for PLA (40–70°C) [119]. Below T_g , the limited molecular mobility renders the polymer hard and brittle, hindering the formation of a stable crimped structure. Once the temperature exceeds T_g , the increased chain mobility softens the polymer, facilitating the effective formation of the crimped structure during the heat-setting process.

The second transition is marked by an endothermic peak at 168.88° C, indicating the T_m of the PLA, which is closely aligned with the reported value of 167.2° C [120]. At this stage, the crystalline structure of the PLA filaments becomes disrupted, and the molecular chains transition into a highly elastic state. This transition significantly

increases molecular chain mobility, softening the PLA filaments and disturbing their internal structure, which can lead to melting and fusion on the filament surface.

During the cooling process, the DSC curve shows a significant exothermic peak at 108.13°C, indicating the rearrangement of PLA molecular chains into a crystalline structure. This crystallization peak confirms that PLA has good crystallization potential at 108.13°C (crystallization temperature, T_c), which is consistent with the fastest crystallization temperature range of PLA (100°C to 110°C) reported in the previous study [123]. The DSC analysis reveals that the 150D PLA filaments experience typical thermal transitions, including glass transition, melting, and crystallization during heating and cooling, reflecting the characteristic behavior of a semicrystalline polymer. These results provide a foundation for further understanding the changes in PLA filament properties under heat-setting conditions.

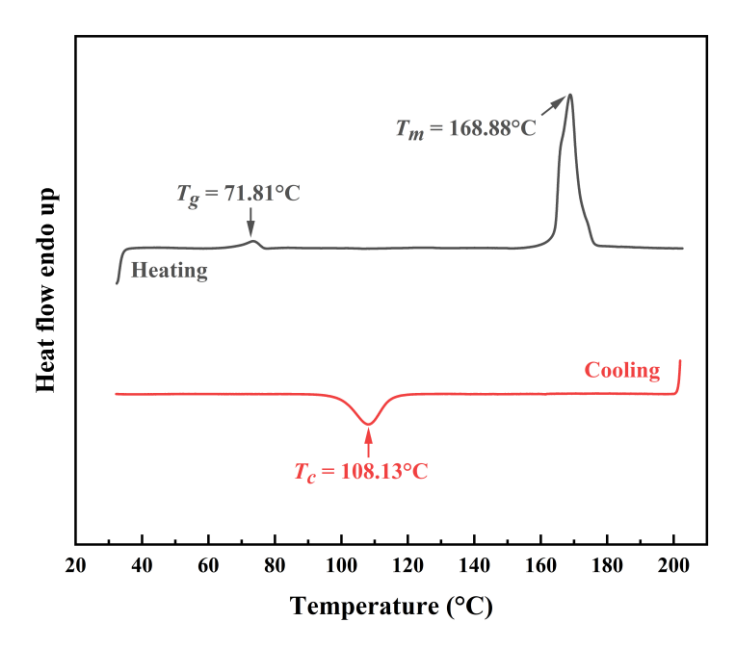


Figure 3.3 DSC curves for the 150D PLA filament.

3.4.2 Crimped properties

The crimped properties, including crimp number, crimp ratio, and crimp elastic ratio, of the produced PLA filaments with varying linear densities (150D, 450D, 600D, and

900D) are evaluated. A detailed analysis of the effects of heat-setting conditions on the crimped performance of these filaments is conducted to identify optimal heat-setting conditions for enhancing crimped properties.

3.4.2.1 Crimp number

Figures 3.4(a)–(d) show the crimp number of various crimped PLA filaments under different heat-setting conditions. For the 150D PLA filament (Figure 3.4(a)), the crimp number gradually increases with rising heat-setting temperatures and times, reaching a peak of 37 crimps/25 mm at 120°C for 120 s. After this point, the crimp number stabilizes, maintaining the same value at higher temperatures (140°C and 160°C) under the same duration of 120 s. This is because, while 80°C and 100°C exceed the T_g of PLA (71.81°C), they remain below its T_c (108.13°C), limiting molecular mobility and resulting in an unstable crimped structure with a lower crimp number. As the temperature rises to 120°C, surpassing the T_c , enhanced molecular activity promotes the formation of ordered crystalline structures, stabilizing the filament's crimped structure and increasing the crimp number. Furthermore, extended heat-setting time allows for greater molecular rearrangement and crystallization, contributing to this stable crimped configuration.

A similar trend is observed for the 450D, 600D, and 900D PLA filaments (Figures 3.4(b)–(d)), with maximum crimp numbers of 14 crimps/25 mm, 13 crimps/25 mm, and 12 crimps/25 mm, respectively. These crimp numbers are significantly lower than those of the 150D filaments, primarily due to differences in the knitting machines used. The 150D PLA filaments were knitted on a 24-gauge circular knitting machine, which has more needles per unit length, making it suitable for finer filaments and producing a denser fabric that unknits into yarns with more crimps. In contrast, the coarser PLA filaments (450D to 900D) can be knitted only on a lower-gauge (10-gauge) machine, resulting in looser fabric structures and fewer crimps. Moreover, differences in crimp numbers are noted among the 450D, 600D, and 900D PLA filaments, despite identical

knitting and heat-setting conditions, which can be attributed to variations in filament linear density. The finer 450D filament has a higher crimp number due to its smaller diameter, which allows for more uniform force distribution during knitting and a better response to heat during heat-setting, making the crimped structure easier to stabilize and maintain.

As shown in Table 3.4, the two-way ANOVA confirms that both heat-setting temperature and time significantly affect the crimped properties of PLA filaments (all $P \le 0.001$). The regression models for predicting crimp numbers across different PLA filaments are presented in Table 3.5, with R^2 values ranging from 0.837 to 0.932, indicating a strong fit. The analysis of crimp numbers suggests that higher heat-setting temperatures (120°C or above) and longer durations (over 60 s) promote the formation of filaments with greater crimp numbers.

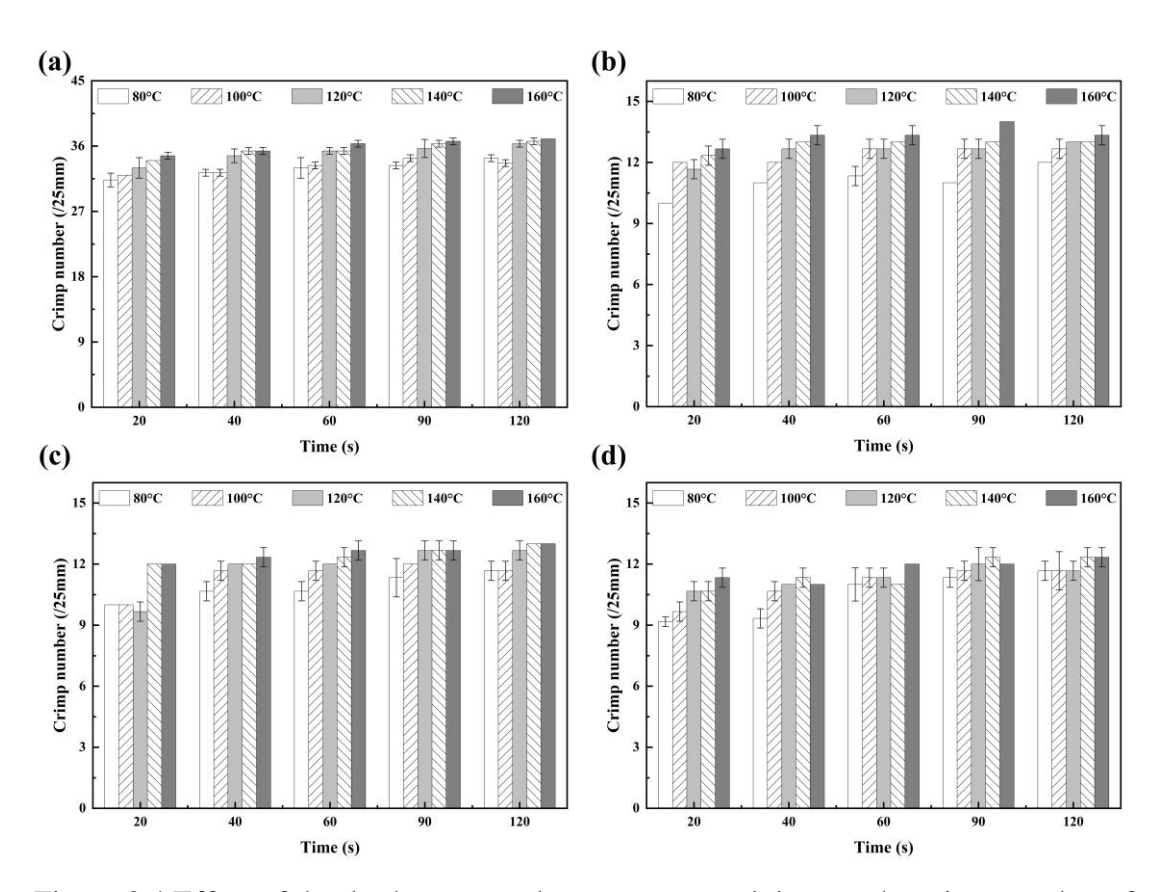


Figure 3.4 Effect of the dry heat-treated temperature and time on the crimp number of crimped PLA filaments: (a) 150D; (b) 450D; (c) 600D; (d) 900D.

Table 3.4 Two-way ANOVA results for the crimp number of PLA filaments

| Dependent | C | Sum of | J.C | Mean | F value | P |
|-----------|-------------|---------|-----|--------|---------|---------|
| variable | Source | squares | df | square | r value | value* |
| 1500 | Temperature | 40.564 | 4 | 10.141 | 97.993 | < 0.001 |
| 150D | Time | 21.627 | 4 | 5.407 | 52.247 | < 0.001 |
| 450D | Temperature | 14.378 | 4 | 3.595 | 42.526 | < 0.001 |
| 430D | Time | 3.536 | 4 | 0.884 | 10.459 | < 0.001 |
| 600D | Temperature | 9.629 | 4 | 2.407 | 12.575 | < 0.001 |
| 600D | Time | 8.634 | 4 | 2.158 | 11.276 | < 0.001 |
| 000D | Temperature | 4.692 | 4 | 1.173 | 7.413 | 0.001 |
| 900D | Time | 10.446 | 4 | 2.612 | 16.505 | < 0.001 |

^{*} *P* values in bold indicate significance at \leq 0.05.

Table 3.5 Regression models and R^2 values for filament crimp number

| Filament code | Equations | R^2 |
|---------------|--|-------|
| 150D PLA | $f_1(x) = 24.295 + 0.085x_1 + 0.062x_2 - 2.101 \times 10^{-5}x_1x_2$ | 0.932 |
| 450D PLA | $f_2(x) = 3.747 + 0.097x_1 + 0.043x_2 - 9.54 \times 10^{-5}x_1x_2$ | 0.875 |
| 600D PLA | $f_3(x) = 5.336 + 0.053x_1 + 0.054x_2 - 8.149 \times 10^{-5}x_1x_2$ | 0.837 |
| 900D PLA | $f_4(x) = 4.623 + 0.057x_1 + 0.059x_2$ | 0.881 |

Note: x_1 represents the heat-setting temperature (°C), x_2 represents the heat-setting time (s), and f(x) denotes the predicted crimp number for each PLA filament.

3.4.2.2 Crimp ratio

The crimp ratio reflects the degree of crimp formation and is closely related to the crimp number and the amplitude of the crimped filament. Figures 3.5(a)–(d) illustrate the trends in the crimp ratio of crimped PLA filaments under different heat-setting conditions. The results indicate an increase in the crimp ratio with rising heat-setting temperature and time. This relationship is strongly supported by the statistical analysis in Table 3.6, where all P-values are below 0.001. Additionally, the high R^2 values (0.938-0.979) in the regression models in Table 3.7 demonstrate a reliable predictive ability for the relationship between heat-setting conditions and crimp ratio.

The crimp ratio of 150D PLA filaments gradually increases from 42.48% at 80°C and 20 s to 51.77% at 160°C and 120 s. In comparison, the crimp ratios of 450D, 600D, and 900D PLA filaments rise steadily from approximately 8% to around 25.5% as heat-setting temperature and time increase. Although the crimp ratios of coarser filaments are lower than those of the 150D PLA filaments, their overall increase is more pronounced. This indicates that coarser filaments require higher heat-setting temperatures and longer times to achieve sufficient molecular chain mobility and uniform crystallization, thereby resulting in a more stable crimped structure. Figures 3.5(a)–(d) also demonstrate that the crimp ratio increases most rapidly at heat-setting temperatures between 120°C and 140°C and durations of 40 to 90 s. Once the temperature reaches 160°C and the time extends to 120 s, the crimp ratio increase begins to level off, suggesting that further increases in temperature and time have minimal effect. Based on these results, a heat-setting temperature of at least 120°C and a time of 90 s or more are recommended to achieve excellent crimp effects across different PLA filament types.

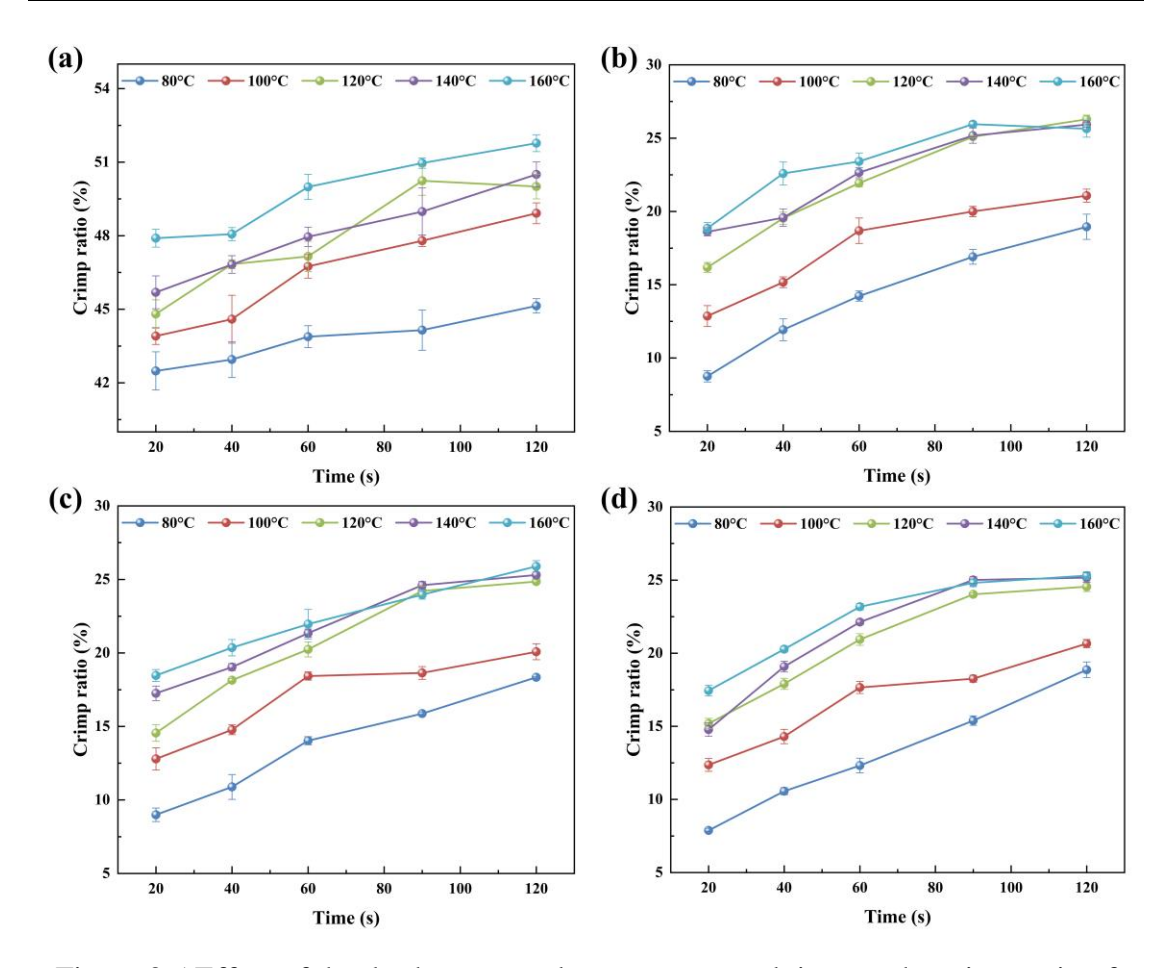


Figure 3.5 Effect of the dry heat-treated temperature and time on the crimp ratio of crimped PLA filaments: (a) 150D; (b) 450D; (c) 600D; (d) 900D.

Table 3.6 Two-way ANOVA results for the crimp ratio of PLA filaments

| Dependent | C | Sum of | J.C | Mean | E 1 | P |
|-----------|-------------|---------|-----|--------|---------|---------|
| variable | Source | squares | df | square | F value | value* |
| 150D | Temperature | 100.867 | 4 | 25.217 | 65.107 | < 0.001 |
| 130D | Time | 63.001 | 4 | 15.750 | 40.665 | < 0.001 |
| 450D | Temperature | 298.688 | 4 | 74.672 | 123.222 | < 0.001 |
| 430D | Time | 245.206 | 4 | 61.301 | 101.158 | < 0.001 |
| 600D | Temperature | 255.643 | 4 | 63.911 | 101.017 | < 0.001 |
| 600D | Time | 239.267 | 4 | 59.817 | 94.546 | < 0.001 |
| 000D | Temperature | 293.463 | 4 | 73.366 | 96.481 | < 0.001 |
| 900D | Time | 288.836 | 4 | 72.209 | 94.960 | < 0.001 |

^{*} *P* values in bold indicate significance at \leq 0.05.

Table 3.7 Regression models and R^2 values for filament crimp ratio

| Filament code | Equations | R^2 |
|---------------|--|-------|
| 150D PLA | $f_5(x) = 28.930 + 0.192x_1 + 0.054x_2 - 0.001x_1^2$ | 0.938 |
| 450D PLA | $f_6(x) = -26.234 + 0.511x_1 + 0.231x_2 - 0.002x_1^2 - 0.001x_2^2$ | 0.979 |
| 600D PLA | $f_7(x) = -21.494 + 0.448x_1 + 0.177x_2 - 0.001x_1^2 - 0.001x_2^2$ | 0.977 |
| 900D PLA | $f_8(x) = -26.032 + 0.491x_1 + 0.219x_2 - 0.002x_1^2 - 0.001x_2^2$ | 0.975 |

Note: x_1 represents the heat-setting temperature (°C), x_2 represents the heat-setting time (s), and f(x) denotes the predicted crimp ratio for each PLA filament.

3.4.2.3 Crimp elastic ratio

The crimp elastic ratio reflects the stability of the filament's crimped structure, with higher values indicating better recovery of the crimped morphology. Figures 3.6(a)–(d) present the crimp elastic ratios of PLA filaments, showing a clear increase in all samples as heat-setting temperature and time rise (P < 0.001, Table 3.8). Specifically, the crimp elastic ratio of 150D PLA filaments rises from 74.02% at 80°C and 20 s to 86.12% at 160°C and 120 s (Figure 3.6(a)). Under identical heat-setting conditions, the crimp elastic ratios of the 450D, 600D, and 900D PLA filaments increase from around 78% to 90.04%, 92.42%, and 93.13%, respectively (Figures 3.6(b)–(d)). This increase stems from higher temperatures and extended durations, which enhance molecular movement and rearrangement, leading to a stable crystalline structure and improved crimp stability.

Although the crimp elastic ratios of all PLA filaments are similar at 80°C and 20 s, the crimp elastic ratios of the 450D, 600D, and 900D filaments eventually exceed 90% as heat-setting temperature and time increase, whereas the 150D PLA filaments reach only 86.12%. This trend differs from those observed in crimp number and crimp ratio and may be related to the variations in filament structure. The 450D, 600D, and 900D filaments are composed of multiple 150D filaments, and this combined structure helps to distribute stress more evenly under external forces. The mutual support and interlocking between the individual filaments effectively reduce stress concentration and protect the crimped structure from damage. Consequently, the 450D, 600D, and

900D PLA filaments exhibit higher crimp elastic ratios.

The regression models in Table 3.9, with R^2 values exceeding 0.95 for all PLA filaments, demonstrate a strong predictive relationship between the crimp elastic ratio and the heat-setting parameters. Similar to the crimp ratio, the most rapid increase in the crimp elastic ratio for all PLA filaments occurs under heat-setting conditions of 120°C to 140°C and 40 to 90 s. Therefore, it is also recommended to maintain a heat-setting temperature at 120°C or above, with a minimum heat-setting time of 90 s.

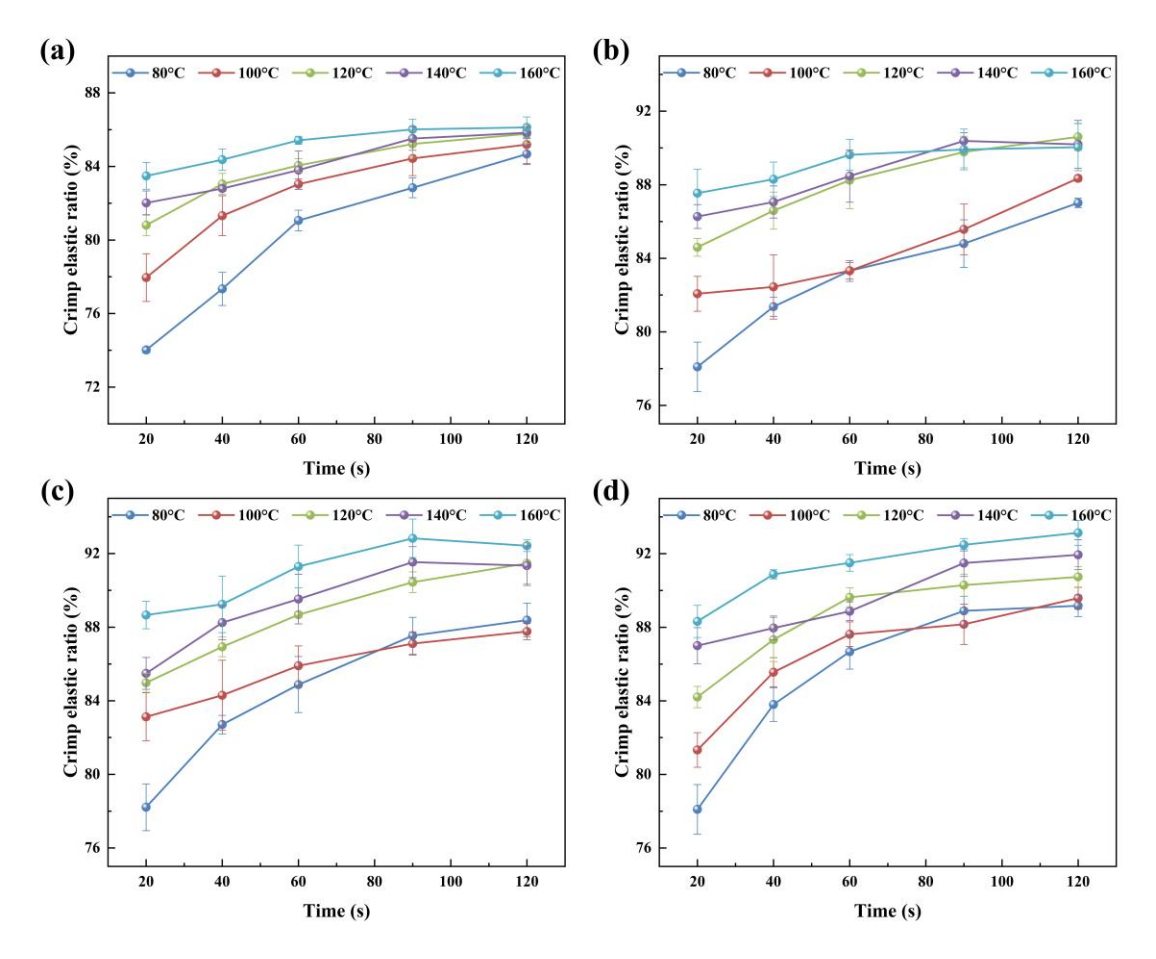


Figure 3.6 Effect of the dry heat-treated temperature and time on the crimp elastic ratio of crimped PLA filaments: (a) 150D; (b) 450D; (c) 600D; (d) 900D.

Table 3.8 Two-way ANOVA results for the crimp elastic ratio of PLA filaments

| Dependent | Source | Sum of | Mean | | | |
|-----------|--------|---------|---------------------|---------|--------|--|
| variable | | squares | <i>df</i> square | F value | value* | |

| 150D | Temperature | 76.937 | 4 | 19.234 | 11.679 | < 0.001 |
|------|-------------|---------|---|--------|--------|---------|
| 130D | Time | 112.374 | 4 | 28.094 | 17.058 | < 0.001 |
| 450D | Temperature | 150.907 | 4 | 37.727 | 34.681 | < 0.001 |
| 450D | Time | 97.920 | 4 | 24.480 | 22.504 | < 0.001 |
| (00D | Temperature | 143.246 | 4 | 35.811 | 37.185 | < 0.001 |
| 600D | Time | 132.825 | 4 | 33.206 | 34.480 | < 0.001 |
| 900D | Temperature | 111.612 | 4 | 27.903 | 18.917 | < 0.001 |
| | Time | 163.330 | 4 | 40.833 | 27.683 | < 0.001 |

^{*} *P* values in bold indicate significance at ≤ 0.05 .

Table 3.9 Regression models and R^2 values for filament crimp elastic ratio

| Filament code | Equations | R^2 |
|---------------|--|-------|
| 150D PLA | $f_9(x) = 53.654 + 0.282x_1 + 0.247x_2 - 0.001x_1^2 - 0.001x_2^2$ | 0.964 |
| 130D FLA | $-0.001x_1x_2$ | 0.904 |
| 450D PLA | $f_{10}(x) = 55.178 + 0.331x_1 + 0.173x_2 - 0.001x_1^2 - 0.001x_1x_2$ | 0.951 |
| 600D PLA | $f_{11}(x) = 63.942 + 0.176x_1 + 0.212x_2 - 0.001x_2^2$ | 0.956 |
| 900D PLA | $f_{12}(x) = 67.008 + 0.104x_1 + 0.275x_2 + 7.036 \times 10^{-5}x_1^2$ | 0.055 |
| | $-\ 0.001x_2^2 - 0.001x_1x_2$ | 0.955 |

Note: x_1 represents the heat-setting temperature (°C), x_2 represents the heat-setting time (s), and f(x) denotes the predicted crimp elastic ratio for each PLA filament.

3.4.3 Tensile properties

Tensile properties, particularly tenacity and elongation at break, are essential for evaluating the resistance of yarns to external forces during processing and end-use [124]. These parameters directly affect textile processability and durability, making them critical for determining optimal heat-setting conditions. Therefore, this study also conducts a comprehensive analysis to investigate the impact of varying heat-setting conditions on the tensile performance of PLA filaments.

3.4.3.1 Tenacity

Figures 3.7(a)–(d) show the breaking tenacity of different crimped PLA filaments. The results reveal a notable decrease in the breaking tenacity of PLA filaments after heat

treatment, consistent with prior findings that heat-setting typically reduces yarn tenacity [125]. Statistical analysis further confirms a strong correlation between heat-setting conditions and filament tenacity (Table 3.10, all P < 0.001). This reduction in tenacity becomes especially evident at higher temperatures (140°C and 160°C) and extended times (90 s and 120 s). This likely results from the increased susceptibility of molecular chains to slippage and breakage under these conditions, disrupting their continuity and stability. Consequently, the tenacity, which relies on molecular chain integrity, shows a significant decrease.

Specifically, the tenacity of the 150D PLA filament gradually decreases from 21.73 cN/tex at 80°C for 20 s to 18.52 cN/tex at 160°C for 120 s (Figure 3.7(a)). Similarly, the tenacity of the 450D PLA filament drops from 17.88 to 12.21 cN/tex (Figure 3.7(b)), while the tenacity of the 600D PLA filament declines from 19.25 to 11.96 cN/tex (Figure 3.7(c)). The 900D PLA filament exhibits the most significant decline, from 16.78 to 9.36 cN/tex (Figure 3.7(d)). Notably, the tenacity of the 450D, 600D, and 900D PLA filaments is consistently lower than that of the 150D PLA filaments. The primary reason for this phenomenon may be that thicker yarns contain more PLA fibers, increasing the possibility of defects within the fibers. Consequently, these thicker yarns are more prone to early break at weak points under higher tensile stresses, leading to a more significant reduction in tenacity.

The tenacity regression models in Table 3.11 demonstrate strong predictive accuracy for PLA filaments, with R^2 values ranging from 0.932 to 0.953. Although heat-setting promotes the formation of the PLA filament's crimped structure, excessively high temperatures (over 140°C or 160°C) and prolonged times (120 s) can damage the internal fiber structure, resulting in decreased yarn tenacity. To achieve an optimal balance between crimped properties and tenacity, a heat-setting temperature of 120°C and a duration of 90 s is suitable for PLA filaments.

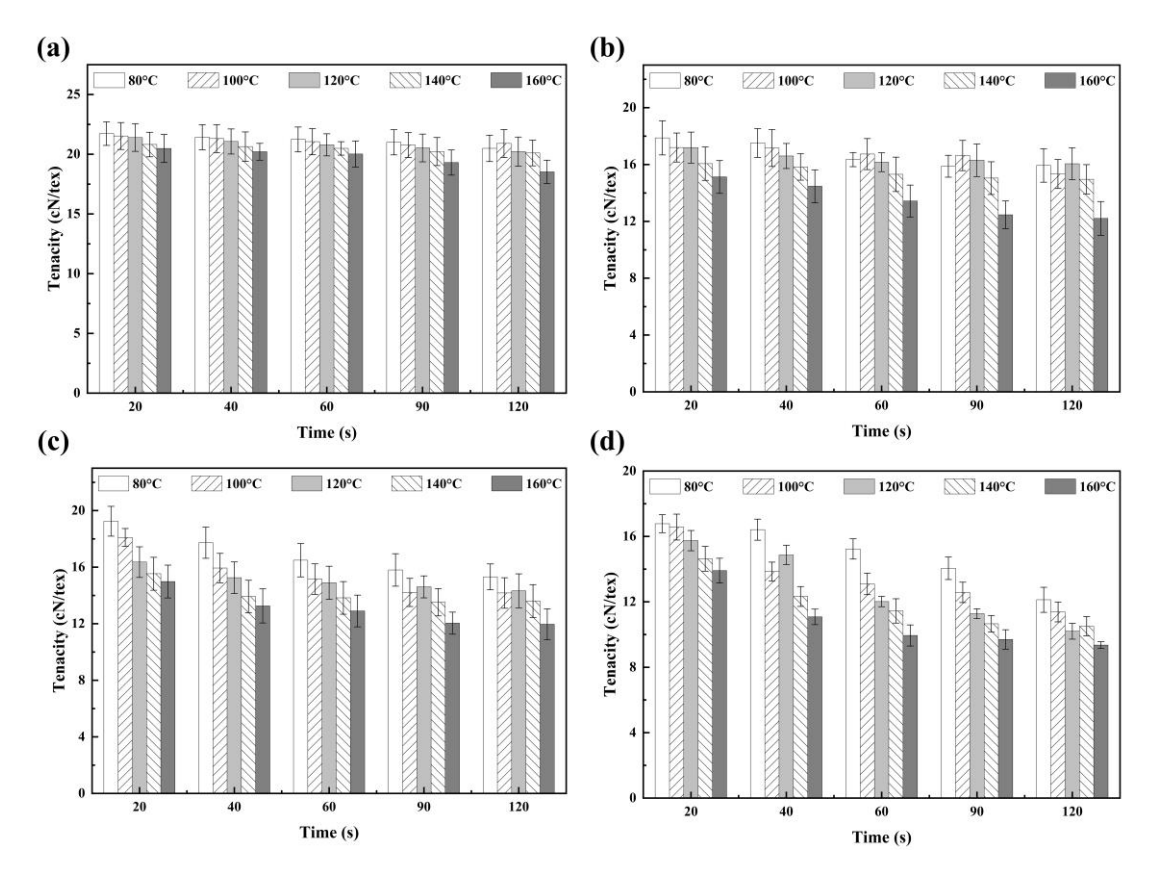


Figure 3.7 Effect of the dry heat-treated temperature and time on the tenacity of crimped PLA filaments: (a) 150D; (b) 450D; (c) 600D; (d) 900D.

Table 3.10 Two-way ANOVA results for the tenacity of PLA filaments

| Dependent | C | Sum of | 10 | Mean | F 1 | P |
|-----------|-------------|---------|----|--------|---------|---------|
| variable | Source | squares | df | square | F value | value* |
| 150D | Temperature | 7.189 | 4 | 1.797 | 33.600 | < 0.001 |
| 130D | Time | 4.088 | 4 | 1.022 | 19.109 | < 0.001 |
| 450D | Temperature | 35.809 | 4 | 8.952 | 49.329 | < 0.001 |
| 430D | Time | 10.961 | 4 | 2.740 | 15.100 | < 0.001 |
| (00D | Temperature | 43.275 | 4 | 10.819 | 55.200 | < 0.001 |
| 600D | Time | 28.684 | 4 | 7.171 | 36.589 | < 0.001 |
| 000D | Temperature | 48.883 | 4 | 12.221 | 30.147 | < 0.001 |
| 900D | Time | 70.565 | 4 | 17.641 | 43.518 | < 0.001 |

^{*} P values in bold indicate significance at ≤ 0.05 .

Table 3.11 Regression models and R^2 values for filament tenacity

| Filament code | Equations | R^2 |
|---------------|-----------|-------|
|---------------|-----------|-------|

| 150D PLA | $f_{13}(x) = 19.543 + 0.047x_1 - 0.003x_2 + 9.235 \times 10^{-6}x_2^2$ $-8.184 \times 10^{-5}x_1x_2$ | 0.940 |
|----------|--|-------|
| 450D PLA | $f_{14}(x) = 10.493 + 0.159x_1 - 0.026x_2 - 0.001x_1^2$ $-6.492 \times 10^{-5}x_1x_2$ | 0.932 |
| 600D PLA | $f_{15}(x) = 25.673 - 0.064x_1 - 0.11x_2 + 2.036 \times 10^{-5}x_1^2$ | 0.953 |
| 900D PLA | $f_{16}(x) = 25.063 - 0.073x_1 - 0.118x_2 + 6.929 \times 10^{-5}x_1^2$ | 0.939 |

Note: x_1 represents the heat-setting temperature (°C), x_2 represents the heat-setting time (s), and f(x) denotes the predicted tenacity for each PLA filament.

3.4.3.2 Elongation

The elongation at break serves as another key indicator for evaluating a yarn's ductility and resistance to deformation. Figures 3.8(a)–(d) show the effect of heat-setting conditions on the elongation at the break of PLA filaments. The results indicate a significant increase in elongation as both heat-setting temperature and time rise (Table 3.12, all P < 0.001). This increase is due to the greater energy absorbed by the PLA molecular chains under elevated heat-setting conditions, which enhances molecular chain relaxation and mobility. Furthermore, elongation at break clearly declines as the linear density of the PLA filaments increases. This trend is driven by the same factors that cause the reduction in yarn tenacity. During stretching, breakage typically occurs first in the filament's weakest or defective regions, while elongation in other regions remains relatively limited. Filaments with higher linear densities (450–900D) contain more individual fibers, increasing the likelihood of defects, which ultimately results in reduced elongation at break.

Table 3.13 shows that the R^2 values of the elongation regression models for all PLA filaments range from 0.944 to 0.963, indicating a high degree of model fit. The elongation at break of PLA filaments increases significantly when the heat-setting temperature and time reach 140°C and 60 s, respectively. However, excessive elongation may cause permanent deformation in products made from crimped PLA filaments during manufacturing and use. This deformation negatively impacts their

performance, such as reduced dimensional stability. Based on the analysis of elongation and other properties, the heat-setting conditions for crimped PLA filaments in subsequent studies are set at 120°C for 90 s to achieve optimal crimped and tensile properties.

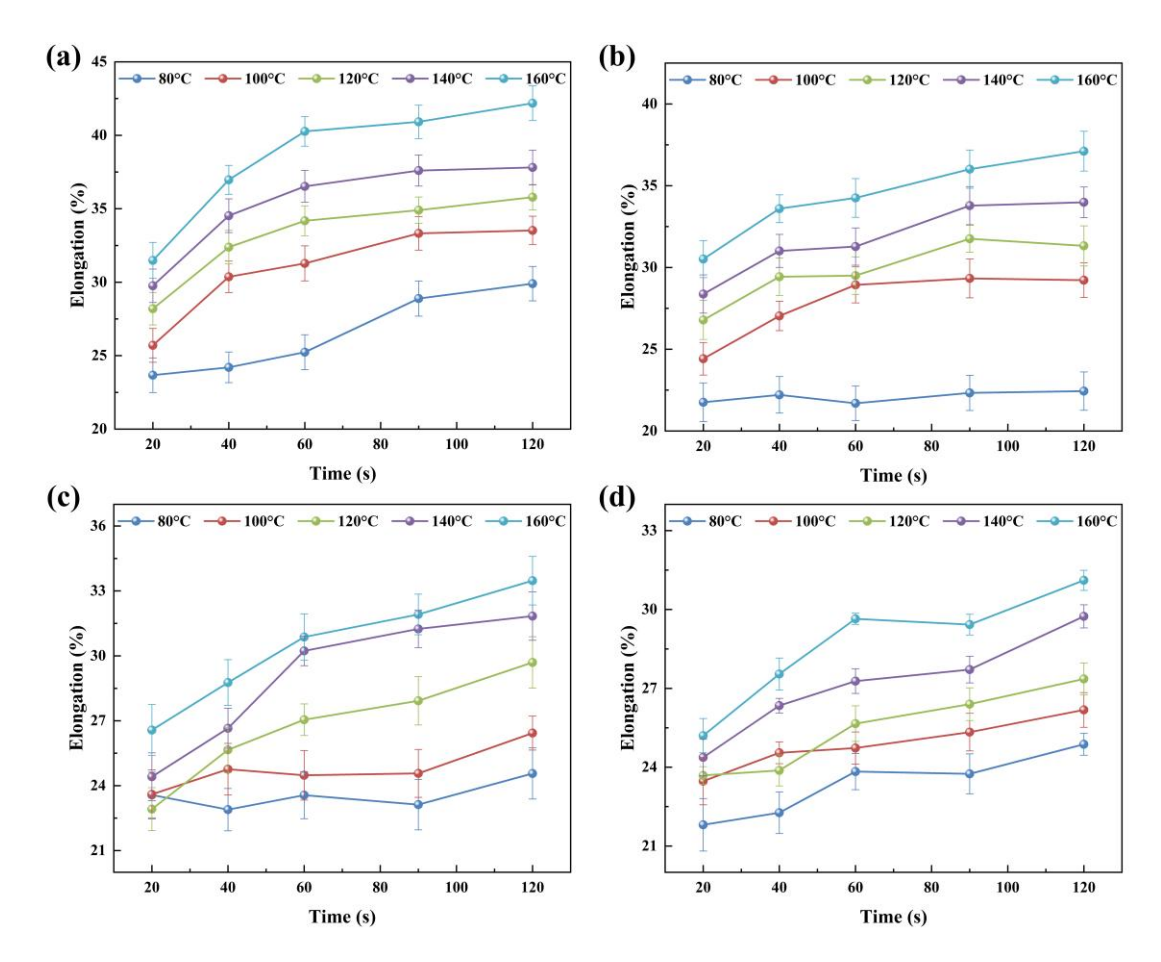


Figure 3.8 Effect of the dry heat-treated temperature and time on the elongation of crimped PLA filaments: (a) 150D; (b) 450D; (c) 600D; (d) 900D.

Table 3.12 Two-way ANOVA results for the elongation of PLA filaments

| Dependent | Carres | Sum of | J.C | Mean | F 1 | P |
|-----------|-------------|---------|-----|---------|---------|---------|
| variable | Source | squares | df | square | F value | value* |
| 150D | Temperature | 410.293 | 4 | 102.573 | 91.098 | < 0.001 |
| | Time | 208.720 | 4 | 52.180 | 46.342 | < 0.001 |
| 450D | Temperature | 425.102 | 4 | 106.276 | 108.381 | < 0.001 |
| 450D | Time | 64.799 | 4 | 16.200 | 16.521 | < 0.001 |
| 600D | Temperature | 157.385 | 4 | 39.346 | 21.740 | < 0.001 |

| | Time | 73.278 | 4 | 18.320 | 10.122 | < 0.001 |
|------|-------------|--------|---|--------|--------|---------|
| 900D | Temperature | 83.512 | 4 | 20.878 | 53.740 | < 0.001 |
| | Time | 50.344 | 4 | 12.586 | 32.396 | < 0.001 |

^{*} *P* values in bold indicate significance at \leq 0.05.

Table 3.13 Regression models and R^2 values for filament elongation

| Filament code | Equations | R^2 |
|---------------|--|-------|
| 150D PLA | $f_{17}(x) = 2.523 + 0.243x_1 + 0.184x_2 - 0.001x_2^2$ | 0.963 |
| 450D PLA | $f_{18}(x) = -2.923 + 0.369x_1 + 0.042x_2 - 0.001x_1^2$ | 0.963 |
| | $-0.001x_2^2 + 0.001x_1x_2$ | 0.703 |
| 600D PLA | $f_{19}(x) = 20.560 + 0.001x_1 - 0.014x_2 + 0.001x_1x_2$ | 0.944 |
| 900D PLA | $f_{20}(x) = 20.139 - 0.004x_1 + 0.026x_2$ | 0.956 |

Note: x_1 represents the heat-setting temperature (°C), x_2 represents the heat-setting time (s), and f(x) denotes the predicted elongation for each PLA filament.

3.4.4 Production process optimization

Although heat-setting facilitates the stable formation of the crimped structure in PLA filaments, it also impacts their tensile properties. To achieve a balance between crimped and tensile properties, the optimal heat-setting parameters were determined to be 120°C for 90 s, based on the previous analysis. Following this, the study further optimized the production process for crimped PLA filaments by designing and manufacturing a small circular knitting machine with a heating device and a de-knit winding machine (Figures 3.9(a) and (b)). The small circular knitting machine (Figure 3.9(a)) is equipped with two 19 cm heating tubes, enabling adjustable heat-setting temperatures ranging from 30°C to 200°C, which allows for immediate heat treatment of the fabric after knitting. The heat-setting time is controlled by adjusting the winding speed of the fabric. The de-knit winding machine (Figure 3.9(b)) is specifically designed for the de-knitting and winding processes, consisting primarily of feeding rollers, yarn guide wheels, and winding bobbins. During operation, the crimped filaments are unraveled from the heat-treated fabric under controlled tension from the feeding rollers and then wound in a spiral pattern onto the bobbin surface. To preserve the crimped structure of the PLA

filaments, the feeding roller speed is set higher than the winding bobbin speed. These custom-designed machines simplify the production process, enhancing the efficiency of crimped filament manufacturing while ensuring the stability of the crimped structure.

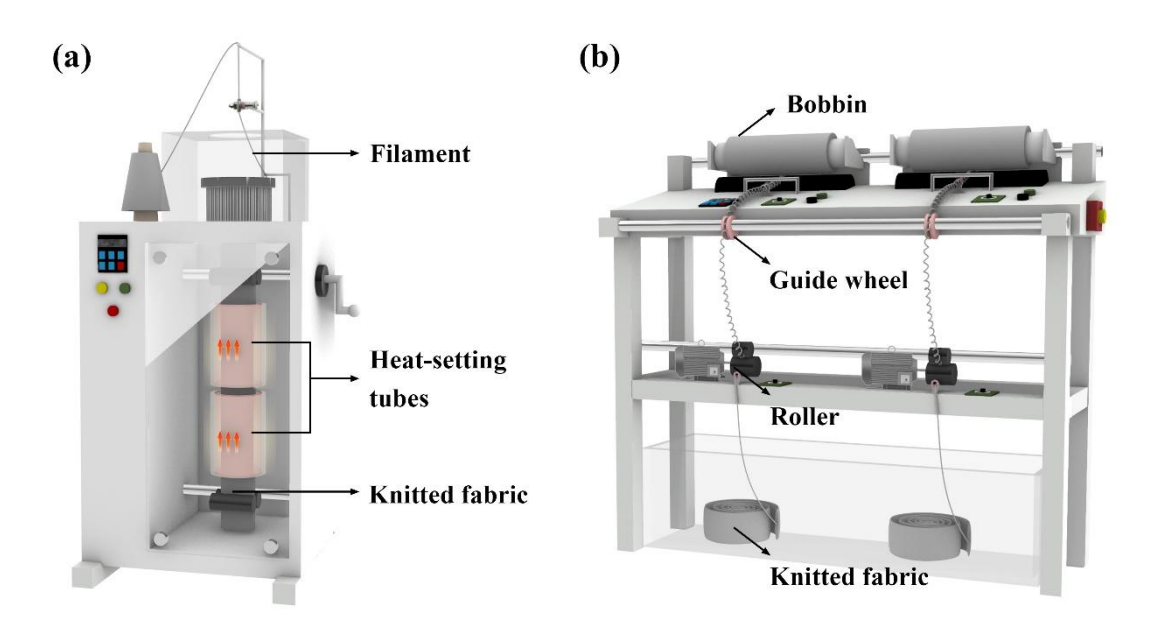


Figure 3.9 The designed machines: (a) circular knitting machine; (b) de-knit winding machine.

Figures 3.10(a)–(h) display digital photos of bobbins for four types of crimped PLA filaments produced under optimal heat-setting conditions, along with microscopic images of each filament type. All PLA filaments exhibit regular and uniform knitted loop crimps, confirming the effectiveness of the optimized fabrication process and improvements to the equipment. Table 3.14 summarizes the properties of these crimped PLA filaments, demonstrating an optimal balance between crimped and tensile performance.

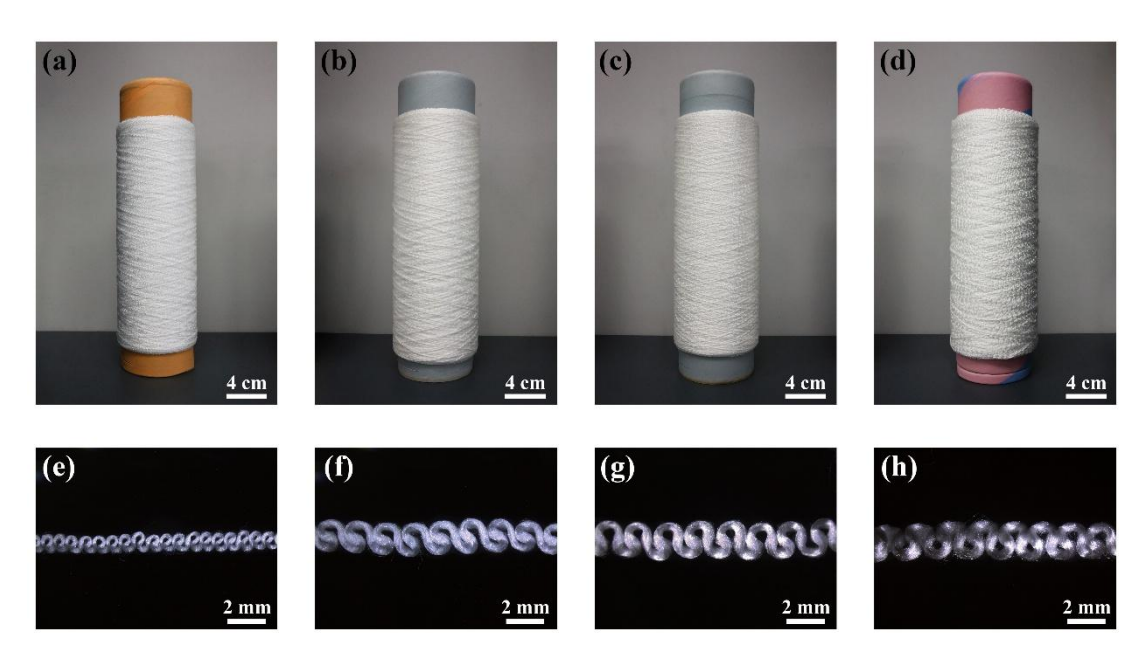


Figure 3.10 The digital photos of bobbins and corresponding microscopic images of the crimped PLA filaments produced under optimal dry heat-setting conditions: (a) and (e) 150D; (b) and (f) 450D; (e) and (g) 600D; (d) and (h) 900D.

Table 3.14 Properties of crimped PLA filaments produced under optimal dry heatsetting conditions

| Filomonto | Crimp number | Crimp | Crimp elastic | Tenacity | Elongation |
|--------------|--------------|----------------|----------------|--------------|----------------|
| Filaments | (/25mm) | ratio (%) | ratio (%) | (cN/tex) | (%) |
| 150D crimped | 35.67 | 50.24 | 85.22 | 20.53 | 34.91 |
| PLA filament | (± 1.25) | (± 0.59) | (± 0.71) | (± 1.16) | $(\pm \ 0.90)$ |
| 450D crimped | 12.67 | 25.10 | 89.78 | 16.30 | 31.76 |
| PLA filament | (± 0.47) | $(\pm \ 0.07)$ | $(\pm \ 0.86)$ | (± 1.15) | $(\pm \ 0.83)$ |
| 600D crimped | 12.67 | 24.22 | 90.44 | 14.61 | 27.93 |
| PLA filament | (± 0.47) | (± 0.31) | $(\pm \ 0.56)$ | (± 0.78) | (± 1.12) |
| 900D crimped | 12.00 | 24.03 | 90.29 | 11.28 | 26.40 |
| PLA filament | (± 0.82) | (± 0.09) | (± 0.60) | (± 0.30) | (± 0.62) |

Note: Standard deviations are given in parentheses.

3.4.5 Micromorphology and crystallization analysis

Understanding the microstructural changes in crimped PLA filaments is essential to comprehensively analyze their macroscopic property variations [126]. This study

analyzes the micromorphology and crystallinity of 150D PLA filaments subjected to various heat-setting conditions. The 150D filaments were selected as representative samples, as the 450D, 600D, and 900D filaments are composed of multiple strands of 150D filaments, all of which have similar fundamental structures and molecular arrangements. Analyzing property changes in 150D filaments establishes a foundation for understanding the behavior of higher-denier PLA filaments during heat-setting.

3.4.5.1 Micromorphology

The longitudinal morphologies of 150D crimped PLA filaments, treated under various heat-setting conditions, were observed by SEM, as shown in Figures 3.11(a)–(y). At lower temperatures (80°C and 100°C), the filament surfaces appear smooth, with no significant morphological changes observed (Figures 3.11(a)–(j)). Even as the temperature rises to 120°C, the PLA filament surfaces maintain a smooth morphology (Figures 3.11(k)–(o)), suggesting that temperatures at or below 120°C have only minimal impact on the filament surface.

As the temperature rises to 140°C, the filament surfaces begin to show deformation, with partial bulging and sticking observed (Figures 3.11(p)–(t)), likely due to the enhanced mobility of PLA molecular chains. The surface deformation intensifies at 160°C, particularly at heat-setting times of 90 and 120 s, where significant melting and adhesion further compromise the filament's morphological integrity. This behavior can be attributed to the substantial increase in molecular chain mobility at temperatures approaching the T_m of PLA (168.88°C), which destabilizes the surface structure and induces partial melting. Micromorphological analysis confirms that excessive heat-setting temperatures (140°C and 160°C) should be avoided, as they severely disrupt the microstructure of PLA filaments, leading to a direct reduction in their tensile properties.

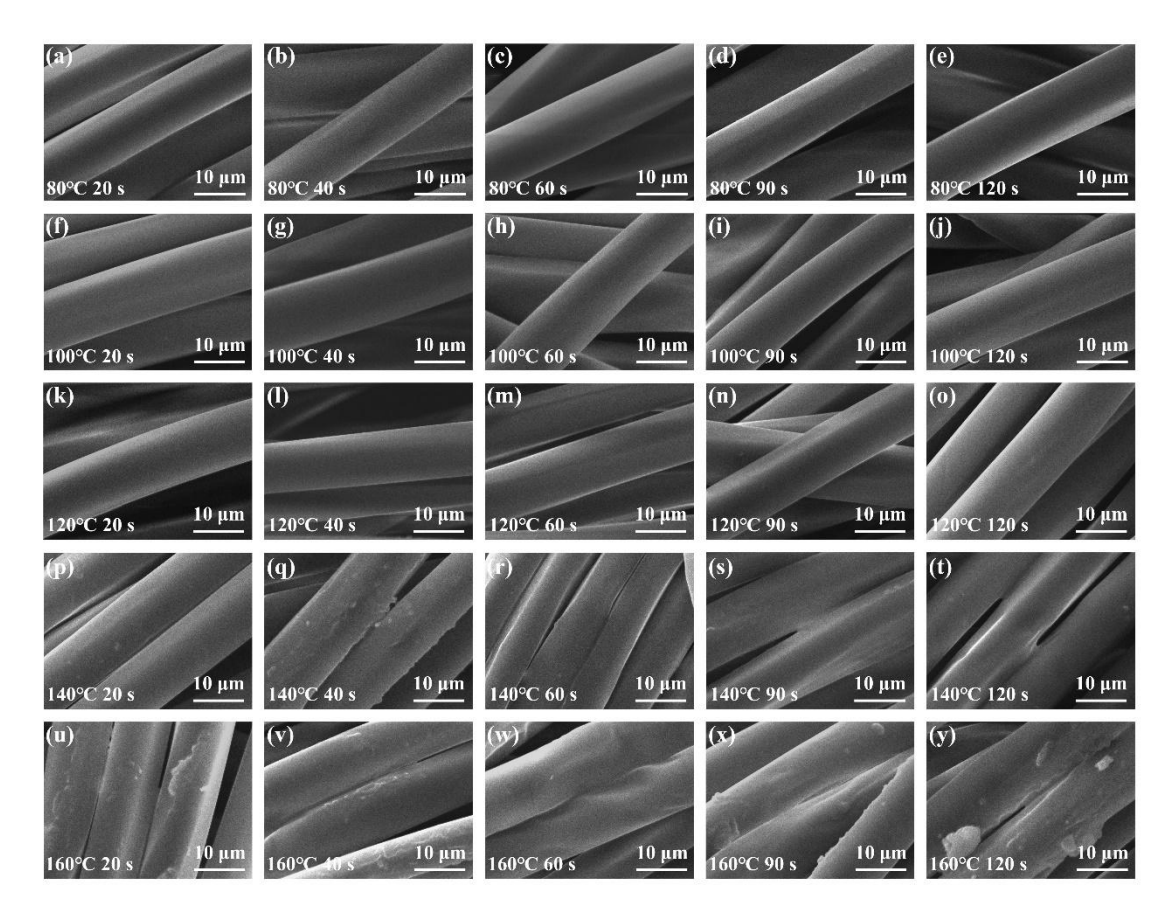


Figure 3.11 The longitudinal morphologies of 150D crimped PLA filaments under different heat-setting conditions: (a)–(e) 80° C for 20-120 s; (f)–(j) 100° C for 20-120 s; (k)–(o) 120° C for 20-120 s; (p)–(t) 140° C for 20-120 s; (u)–(y) 160° C for 20-120

S.

3.4.5.2 Crystallization

The XRD patterns of 150D crimped PLA filaments subjected to various heat-setting conditions are presented in Figures 3.12(a)–(e), with crystallinity displayed in Figure 3.12(f). The primary diffraction peaks (2θ) of PLA appear at 14.9°, 16.5°, and 18.9°, closely matching previously reported values for PLA at 14.8°, 16.5–16.8°, and 19.02–19.1° [123, 127-129], which correspond to the (010), (200/110), and (203) planes, respectively. The results indicate that at lower heat-setting temperatures (80°C and 100°C), the diffraction peaks of 150D crimped PLA filaments exhibit relatively weak intensities, with the (010) peak nearly undetectable and a low degree of crystallinity observed in Figure 3.12(f). As the heat-setting temperature and time increase, these

diffraction peaks become more intense and sharper, corresponding to a significant rise in crystallinity. The increased crystallinity results from the added thermal energy, which enhances molecular mobility and facilitates structural reorganization. During thermal stretching and heat-setting in the spinning process, the crystallization time is relatively short, leaving some molecular chains frozen in an unstable, non-equilibrium state. When the PLA filaments are reheated, these frozen chain segments start to thaw, enhancing molecular chain mobility. This increased activity allows the chains to rearrange and form more ordered structures within the amorphous regions, thereby raising the degree of crystallinity [130].

The fastest crystallization rate for PLA is reported within the temperature range of $100-130^{\circ}$ C [131], consistent with our observation of the steepest increase in crystallinity at 120° C (Figure 3.12(f)), above its T_c of 108.13° C. However, when the heat-setting time at 120° C is extended to 120 s, the diffraction peak intensities begin to decline. This reduction becomes even more pronounced at 140° C and 160° C with longer heat-setting times. This reduction likely results from excessive molecular mobility at elevated temperatures, which disrupts the crystal structure and induces partial melting, especially as the temperature nears the T_m of PLA (168.88° C) and heat-setting time extends. XRD analysis suggests that a heat-setting condition of 120° C for 90 s is appropriate for achieving a stable crystalline phase in PLA filaments, whereas excessively high temperatures and prolonged times negatively impact the crystal structure, reducing crystallinity and potentially compromising the filament's mechanical properties.

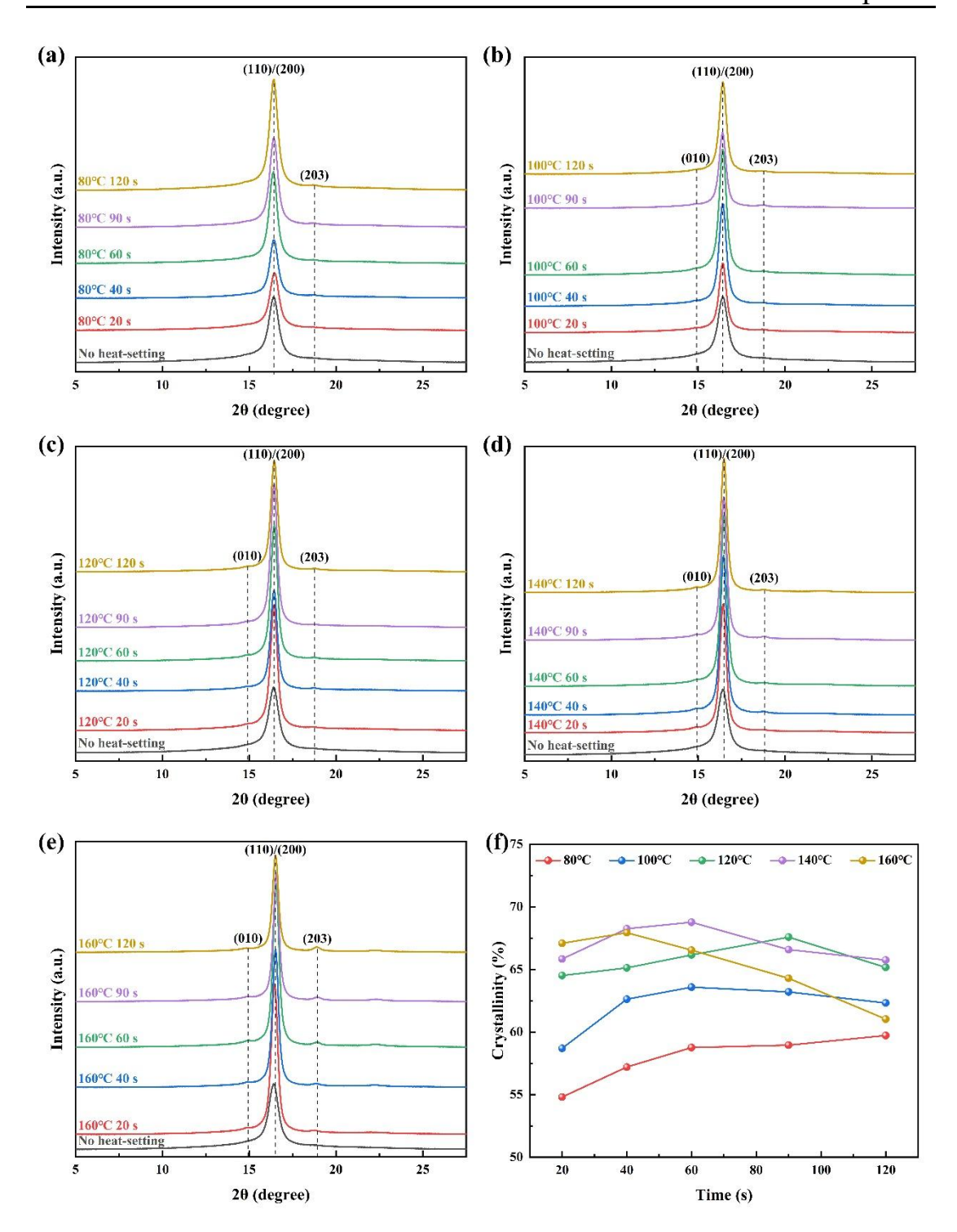


Figure 3.12 The XRD patterns and crystallinity of 150D crimped PLA filaments treated with different heat-setting conditions: (a) 80°C; (b) 100°C; (c) 120°C; (d) 140°C; (e) 160°C; (f) crystallinity.

3.5 Conclusions

This chapter successfully developed crimped PLA filaments with varying linear

densities (150D, 450D, 600D, and 900D) using the knit-de-knit technique, achieving desirable crimped and tensile properties. Based on the experimental results and analysis, the following key conclusions are drawn:

- (1) The crimp number, crimp ratio, and crimp elastic ratio of PLA filaments show significant increases with higher heat-setting temperatures and longer durations, as confirmed by two-way ANOVA. Regression models demonstrate strong correlations (R^2 values ranging from 0.837 to 0.979), indicating high accuracy. A minimum heat-setting temperature of 120°C and a duration of 90 s are required to achieve an optimal crimped structure.
- (2) Increasing heat-setting temperatures and durations lead to decreased breaking tenacity and increased elongation at break in crimped PLA filaments. The regression models for these tensile properties show R^2 values ranging from 0.932 to 0.963, also confirming strong correlations. Conditions exceeding 140°C or 90 s result in significantly reduced tenacity and increased elongation, affecting durability and stability. Heat-setting at 120°C for 90 s is determined as the optimal condition for balancing crimped and tensile properties.
- (3) A small circular knitting machine equipped with heating tubes and a winding device has been developed to enhance production efficiency while preserving the crimped structure, enabling the mass production of high-quality crimped PLA filaments. Filaments produced under optimal conditions exhibit excellent crimped shapes and performance, making them ideal for mattress surface fabric applications.
- (4) SEM analysis of 150D crimped PLA filaments shows that temperatures between 80°C and 120°C have little effect on the filament surface, while temperatures above 140°C cause surface deformation, worsening at 160°C. Crystallinity analysis further supports these findings, showing that heat-setting at 80–120°C enhances crystallinity,

while temperatures of 140–160°C reduce it, disrupting the crystalline structure and impairing filament mechanical properties. A heat-setting condition of 120°C for 90 s is optimal for stable crystallinity, consistent with the identified optimal heat-setting conditions.

Chapter 4 Design and Fabrication of PLA Weft-Knitted Inlaid Fabric

4.1 Introduction

As mentioned in Chapter 2, mattress surface fabrics, being the closest layer to the human body, are crucial for maintaining physiological balance and providing comfortable support, directly influencing sleep quality. Key comfort properties, such as air permeability, water vapor permeability, and thermal insulation, are vital indicators for assessing their functionality. An ideal mattress surface fabric should facilitate a balance of air, heat, and moisture transfer between the body and the surrounding environment [25]. Although several studies have investigated the comfort enhancement of mattress surface fabrics, most rely on PET fibers, posing significant environmental concerns [13, 21, 22, 103]. Currently, no research focuses exclusively on the use of PLA yarns for mattress surface fabric production, particularly weft-knitted inlaid fabrics inserted with crimped PLA filaments.

This chapter aims to develop sustainable, comfortable, and durable weft-knitted inlaid fabrics made entirely from PLA materials and to evaluate the effects of structural parameters on their performance. PLA weft-knitted inlaid fabrics are produced using thicker 450D, 600D, and 900D crimped PLA filaments, optimized in Chapter 3, to achieve greater fabric thickness for mattress surface applications, with commercially available PET filaments included for comparison. The chapter begins by detailing the raw materials, production processes, testing procedures, and statistical analysis methods for the weft-knitted inlaid fabrics. It then analyzes the effects of structural parameters, including connection rates and shapes of stitching patterns, as well as inlaid and surface yarn types, on the physical properties, comfort, and compression performance of the PLA fabrics. Additionally, the pilling and abrasion resistance of the fabrics are evaluated. Finally, the chapter summarizes the findings, recommends structural parameters for producing PLA weft-knitted inlaid fabrics, and highlights their

commercialization potential as mattress surface materials.

4.2 Materials and methods

4.2.1 Materials

The developed multilayer PLA weft-knitted inlaid fabric structure consists of an upper layer, a middle layer, and a lower layer (Figure 4.1). These layers are connected using a portion of the yarn in the lower layer as the connecting yarn, with the weft-knitted technique enabling their simultaneous knitting and connection in a single step. The upper layer was fabricated using white 150D PLA filaments, while blue 150D PLA filaments were used for the lower layer and the connecting yarns. Further details are provided in Table 4.1. For comparative analysis, 32Ne PLA staple yarns (Table 4.2) and 150D PET filaments (Table 4.1) were also used as surface yarns for these layers. To ensure sufficient thickness suitable for mattress surfaces, crimped 450D, 600D, and 900D PLA filaments were used as inlaid yarns in the middle layer. These crimped PLA filaments were produced in Chapter 3 under the optimal heat-setting conditions (120°C for 90 s), and their crimped and tensile properties are listed in Table 3.14. Additionally, 600D textured PET filaments, commonly used as inlaid yarns in commercial weftknitted inlaid fabrics, were also utilized in this study for comparison (Table 4.1). All PLA filaments were sourced from Ruomi Technology Co., Ltd. (Qingdao, China), while the PLA staple yarn and PET filaments were supplied by Smartwin International Group Co., Ltd. (Quanzhou, China).

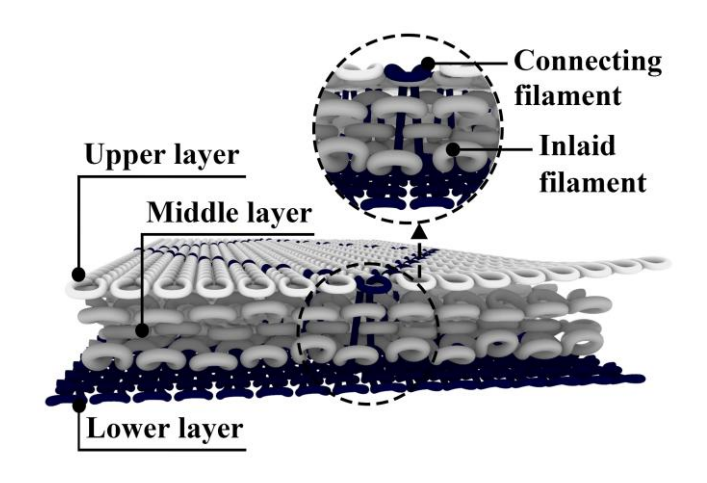


Figure 4.1 The schematic illustration of the fabric structure.

Table 4.1 Technical details of filaments

| Filament type | Linear density (D) | Tenacity (cN/tex) | Elongation (%) | |
|-------------------------|--------------------|-------------------|----------------|--|
| White 150D PLA filament | 152.62 | 28.48 | 25.06 | |
| Wille 130D PLA mament | (± 0.12) | (± 0.89) | (± 0.64) | |
| Blue 150D PLA filament | 149.85 | 21.50 | 23.72 | |
| Blue 130D PLA mament | (± 1.10) | (± 0.97) | (± 0.63) | |
| 150D PET | 148.51 | 30.79 | 14.33 | |
| ISOD PET | (± 0.40) | (± 1.82) | (± 1.25) | |
| 600D textured PET | 610.99 | 38.79 | 33.52 | |
| oood textured PET | (± 0.89) | (± 1.02) | (±2.32) | |

Note: Standard deviations are given in parentheses.

Table 4.2 Technical details of PLA staple yarn

| Yarn | Yarn count | Tenacity | Elongation | Unevenness | Hairiness | Twist |
|------------|----------------|--------------|--------------|----------------|--------------|--------------|
| | (Ne) | (cN/tex) | (%) | (%) | (H) | (per inch) |
| PLA staple | 31.62 | 13.85 | 6.71 | 6.96 | 4.75 | 19.80 |
| yarn | $(\pm \ 0.14)$ | (± 0.50) | (± 0.38) | $(\pm \ 0.05)$ | (± 0.18) | (± 0.39) |

Note: Standard deviations are given in parentheses.

4.2.2 Fabric production

Adjusting the distribution of connecting yarns in the upper layer generates different connection loops, which result in distinct stitching patterns on the fabric surface. As shown in Figure 4.2, five distinct stitching patterns (A, B, C, D, and E) were designed with regular repeat units to systematically investigate the relationship between stitching patterns and fabric properties. Table 4.3 presents the specifications of these patterns, including the repeat unit size (wales × courses), the total number of connection loops per unit, and the connection rate, which is defined as the ratio of connection loops to the total number of loops within a repeat unit. Patterns A, B, and C share a rhombic layout but differ in connection rate, whereas patterns D and E feature triangular and hexagonal shapes, respectively, with connection rates similar to that of pattern B.

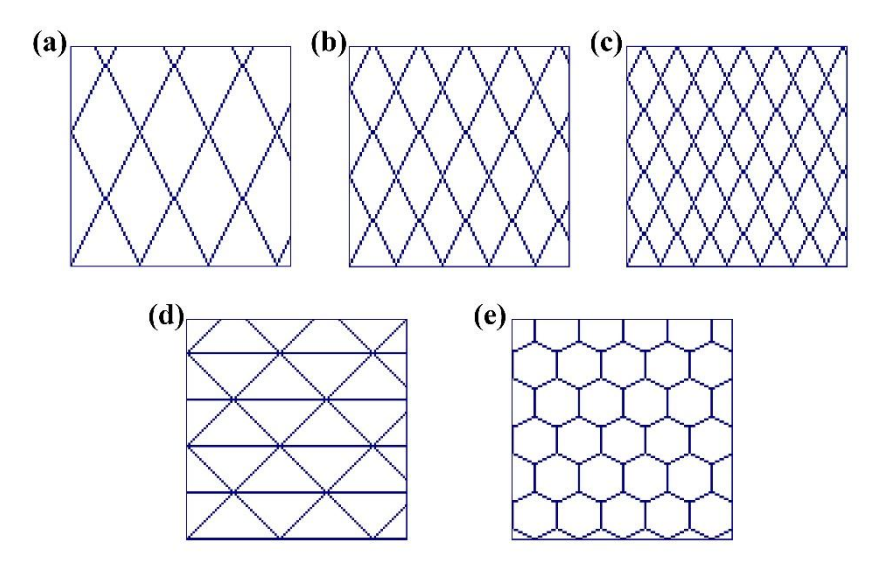


Figure 4.2 Designed stitching patterns of weft-knitted inlaid fabrics: (a) pattern A; (b) pattern B; (c) pattern C; (d) pattern D; (e) pattern E.

Table 4.3 Details of the designed stitching patterns

| Pattern | Repeat unit | Connection loops per | Connection rate |
|---------|-------------------|----------------------|-----------------|
| code | (wales × courses) | unit | (%) |
| A | 31 × 60 | 118 | 6.34 |
| В | 21 × 40 | 98 | 9.29 |
| C | 15 × 28 | 54 | 12.86 |
| D | 42 × 42 | 164 | 9.30 |
| Е | 34 × 20 | 63 | 9.26 |

As shown in Figures 4.3(a)–(c), pattern B is used as an example to demonstrate the knitting process. The pattern (Figure 4.3(a)) was first created using an Autopaint software and then transferred to a UCC548 22-gauge electronic double jacquard circular knitting machine (Terrot, Germany) for production (Figure 4.3(b)). Each knitting cycle included two knitting courses: one with loop connection (course A) and one without loop connection (course B). As shown in Figure 4.3(c), six feeders were required to complete each knitting cycle. During the process for each knitting cycle, inlaid PLA filaments were inserted between the cylinder and dial needles by the first

and fourth feeders without forming loops, while surface yarns were fed to the cylinder needles, dial needles, or both by the second, third, fifth, and sixth feeders to create face loops, back loops, or both, respectively. The connection between the upper and lower fabric layers was achieved by simultaneously forming face and back loops at the second feeder, using specific cylinder needles selected based on the designed pattern. Consistent knitting conditions, including yarn input tension, fabric take-down tension, and cam settings, were maintained for all fabrics in this study. A total of 12 weft-knitted inlaid fabrics were fabricated, differing in connection rates, pattern shapes, inlaid filaments, and surface yarns. For clarity, each fabric is labeled using a format "Pattern-Denier and type of inlaid filament" (e.g., A-600C, B-450N, B-600C-S, B-600T-P), as detailed in Table 4.4. In this notation, A/B/C/D/E indicate the pattern shape, the number (e.g., 600/450) refers to the denier of the inlaid filament, and C/N/T represent crimped PLA, normal PLA, and textured PET, respectively. The suffix "-S" or "-P" denotes that the default 150D PLA surface filament is replaced with staple PLA yarn or PET filament. Actual images of the produced fabrics are shown in Figures 4.4(a)–(1).

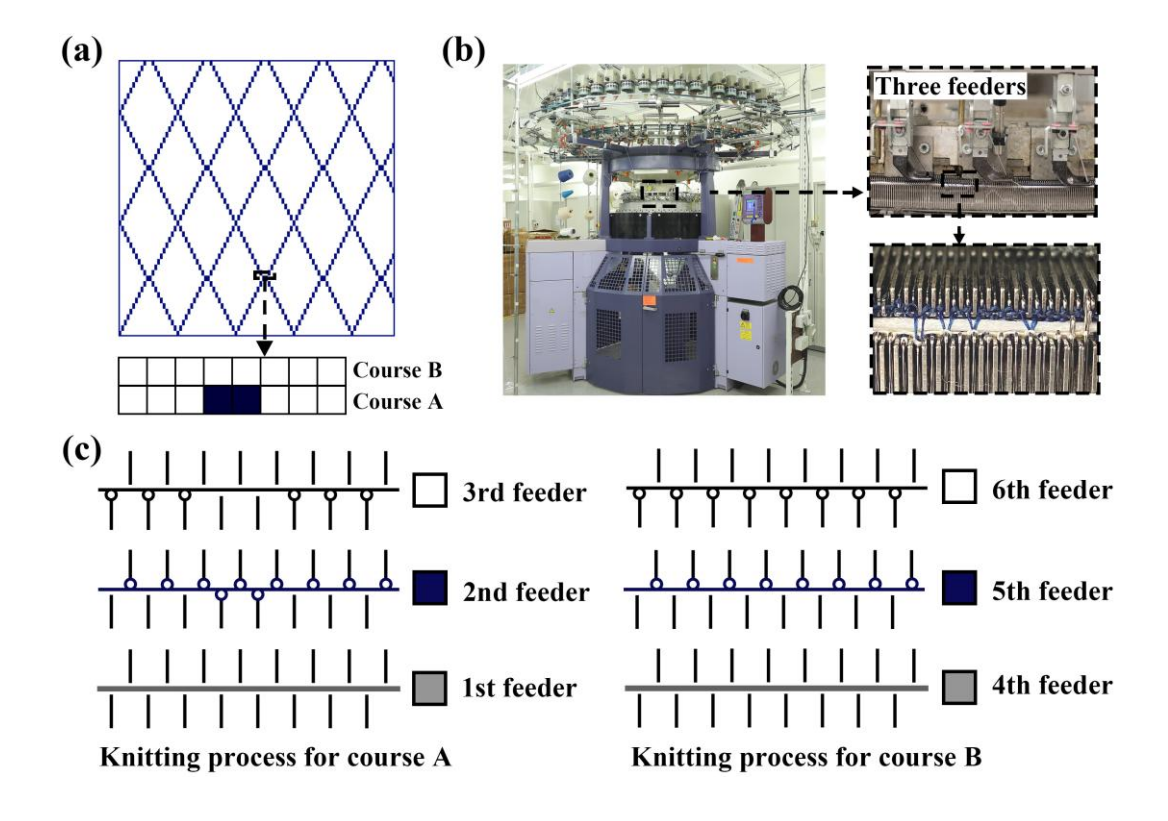


Figure 4.3 The knitting process of weft-knitted inlaid fabric: (a) the designed stitching pattern B; (b) the circular knitting machine used; (c) the knitting process for a knitting cycle.

Table 4.4 Production details of weft-knitted inlaid fabrics

| Sample | Knitted | Yarn used for the upper and lower | V 10 4 111 1 |
|----------|---------|-----------------------------------|--------------------------------|
| code | pattern | layers* | Yarn used for the middle layer |
| A-600C | A | White and blue 150D PLA filaments | 600D crimped PLA filament |
| B-600C | В | White and blue 150D PLA filaments | 600D crimped PLA filament |
| C-600C | C | White and blue 150D PLA filaments | 600D crimped PLA filament |
| D-600C | D | White and blue 150D PLA filaments | 600D crimped PLA filament |
| E-600C | E | White and blue 150D PLA filaments | 600D crimped PLA filament |
| B-450C | В | White and blue 150D PLA filaments | 450D crimped PLA filament |
| B-900C | В | White and blue 150D PLA filaments | 900D crimped PLA filament |
| B-450N | В | White and blue 150D PLA filaments | 450D normal PLA filament |
| B-600N | В | White and blue 150D PLA filaments | 600D normal PLA filament |
| B-900N | В | White and blue 150D PLA filaments | 900D normal PLA filament |
| B-600C-S | В | White 32Ne PLA staple yarn | 600D crimped PLA filament |
| B-600T-P | В | White 150D PET filament | 600D textured PET filament |

^{*}D (denier) and Ne (English cotton count) are linear density units commonly used for filament and staple yarns, respectively. 32Ne is approximately 166D, which is close to 150D.

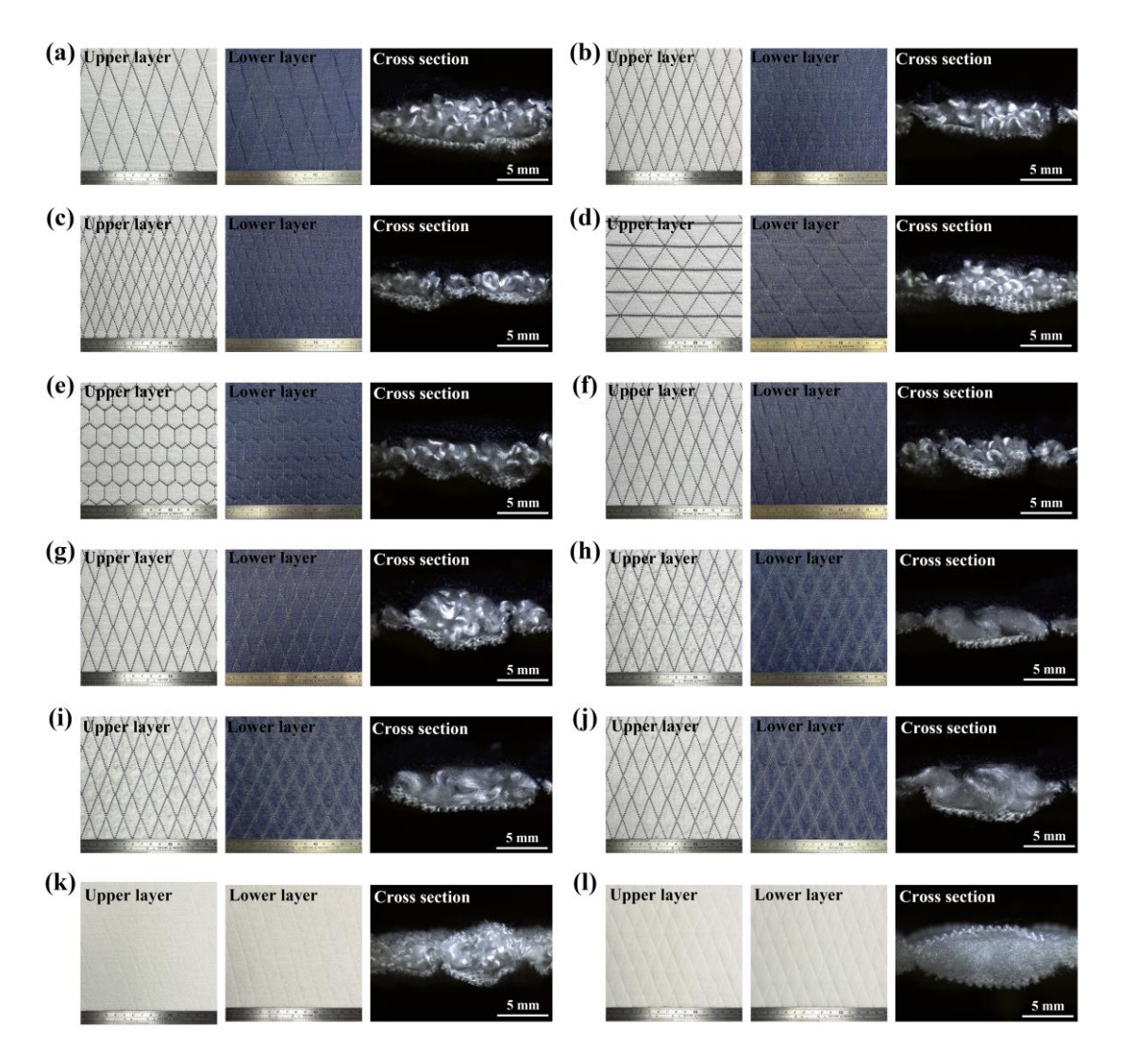


Figure 4.4 The upper layer, lower layer, and cross-section of fabricated weft-knitted inlaid fabrics: (a) fabric A-600C; (b) fabric B-600C; (c) fabric C-600C; (d) fabric D-600C; (e) fabric E-600C; (f) fabric B-450C; (g) fabric B-900C; (h) fabric B-450N; (i) fabric B-600N; (j) fabric B-900N; (k) fabric B-600C-S; (l) fabric B-600T-P.

4.3 Property evaluation

After fabrication, all fabric specimens underwent an initial washing and drying process according to the ISO 6330 standard [132]. This procedure removes water-soluble impurities and reduces dimensional instability in the fabrics. Before measurements, all samples were conditioned for 24 hours under standard atmospheric conditions $(20 \pm 2^{\circ}\text{C} \text{ and } 65 \pm 2\% \text{ relative humidity}).$

4.3.1 Physical properties

The fabric morphology was analyzed using an M165C optical microscope (Leica, Germany). The fabric's grams per square meter (GSM) were measured using a BX 300 electronic balance (Shimadzu, Japan) in accordance with ASTM D3776-09 [116]. Thickness measurements were obtained using an RME5 thickness tester, following the guidelines of ASTM D1777-96 [117]. Stitch density was assessed by counting the wales and courses per unit length on the upper fabric layer, using a counting glass and adhering to ASTM D3887-96 [118]. To ensure accuracy, three measurements were performed at separate locations on each sample, with the results averaged.

4.3.2 Air permeability

Air permeability was evaluated using the KES-F8-AP1 Air Permeability Tester (Kawabata, Japan). During testing, the instrument delivered a constant airflow to the fabric sample by moving a plunger and cylinder piston. Air was either drawn from the atmosphere or released through the specimen, with the resulting pressure measured and recorded as the fabric's air resistance (kPa·s/m). Each test was conducted on a 12 cm × 12 cm fabric sample, with five samples prepared for each fabric type to ensure reliability.

4.3.3 Water vapor permeability

The water vapor permeability was measured following British Standard 7209 using an M261 Water Vapor Permeability Tester (SDL Atlas, USA). In each test, 46 cm³ of water was placed in an open dish with an 83 mm inner diameter. The sample holder, fabric sample, and cover ring were sequentially placed over the dish, and the assembly was sealed with adhesive tape. Each prepared dish was then placed on a turntable rotating at 2 rpm for 24 hours. The dish was weighed before and after testing to calculate the water vapor transmission rate (WVTR, g/(m²·24 h)) using Equation (4.1). Three specimens were tested per fabric, and the average and standard deviation were reported.

$$WVTR = \frac{m_0 - m_1}{A} \tag{4.1}$$

$$A = \left(\frac{\pi d^2}{4}\right) \times 10^{-6}$$

where m_0 and m_1 are the weight of the dish with the water and fabric sample at the beginning and after 24 h of the test (g), A denotes the test area (m²), and d is the inner diameter of the test dish (83 mm).

4.3.4 Thermal insulation

The thermal insulation of the weft-knitted inlaid fabrics was assessed using the keeping warmth ratio, measured with the KES-F7 Thermo Labo II (Kawabata, Japan). During each test, fabric samples were placed on a 100 cm² heated plate, maintained at 10°C above the ambient room temperature. A controlled wind flow at a steady velocity of 30 cm/s was applied to the sample surface. Heat loss through the fabric was recorded and used to calculate the keeping warmth ratio based on Equation (4.2). Each measurement was tested five times to ensure accuracy and repeatability.

$$\alpha = \frac{W - W_0}{W_0} \times 100 \tag{4.2}$$

where α represents the keeping warmth ratio of the fabric (%), W denotes the heat loss with the fabric, and W_0 represents the heat loss without the fabric.

4.3.5 Compression durability

Compression durability was assessed by subjecting the fabrics to 1000 continuous compression cycles. These tests were performed on a 5566 tensile testing machine (Instron, USA) in compressive mode, as illustrated in Figure 4.5(a). A compression platen with a diameter of 5 cm and a 19.63 cm² area (Figure 4.4(b)) was used for testing, with specimen dimensions matching the platen area. The loading and unloading speeds were set to 15.0 mm/min, with the compressive stress gradually increasing to a fixed value of 6 kPa. This maximum stress level was selected based on findings from a mattress pressure distribution study, which identified optimal comfort pressure ranges.

For males, back, waist, and hip pressures ranged from 5.1–5.5 kPa, 4.1–4.5 kPa, and 5.4–9.4 kPa, respectively, while for females, the corresponding ranges were 4.1–6.4 kPa, 3.1–3.6 kPa, and 5.2–8.2 kPa [133].

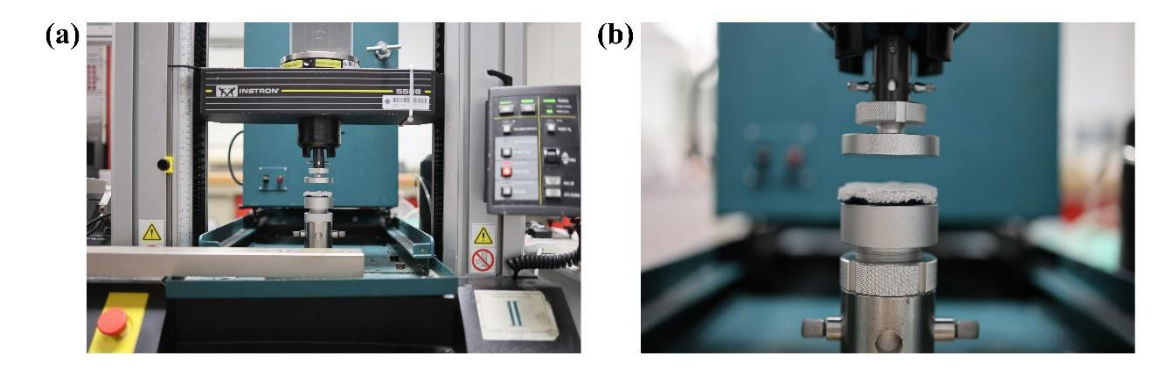


Figure 4.5 The Instron 5566 testing machine: (a) the primary testing components; (b) the compression platen.

Prior to testing, the initial fabric thickness (T_0) was measured under a light pressure of 4 gf/cm². Then, the fabric thickness after r compression cycles (T_r) was recorded. Thickness loss (T_l) was calculated as the difference between the initial thickness and the thickness after r cycles and was used to evaluate the compression durability of the fabrics. It was determined using Equation (4.3):

$$T_l = \frac{T_0 - T_r}{T_0} \times 100 \tag{4.3}$$

where T_0 represents the initial fabric thickness (mm), T_r denotes the fabric thickness after r cycles (mm), and T_l represents the thickness loss after r cycles (%).

Additionally, the energy absorbed during compression (E_a , kgf·mm) was calculated from the compression stress–strain curves recorded during the loading process. The calculation was performed using the following equation:

$$E_a = \int_{T_0}^{T_n} P dT \tag{4.4}$$

where T_0 is the initial fabric thickness (mm), T_n is the fabric thickness at maximum pressure during compression (mm), and P is the applied compressive pressure (kPa).

4.3.6 Pilling and abrasion resistance tests

The pilling resistance of the fabrics was evaluated with a M235 Martindale Tester (SDL Atlas, USA) following ASTM D4970/D4970M [134]. The fabric specimen was cut into a 38-mm diameter circle and placed in a holder along with a 3-mm polyurethane foam disk. After 7000 pilling cycles, the tested fabrics were evaluated in a viewing cabinet and graded by comparison with visual standards on a scale of 5 to 1, where 5 indicates no pilling and 1 indicates very severe pilling.

The abrasion resistance of the fabrics was assessed in accordance with ASTM D4966-22 [135] using the same M235 Martindale Tester (SDL Atlas, USA). As in the pilling resistance test, fabric specimens were prepared by cutting 38-mm diameter circles and placing them in holders with a 3-mm polyurethane foam disk. Unlike the pilling resistance test, an additional pressure of 9 ± 0.2 kPa was applied to each assembled holder during the abrasion test. The abrasion resistance was determined by recording the number of cycles at which a hole appeared in the fabric. Three specimens were prepared for each type of fabric and tested in triplicate for pilling and abrasion resistance.

4.3.7 Statistical analysis

Statistical analysis was conducted using SPSS version 26.0 (IBM Corp., USA). Analysis of variance (ANOVA) was employed to evaluate the relationship between the structural parameters and the physical and comfort properties of the weft-knitted inlaid fabrics. A significance level of 0.05 was used for all analyses. Sample B-600T-P, fabricated entirely with PET filaments, was excluded from the statistical analysis to

ensure consistency in material comparisons.

4.4 Results and discussion

4.4.1 Physical properties

Figures 4.6(a)–(h) present the course and wale densities, GSM, and thickness of the washed PLA weft-knitted inlaid fabrics, with Table 4.5 summarizing the corresponding ANOVA results. The findings indicate that varying the connection rate, stitching pattern, inlaid, and surface yarns significantly influences the physical properties of PLA weft-knitted inlaid fabrics. Such variations in physical properties are crucial because they directly influence the functional performance of the fabrics.

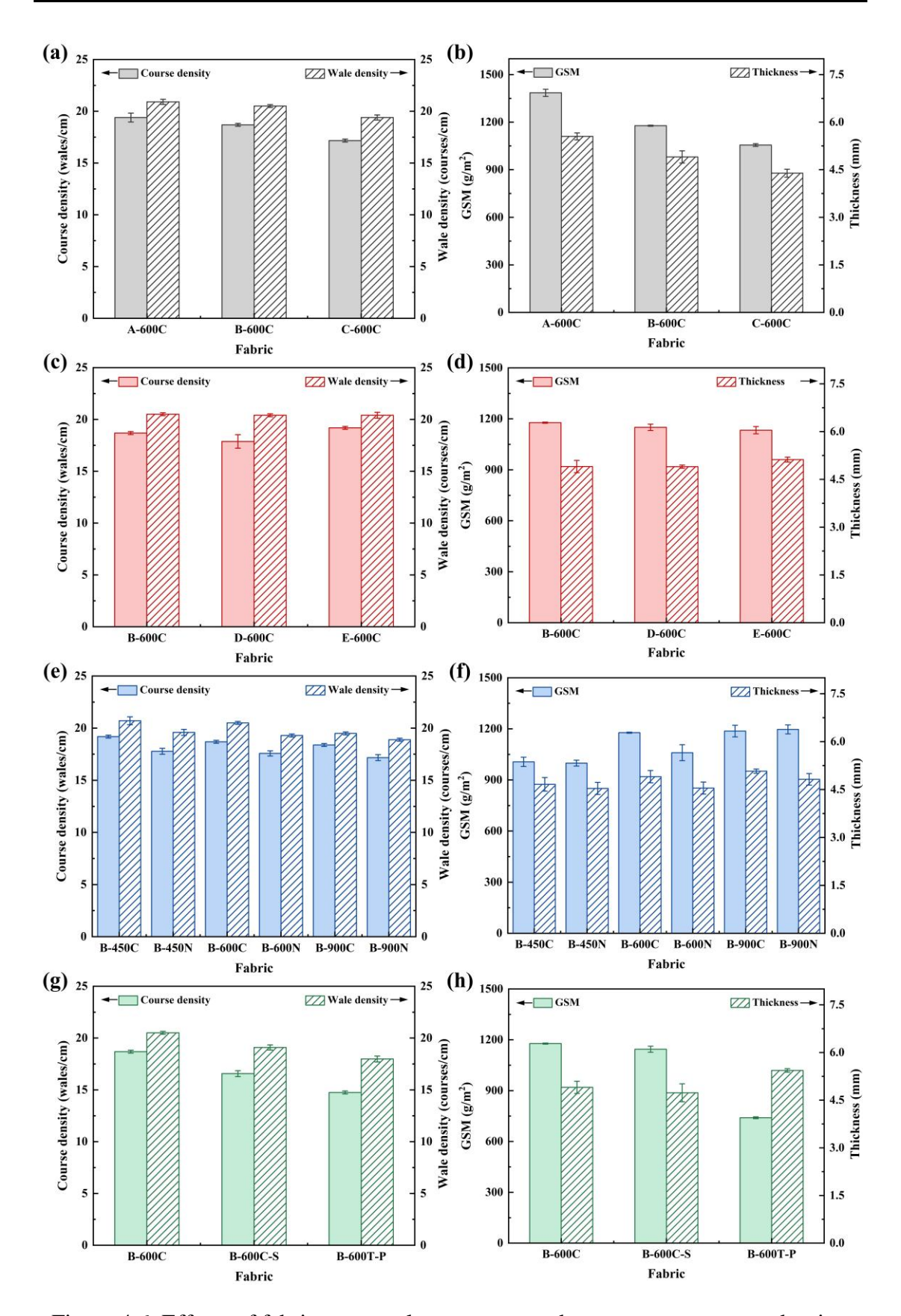


Figure 4.6. Effects of fabric structural parameters and yarn types on course density, wale density, GSM, and thickness: (a) and (b) effect of connection rate (Pattern A:

6.34%, B: 9.29%, C: 12.86%); (c) and (d) effect of stitching pattern shape (Pattern B: rhombus, D: triangle, E: hexagon); (e) and (f) effect of inlaid yarn type and linear density (C = crimped PLA, N = normal PLA); (g) and (h) effect of surface yarn type (S = PLA staple, P = PET filament).

Table 4.5 ANOVA results for physical properties of weft-knitted inlaid fabrics

| Property | Statistic | Connection | Stitching | Inlaid | Surface |
|--------------|-----------|------------|-----------|----------|---------|
| | Statistic | rate | pattern | filament | yarn |
| Course | F value | 34.455 | 5.609 | 23.957 | 88.200 |
| density | P value* | 0.001 | 0.042 | < 0.001 | 0.001 |
| Wale density | F value | 25.857 | 0.167 | 19.800 | 49.000 |
| | P value* | 0.001 | 0.850 | < 0.001 | 0.002 |
| GSM | F value | 283.404 | 3.701 | 20.442 | 6.584 |
| GSM | P value* | < 0.001 | 0.090 | < 0.001 | 0.062 |
| Thickness | F value | 62.644 | 4.179 | 5.799 | 1.013 |
| | P value* | < 0.001 | 0.042 | 0.001 | 0.344 |

^{*}P values in bold indicate significance at ≤ 0.05 .

As shown in Figure 4.6(a), the course and wale densities of PLA weft-knitted inlaid fabrics increase as the connection rate decreases (P = 0.001 for both). This trend is closely associated with the structural recovery behavior of the crimped PLA filaments in the middle layer. During knitting, these filaments are elongated and temporarily straightened due to production tension. Once the fabrics are removed from the machine and subjected to post-treatment processes such as washing, the inlaid filaments gradually recover their original crimped morphology, resulting in filament shortening and overall fabric shrinkage. In fabrics with lower connection rates, such as A-600C (6.34%), the layer connections are looser, allowing the crimped filaments to retract more freely and fully recover their crimped configuration. This enhanced recovery promotes fabric shrinkage, thereby contributing to higher course and wale densities. In addition, the shrinkage compacts the fiber structure, increasing fiber packing density and volume occupancy, which in turn leads to higher GSM and thickness (Figure 4.6(b),

both P < 0.001). Conversely, higher connection rates, as seen in fabric C-600C (12.86%), strengthen interlayer bonding, restricting filament retraction and limiting crimp recovery. As a result, these fabrics exhibit reduced shrinkage and, consequently, lower stitch density, GSM, and thickness.

For a similar connection rate, different stitching patterns lead to significant variation in fabric course density (P = 0.042), whereas no significant difference is observed in wale density (P = 0.850), as illustrated in Figure 4.6(c). Among the tested samples, fabric E-600C with a hexagonal stitching pattern exhibits the highest course density, followed by the rhombic pattern (B-600C), whereas the triangular pattern (D-600C) shows the lowest. These differences are attributed to the distinct distribution of connection loops in each pattern. The hexagonal (Figure 4.2(e)) and rhombic (Figure 4.2(b)) patterns have symmetrical and uniformly distributed connection loops, which facilitate more consistent shrinkage of the fabric layers with the inlaid filaments, thereby increasing course density. In contrast, the triangular pattern (Figure 4.2(d)) concentrates its connection loops along the bottom edge, where densely arranged junctions hinder filament shrinkage, leading to reduced course density. This structural constraint also contributes to a similar trend in fabric thickness, with fabric D-600C exhibiting the lowest thickness (Figure 4.6(d), P = 0.042). However, the stitching pattern design does not have a statistically significant effect on GSM (P = 0.09).

The effect of inlaid filaments on course and wale densities is demonstrated in Figure 4.6(e). Fabrics knitted with crimped PLA filaments exhibit higher surface fabric densities than those with non-crimped PLA filaments (both P < 0.001). This difference arises from the shrinkage of crimped PLA filaments, which reduces the overall fabric dimensions and increases fabric density. The shrinkage of these filaments also enhances fabric GSM and thickness (Figure 4.6(f), P < 0.001 and = 0.001, respectively). In addition, inlaid filaments with higher linear density further increase GSM and thickness, as expected, since thicker filaments increase the number of fibers per unit area.

On the other hand, as shown in Figure 4.6(g), the surface yarn type significantly influences the fabric's course and wale densities (P = 0.001 and 0.002). Fabric B-600C, which employs PLA filament as the surface yarn, exhibits higher surface densities, likely due to the filament's tighter structure and lower linear density compared to PLA staple yarn, which together promote denser fabric formation during knitting. B-600C also shows slightly higher GSM and thickness (Figure 4.6(h)), although these differences are not statistically significant (P = 0.062 and 0.344). Compared with B-600T-P, which uses PET filament of the same linear density, B-600C displays higher surface density and GSM but lower thickness. This may be attributed to the greater shrinkage of crimped PLA filaments, which increases surface density and GSM, whereas smaller interlayer gaps in PLA fabrics contribute to reduced thickness.

4.4.2 Air permeability

Air permeability is a crucial factor in assessing fabric comfort, as it reflects the fabric's capacity to regulate gas exchange between the body and the surrounding environment. It can be quantified by air resistance (kPa·s/m), with lower air resistance indicating greater air permeability. Enhanced air permeability enables the skin to breathe more effectively, thereby reducing the sensation of heat and moisture accumulation. Figures 4.7(a)–(d) and Table 4.6 present the air resistance results and the corresponding statistical analysis for the PLA weft-knitted inlaid fabrics.

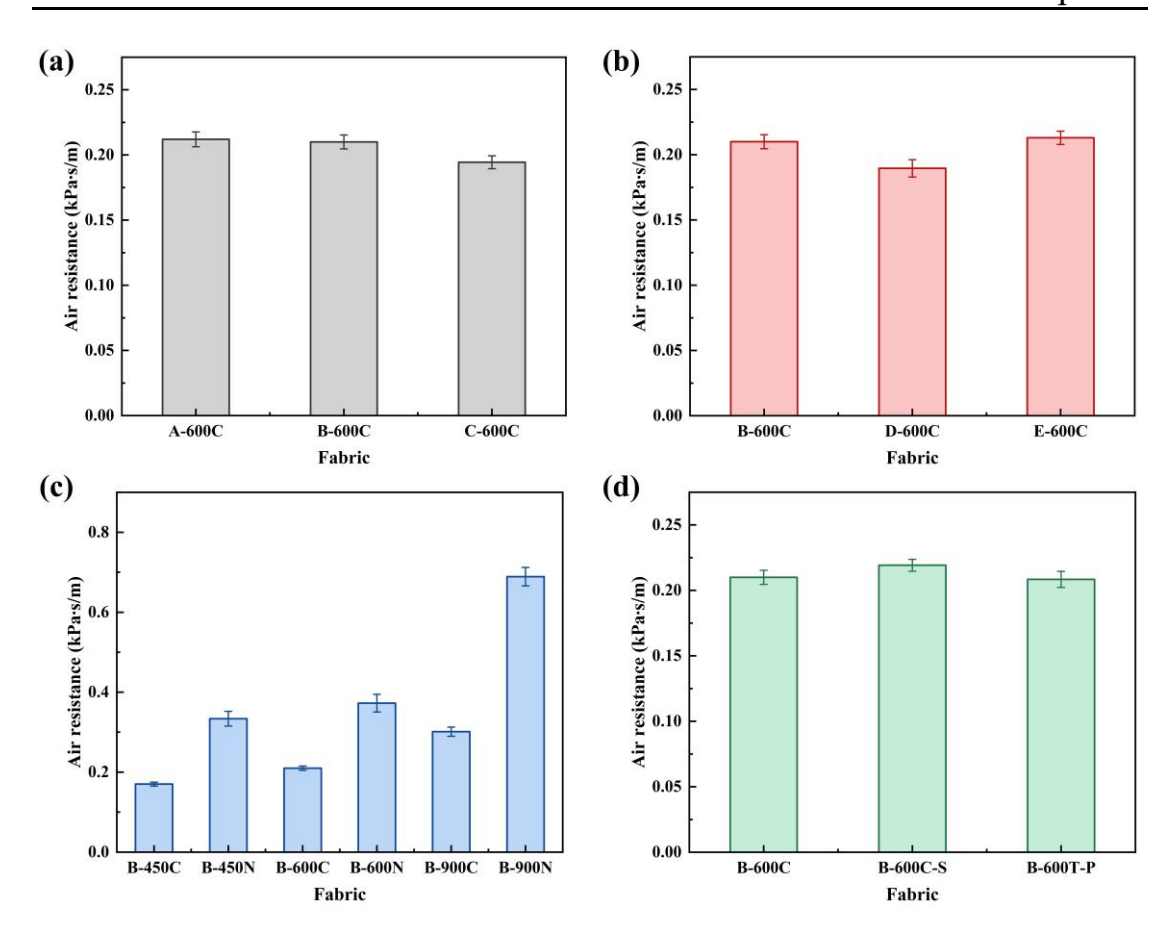


Figure 4.7 Effects of fabric structural parameters and yarn types on air resistance: (a) effect of connection rate (Pattern A: 6.34%, B: 9.29%, C: 12.86%); (b) effect of stitching pattern shape (Pattern B: rhombus, D: triangle, E: hexagon); (c) effect of inlaid yarn type and linear density (C = crimped PLA, N = normal PLA); (d) effect of surface yarn type (S = PLA staple, P = PET filament).

Table 4.6 ANOVA results for air resistance of weft-knitted inlaid fabrics

| Property | Statistic | Connection rate | Stitching pattern | Inlaid filament | Surface yarn |
|----------------|-----------|-----------------|-------------------|-----------------|--------------|
| Air resistance | F value | 13.041 | 19.643 | 524.505 | 6.859 |
| | P value* | 0.001 | < 0.001 | < 0.001 | 0.031 |

^{*}*P* values in bold indicate significance at \leq 0.05.

Figure 4.7(a) shows that fabric A-600C, with a lower connection rate of 6.34%, exhibits significantly higher air resistance (P = 0.001), indicating reduced air permeability. This increase in air resistance is likely due to the greater shrinkage of crimped PLA filaments

in such patterns, which increases the surface density, GSM, and thickness of the fabric, thereby restricting airflow. As illustrated in Figure 4.7(b), the stitching pattern also significantly influences air permeability (P < 0.001). Fabric E-600C, with a hexagonal pattern, displays the highest air resistance and therefore the lowest air permeability. This is likely caused by its higher course density and thickness, along with smaller inter-yarn gaps and more restricted airflow channels. In comparison, the rhombic stitching pattern (B-600C) results in moderate structural tightness and air resistance. The triangular pattern (D-600C), which has the lowest course density and thickness, creates larger surface micropores and inter-yarn gaps, allowing air to pass through more easily and resulting in the lowest air resistance and highest air permeability.

The type of inlaid filament significantly affects the fabric's air resistance, as illustrated in Figure 4.7(c) (P < 0.001). Higher air resistance is observed with increasing linear density of the inlaid filaments, as it raises the number of fibers per unit area, thereby obstructing airflow. Fabrics inlaid with crimped filaments exhibit lower air resistance than those with non-crimped filaments, likely due to the bulky morphology of crimped filaments, which enhances internal porosity and improves air permeability. Figure 4.7(d) further illustrates that fabric B-600C-S, knitted with PLA staple yarns, demonstrates higher air resistance than B-600C, made with PLA filaments (P = 0.031). This variation arises from structural differences between the two yarn types. Staple yarns, composed of short fibers twisted together, possess surface hairiness that impedes airflow, whereas filament yarns, made of smooth and continuous long fibers, facilitate better air passage. Moreover, the air resistance of PLA fabrics is comparable to that of fabrics made with PET yarns, indicating minimal differences in air permeability between the two materials.

4.4.3 Water vapor permeability

Water vapor permeability measures a fabric's ability to release perspiration in the form of water vapor from the skin to the environment, with higher permeability enhancing comfort by allowing moisture to evaporate more efficiently. This property is typically

assessed using WVTR, where higher values indicate superior water vapor permeability. The WVTR results for PLA weft-knitted inlaid fabrics, along with the ANOVA analysis, are presented in Figures 4.8(a)–(d) and Table 4.7, respectively.

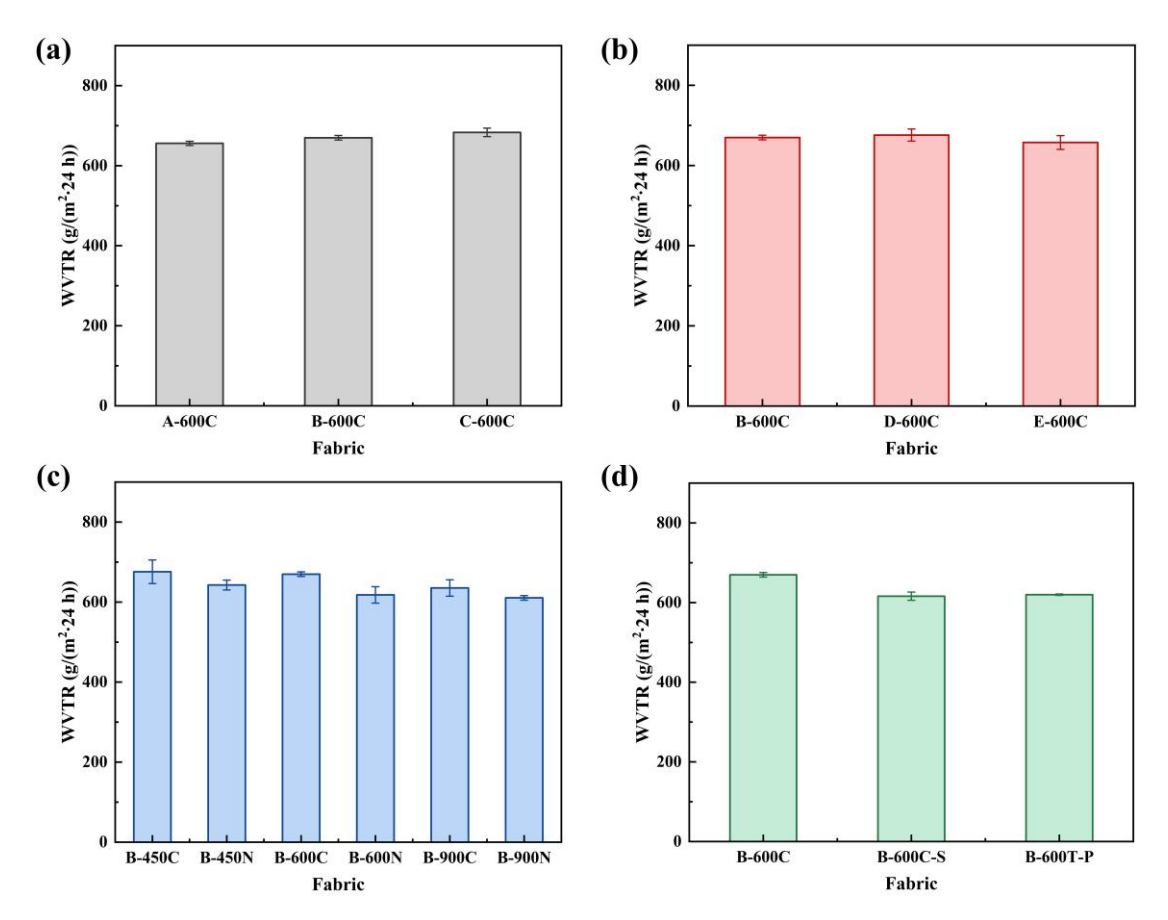


Figure 4.8 Effects of fabric structural parameters and yarn types on WVTR: (a) effect of connection rate (Pattern A: 6.34%, B: 9.29%, C: 12.86%); (b) effect of stitching pattern shape (Pattern B: rhombus, D: triangle, E: hexagon); (c) effect of inlaid yarn type and linear density (C = crimped PLA, N = normal PLA); (d) effect of surface yarn type (S = PLA staple, P = PET filament).

Table 4.7 ANOVA results for WVTR of weft-knitted inlaid fabrics

| Property | Statistic | Connection rate | Stitching pattern | Inlaid filament | Surface yarn |
|----------|-----------|-----------------|-------------------|-----------------|--------------|
| WVTR | F value | 6.526 | 0.956 | 4.384 | 41.589 |
| | P value* | 0.031 | 0.436 | 0.017 | 0.003 |

^{*}*P* values in bold indicate significance at \leq 0.05.

As illustrated in Figure 4.8(a), the fabric with a higher connection rate (C-600C) exhibits slightly increased WVTR values (P = 0.031), indicating superior water vapor permeability. This enhancement can be attributed to the fabric's lower surface density, which increases surface porosity and facilitates more efficient vapor diffusion. Owing to their lower GSM and reduced thickness, high-connection fabrics tend to have fewer fiber-to-fiber contact points, which further reduces resistance to vapor migration. In contrast, the densely packed fibers in the lower-connection fabric A-600C obstruct continuous inter-fiber pathways for vapor transmission, thereby reducing WVTR values. Although variations in WVTR are observed among fabrics with different stitching patterns (Figure 4.8(b)), these differences are not statistically significant (P = 0.436), suggesting that the stitching patterns with identical connection rates selected in this study have minimal impact on water vapor permeability.

Reducing the linear density of the inlaid filaments or incorporating crimped filaments significantly improves the WVTR values of the fabric (P = 0.017), as shown in Figure 4.8(c). Inlaid filaments with lower linear density and a crimped structure create larger inter-fiber spaces in the fabric (B-450C), thereby reducing resistance to water vapor transmission and facilitating its diffusion. The surface yarn type also has a notable impact on WVTR values (Figure 4.8(d), P = 0.003). Fabric with PLA staple yarns on the surface (B-600C-S) exhibits slightly lower WVTR values compared to that with PLA filaments (B-600C). This variation likely results from the surface hairiness of staple yarns, which hinders water vapor transfer between fibers. Moreover, PLA fabrics demonstrate slightly higher WVTR values than PET fabrics, potentially due to the bulky and porous structure formed by crimped PLA filaments.

4.4.4 Thermal insulation

Thermal insulation is another key parameter in evaluating fabric comfort and can be represented by the keeping warmth ratio. A higher keeping warmth ratio indicates a greater ability of the fabric to resist heat transfer and retain warmth. Figures 4.9(a)–(d) display the keeping warmth ratio results for various fabric samples, while Table 4.8

provides the related statistical analyses.

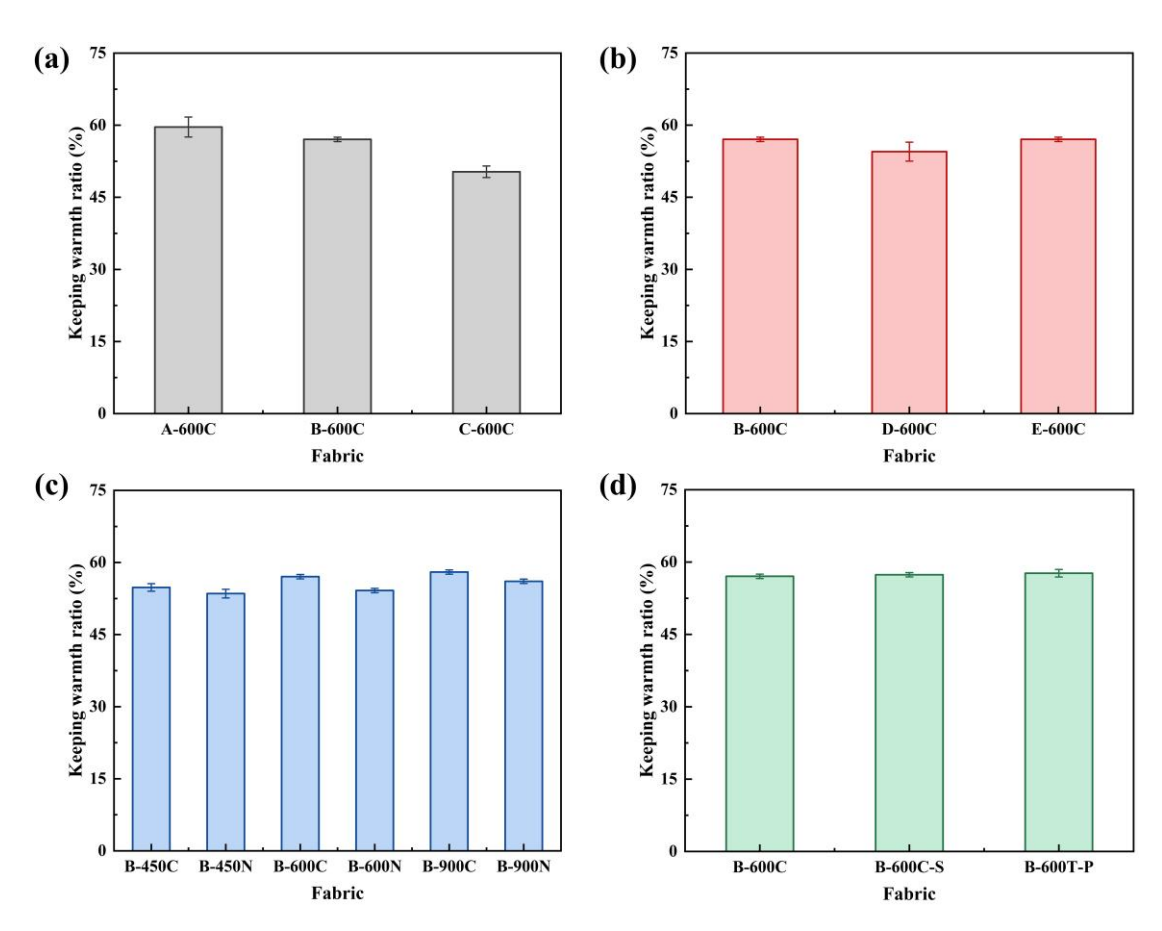


Figure 4.9 Effects of fabric structural parameters and yarn types on keeping warmth ratio: (a) effect of connection rate (Pattern A: 6.34%, B: 9.29%, C: 12.86%); (b) effect of stitching pattern shape (Pattern B: rhombus, D: triangle, E: hexagon); (c) effect of inlaid yarn type and linear density (C = crimped PLA, N = normal PLA); (d) effect of surface yarn type (S = PLA staple, P = PET filament).

Table 4.8 ANOVA results for keeping warmth ratio of weft-knitted inlaid fabrics

| Property | Statistic | Connection | Stitching | Inlaid | Surface |
|--------------|-----------|------------|-----------|----------|---------|
| | Statistic | rate | pattern | filament | yarn |
| Keeping | F value | 23.206 | 3.047 | 16.087 | 0.500 |
| warmth ratio | P value* | 0.002 | 0.122 | < 0.001 | 0.519 |

^{*}*P* values in bold indicate significance at \leq 0.05.

As shown in Figure 4.9(a), fabric A-600C with a low connection rate exhibits

significantly higher warmth retention (P = 0.002). This is likely due to the enhanced crimp recovery of the inlaid filaments, which increases the fabric's bulkiness and thickness. The resulting structure traps more still air within the fabric, which plays a critical role in enhancing thermal insulation, as air has a lower thermal conductivity than fibers [136]. This increased air retention further reduces the fabric's thermal conductivity, slowing heat transfer and improving overall insulation performance. In contrast, differences in keeping warmth ratio among fabrics with various stitching patterns do not reach statistical significance (P = 0.122), despite some variation observed in Figure 4.9(b). This result is consistent with the findings for water vapor permeability, indicating that the chosen stitching patterns with the same connection rate are not a major determinant of fabric thermal insulation.

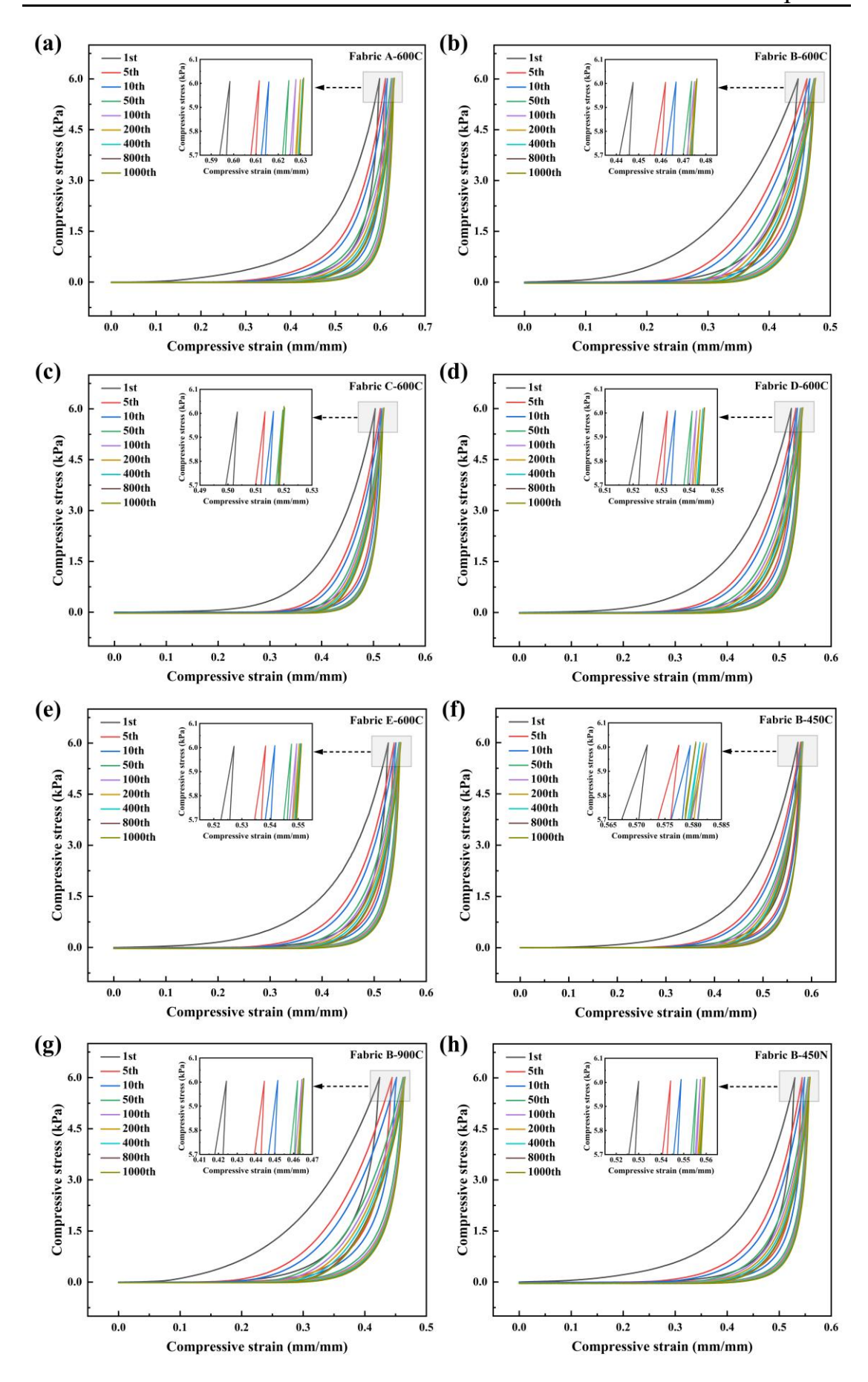
Additionally, increasing the linear density of the inlaid filaments or using crimped filaments significantly enhances the keeping warmth ratio of the fabrics (Figure 4.9(c), P < 0.001). Filaments with higher linear density increase the GSM and thickness of the fabric, effectively reducing heat transfer. The bulky structure of crimped filaments further improves thermal insulation by creating additional air-retention areas within the fabric. Although no statistically significant difference is observed (P = 0.519), fabric B-600C-S, with a surface layer knitted from PLA staple yarns, exhibits a slightly higher keeping warmth ratio than B-600C, which is knitted from PLA filaments (Figure 4.9(d)). This slight variation may be related to the surface hairiness of PLA staple yarns, which could obstruct heat transfer. While the hairiness of staple yarns negatively affects air and water vapor permeabilities of the fabric, it may contribute positively to thermal insulation. However, further investigation is necessary to validate this observation. Moreover, the similarity in keeping warmth ratio between PLA and PET fabrics suggests that these fiber types have comparable thermal insulation properties.

4.4.5 Compression durability

The compression durability test evaluates the ability of fabrics to recover from deformation after repeated compression, reflecting their performance and longevity in

daily use. The fabricated weft-knitted inlaid fabrics were subjected to 1000 cycles of compression, and their compression stress-strain curves are presented in Figures 4.10(a)–(1).

The results reveal that all weft-knitted inlaid fabrics follow a similar trend over 1000 compression cycles. During the first cycle, the stress values are relatively high, reflecting the fabrics' strong resistance to initial compression. With increasing cycles, the stress—strain curves gradually shift to the right, indicating an increase in compression strain under the same applied force. This shift is particularly pronounced during the first 10 cycles, which can be explained by structural adjustments within the fabric, including fiber rearrangement, rapid pore compression, and stress relaxation effects. By the 50th cycle, the stress—strain curves gradually stabilize, suggesting that the internal structural adjustments are nearly complete, and the fabrics' compression behavior is approaching equilibrium. Notably, even the PET weft-knitted inlaid fabric (B-600T-P), manufactured using commercialized methods (Figure 4.10(1)), exhibits the same trend, highlighting that this initial structural adjustment is an inherent and unavoidable characteristic of weft-knitted inlaid fabrics under repeated compression.



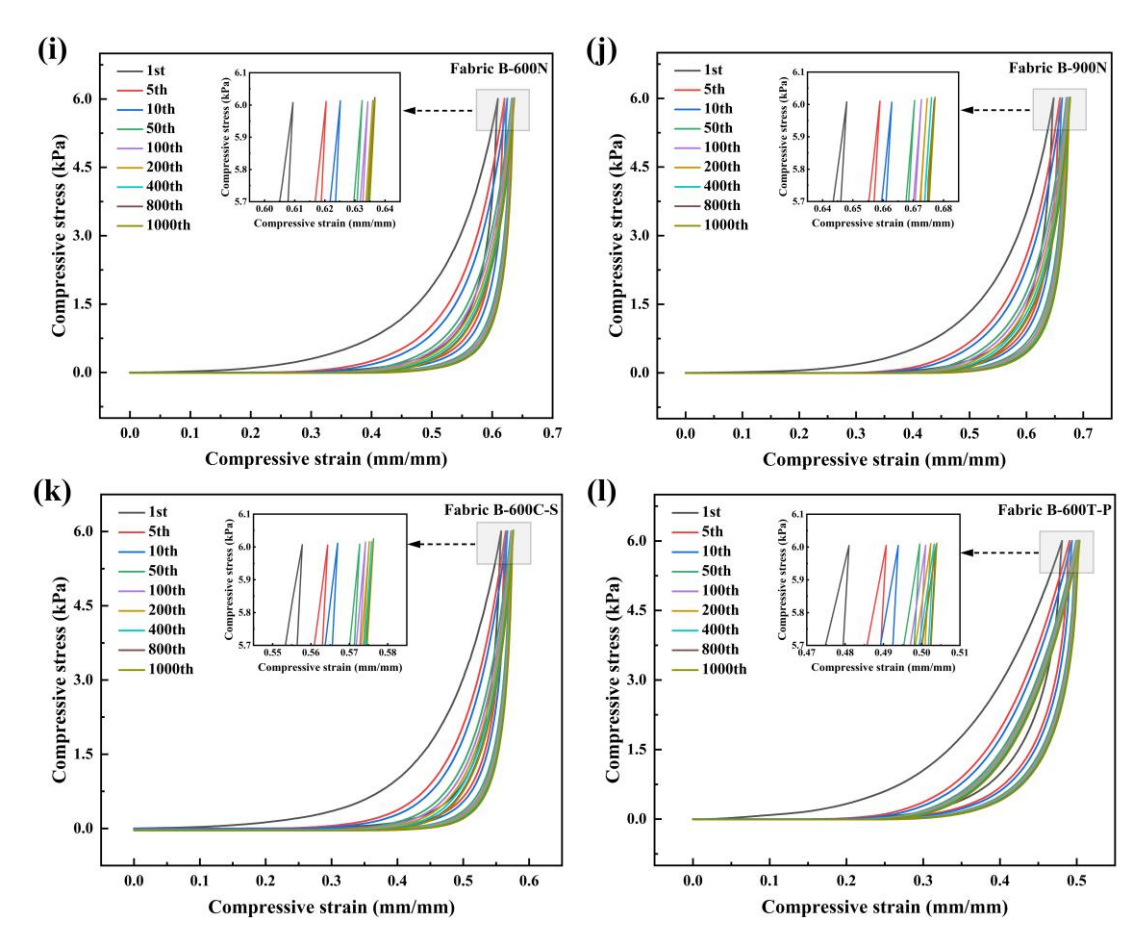


Figure 4.10 Compression stress—strain curves of weft-knitted inlaid fabrics: (a) fabric A-600C; (b) fabric B-600C; (c) fabric C-600C; (d) fabric D-600C; (e) fabric E-600C; (f) fabric B-450C; (g) fabric B-900C; (h) fabric B-450N; (i) fabric B-600N; (j) fabric B-900N; (k) fabric B-600C-S; (l) fabric B-600T-P.

To further investigate the impact of compression on the dimensional stability of fabrics, thickness loss was evaluated, as presented in Figures 4.11(a)–(d). Overall, all fabrics exhibit significant thickness loss during the first compression cycle, with losses ranging from 7.74% to 12.5%. After the 10th compression, the thickness loss gradually stabilizes, with a range of 3.75% to 11.46% between the 10th and 1000th cycles. Thickness loss also varies considerably among fabrics. As depicted in Figure 4.11(a), fabric A-600C with a lower connection rate exhibits greater thickness loss, likely due to its looser structure, which is more prone to deformation under compression. Figure 4.11(b) demonstrates that thickness loss does not consistently correlate with the uniformity of connection loop distribution among different stitching patterns,

suggesting that selected stitching patterns have a limited effect on thickness loss.

A notable difference is observed between fabrics with crimped and non-crimped inlaid filaments (Figure 4.11(c)). Fabrics with non-crimped filaments exhibit greater thickness loss, likely because the absence of a bulky structure makes these yarns more susceptible to slippage and collapse under compression, leading to plastic deformation. In contrast, the bulky morphology of crimped filaments provides cushioning, mitigates structural deformation, and facilitates partial recovery after compression, thereby reducing thickness loss. Additionally, Figure 4.11(d) reveals that fabric B-600C-S made with PLA staple yarns exhibits greater thickness loss, possibly due to the hairiness of staple yarns and the looser arrangement of fibers within the fabric. Furthermore, PLA weft-knitted inlaid fabrics show higher overall thickness loss than PET fabric (B-600T-P), likely stemming from differences in raw material properties and internal fabric structure. However, this higher thickness loss may offer PLA fabrics a potential advantage in terms of enhanced softness and comfort.

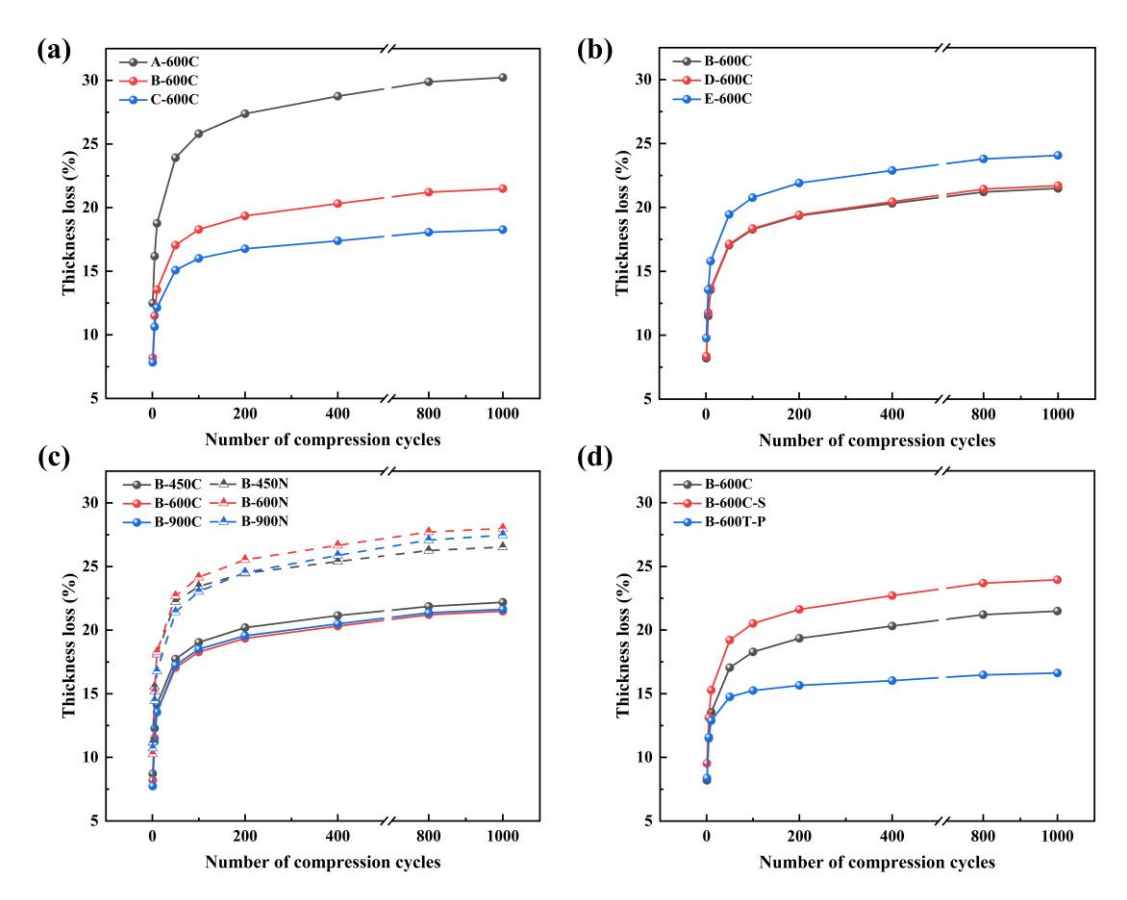


Figure 4.11 Effects of fabric structural parameters and yarn types on thickness loss:

(a) effect of connection rate (Pattern A: 6.34%, B: 9.29%, C: 12.86%); (b) effect of stitching pattern shape (Pattern B: rhombus, D: triangle, E: hexagon); (c) effect of inlaid yarn type and linear density (C = crimped PLA, N = normal PLA); (d) effect of surface yarn type (S = PLA staple, P = PET filament).

The energy absorbed by the weft-knitted inlaid fabrics during compression was also evaluated, with the results presented in Figures 4.12(a)–(d). At the initial compression stage, fabrics exhibit higher energy absorption due to substantial structural rearrangement within the fabric, which requires greater energy and causes noticeable deformation. As the number of compression cycles increases, the decline in energy absorption becomes less pronounced, indicating a gradual stabilization of the fabric structure. Figure 4.12(a) reveals that fabric C-600C, with a high connection rate, absorbs the least energy. This is likely because its tightly arranged and structurally stable internal fibers undergo less deformation during compression, resulting in lower resistance and reduced energy absorption. Figure 4.12(b) shows no significant trends in

energy absorption among fabrics with different stitching patterns, consistent with the thickness loss results. This suggests that selected stitching patterns also play a minimal role in determining energy absorption.

In contrast, Figure 4.12(c) highlights that fabrics using crimped inlaid filaments absorb more energy, which increases with the linear density of the inlaid yarns as well. The bulky structure of crimped filaments increases fabric elasticity and compression resistance, thereby elevating the energy absorption. Additionally, higher linear density filaments increase fabric thickness and fiber contact points, enhancing friction and internal resistance during compression, thus improving energy absorption. Finally, Figure 4.12(d) shows that the energy absorption varies with fabric material, with the PET fabric (B-600T-P) absorbing the most, followed by the PLA filament fabric (B-600C), and the PLA staple yarn fabric (B-600C-S) absorbing the least. The high stiffness and compression resistance of B-600T-P contribute to its greater energy absorption, whereas the looser structure of B-600C-S results in lower absorption. B-600C exhibits intermediate behavior.

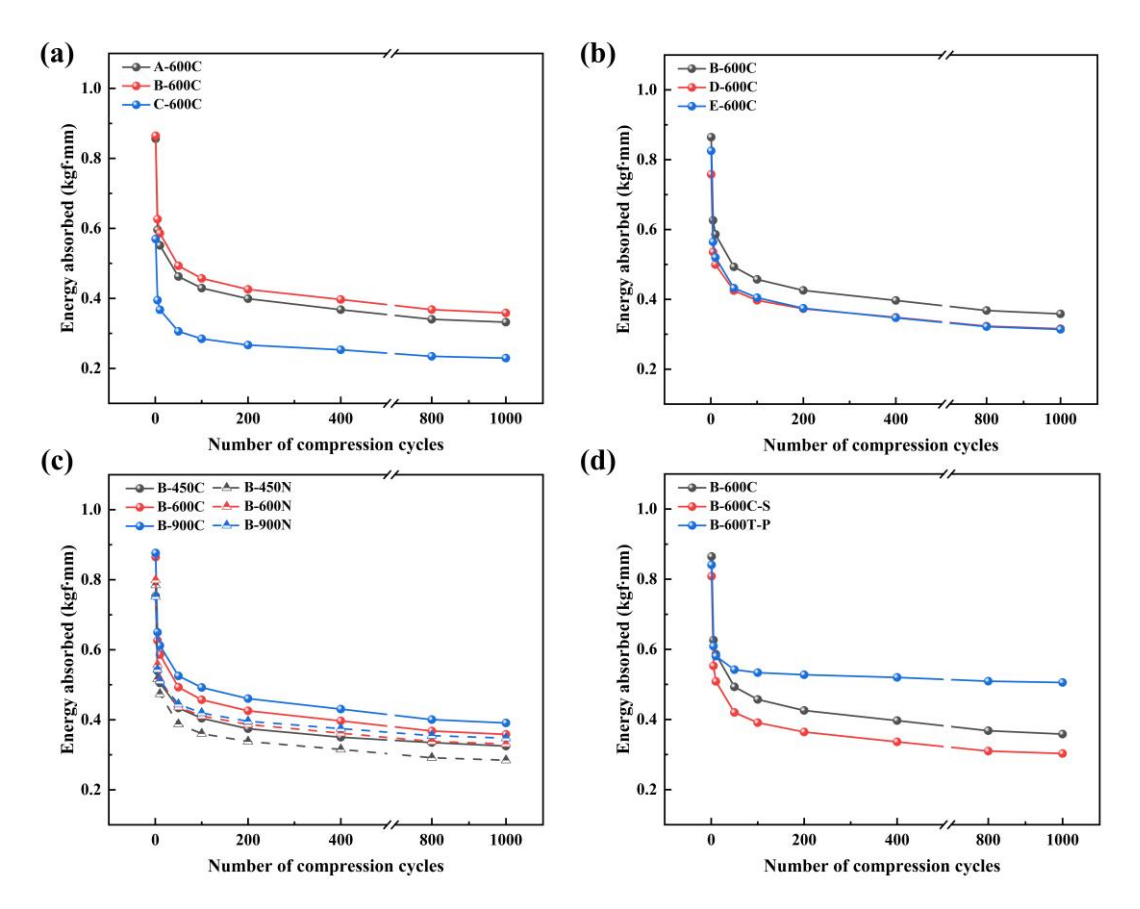


Figure 4.12 Effects of fabric structural parameters and yarn types on energy absorption: (a) effect of connection rate (Pattern A: 6.34%, B: 9.29%, C: 12.86%); (b) effect of stitching pattern shape (Pattern B: rhombus, D: triangle, E: hexagon); (c) effect of inlaid yarn type and linear density (C = crimped PLA, N = normal PLA); (d) effect of surface yarn type (S = PLA staple, P = PET filament).

4.4.6 Pilling and abrasion resistance

Pilling and abrasion resistance are key indicators of a mattress surface fabric's durability and functionality. Superior pilling resistance ensures a smooth and hairball-free surface, while high abrasion resistance allows the fabric to endure repeated friction with minimal damage. As shown in Table 4.9, all tested fabrics achieve pilling ratings of 3–4 or higher, even after 7,000 rubs, demonstrating their ability to maintain a high-quality appearance under regular use. The PLA weft-knitted inlaid fabrics also exhibit excellent abrasion resistance, withstanding more than 10,000 rubs before visible damage occurs. These results confirm the durability of PLA fabrics and their ability to meet pilling and abrasion resistance requirements for long-term use. Furthermore, the

findings indicate that the pure PLA weft-knitted inlaid fabrics developed in this study exhibit pilling and abrasion resistance comparable to those of PET weft-knitted inlaid fabrics, reinforcing their suitability for commercial applications.

Table 4.9 The pilling degree and abrasion resistance cycles of weft-knitted inlaid fabrics

| Fabric code | Pilling degree | Abrasion resistance cycles |
|-------------|----------------|----------------------------|
| A-600C | 4 | 11767 ± 170 |
| B-600C | 4 | 11417 ± 103 |
| C-600C | 4 | 10787 ± 147 |
| D-600C | 4 | 11500 ± 216 |
| E-600C | 3–4 | 10533 ± 249 |
| B-450C | 3–4 | 10367 ± 125 |
| B-900C | 4 | 12033 ± 205 |
| B-450N | 4 | 11500 ± 374 |
| B-600N | 3–4 | 11167 ± 330 |
| B-900N | 4 | 11233 ± 205 |
| B-600C-S | 4 | 11833 ± 262 |
| B-600T-P | 4 | 11400 ± 163 |

4.5 Conclusions

This chapter fabricated PLA weft-knitted inlaid fabrics using crimped PLA filaments developed in Chapter 3. The effects of fabric structural parameters and yarn types on fabric physical properties, comfort, compression, pilling, and abrasion resistance were analyzed and compared to those of PET-based weft-knitted inlaid fabrics, leading to the following conclusions:

(1) Higher connection rates decrease fabric surface density, GSM, and thickness, which in turn enhances air and water vapor permeabilities but reduces thermal insulation. These fabrics also exhibit lower thickness loss and absorb less compression energy during cyclic compression.

- (2) Stitching pattern shape influences fabric properties, with the hexagonal pattern (E-600C) exhibiting the highest course density and thickness, the triangular pattern (D-600C) showing the opposite, and the rhombic pattern (B-600C) falling in between. The triangular pattern provides the best air permeability, while the hexagonal pattern experiences greater thickness loss, and the rhombic pattern absorbs more compression energy.
- (3) Fabrics inlaid with crimped PLA filaments exhibit higher surface density, GSM, and thickness, and provide better air permeability, water vapor permeability, and thermal insulation compared to those with non-crimped filaments. Additionally, fabrics with crimped filaments show less thickness loss and absorb more energy during cyclic compression.
- (4) Fabric surfaces made with PLA filament demonstrate higher surface density, better air and water vapor permeabilities, less thickness loss, and greater energy absorption than staple yarn fabrics. Compared to PET fabrics, they offer higher surface density and GSM but lower thickness, improved water vapor permeability, comparable air permeability and thermal insulation, greater thickness loss, and reduced energy absorption.
- (5) Pilling and abrasion resistance tests show that all weft-knitted inlaid fabrics achieve a pilling grade of at least 3–4 after 7,000 rubs, with abrasion resistance exceeding 10,000 cycles.

In summary, structural parameters significantly influence the performance of PLA weft-knitted inlaid fabrics. The incorporation of crimped PLA filaments significantly enhances fabric comfort and compression properties. To further improve air and water vapor permeabilities and compression stability, stitching patterns with higher connection rates and connection loops designed to limit crimped filament shrinkage,

and PLA filament surface yarns are recommended. Conversely, for improved thermal insulation, stitching patterns with lower connection rates and connection loops that allow crimped filaments to fully shrink, along with PLA staple surface yarns, are more suitable. The pure PLA weft-knitted inlaid fabrics produced in this study exhibit excellent physical properties, comfort, and durability comparable to those of PET fabrics, confirming their suitability and potential for mattress surface applications. Building on this, the next chapter will explore the development of PLA sensors based on weft-knitted inlaid fabrics, expanding their applications in smart sleep monitoring.

Chapter 5 Development of PLA Textile Capacitive Pressure Sensor

5.1 Introduction

The previous chapter demonstrated the suitability of pure PLA weft-knitted inlaid fabrics, produced with crimped PLA filaments on an electronic double jacquard circular knitting machine, as effective materials for mattress surface applications. These fabrics exhibit physical properties, comfort, and durability comparable to those made from commercially available PET yarns. However, driven by advancements in smart home and health monitoring technologies, mattress surface fabrics are no longer limited to providing basic comfort and durability but are increasingly expected to integrate intelligent functionalities for real-time sleep monitoring. Previous research has explored sleep monitoring applications in mattress surface fabrics, including body pressure distribution [11], sleep posture and position [53, 54], electrocardiogram (ECG) and ballistocardiogram (BCG) signals [55, 56], and respiratory rate [57]. Despite these advancements, most such fabrics are produced by embedding sensors or electrodes through additional connection processes, which can compromise comfort and require more maintenance. In contrast, knitting technology offers a more efficient approach by directly integrating conductive yarns during fabric production. This single-step manufacturing process simplifies the manufacturing of smart mattress surface fabrics, making it a promising method for their development.

The objective of this chapter is to develop a textile capacitive pressure sensor (TCPS) based on PLA weft-knitted inlaid fabrics by integrating conductive yarns and utilizing intarsia knitting technology on a Shima Seiki computerized flat-knitting machine. It is noteworthy that the knitting machine used in this chapter differs from the one employed in the previous chapter; however, the PLA-based TCPS maintains the same PLA weft-knitted inlaid structure as before. The computerized flat knitting machine was selected for its advanced features, including the versatile fabric design system, precise single-

needle selection mechanism, and easily motion-controlled yarn carriers. These capabilities enable the accurate integration of conductive yarns into designated regions and facilitate the simultaneous fabrication of various conductive and non-conductive areas, thereby enhancing structural precision and productivity. Using the computerized flat-knitting machine, this chapter systematically investigates the effects of conductive yarns, inlaid filaments, and arrangements of electrode wales and courses on the sensing performance of the TCPS to achieve enhanced functionality. The improved TCPS is evaluated for its capacitive response and dynamic properties under varying pressure loads, compression rates, and repeated washing and loading cycles. Furthermore, the air permeability, water vapor permeability, thermal insulation, and compression properties of the TCPS fabric are measured and compared with those of commercial PET mattress fabrics, validating its potential as a smart mattress material.

5.2 Fabrication and working principle of the TCPS

5.2.1 Materials

Crimped PLA filaments with linear densities of 450D, 600D, and 900D were produced in Chapter 3 under the optimal heat-setting conditions, and their properties are provided in Table 3.14. White and yellow 150D PLA filaments, purchased from Ruomi Technology Co., Ltd. (Qingdao, China), are described in detail in Table 5.1. Silver-coated nylon conductive yarns with linear densities of 280D, 350D, and 400D were procured from Shengxin Special Rope Co., Ltd. (Dongguan, China), and their specifications are listed in Table 5.2. For comparative analysis, five types of commercial mattress surface fabrics were obtained from Tianye Jacquard Co., Ltd. (Hangzhou, China).

Table 5.1 Technical details of 150D PLA filaments

| Filament type | Linear density (D) | Tenacity (cN/tex) | Elongation (%) |
|--------------------------|--------------------|-------------------|----------------|
| White 150D PLA filament | 152.62 | 28.48 | 25.06 |
| white 130D PLA mament | (± 0.12) | (± 0.89) | $(\pm \ 0.64)$ |
| Yellow 150D PLA filament | 149.77 | 18.22 | 19.21 |

| $(\pm \ 0.85)$ | (± 1.66) | (± 3.28) | |
|----------------|--------------|--------------|--|

Note: Standard deviations are given in parentheses.

Table 5.2 Technical details of silver-coated nylon conductive yarns

| Filament type | Diameter (mm) | Resistance (Ω/cm) |
|----------------------|---------------|-------------------|
| 280D conductive yarn | 0.152-0.163 | 2.4–3.0 |
| 350D conductive yarn | 0.172-0.181 | 1.4–1.6 |
| 400D conductive yarn | 0.212-0.232 | 1.2–1.4 |

5.2.2 Structure and fabrication

As shown in Figure 5.1(a), the TCPS refers specifically to the grey sensing region, which is entirely textile-based and features a multilayer 'sandwich' structure comprising an upper, middle, and lower layers. In this region, conductive yarns are employed in the upper and lower surface layers to form a pair of parallel electrodes, while bulky PLA filaments are inlaid between them to serve as a compressible dielectric spacer that also separates the electrodes. When external pressure is applied, the electrode spacing decreases, resulting in a change in capacitance that allows the fabric to convert mechanical pressure into an electrical signal. The TCPS unit is seamlessly integrated with the surrounding yellow and white non-sensing regions, collectively forming a multilayer TCPS fabric. Within this fabric, the non-sensing regions share the TCPS middle layer, which increases the overall bulkiness of the fabric. In contrast to the TCPS, conventional PLA filaments are used in the upper and lower layers of the non-sensing regions, forming a jacquard pattern and structurally connecting the fabric layers.

The TCPS fabric was first designed using an SDS-ONE Apex3 system based on a weft-knitted inlaid fabric structure, and then knitted on a 14-gauge SVR123SP computerized flat-knitting machine (Shima Seiki, Japan) in a single step (Figure 5.1(b)). During knitting, one silver-coated nylon conductive yarn (Figure 5.1(c)) and three 150D PLA filaments in yellow (Figure 5.1(d)) and white (Figure 5.1(e)) were alternately knitted to

form the sensing and non-sensing surface layers, respectively. This precise arrangement of yarns was achieved by employing the intarsia knitting technique, which allows distinct functional regions to be accurately created within each course [137]. After each surface layer row, the middle layer was formed by inlaying two crimped PLA filaments (Fig. 1(f)) between the upper and lower layers without loop formation. Once the sensing region was fully knitted, the conductive yarns were guided to the fabric edge by the yarn carrier, allowing direct connection to the measurement instrument. Consequently, the entire TCPS fabric requires no additional assembly or chemical treatment, owing to the precise single-needle selection and motion-controlled yarn carriers of the knitting system. To investigate the effects of key structural factors, including the linear density of conductive yarns, the linear density of inlaid filaments, and the arrangement of electrode wales (m) and courses (n) within the sensing region, seven distinct TCPS fabrics were fabricated. The production details are provided in Table 5.3, the actual sample images are shown in Figures 5.2(a)–(g), and their corresponding technical specifications are summarized in Table 5.4.

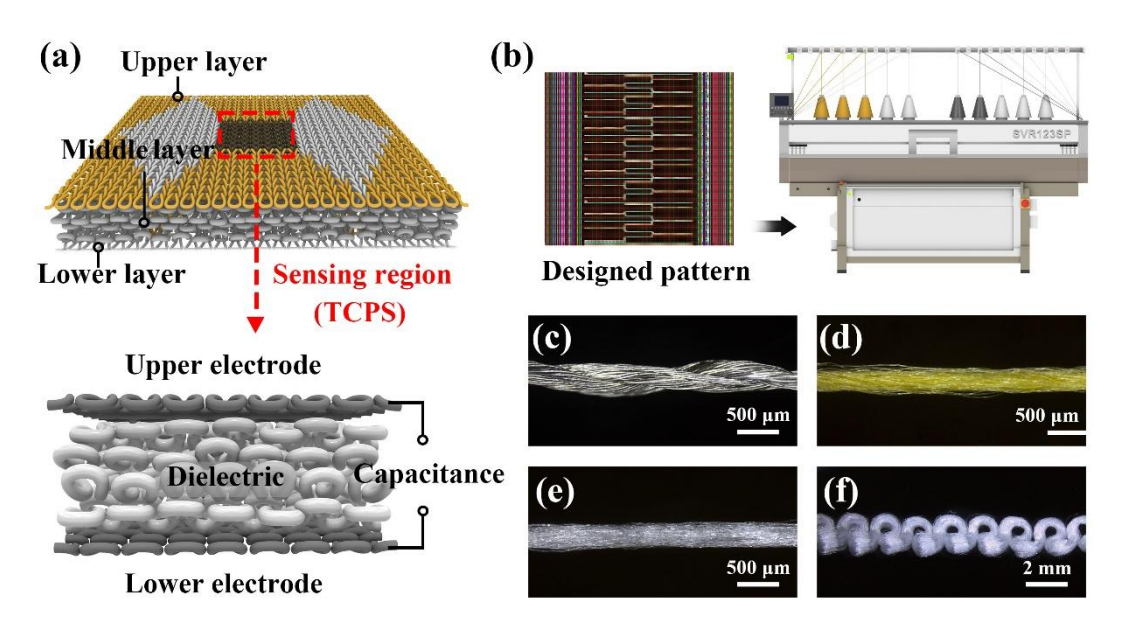


Figure 5.1 Structure and fabrication of the TCPS fabric: (a) schematic diagram of the entire TCPS fabric and a magnified cross-section of the integrated TCPS; (b) the designed pattern and computerized flat-knitting machine used for fabrication; (c)

silver-coated nylon conductive yarn; (d) yellow PLA filament; (e) white PLA filament; (f) crimped PLA filament.

Table 5.3 Production details of TCPS fabrics

| F-111- | Conductive vers | Inlaid filomont | Electrode wales and courses |
|-------------|-----------------|-----------------------------|--------------------------------------|
| rabric code | Conductive yarn | Inlaid filament | in the sensing region $(m \times n)$ |
| 1 | 2 × 280D | 2 × 600D crimped PLA | 34 × 36 |
| 2 | 2 × 350D | $2 \times 600D$ crimped PLA | 34 × 36 |
| 3 | 2 × 400D | $2 \times 600D$ crimped PLA | 34 × 36 |
| 4 | 2 × 400D | $2 \times 450D$ crimped PLA | 34 × 36 |
| 5 | 2 × 400D | $2 \times 900D$ crimped PLA | 34 × 36 |
| 6 | 2 × 400D | $2 \times 450D$ crimped PLA | 30 × 40 |
| 7 | 2 × 400D | 2 × 450D crimped PLA | 40 × 30 |

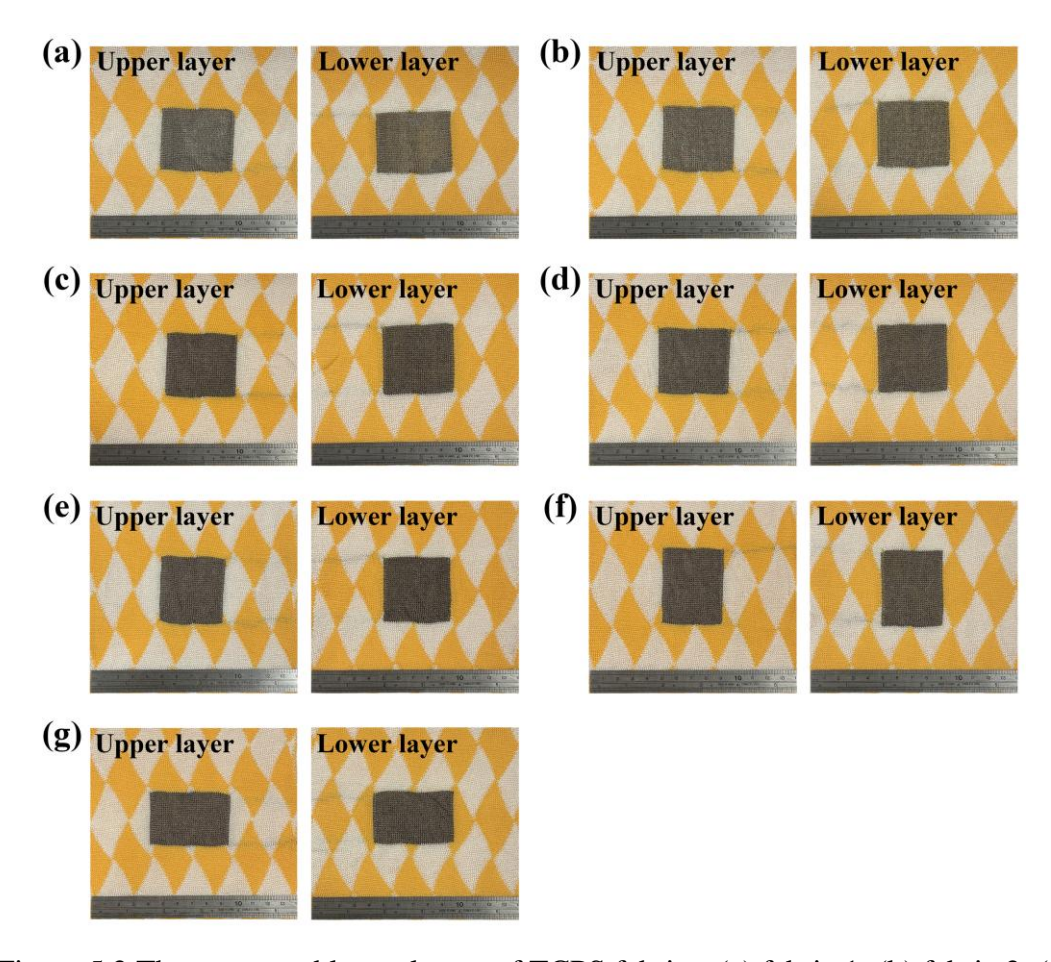


Figure 5.2 The upper and lower layers of TCPS fabrics: (a) fabric 1; (b) fabric 2; (c) fabric 3; (d) fabric 4; (e) fabric 5; (f) fabric 6; (g) fabric 7.

Table 5.4 Technical specifications of TCPS fabrics

| Fabric | Fabric density | | - GSM | Thickness | Actual area of | |
|--------|----------------|----------------|--------------------------|---------------|----------------|--------------------|
| code | Course density | Wale density | Stitch density | (g/m^2) | (mm) | the electrodes |
| code | (wales/cm) | (courses/cm) | (loops/cm ²) | (g/III) | (111111) | (cm ²) |
| 1 | 7.35 | 8.14 | 59.78 | 548.81 | 3.42 | 19.79 |
| 1 | $(\pm \ 0.19)$ | (± 0.19) | (± 1.47) | (± 24.88) | (± 0.08) | (± 0.12) |
| 2 | 7.61 | 8.40 | 63.91 | 557.12 | 3.40 | 19.56 |
| 2 | $(\pm \ 0.19)$ | (± 0.19) | (± 1.47) | (± 6.55) | (± 0.09) | (± 0.12) |
| 2 | 7.68 | 8.14 | 62.36 | 542.84 | 3.40 | 19.68 |
| 3 | $(\pm \ 0.28)$ | (± 0.37) | (± 0.51) | (± 15.23) | (± 0.10) | $(\pm \ 0.09)$ |
| 4 | 7.41 | 8.53 | 63.24 | 519.91 | 3.02 | 19.56 |
| 4 | $(\pm \ 0.09)$ | (± 0.19) | (± 1.21) | (± 3.34) | (± 0.04) | $(\pm \ 0.19)$ |
| 5 | 7.87 | 8.27 | 65.10 | 697.77 | 4.20 | 19.43 |
| 5 | $(\pm \ 0.00)$ | $(\pm \ 0.00)$ | (± 0.00) | (± 8.79) | (± 0.09) | (± 0.11) |
| (| 7.55 | 8.33 | 62.88 | 516.25 | 3.03 | 20.32 |
| 6 | $(\pm \ 0.09)$ | $(\pm \ 0.09)$ | (± 0.73) | (± 4.47) | (± 0.06) | (± 0.20) |
| 7 | 7.55 | 8.27 | 62.39 | 517.65 | 2.98 | 18.90 |
| | (± 0.09) | (± 0.00) | (± 0.77) | (± 1.45) | (± 0.05) | $(\pm \ 0.07)$ |

Note: Standard deviations are given in parentheses.

5.2.3 Modeling and working principle of the TCPS

The TCPS is designed to convert external mechanical pressure into measurable electrical signals by employing a fixed-area parallel-plate capacitor structure. Based on the fundamental principle of parallel-plate capacitance [138], the theoretical capacitance C(F) of the TCPS is determined primarily by its geometric parameters and the dielectric properties of the materials used, as mathematically described by Equation (5.1) [139]:

$$C = \frac{\varepsilon_r \varepsilon_0 A}{d} \tag{5.1}$$

where ε_r is the relative static permittivity of the dielectric layer (dimensionless), ε_θ

denotes the vacuum permittivity $(8.85 \times 10^{-12} \text{ F/m})$ [140], A is the effective electrode area (m²), and d is the thickness of the dielectric layer (m).

The relative static permittivity ε_r depends on the intrinsic properties and volume fractions of the materials within the dielectric layer. In this study, the dielectric layer of the TCPS is composed of air and crimped PLA filaments. To evaluate ε_r , it is necessary to quantify the volume fractions of these two components between the capacitor electrodes. This requires first calculating the total dielectric volume $V(m^3)$ between the electrodes:

$$V = Ad (5.2)$$

The total dielectric volume V can be further decomposed into the volumes occupied by air (V_{air}, m^3) and crimped PLA filaments (V_{PLA}, m^3) , as described in Equation (5.3):

$$V = V_{air} + V_{PLA} \tag{5.3}$$

The corresponding volume fractions of each component can then be expressed as follows:

$$\frac{V_{PLA}}{V} = \frac{V_{PLA}}{Ad} \tag{5.4}$$

$$\frac{V_{air}}{V} = \frac{Ad - V_{PLA}}{Ad} \tag{5.5}$$

Therefore, the effective relative permittivity ε_r of this two-phase dielectric layer is calculated as a volume-weighted average of the permittivities of air and crimped PLA filaments, as shown in Equation (5.6):

$$\varepsilon_{r} = \frac{V_{air}}{V} \varepsilon_{air} + \frac{V_{PLA}}{V} \varepsilon_{PLA}$$

$$= (1 - \frac{V_{PLA}}{Ad}) \varepsilon_{air} + \frac{V_{PLA} \varepsilon_{PLA}}{Ad}$$
(5.6)

where ε_{air} is the relative static permittivity of air (\approx 1) [138], and ε_{PLA} represents the relative static permittivity of PLA, typically ranging from 2.7 to 3.1 [141].

Given $\varepsilon_{air} = 1$, Equation (5.6) simplifies to:

$$\varepsilon_r = 1 + \frac{V_{PLA}}{Ad} (\varepsilon_{PLA} - 1) \tag{5.7}$$

Finally, by substituting ε_r (from Equation (5.7)) into Equation (5.1), the theoretical capacitance C of the TCPS is derived as:

$$C = \frac{\varepsilon_0 A}{d} \left[1 + \frac{V_{PLA}}{dA} (\varepsilon_{PLA} - 1) \right]$$
 (5.8)

where ε_0 is the vacuum permittivity (8.85×10⁻¹² F/m), A represents the effective electrode area (m²), d denotes the dielectric thickness (m), V_{PLA} is the volume occupied by crimped PLA filaments in the dielectric layer (m³), and ε_{PLA} is the relative static permittivity of PLA (2.7–3.1).

Equation (5.8) shows that the capacitance C of the TCPS primarily depends on three geometric parameters: the effective electrode area A, the dielectric thickness d, and the volume of crimped PLA filaments in the dielectric layer V_{PLA} . During fabrication, key knitting parameters such as cam setting, yarn feeding tension, and take-down tension were fixed based on preliminary trials. Consequently, A is mainly influenced by the arrangement of electrode wales (m) and courses (n) in the sensing region. Additionally, the linear density of the conductive yarn also influences A, as variations in yarn diameter affect loop tightness and thereby the effective electrode area. Under the same

knitting conditions, both d and V_{PLA} are primarily determined by the linear density of the crimped PLA filaments. Therefore, these three structural factors, including the arrangement of electrode wales and courses, the linear density of conductive yarns, and the linear density of crimped PLA filaments, were systematically varied in Section 5.2.2 to fabricate seven TCPS fabrics and analyze their individual effects on TCPS sensing performance.

Equation (5.8) also indicates that, for a TCPS with fixed electrode area and material composition, capacitance variations primarily arise from changes in the dielectric layer thickness under applied pressure. As illustrated in Figure 5.3, the application of external pressure reduces the distance between the two capacitor plates. This reduction not only modifies the dielectric layer thickness but also alters its effective permittivity. The combined effect of these changes leads to measurable variations in capacitance, forming the basis of the TCPS's fundamental pressure-sensing mechanism.

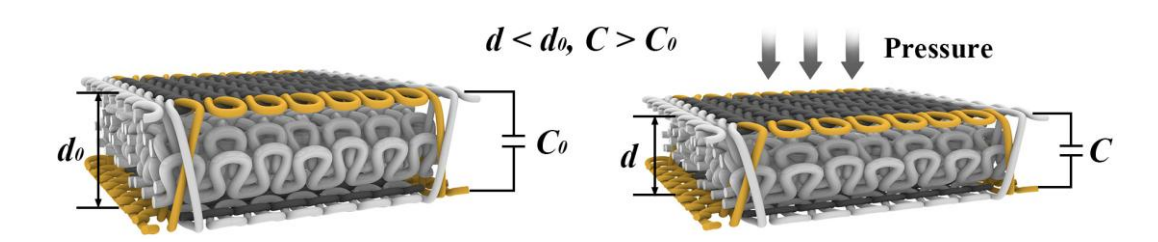


Figure 5.3 Working principle of the TCPS.

5.3 Property evaluation

5.3.1 Physical properties

The physical properties of the fabric were tested using the same methods described in Chapter 4, subsection 4.3.1. The morphology of the fabric was observed on an M165C optical microscope (Leica, Germany). The grams per square meter (GSM) of the fabric was determined using a BX 300 electronic balance (Shimadzu, Japan) following the ASTM D3776-09 standard [116]. Fabric thickness was measured by an RME5 thickness tester in accordance with ASTM D1777-96 [117]. Prior to testing, all fabric

samples were conditioned for 24 hours under standard atmospheric conditions of 20 ± 2 °C and 65 ± 2 % relative humidity.

5.3.2 Sensing performance

5.3.2.1 Measurement setup

The sensing performance of the TCPS was characterized by measuring its capacitance during the compression process. As shown in Figure 5.4, the compression was conducted using a 5566 tensile testing machine (Instron, USA), while the capacitance was monitored and recorded in real-time with a TH2830 LCR meter (Tonghui, China). The two electrodes of the sensor were connected to the LCR meter using copper wires, ensuring accurate data acquisition throughout the testing process.

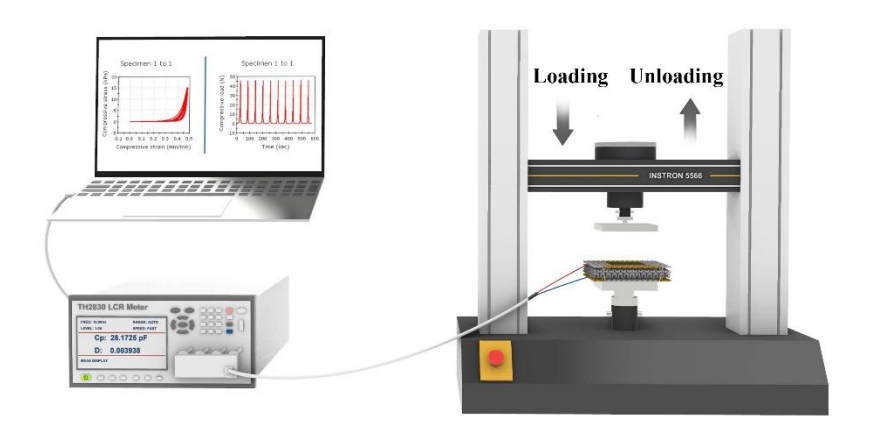


Figure 5.4 Experimental setup for measuring the capacitance of the TCPS during compression.

5.3.2.2 Sensitivity

The sensitivity of the TCPS was determined by gradually increasing the pressure to 15 kPa at a constant compression rate of 10 mm/min. For a capacitive sensor, sensitivity is typically defined as the ratio of the relative capacitance change to the change in applied pressure, as expressed in Equation (5.9) [142].

$$S = \frac{\frac{\Delta C}{C_0}}{\Delta P} = \frac{C - C_0}{\Delta P} \tag{5.9}$$

where S represents the sensitivity of the capacitive sensor (kPa⁻¹), $\Delta C/C_{\theta}$ is denotes the relative capacitance change (dimensionless), ΔC is the capacitance change (pF), C_{θ} and C are the capacitance values before and after pressure loading (pF), respectively, and ΔP is the applied pressure (kPa).

5.3.2.3 Different compression conditions

The sensing performance of the TCPS under varying compression conditions was evaluated by analyzing the effects of applied pressures and compression rates on its capacitance response. Incremental pressures of 1, 3, 6, 9, 12, and 15 kPa were applied at a constant rate of 10 mm/min, while for the compression rate analysis, the pressure was gradually increased to 15 kPa at rates of 5, 10, 15, and 20 mm/min. The capacitance response during these compression processes was monitored in real-time using the TH2830 LCR meter (Tonghui, China).

5.3.2.4 Washing test

To assess the washing durability of the TCPS, the sensor was subjected to five repetitive washing cycles following the ISO 6330:2021 standard [132]. The specimens were weighed, and 100% cotton ballast was added to achieve a total load mass of 2.0 kg. These materials were then placed in a Type B washing machine filled with 72 ± 4 L water at a temperature of 41 ± 3 °C. A detergent mass of 66 ± 1 g of 1993 AATCC standard reference detergent with optical brightener was also added. The washing procedure followed the delicate cycle, as specified in the standard. After washing, the specimens were dried using the drying procedure F (tumble dry) at 60°C. The capacitance response of the specimens was subsequently measured after the first, third, and fifth washing cycles under a gradually applied pressure of up to 15 kPa at a constant rate of 10 mm/min.

5.3.2.5 Response and recovery times

The response and recovery times of the TCPS are critical parameters for minimizing

delays in practical applications [143]. To evaluate the electrical response of the TCPS, a 330 g weight with a contact area of 30.25 cm² (corresponding to a pressure of 1.07 kPa) was applied to the sensor surface, instead of using the Instron 5566 instrument for compression. The response time during loading and the recovery time during unloading were recorded to assess the sensor's dynamic performance.

5.3.2.6 Repeatability

The repeatability of a sensor assesses its reliability in consistently reproducing capacitance responses under identical pressure conditions. For the TCPS, repeatability was evaluated by applying cyclic loading at a constant pressure of 15 kPa and recording the capacitance response over 5000 loading and unloading cycles.

5.3.3 Comfort properties

The comfort properties of the fabric, including thermal insulation, air permeability, water vapor permeability, and compression performance, were systematically evaluated. Thermal insulation, air permeability, and water vapor permeability were measured using the KES-F7 Thermo Labo II (Kawabata, Japan), KES-FB-AP1 Air Permeability Tester (Kawabata, Japan), and the M261 Water Vapor Permeability Tester (SDL Atlas, USA), respectively, following the methods detailed in Sections 4.3.4, 4.3.2, and 4.3.3 of Chapter 4. Compression properties were assessed using the KES-FB3-A Compression Tester (Kawabata, Japan), in accordance with the guidelines provided by Kato Tech Co., Ltd. The compression area corresponded to the circular pressing plate of the tester, with an area of 2 cm², and the maximum applied pressure was 100 gf/cm². Test specimens were prepared with dimensions of 20 cm × 20 cm, and each sample was tested three times.

5.4 Results and discussion

5.4.1 Effect of structural parameters

To improve the sensing performance of the TCPS, seven TCPS fabrics were fabricated

with different conductive yarns, inlaid filaments, and arrangements of electrode wales (m) and courses (n) (Figure 5.5(a)). Their capacitance change ratios $(\Delta C/C_0)$ were compared under same compression conditions to investigate the influence of these three factors. The resulting $\Delta C/C_0$ values are presented in Figures 5.5(b)–(d).

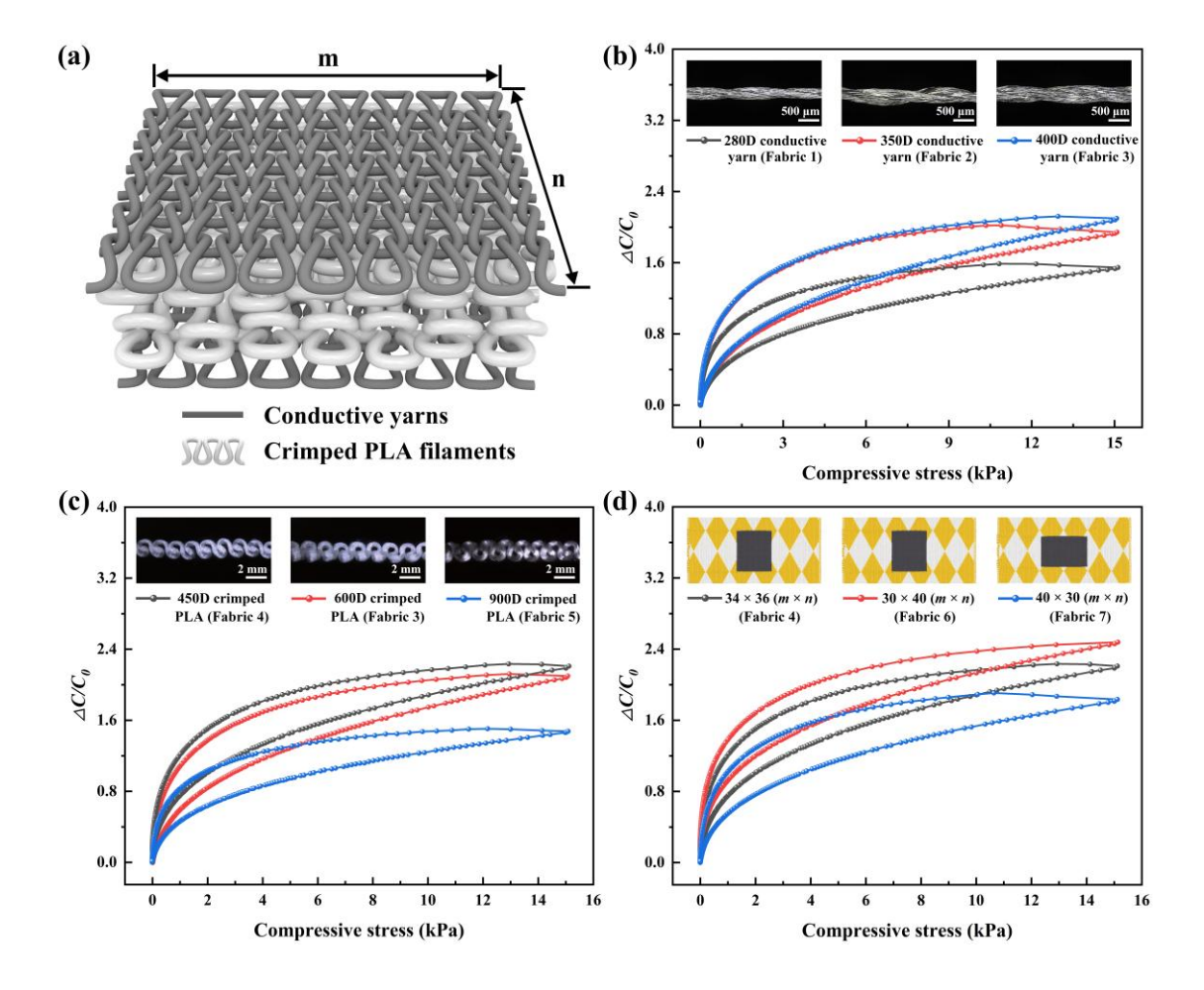


Figure 5.5 $\Delta C/C_0$ of TCPS under single compression: (a) schematic diagram of the TCPS; (b) effect of conductive yarns; (c) effect of inlaid filaments; (d) effect of electrode wales (m) and courses (n).

Figure 5.5(b) shows that the $\Delta C/C_0$ of the TCPS increases significantly as the linear density of the conductive yarns rises from 280D to 400D. This enhancement is attributed to the more compact electrode structure formed by the thicker conductive yarns (e.g., 400D), which reduces the inter-yarn gaps compared to finer yarns. Consequently, the effective electrode area is expanded, thereby enhancing the

capacitive performance of the TCPS. Additionally, thicker conductive yarns exhibit lower electrical resistance (Table 5.2), which reduces the equivalent series resistance and improves electrode conductivity, further contributing to the enhanced TCPS performance. Conversely, Figure 5.5(c) reveals an inverse relationship between $\Delta C/C_0$ and the linear density of crimped PLA filaments. Specifically, TCPS incorporating thinner crimped PLA filaments (e.g., 450D) exhibit higher $\Delta C/C_0$ values. This improvement results from the reduced fabric thickness achieved by thinner crimped PLA filaments, leading to decreased electrode separation and enhanced capacitive sensitivity.

Furthermore, Figure 5.5(d) indicates that $\Delta C/C_0$ is notably influenced by the arrangement of electrode wales (m) and courses (n). Among the tested combinations, the 30×40 ($m \times n$) arrangement achieves the highest $\Delta C/C_0$, followed by 34×36 , while 40×30 exhibits the lowest value. Although the total number of electrode loops remains approximately constant across arrangements, variations in electrode area account for the observed differences. As shown in Table 5.4, the electrode areas for the 34×36 , 30 \times 40 and 40 \times 30 arrangements are 19.56 cm², 20.32 cm² and 18.90 cm², respectively. Since a larger electrode area enhances sensing performance, the 30 × 40 arrangement achieves the highest $\Delta C/C_0$. Further analysis reveals that electrode area increases with more courses and decreases with additional wales due to vertical knitting tension, which elongates fabric loops more vertically than horizontally. Therefore, with a fixed number of loops, fewer wales combined with more courses effectively enlarge the electrode area, thereby enhancing capacitive sensing performance. Based on these findings, the TCPS integrated into fabric 6, employing 400D conductive yarn, 450D crimped PLA filament, and an electrode arrangement of 30 wales and 40 courses, exhibits the highest $\Delta C/C_0$ and is selected for further evaluation of its sensing performance.

5.4.2 Sensing performance of the TCPS

5.4.2.1 Sensitivity

The sensing performance of the selected TCPS (fabric 6) was further evaluated,

beginning with a sensitivity analysis. Figure 5.6 illustrates the relationship between $\Delta C/C_0$ and the applied compressive pressure, where the slope of the curve corresponds to the sensor's sensitivity.

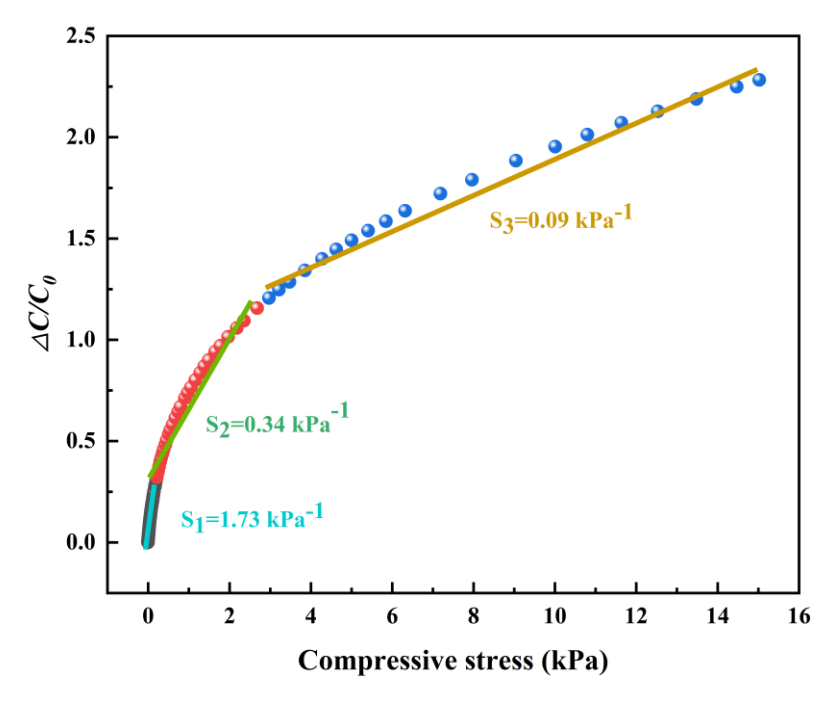


Figure 5.6 Sensitivity of the TCPS across different compressive pressure ranges.

The sensitivity varies across different pressure ranges, which can be explained by the structural deformation of the sensor. In the initial low-stress range (0–0.2 kPa), the TCPS exhibits a high sensitivity of 1.73 kPa⁻¹. This high sensitivity arises from the large gaps between fibers in the sensor's initial state, which allow the TCPS to compress easily, significantly reducing the electrode spacing and increasing capacitance. In the intermediate stress range (0.2–2.9 kPa), the sensitivity decreases to 0.34 kPa⁻¹, primarily due to the progressive densification of the TCPS structure. As the stress increases, further deformation becomes more challenging, resulting in a slower rate of capacitance change. In the high-stress range (2.9–15 kPa), the sensitivity further decreases to 0.09 kPa⁻¹. At this stage, the structure of the TCPS approaches its compressive limit, leading to reduced sensitivity. Despite the decrease in sensitivity at higher pressures, the TCPS maintains a reliable and predictable response across all pressure ranges. Moreover, the sensitivity of the TCPS in this study surpasses that of

previously reported textile-based pressure sensors, which exhibited sensitivities of 0.025 kPa⁻¹[144] and 0.045–0.022 kPa⁻¹ [142].

5.4.2.2 Influence of compression conditions

Figures 5.7(a) and (b) illustrate the sensing response of the TCPS under varying compression conditions. In Figure 5.7(a), $\Delta C/C_0$ exhibits a gradual increase with rising pressure. This behavior results from the compression of the electrodes and dielectric layer within the TCPS, which reduces the electrode spacing and consequently increases the capacitance. Such a consistent response to pressure highlights the sensor's potential for precise pressure monitoring applications. Similarly, Figure 5.7(b) shows that the TCPS maintains stable capacitance responses across different compression rates, with consistent signal profiles observed in all cases. This stability suggests that the compression rate has minimal influence on capacitance changes, emphasizing the sensor's robustness and adaptability to dynamic operating conditions.

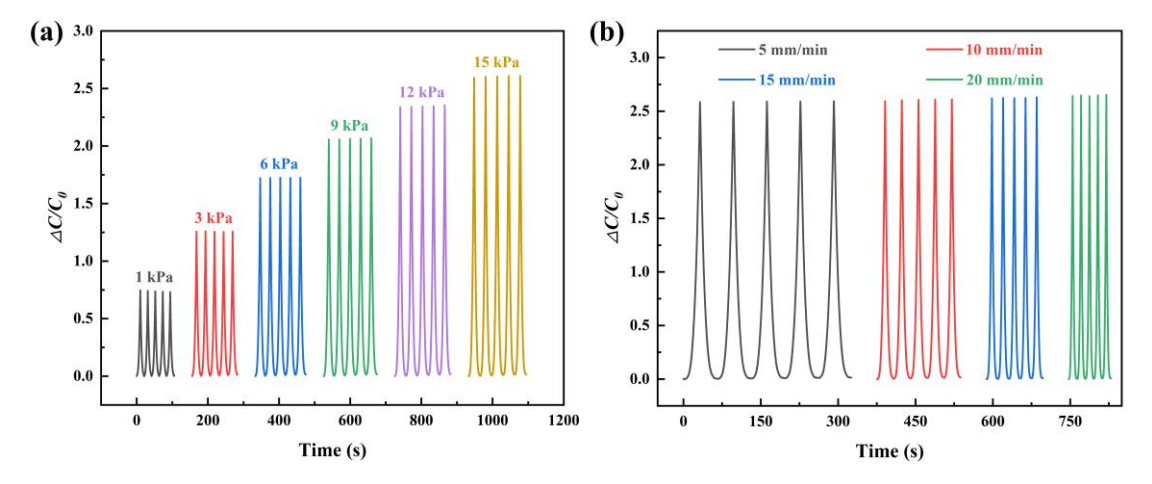


Figure 5.7 $\Delta C/C_0$ of the TCPS under different compression conditions: (a) varying compressive pressures (1, 3, 6, 9, 12, and 15 kPa); (b) varying compression rates (5, 10, 15, and 20 mm/min).

5.4.2.3 Influence of washing cycles

Figure 5.8 illustrates the capacitance response of the TCPS under different washing cycles. The results demonstrate that the sensing performance of the fabric remains

stable, with no significant degradation observed even after five washing cycles. This stability indicates that the structural integrity and functionality of the capacitive sensor are well-preserved, despite the friction and deformation experienced during repeated washing.

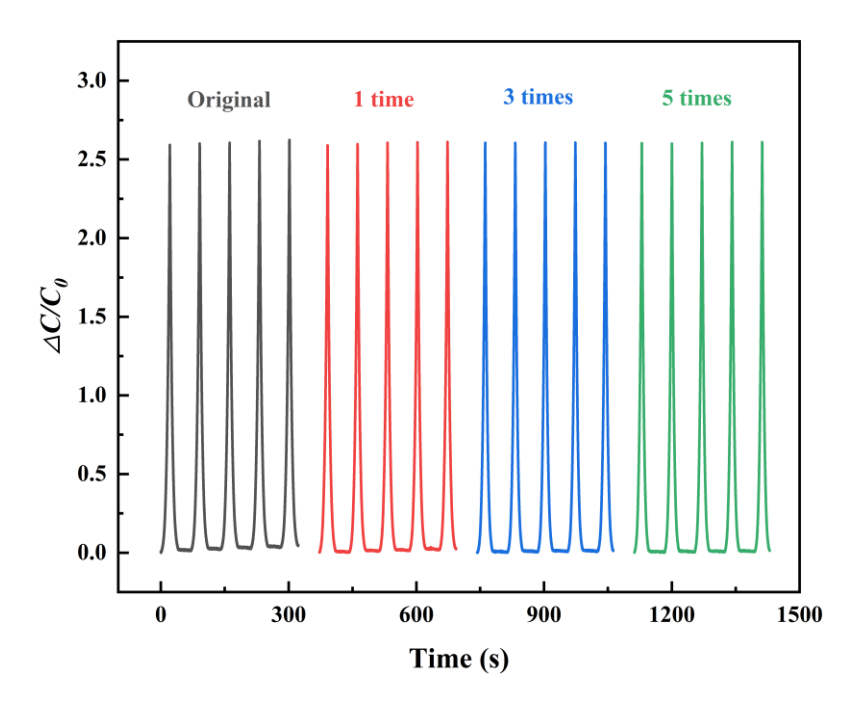


Figure 5.8 $\Delta C/C_0$ of the TCPS after different washing cycles.

5.4.2.4 Response and recovery times

Response time refers to the duration a sensor requires to produce a stable output signal after the application of instantaneous pressure, while recovery time is the period needed for the sensor to return to its baseline state after the pressure is removed. As shown in Figure 5.9, under a vertical pressure of 1.07 kPa, the TCPS exhibits a response time of approximately 130 ms during loading and a recovery time of about 90 ms during unloading. The sharp increase and decrease in capacitance observed during these processes emphasize the sensor's ability to rapidly and effectively respond to pressure changes.

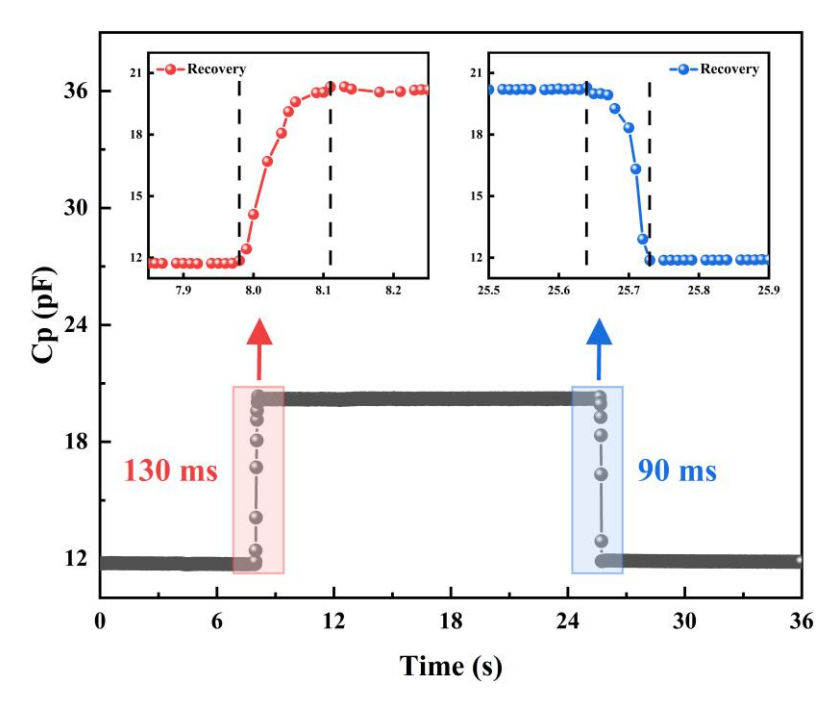


Figure 5.9 Response and recovery times of the TCPS under a vertical pressure of 1.07 kPa.

5.4.2.5 Repeatability

Figure 5.10 presents the capacitance variation of the TCPS during cyclic compression at 15 kPa. The results show that $\Delta C/C_0$ remains stable over 5000 compression cycles, demonstrating the TCPS's stability and durability. The capacitance response curves around 250, 2500, and 4700 cycles exhibit distinct, sharp peaks with nearly identical shapes, further validating the TCPS's reliability. This consistent behavior underscores the TCPS's ability to maintain accurate and stable signal output during prolonged cyclic use, highlighting its suitability for long-term applications.

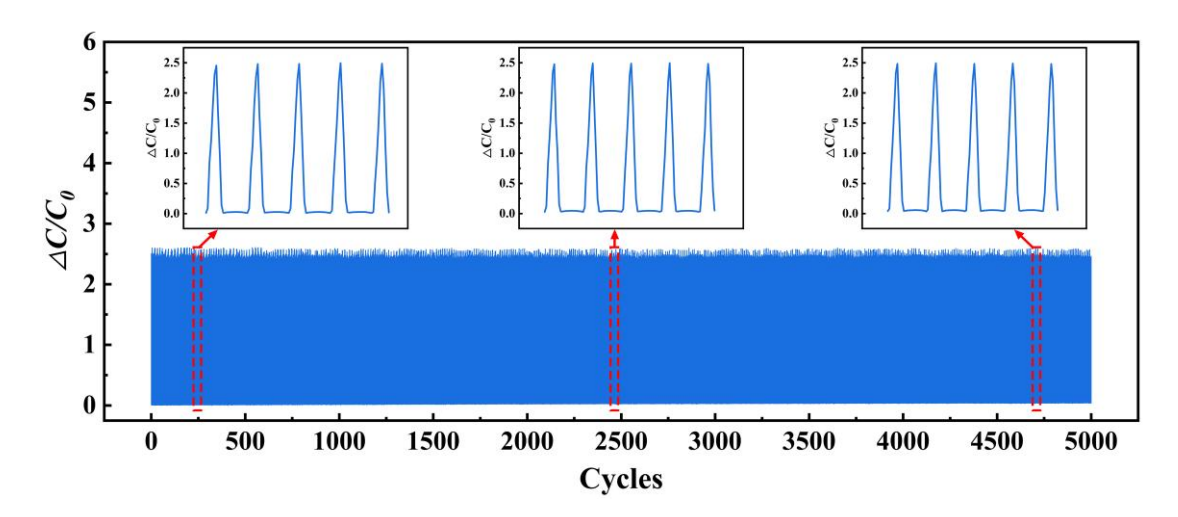


Figure 5.10 Repeatability of the TCPS over 5000 compression cycles.

5.4.3 Comfort performance of the TCPS

In addition to the sensing performance, the comfort performance of the entire TCPS fabric 6, fabricated with the structural parameters selected in Section 5.4.1, was systematically evaluated and compared with five commercially available mattress surface fabrics (Figures 5.11(a)–(e)). The physical properties of all tested fabrics are listed in Table 5.5, and their comfort properties are presented in Figures 5.12(a)–(e).

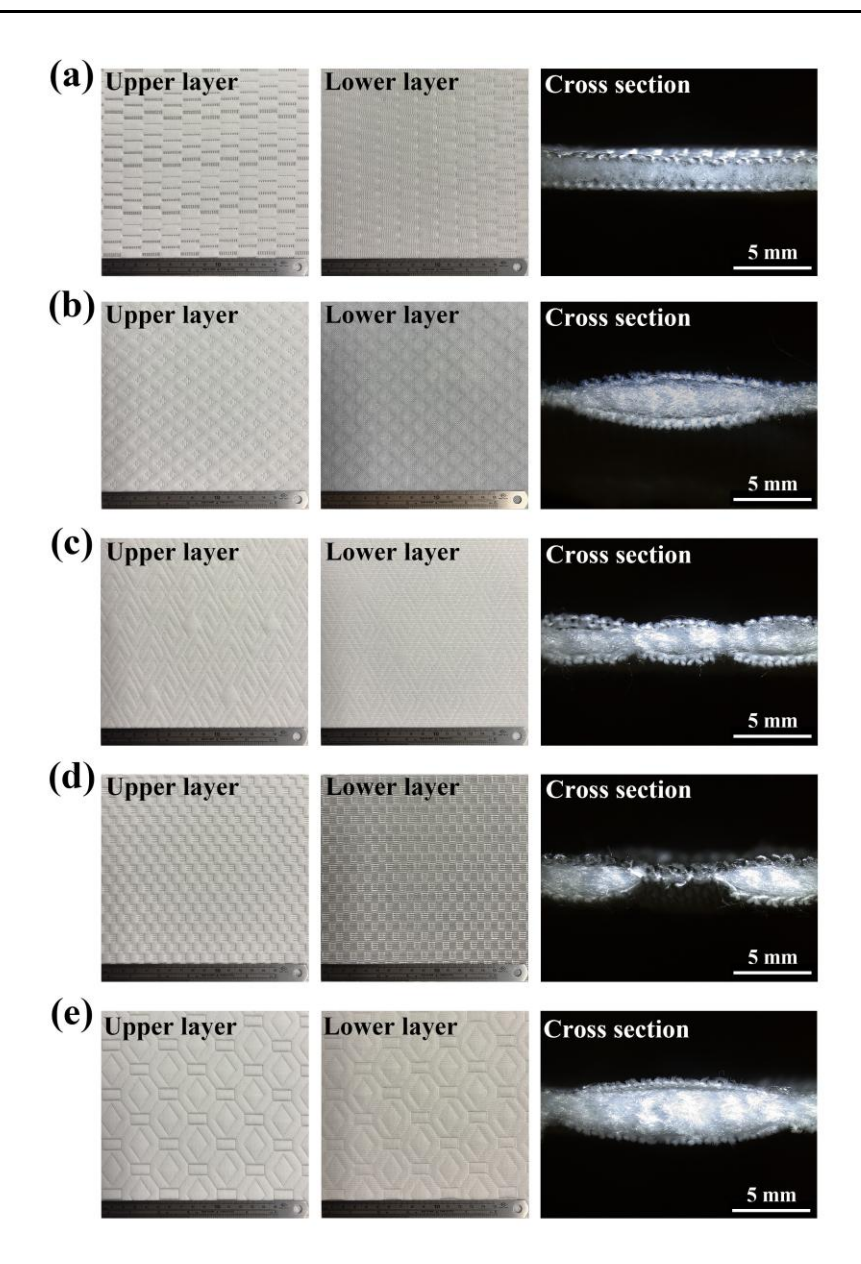


Figure 5.11 Morphology of commercial mattress surface fabric for comparison: (a) fabric a; (b) fabric b; (c) fabric c; (d) fabric d; (e) fabric e.

Table 5.5 Physical properties of the TCPS fabric and commercial mattress surface fabrics

| Physical property | TCPS fabric | Fabric a | Fabric b | Fabric c | Fabric d | Fabric e |
|-------------------------|----------------|----------------|----------------|----------------|----------------|--------------|
| GSM (g/m ²) | 516.25 | 330.59 | 362.29 | 422.29 | 486.42 | 588.43 |
| | (± 4.47) | (± 2.80) | (± 1.84) | (± 4.22) | (± 5.15) | (± 4.84) |
| Thickness (mm) | 3.03 | 2.10 | 2.25 | 2.14 | 2.52 | 2.90 |
| | $(\pm \ 0.06)$ | $(\pm \ 0.03)$ | $(\pm \ 0.03)$ | $(\pm \ 0.03)$ | $(\pm \ 0.06)$ | $(\pm~0.08)$ |

Note: Standard deviations are given in parentheses.

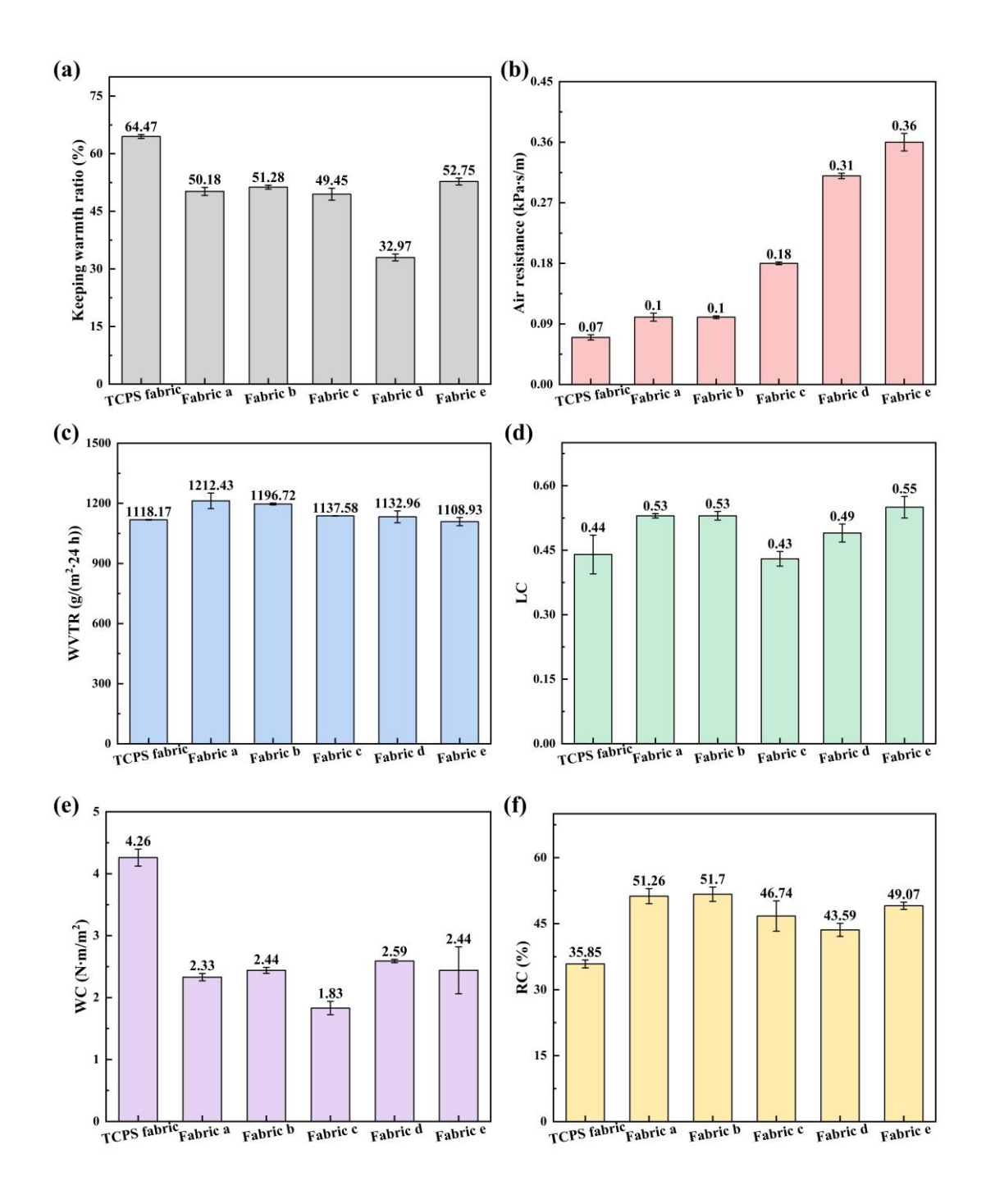


Figure 5.12 Comparison of comfort properties between the TCPS fabric and commercial mattress surface fabrics (fabrics a–e): (a) keeping warmth ratio; (b) air resistance; (c) water vapor transmission rate (WVTR); (d) compressional linearity (LC); (e) compressional energy (WC); (f) compressional recoverability (RC).

Figure 5.12(a) shows that the keeping warmth ratio of the TCPS fabric reaches 64.47%,

significantly higher than that of all the commercial mattress surface fabrics, which range from 32.97% to 52.75%. This superior thermal insulation is attributed to its high GSM (516.25 g/m²) and greatest thickness (3.03 mm) (Table 5.5), effectively reducing heat loss. Despite its large GSM and thickness, the TCPS fabric also demonstrates excellent air permeability, with an air resistance of 0.07 kPa·s/m, as shown in Figure 5.12(b). This exceptional air permeability is likely due to the use of crimped PLA filaments in the middle layer of the TCPS fabric, which increases the fabric's porosity and significantly enhances airflow. Furthermore, Figure 5.12(c) shows that the TCPS fabric achieves a water vapor transmission rate (WVTR) of 1118.17 g/(m²·24 h), comparable to commercial fabrics (1108.93–1212.43 g/(m²·24 h)), indicating its adequate water vapor permeability.

The compression properties of these fabrics, including compressional linearity (LC), compressional energy (WC), and compressional recoverability (RC), are presented in Figures 5.12(d)–(f), respectively. LC represents the linearity of the compression-thickness curve, with lower LC values signifying greater softness as the material compresses more easily under light loads. WC denotes the energy required for compressive deformation under a specific pressure and serves as an indicator of bulkiness, where higher WC values suggest a bulkier fabric. RC evaluates the fabric's ability to recover its original thickness after compression, with RC values closer to 100 indicating better recoverability [145]. The results suggest that the TCPS fabric demonstrates a lower LC, the highest WC, and the lowest RC compared to other mattress surface fabrics. These findings suggest that the TCPS fabric is softer and bulkier but exhibits relatively poor recovery after compressive deformation.

5.5 Conclusions

In this chapter, the TCPS was successfully developed by incorporating conductive yarns into PLA weft-knitted inlaid fabrics using the intarsia knitting technique. The effects of conductive yarns, inlaid filaments, and arrangements of electrode wales (*m*) and courses

(n) on the TCPS's sensing performance were systematically investigated. The findings reveal that the TCPS fabricated with 400D conductive yarns, 450D crimped PLA filaments, and an electrode arrangement of 30 wales and 40 courses achieves the highest ΔC/C₀. The improved TCPS demonstrates sensitivities of 1.73 kPa⁻¹, 0.34 kPa⁻¹, and 0.09 kPa⁻¹ across the pressure ranges of 0–0.2 kPa, 0.2–2.9 kPa, and 2.9–15 kPa, respectively. It exhibits a stable capacitive response under various compressive pressures (1–15 kPa) and compression rates (5–20 mm/min). Additionally, the TCPS retains consistent sensing performance after five washing cycles, with response and recovery times of 130 ms and 90 ms, respectively, at a load of 1.07 kPa. The TCPS also demonstrates outstanding durability, maintaining stable performance over 5000 compression cycles.

Compared to commercially available mattress surface fabrics, the TCPS fabric demonstrates significantly better overall comfort performance, characterized by superior thermal insulation, air permeability, water vapor permeability, softness, and bulkiness, despite its slightly weaker compression recovery. Building on these advantages, the improved TCPS fabricated in this chapter will be utilized to produce a smart mattress surface fabric, further expanding its potential applications in intelligent sleep monitoring.

Chapter 6 Development of PLA Smart Mattress Surface Fabrics for Real-Time Sleep Monitoring

6.1 Introduction

The previous chapter highlighted the successful development of textile capacitive pressure sensors (TCPS) based on PLA weft-knitted inlaid fabrics, demonstrating their suitability for mattress surface applications due to their excellent sensing performance, durability, and comfort. However, single-point or limited-area sensing is inadequate for capturing the complexities of sleep behaviors and distinguishing individual characteristics. To address these limitations, it is essential to expand sensor coverage and integrate advanced data acquisition systems with machine learning algorithms, enabling more precise recording and analysis of sleep behaviors while achieving accurate individual recognition.

Building on this foundation, this chapter explores the development of sustainable and comfortable PLA mattress surface fabrics equipped with a TCPS array for advanced sleep monitoring, employing single-step intarsia knitting technology. The study focuses on integrating a 4 × 4 matrix of 16 TCPS units into PLA weft-knitted inlaid fabrics and designing a wireless capacitance data acquisition system to enable real-time measurement of capacitance distributions induced by human body pressure changes. Using this integrated platform, five typical sleep behaviors, including getting into and out of bed, lying flat, lying on the left side, and lying on the right side, are recorded across seven volunteers. Furthermore, a deep learning model is applied for multi-task analysis of the capacitance data, aiming to achieve accurate classification of sleep behaviors and reliable individual recognition.

6.2 Design and fabrication

As shown in Figure 6.1(a), the primary stress regions of the human body during sleep

are concentrated in the shoulders, elbows, hip bones, and heels. These regions generate a specific pressure distribution on the mattress surface fabric, which can be reflected as capacitance values by the TCPS developed in previous chapters, enabling real-time monitoring of the sleep state. However, a single TCPS is insufficient to capture the complex and dynamic pressure distributions associated with various sleep behaviors, such as getting into and out of bed, or different sleeping positions, including supine and lateral positions. To address this challenge, a smart weft-knitted inlaid fabric consisting of four sensing regions was designed using the SDS-ONE Apex 3 system (Figure 6.1(b)). Each region contains four sensors, forming a 4 × 4 matrix of 16 TCPS units. This design enables localized monitoring of capacitance variations induced by body pressure, thereby providing essential foundational data for the subsequent recognition of sleep behaviors and postures.

During knitting, all TCPS units of the smart fabric were fabricated according to the sensor parameters selected in Section 5.4.1. Specifically, each TCPS employed a 400D conductive yarn to create parallel electrodes consisting of 30 wales and 40 courses, and inlaid two 450D crimped PLA filaments to form the dielectric. The surface and middle layers of the non-sensing regions were knitted with three 150D yellow or white PLA filaments and two 450D crimped PLA filaments, respectively. The entire smart mattress surface fabric was also fabricated in a single step using the intarsia knitting technique on the 14-gauge SVR123SP flat-knitting machine (Shima Seiki, Japan) used in Chapter 5, as illustrated in Figure 6.1(c). Details of the knitting process and yarn specifications are provided in Section 5.2. Figure 6.1(d) shows the final 0.7 × 1.5 m fabric, in which 16 gray sensing regions are seamlessly integrated into the surrounding yellow and white non-sensing regions. After knitting, the excess conductive yarns of each TCPS at the fabric edges were organized and connected to DuPont wires using conductive tape. The insulating tape was then applied to secure the connections, preparing the fabric for subsequent testing and signal acquisition.

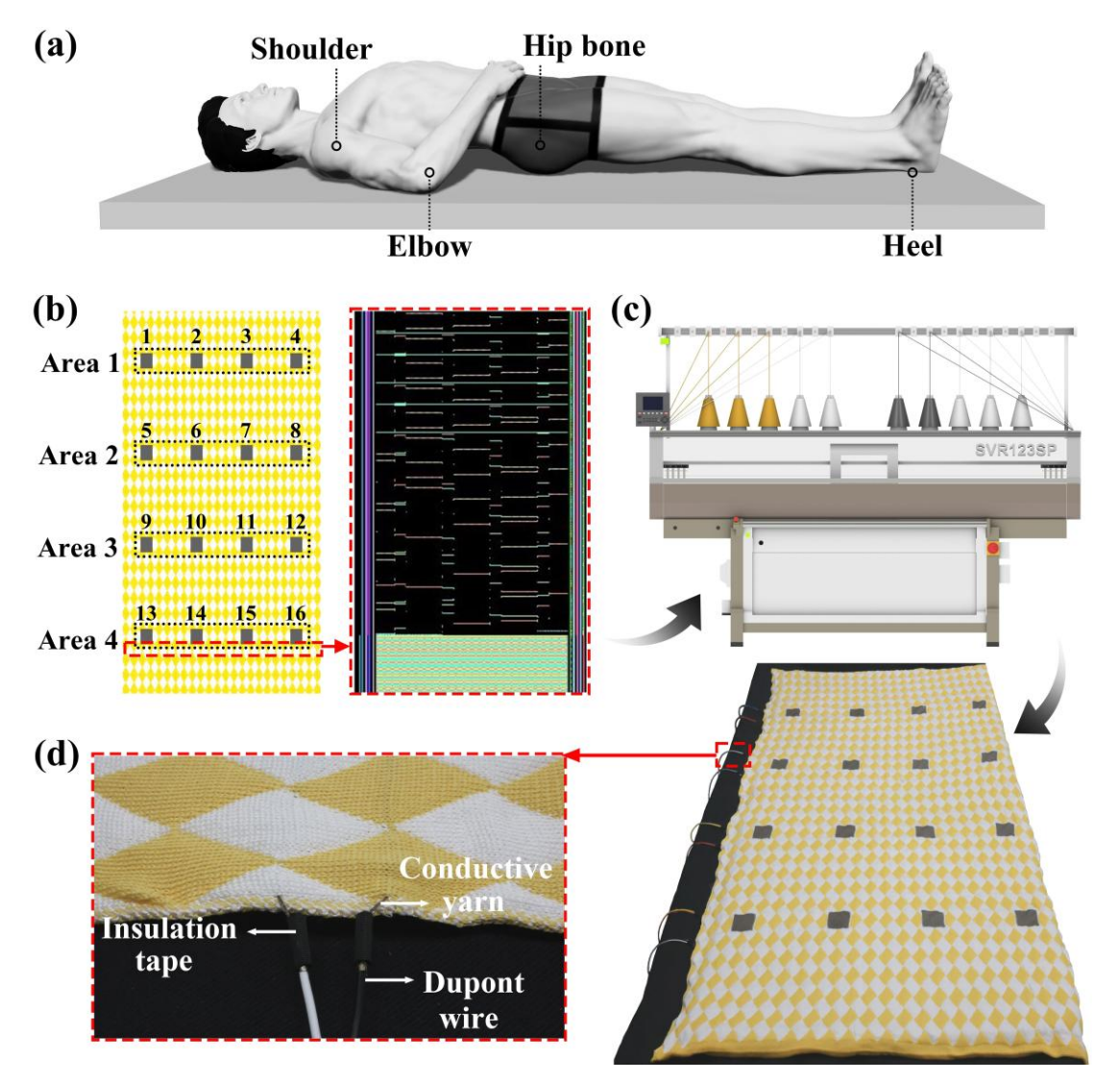


Figure 6.1 Design and fabrication of the PLA smart mattress surface fabric: (a) key stress regions; (b) fabric design; (c) computerized flat-knitting machine used; (d) produced fabric with 16 integrated TCPS units.

6.3 Development of capacitance data acquisition system

To enable the simultaneous capacitance measurement of all 16 TCPS units while enhancing convenience and real-time performance, this study designed a dynamic capacitance data acquisition system, with the measurement flowchart presented in Figure 6.2(a). Compared to the TH2830 LCR meter employed in Chapter 5, the proposed system is more compact and can measure multiple capacitance channels simultaneously. By eliminating cumbersome cable connections, it enhances usability, making it particularly well-suited for real-time sleep monitoring applications.

The system utilizes an STM32F103ZET6 microcontroller unit (MCU) as the core control unit. It is powered by a 5V portable lithium battery, with the AMS1117-3.3 voltage regulator converting the voltage to a stable 3.3V low-voltage supply for the MCU, capacitance detection module, and Bluetooth module. The capacitance detection module integrates the PCap01-AD chip, which can connect up to 7 capacitive sensors and 1 reference sensor (Figure 6.2(b)). However, a single PCap01-AD chip is insufficient to meet the requirement of simultaneously measuring 16 TCPS units. To address this, three PCap01-AD chips were employed to form a distributed capacitance detection module, where capacitance values are measured using the single-ended grounding mode and transmitted to the MCU through the Serial Peripheral Interface (SPI), enabling synchronized multi-channel data acquisition.

To facilitate real-time data transmission, the BT11 Bluetooth Module communicates with the MCU through the Universal Asynchronous Receiver-Transmitter (UART) interface, wirelessly transmitting capacitance data to the host computer for remote monitoring and recording. The system's hardware implementation is illustrated in Figure 6.2(c). For effective data visualization, two Qt-based interfaces were developed: a graph-based interface plotting capacitance curves for all TCPS units and a grid-based interface displaying real-time capacitance for the TCPS matrix (Figure 6.2(d)). This comprehensive system enables users to monitor dynamic changes in capacitance values across all sensors in real-time, providing accurate and efficient data support for subsequent sleep posture recognition and behavioral analysis.

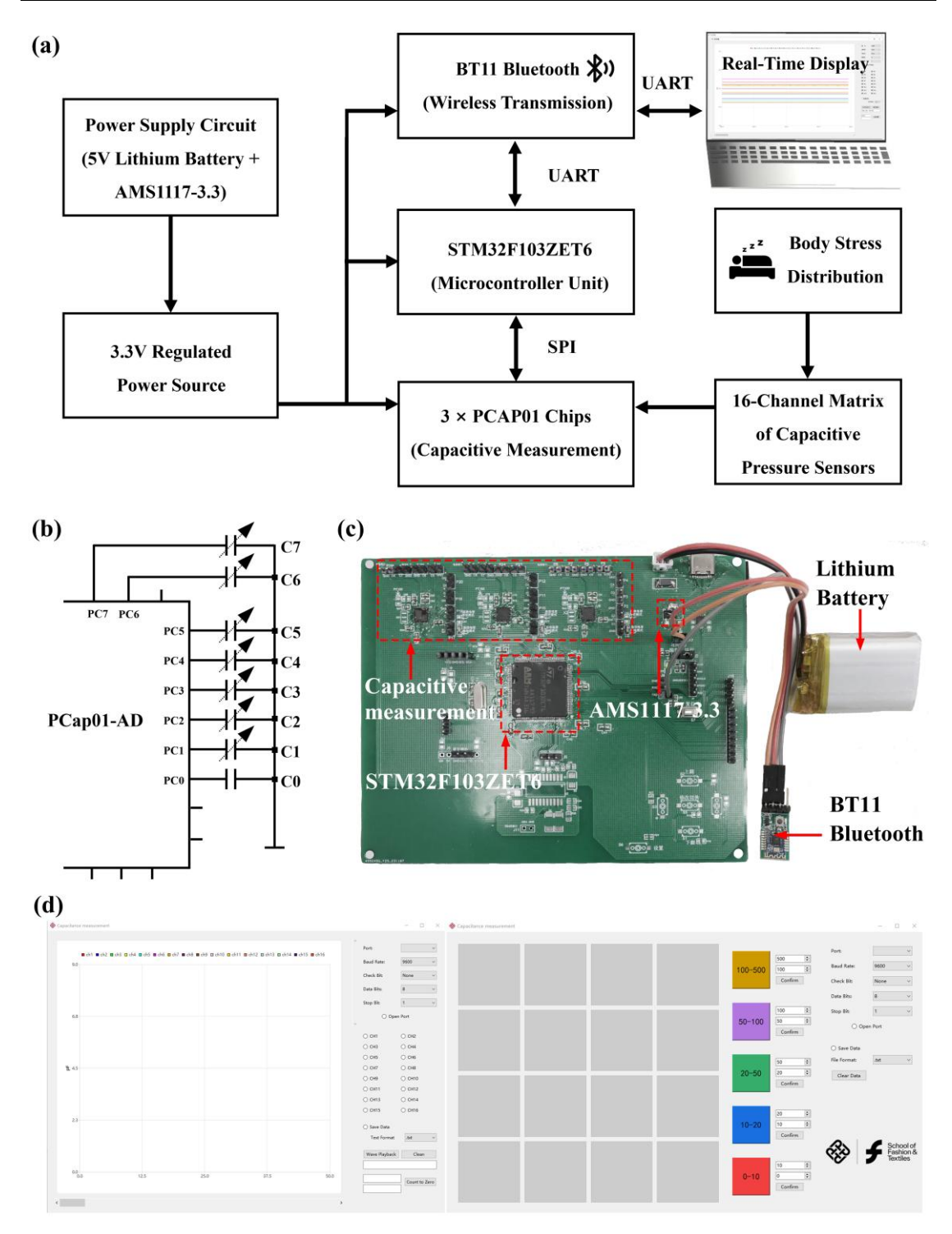


Figure 6.2 Illustration of the capacitance data acquisition system: (a) measurement flowchart; (b) diagram of the PCap01-AD chip; (c) hardware module; (d) visualization interfaces.

6.4 Sleep behavior data collection

Sleep behavior data were collected from seven volunteers using the PLA smart mattress

surface fabric integrated with a capacitance data acquisition system. Before participating, all volunteers provided informed consent in accordance with ethical research guidelines. Following predefined instructions, each participant performed a series of prescribed sleep states, including getting into bed, lying flat (supine position), lying on the left side (left lateral position), lying on the right side (right lateral position), and getting out of bed. In this process, participants were instructed to remain quiet and maintain a relaxed posture, with each sleep state repeated at least 10 times. Simultaneously, the capacitance data acquisition system continuously recorded real-time capacitance data generated by the PLA smart mattress surface fabric. These data were wirelessly transmitted to a host computer for visualization and storage. Ultimately, 350 valid samples were collected, each containing more than 2,000 capacitance data points. The resulting dataset serves as the foundation for training and validating a multitask learning model for sleep behavior analysis and individual identification.

6.5 Sleep behavior analysis through deep learning

A one-dimensional convolutional neural network (1D-CNN) was developed to classify sleep behaviors and identify individuals based on capacitance data collected from the PLA smart mattress surface fabric. As illustrated in Figure 6.3, the 1D-CNN architecture primarily consists of an input layer, three 1D convolutional layers, three average pooling layers, two fully connected layers, and two output layers.

For model training and validation, the collected dataset of 350 samples, consisting of multivariate time-series data with dimensions 16×2000 , was divided into 70% for training and 30% for testing using stratified sampling. The 16 channels correspond to capacitance signals from different sensors, and 2000 denotes the number of data points recorded within a specific time interval. The first convolutional layer applies 24 filters (kernel size: 101, padding: 50) to produce outputs of size 24×2000 . Batch normalization is then applied to stabilize training, followed by a rectified linear unit (ReLU) activation function to introduce non-linearity. A dropout layer (rate = 0.5) is

incorporated to prevent overfitting. To reduce the temporal resolution, an average pooling layer (kernel size: 4) reduces the output size to 24×500 .

The second convolutional layer applies 16 filters (kernel size: 5, padding: 2), further refining the extracted features and producing outputs of size 16×500 . Similar to the first layer, batch normalization, ReLU activation, and a dropout layer (rate = 0.5) are applied. An average pooling layer (kernel size: 4) subsequently reduces the output size to 16×125 . The third convolutional layer utilizes 8 filters (kernel size: 3, padding: 1) to produce outputs of size 8×125 . As before, batch normalization, ReLU activation, and a dropout layer (rate = 0.5) are applied. Finally, an average pooling layer (kernel size: 5) reduces the temporal resolution to 8×25 .

The flattened feature vector, comprising 200 elements (8×25), is fed into two fully connected layers. The first fully connected layer, containing 5 neurons, classifies sleep behaviors, while the second layer, containing 7 neurons, identifies individual participants. The shared convolutional layers efficiently extract general features, while the task-specific fully connected layers optimize classification performance for each objective, allowing this 1D-CNN architecture to effectively address the dual tasks of sleep behavior analysis and individual identification.

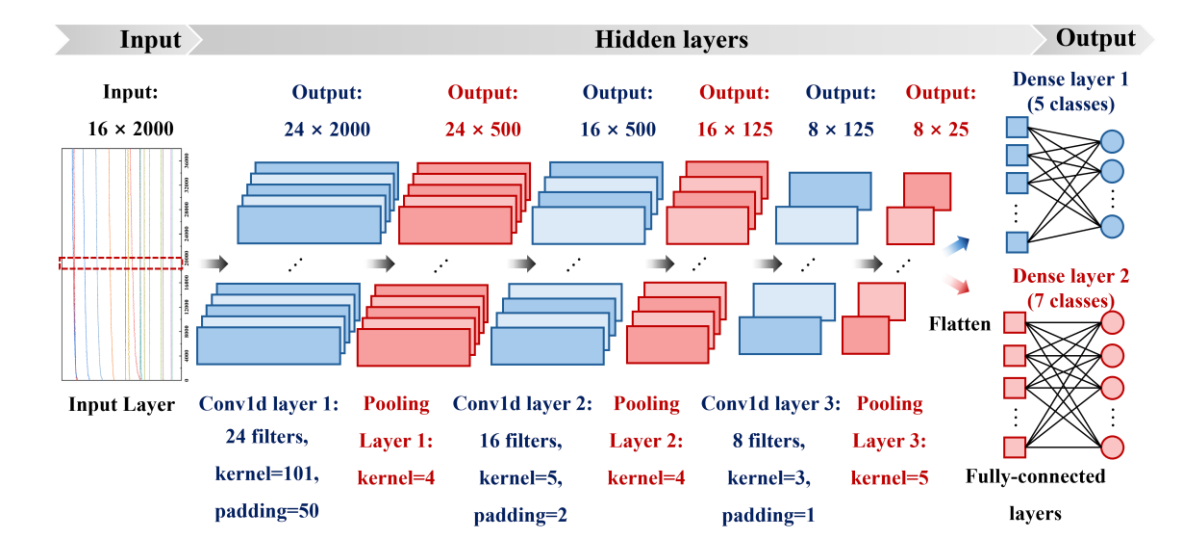


Figure 6.3 Architecture of the 1D-CNN model for sleep behavior analysis and individual identification.

6.6 Results and discussion

6.6.1 Getting into bed

Figure 6.4(a) shows a schematic diagram of a volunteer preparing to get into bed, while Figures 6.4(b)–(h) display typical capacitance heat maps for seven volunteers, illustrating their dynamic pressure distribution during the getting-into-bed process. These heat maps were generated using data collected from the 16 TCPS units embedded in the PLA smart mattress surface fabric. These sensors are numbered sequentially from 1 to 16, corresponding to the sensor numbers in the TCPS matrix shown in Figure 6.1(b), and are arranged from bottom to top in the heat maps. Red regions indicate relatively high capacitance values, corresponding to areas of greater pressure, whereas blue regions represent relatively low capacitance values, reflecting areas of lighter pressure.

The results indicate that during the initial stage of getting into bed, the capacitance values of most sensors remain at low levels, predominantly in the blue or light blue regions, reflecting minimal or no contact between the subject and the mattress surface. As the volunteer gradually contacts the mattress, the capacitance values of specific sensors, such as TCPS 6, 9, and 10, increase sharply before decreasing, marked by the appearance of small white or red regions. This pattern suggests that these areas experience significant transient pressure, likely corresponding to a temporary stress point at the buttocks. As the volunteer continues to move and adjust their posture, the capacitance values of sensors located in the central region of the mattress surface fabric, including TCPS 2, 3, 6, 7, 10, and 11, progressively increase. These values reach their peak when the volunteer is entirely lying down, stabilizing in light red or red regions, which indicate sustained pressure in these areas.

Although the overall trend in capacitance changes of the sensors is consistent,

individual differences in movement patterns, rhythm, and body weight lead to variations in the timing and magnitude of the capacitance values. This time-series capacitance data not only provides a detailed representation of the getting-into-bed process but also offers valuable insights for individual identification by capturing the unique behavioral and physical characteristics of each volunteer.

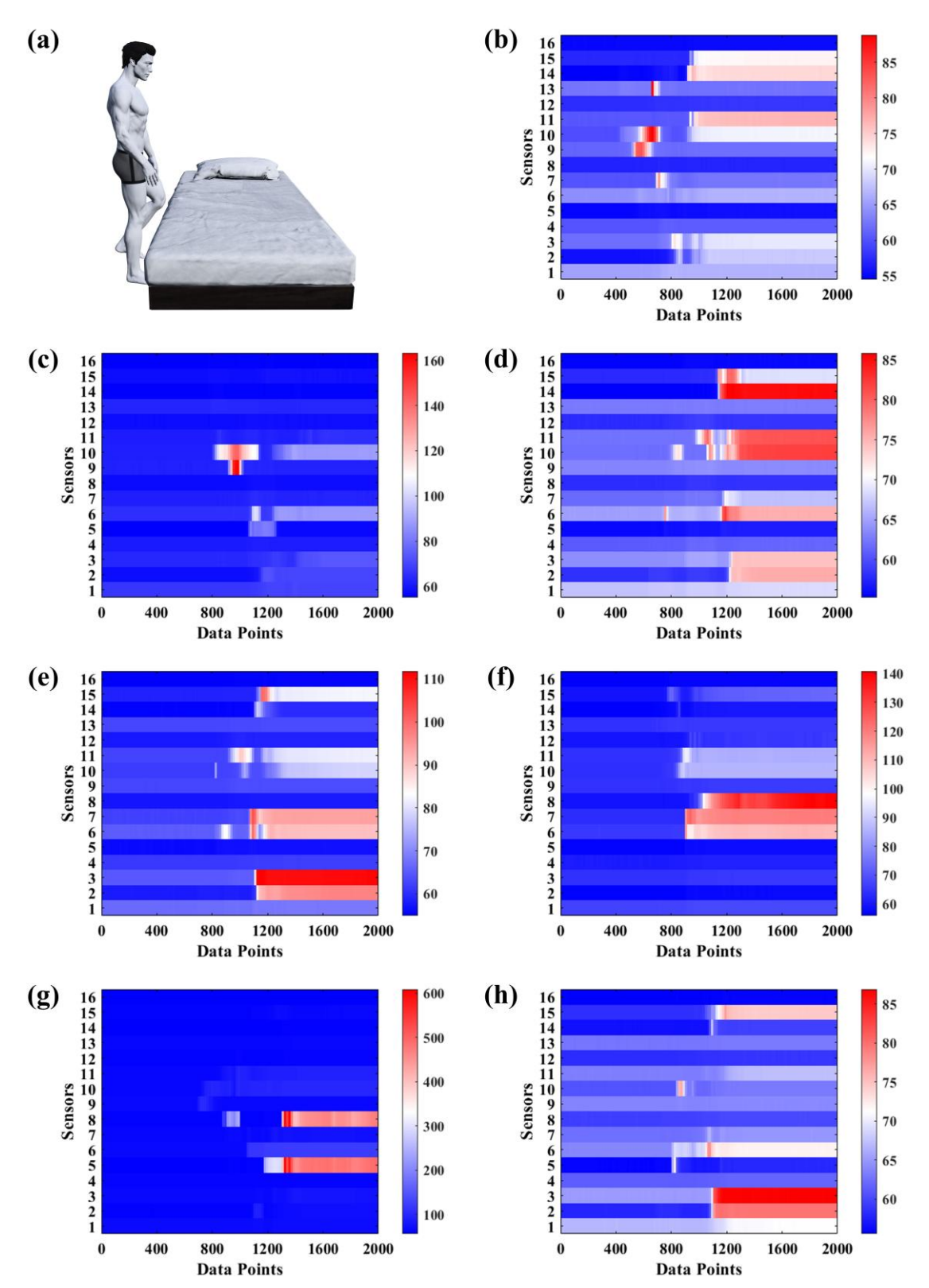


Figure 6.4 Dynamic capacitance variation during the getting-into-bed process: (a) schematic of a volunteer preparing to get into bed; (b)–(h) heat maps for volunteers 1–

7.

6.6.2 Getting out of bed

The schematic in Figure 6.5(a) illustrates a volunteer preparing to get out of bed, while Figures 6.5(b)–(h) present capacitance heat maps of seven volunteers, revealing the dynamic pressure distribution throughout this process. The heat maps show that during the initial stage, certain sensors maintain medium-to-high capacitance values (represented by light red or red regions), closely associated with the subject's pre-existing sleeping positions. As the volunteers gradually raise their bodies and move off the mattress, the regions of high capacitance progressively shrink and transition to lower values (depicted in blue or light blue regions), reflecting the redistribution of pressure. During this transition, specific sensors (e.g., TCPS 6, 7, and 10) exhibit temporary increases in capacitance, likely resulting from the transient force exerted by the volunteers' arms or legs to support their movement away from the mattress surface. Following this, the capacitance values of these sensors decrease rapidly and stabilize at low levels, indicating that the body has completely left the mattress.

Similar to the getting-into-bed process, variations in capacitance values across different sensors are observed among individuals. These differences stem from variations in the manner, speed, and pressure distribution during the process of getting out of bed. Despite these individual differences, the overall trend consistently demonstrates a transition from higher or medium capacitance values to lower values, effectively characterizing the getting-out-of-bed process. These findings provide valuable data for developing more accurate models for sleep behavior analysis and individual identification.

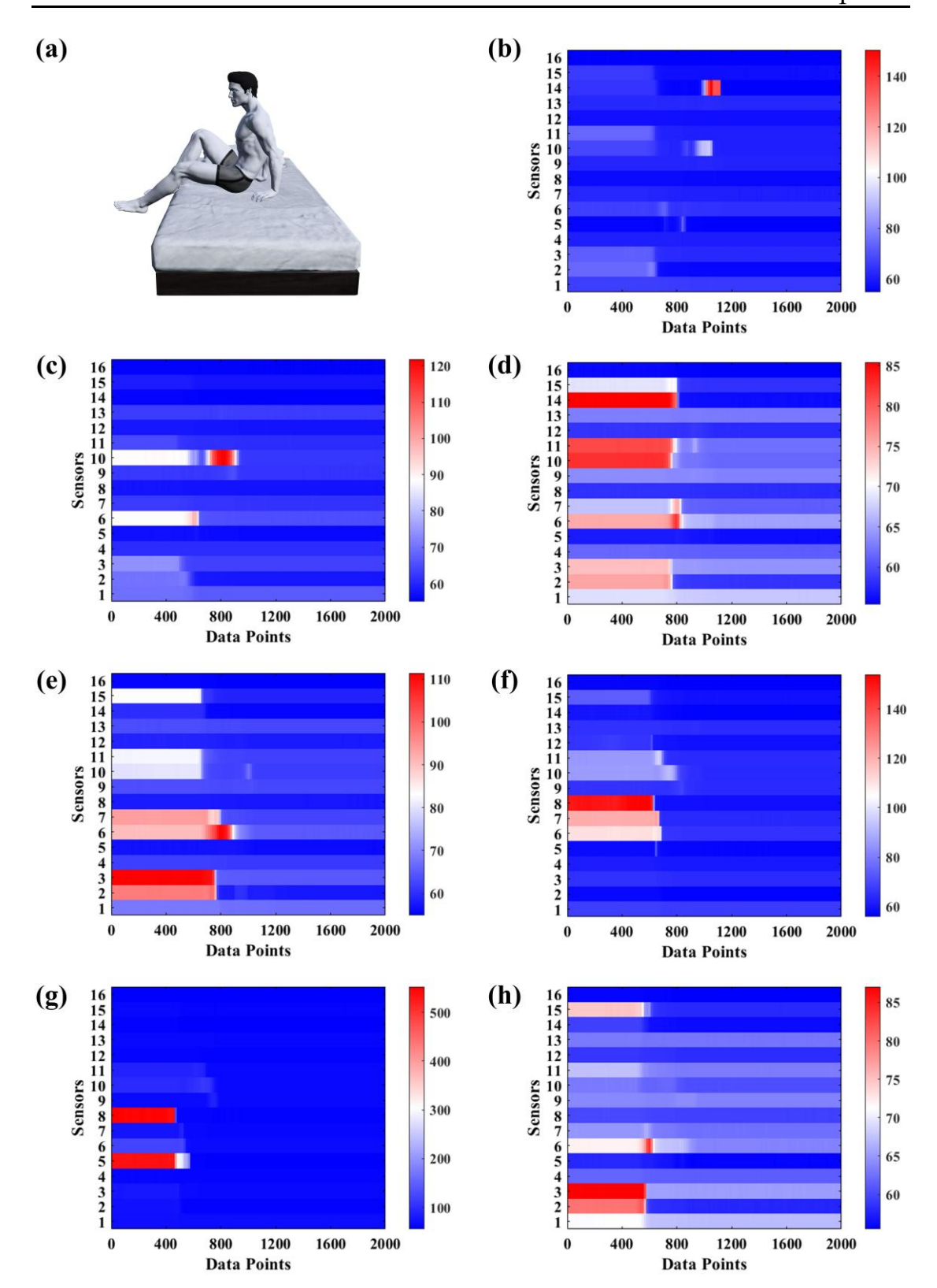


Figure 6.5 Dynamic capacitance variation during the getting-out-of-bed process: (a) schematic of a volunteer preparing to get out of bed; (b)–(h) heat maps for volunteers 1–7.

6.6.3 Lying flat

Following the systematic analysis of capacitance changes during the dynamic processes of getting into and out of bed, this section focuses on the relatively static lying-flat posture, as illustrated in Figure 6.6(a). As depicted in Figures 6.6(b)–(h), the capacitance values recorded in the lying-flat position across different subjects exhibit higher stability and a more distinct gradient across the sensors. High-capacitance regions (red or light red areas) are primarily concentrated in the central sensors (e.g., TCPS 6, 7, 10, and 11), corresponding to the main pressure areas of the back, buttocks, and legs. For some participants, sensors along the mattress edges (e.g., TCPS 2, 3, 14, and 15) also display higher capacitance values, likely associated with contact from the head or feet. These capacitance values remain consistent over time, indicating that participants maintained a relatively stable sleep posture throughout the lying-flat process.

While the highest capacitance values are generally concentrated in the mattress's central region, notable variations are observed in the heat maps among different participants. These differences are primarily attributed to individual factors, such as body shape and preferred sleeping posture. Overall, these results demonstrate the characteristic capacitance distribution of the lying-flat posture while illustrating the individualized variations inherent to different subjects.

Chapter 6

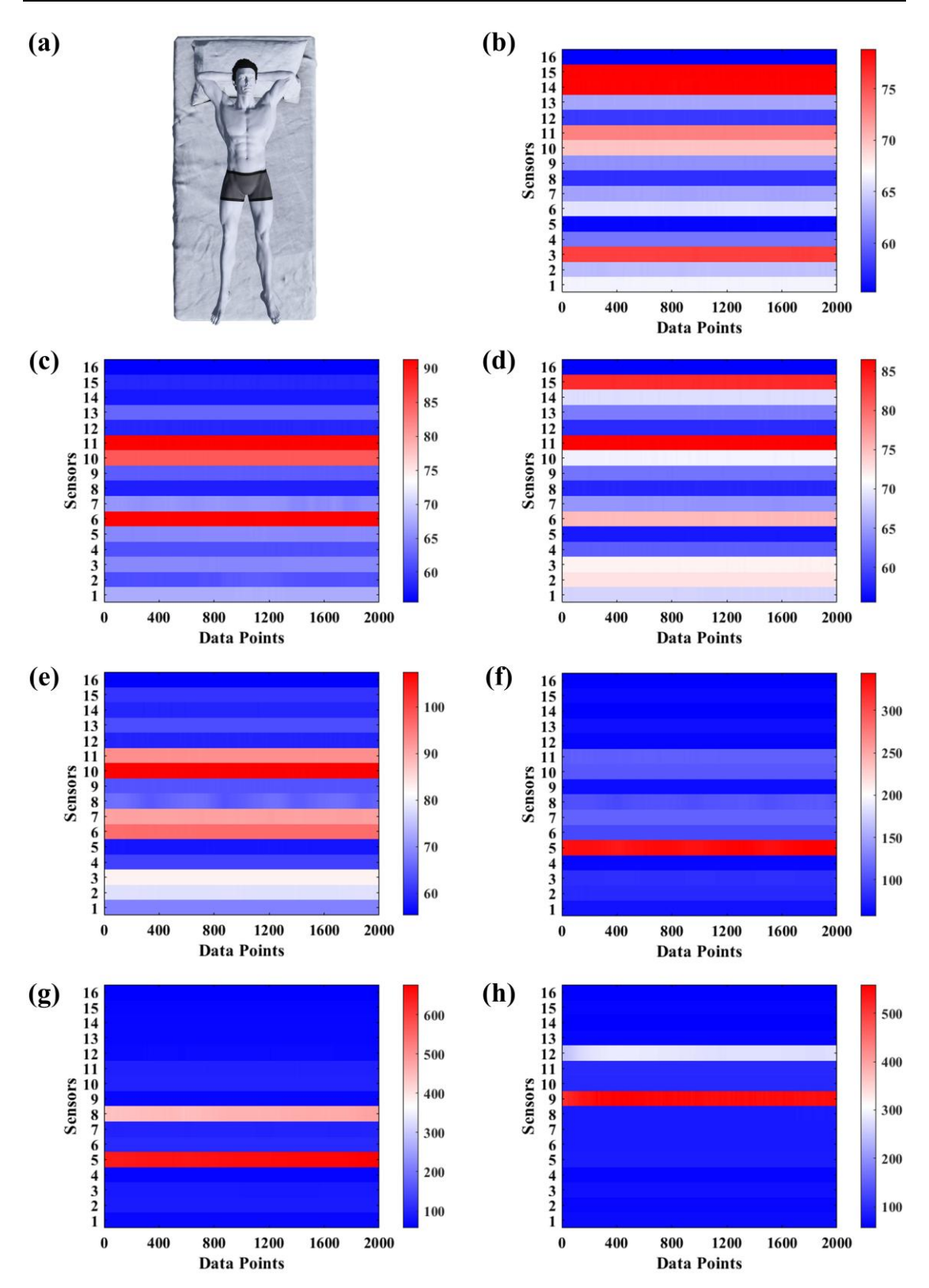


Figure 6.6 Dynamic capacitance variation during the lying-flat process: (a) schematic of a volunteer lying flat; (b)–(h) heat maps for volunteers 1–7.

6.6.4 Lying on the left

Figures 6.7(a)–(h) present the schematic diagram of the lying-left posture alongside the capacitance heat maps of seven volunteers in this position. Compared to the lying-flat posture, the capacitance distribution in the lying-left posture demonstrates a marked asymmetry. High-capacitance regions are primarily concentrated in sensors located on the left side of the mattress surface fabric, such as TCPS 3, 7, and 11. These sensors correspond to the main pressure points where the body contacts the mattress, including the left shoulder, arm, and hip. In contrast, sensors on the right side (e.g., TCPS 1, 5, 9, and 13) show comparatively lower capacitance values, indicating minimal stress in these regions during the lying-left posture. This evident asymmetry provides a crucial basis for accurately classifying sleeping positions.

Furthermore, the capacitance distributions among different volunteers in the lying-left posture exhibit noticeable variations. For instance, the high-capacitance regions for the subject in Figure 6.7(b) primarily emerge at TCPS 3 and 11, which may suggest that only limited body parts, such as the left shoulder and hip, are in contact with the sensor-covered areas of the mattress surface fabric. In contrast, the subject in Figure 6.7(g) displays a more dispersed distribution of high-capacitance regions, covering TCPS 3, 7, 8, and 11. This pattern may indicate a more extended lying-left posture, where multiple body parts make contact with the sensor-covered areas. These differences reflect variations in sleeping habits and interactions with the sensor array, providing critical data for the development of personalized identification models.

Chapter 6

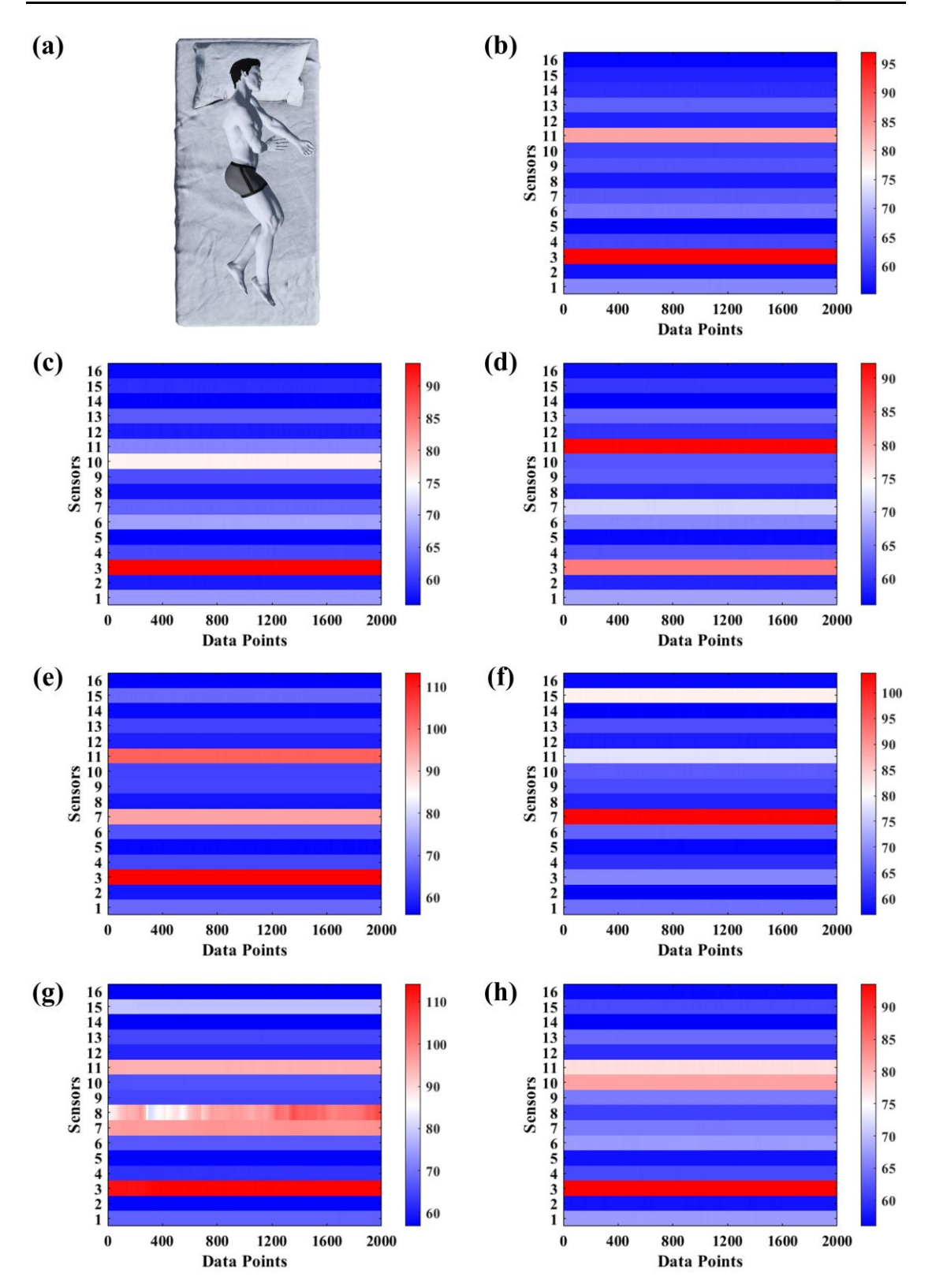


Figure 6.7 Dynamic capacitance variation during the left-side-lying process: (a) schematic of a volunteer lying on the left side; (b)–(h) heat maps for volunteers 1–7.

6.6.5 Lying on the right

The visualization of the lying-right posture and capacitance heat maps recorded from seven volunteers is provided in Figures 6.8(a)–(h). Similar to the lying-left posture, the capacitance distribution in the lying-right posture exhibits significant asymmetry. Specifically, sensors on the right side of the mattress surface fabric (e.g., TCPS 2, 6, and 10) display higher capacitance values (red or light red), likely due to concentrated pressure from the right shoulder and hip. Conversely, sensors on the left side (e.g., TCPS 4, 8, 12, and 16) generally record lower capacitance values (blue or light blue), suggesting minimal pressure in this region. The capacitance distribution in the lying-right posture also demonstrates noticeable individual variations. For instance, some subjects show fewer high-capacitance regions with larger values (Figures 6.8(e) and (f)), while others display more extensive high-capacitance regions with smaller values (Figures 6.8(c) and (h)). These differences may result from variations in physical dimensions, unique adjustments to the lying-right posture, and the extent of contact with the mattress surface.

Overall, the lying-right posture features a distinct asymmetric pressure distribution, similar to the lying-left posture, but with high capacitance values concentrated on the right side, complementing the left-side distribution of the lying-left posture. Combining these results with capacitance data from actions like getting into and out of bed, lying flat, and lying on the left side can improve the understanding of sleep behaviors and support the precise identification of sleeping postures and individuals. It is worth emphasizing that this approach, in addition to the five described sleep behaviors, can also monitor and identify other sleep states, such as rolling over to either side.

Chapter 6

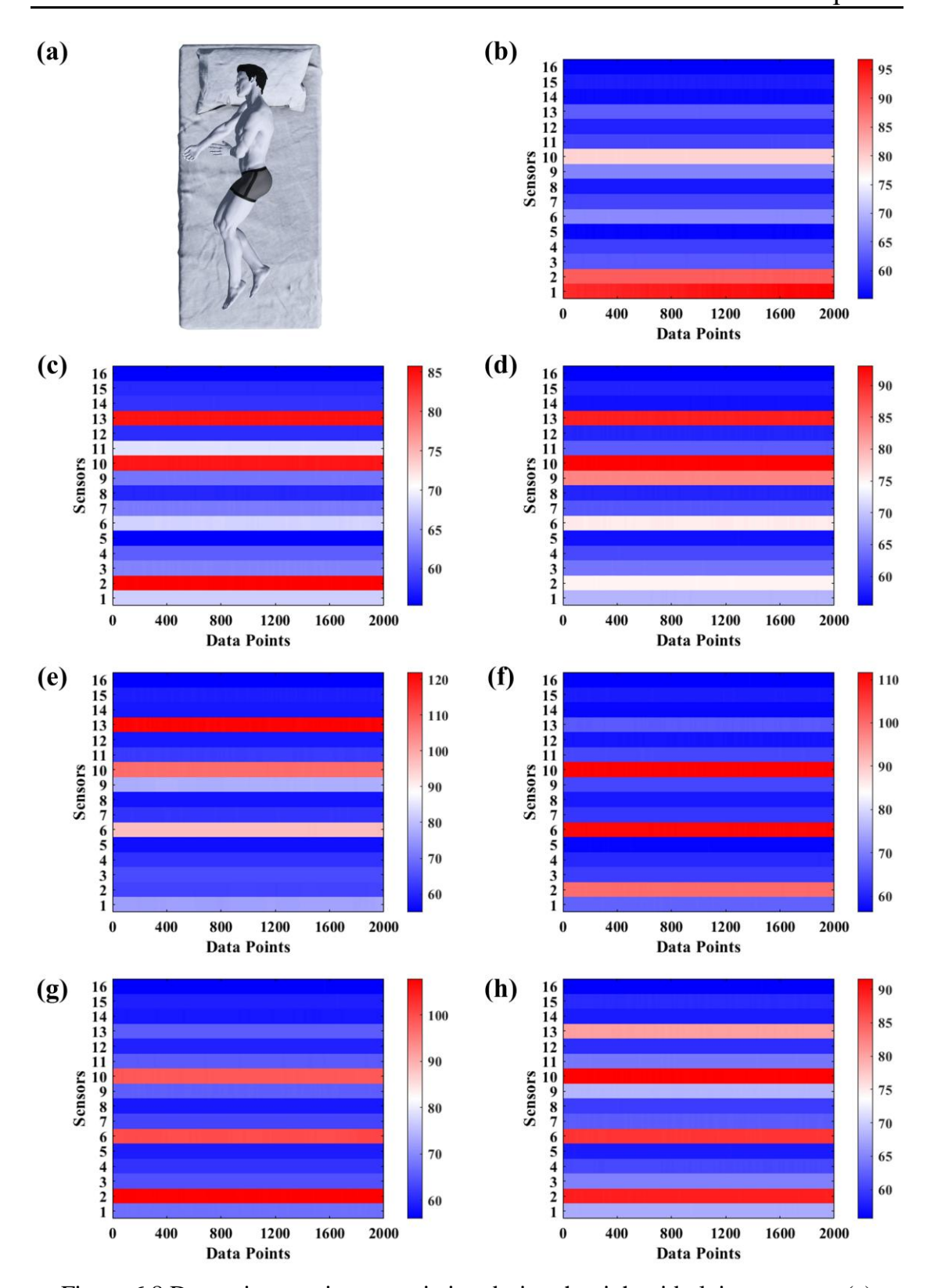


Figure 6.8 Dynamic capacitance variation during the right-side-lying process: (a) schematic of a volunteer lying on the right side; (b)–(h) heat maps for volunteers 1–7.

6.6.6 1D-CNN for sleep behavior and individual recognition

The classification of five sleep behaviors and the individual recognition of seven volunteers are accomplished using the 1D-CNN model shown in Figure 6.3. This model efficiently extracts shared features through a common convolutional layer and performs the dual tasks of classifying the five sleep behaviors and recognizing the seven volunteers via two separate fully connected layers.

Figure 6.9(a) illustrates the training curves of the 1D-CNN model for classifying the five sleep behaviors, including the combined loss function and the accuracy curve. As training progresses, the loss value steadily decreases, reflecting effective convergence, while the accuracy rapidly improves and stabilizes. The classification results, shown in Figure 6.9(b), demonstrate that the model achieves 100% accuracy across all five behaviors: (1) getting into bed, (2) getting out of bed, (3) lying flat, (4) lying on the left side, and (5) lying on the right side. These results highlight that the distinct differences in capacitance distributions provide reliable input features for the 1D-CNN model. Dynamic behaviors, such as getting into (1) and out of (2) the bed, are characterized by significant temporal variations in capacitance, enabling the model to classify them with high accuracy. Similarly, static postures, including lying flat (3), lying on the left side (4), and lying on the right side (5), display unique and stable capacitance values, facilitating precise recognition. Overall, the 1D-CNN model's outstanding performance underscores the effectiveness of combining capacitive sensing data with deep learning techniques and demonstrates its robustness in classifying sleep behaviors.

The training curves for the seven-class individual recognition task are shown in Figure 6.9(c). The combined loss curve is identical to that in Figure 6.9(a), reflecting the same optimization process. However, the accuracy curve improves more slowly compared to the five-class task, highlighting the increased complexity of the seven-class task. The classification results, presented in Figure 6.9(d), indicate that most volunteers (numbers 3 to 7) achieve 100% accuracy, while volunteers 1 and 2 experience some degree of misclassification. This confusion likely arises from similarities in their physical

dimensions and sleeping habits, which lead to highly similar capacitance distributions and reduce the model's discriminative ability during feature extraction. Despite these challenges, the overall accuracy of the seven-class model exceeds 80%, demonstrating its effectiveness in individual recognition tasks.

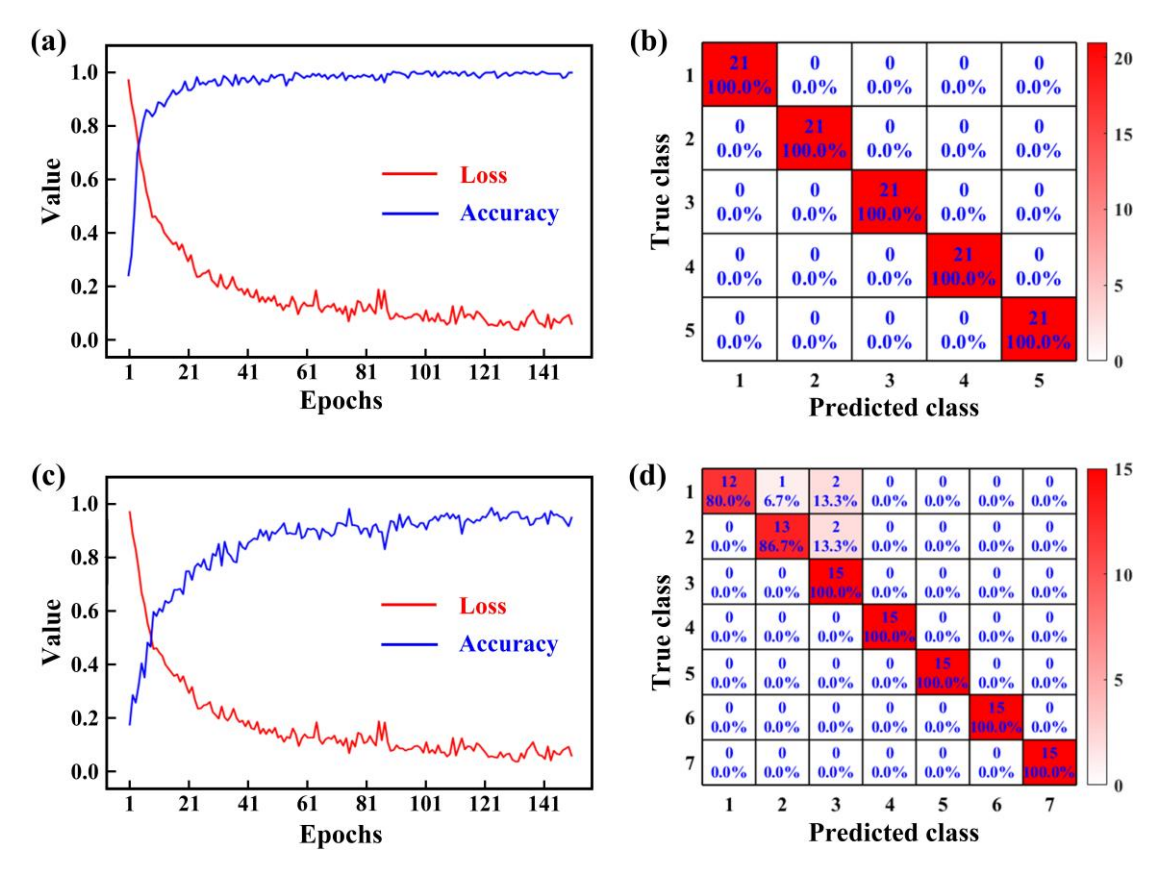


Figure 6.9 Training performance and classification results of the 1D-CNN model: (a) training curve for five-behavior classification; (b) confusion matrix for five-behavior classification; (c) training curve for seven-individual classification; (d) confusion matrix for seven-individual classification.

6.7 Conclusions

This chapter successfully developed a PLA-based smart mattress surface fabric integrated with a 4 × 4 matrix of 16 TCPS and a wireless capacitance measurement system, enabling non-invasive, real-time monitoring of sleep behaviors. Building on this integrated platform, five typical sleep behaviors were systematically analyzed across seven volunteers. Dynamic behaviors, such as getting into and out of bed,

demonstrate pronounced temporal characteristics, with pressure transitions from low to high or high to low effectively illustrating the interaction between the human body and the mattress. Static postures exhibit stable capacitance signals with distinct spatial distributions: high-capacitance regions are primarily concentrated in central sensors for lying flat, in left-side sensors for lying on the left side, and in right-side sensors for lying on the right side. While these behaviors share common characteristics, notable individual differences are also observed among participants.

A 1D-CNN deep learning model was employed to classify recorded sleep behaviors and identify individuals based on the acquired capacitance data. The model achieves 100% accuracy in classifying the five targeted sleep behaviors. Additionally, the sevenclass individual recognition model exceeds 80% accuracy, with most volunteers (numbers 3 to 7) achieving 100%. Misclassifications for some participants (numbers 1 and 2), likely due to similarities in physical dimensions and sleep habits, highlight the need for larger datasets and optimized model architecture to enhance robustness. Overall, these results underscore the potential of PLA-based, eco-friendly smart mattress surface fabrics for diverse applications in sleep monitoring and personalized health management.

Chapter 7 Conclusions and Future Work

7.1 Conclusions

This study has focused on developing sustainable and comfortable PLA mattress surface fabrics with integrated sleep monitoring functionalities, including the production of crimped PLA filaments, PLA weft-knitted inlaid fabrics, PLA-based TCPS, and PLA smart mattress surface fabrics. The main conclusions of this study are as follows:

7.1.1 Fabrication of crimped PLA filaments

Crimped PLA filaments have been successfully prepared using knit-de-knit technology, with an emphasis on the effects of heat-setting temperature and time on filament properties. Systematic experiments and analysis have determined the optimal production conditions: a heat-setting temperature of 120°C and a duration of 90 s. Under these conditions, the crimped filaments exhibit excellent crimped and tensile properties, meeting the requirements for mattress surface fabric applications. To improve production efficiency and quality, a small circular knitting machine equipped with an integrated heating tube and a winding device have been developed. This innovation facilitates the efficient and continuous production of crimped PLA filaments while maintaining their crimped structure. The superior performance of the resulting PLA filaments establishes them as an ideal raw material for mattress surface fabrics.

7.1.2 Fabrication of PLA weft-knitted inlaid fabric

Pure PLA weft-knitted inlaid fabrics incorporating crimped PLA filaments have been designed, fabricated, and evaluated in terms of their physical properties, comfort, and durability across various structural parameters. Results indicate that increasing the connection rate enhances air and water vapor permeability but reduces thermal insulation and energy absorption, highlighting the importance of structural design. The impact of stitching patterns is also notable: the triangular pattern improves air

permeability, the hexagonal pattern results in thickness loss, and the rhombic pattern absorbs more compression energy, providing diverse options for different applications. Crimped PLA filaments improve overall comfort and compression performance compared to non-crimped filaments. Additionally, fabric surfaces made with PLA filaments show better air and water vapor permeabilities, lower thickness loss, and greater energy absorption than those made with staple yarns. Compared to PET fabrics, PLA fabrics exhibit improved water vapor permeability, comparable air permeability, thermal insulation, and pilling and abrasion resistance, confirming their potential as sustainable mattress materials. These findings support the further development of PLA-based capacitive sensors and their applications in intelligent sleep monitoring systems.

7.1.3 Development of PLA-based TCPS

A TCPS based on PLA weft-knitted inlaid fabric has been successfully developed by integrating conductive yarns, meeting the sensitivity, reliability, and comfort requirements for smart mattress applications. Fabricated with 400D conductive yarns, 450D crimped PLA filaments, and an electrode arrangement of 30 wales and 40 courses, the TCPS achieves the highest $\Delta C/C_0$ and exhibits sensitivities of 1.73, 0.34, and 0.09 kPa⁻¹ across pressure ranges of 0–0.2, 0.2–2.9, and 2.9–15 kPa, respectively. The improved TCPS maintains consistent performance under compressive pressures of 1–15 kPa and rates of 5–20 mm/min, as well as after five washing cycles and 5000 compression cycles, with response and recovery times of 130 ms and 90 ms at 1.07 kPa. Additionally, it demonstrates superior comfort properties, including thermal insulation, air permeability, and water vapor permeability, compared to those of commercial mattress surface fabrics, despite exhibiting slightly lower compression recovery. These findings highlight the TCPS's suitability for advancing intelligent sleep monitoring technologies.

7.1.4 Development of PLA smart mattress surface fabrics

A PLA smart mattress surface fabric seamlessly integrating a 4 × 4 matrix of 16 TCPS units has been successfully developed using intarsia knitting technology. Combined

with a wireless capacitance data acquisition system, this fabric allows precise measurement of capacitance distributions, thereby enabling real-time monitoring of sleep behaviors. It effectively captures capacitance changes during dynamic behaviors (e.g., getting in and out of bed) and static postures (e.g., lying flat, lying on the left, and lying on the right), with heat maps validating its high sensitivity and resolution. A 1D-CNN deep learning model has been employed to classify these five typical sleep behaviors, achieving 100% accuracy for both dynamic and static behaviors. Furthermore, the model has been applied to identify seven individual volunteers, with most participants achieving 100% accuracy, while two participants recorded accuracies of 80% and 86.7%, respectively, demonstrating the model's overall robustness and reliability. This study confirms that intarsia knitting enables the seamless integration of the TCPS into sustainable and comfortable PLA fabrics, providing a reliable platform for real-time sleep behavior monitoring and individual recognition.

7.2 Limitations and future research directions

Despite the substantial progress achieved in developing sustainable, comfortable, and sleep-monitoring-integrated PLA smart mattress surface fabrics, several limitations and challenges remain that warrant further investigation and optimization.

7.2.1 Optimization of materials and structures

The production of crimped PLA filaments primarily relies on heat-setting processes. Future research could apply other advanced microstructural characterization techniques, such as fiber orientation analysis, to further investigate the relationship between fiber properties and heat-setting parameters, thereby enhancing filament performance. Furthermore, designing more diverse and intricate jacquard patterns could enhance both the aesthetic appeal and structural complexity of PLA weft-knitted inlaid fabrics, thereby broadening the range of potential applications for these materials.

7.2.2 Enhancing sensitivity and monitoring precision

The sensitivity of the PLA-based TCPS developed in this study can still be improved. Future research could explore the use of materials with higher conductivity and optimize other knitting parameters to enhance sensing accuracy and response speed. Additionally, increasing the number of TCPS units in PLA smart mattress fabrics would enable more precise sleep monitoring by identifying intricate pressure patterns and minor body motions, thereby providing a more comprehensive assessment of sleep behavior.

7.2.3 Algorithm optimization and system portability

Although the developed 1D-CNN deep learning model achieves 100% accuracy in classifying five typical sleep behaviors, it faces challenges in accurately identifying individual sleepers. This highlights the necessity of optimizing the model architecture and expanding the training dataset to enhance its effectiveness in individual recognition. Additionally, developing a lightweight, portable data acquisition system integrated with smartphone applications for data visualization and management could greatly enhance user experience and convenience, thereby promoting broader adoption of this sleep monitoring technology.

7.2.4 Durability and practicality enhancement

This study primarily focuses on evaluating the feasibility of PLA smart mattress surface fabrics for short-term sleep monitoring. Future research should include long-term testing under multi-cycle and varied environmental conditions to assess the durability and performance of the PLA smart fabrics in practical applications. Furthermore, optimizing the integration between conductive yarns and the data acquisition system is crucial to ensuring reliability during routine cleaning and prolonged use. These advancements will contribute to establishing the robustness and practicality of the system for everyday use.

By continuously exploring and improving the aforementioned research directions, the

overall comfort and sensing performance of PLA smart mattress surface fabrics are expected to be further enhanced. These improvements will not only broaden their potential application areas but also contribute to the development of sustainable and comfortable solutions for intelligent monitoring systems.

References

- [1] D. W. Carley and S. S. Farabi, "Physiology of sleep," *Diabetes Spectr.*, vol. 29, no. 1, pp. 5–9, 2016.
- [2] H. R. Colten and B. M. Altevogt, "Sleep physiology," in *Sleep disorders and sleep deprivation: An unmet public health problem*. Washington, USA: National Academies Press, 2006, pp. 33–49.
- [3] J. M. Krueger, M. G. Frank, J. P. Wisor, and S. Roy, "Sleep function: Toward elucidating an enigma," *Sleep Med. Rev.*, vol. 28, pp. 46–54, 2016.
- [4] T. W. Kim, J. H. Jeong, and S. C. Hong, "The impact of sleep and circadian disturbance on hormones and metabolism," *Int. J. Endocrinol.*, vol. 2015, pp. 1–9, 2015.
- [5] M. R. Irwin, "Why sleep is important for health: a psychoneuroimmunology perspective," *Annu. Rev. Psychol.*, vol. 66, pp. 143–172, 2015.
- [6] G. Medic, M. Wille, and M. E. Hemels, "Short-and long-term health consequences of sleep disruption," *Nat. Sci. Sleep*, vol. 9, pp. 151–161, 2017.
- [7] Z. A. Caddick, K. Gregory, L. Arsintescu, and E. E. Flynn-Evans, "A review of the environmental parameters necessary for an optimal sleep environment," *Build. Environ.*, vol. 132, pp. 11–20, 2018.
- [8] B. H. Jacobson, A. Boolani, and D. B. Smith, "Changes in back pain, sleep quality, and perceived stress after introduction of new bedding systems," *J. Chiropr. Med.*, vol. 8, no. 1, pp. 1–8, 2009.
- [9] M. A. Spina, T. Andrillon, N. Quin, J. F. Wiley, S. M. Rajaratnam, and B. Bei, "Does providing feedback and guidance on sleep perceptions using sleep wearables improve insomnia? Findings from "Novel Insomnia Treatment Experiment": a randomized controlled trial," *Sleep*, vol. 46, no. 9, pp. 1–13, 2023.
- [10] Z. Vlaovic, I. Grbac, and K. Maric, "Heat conductivity and moisture permeability through the pocket spring mattress," in XXVIIIth International

- Conference Research for Furniture Industry, Poznan, Poland, 2017, pp. 179–184.
- [11] H. Wong *et al.*, "Efficacy of a pressure-sensing mattress cover system for reducing interface pressure: study protocol for a randomized controlled trial," *Trials*, vol. 16, no. 1, pp. 1–11, 2015.
- [12] A. A. Salama, A. S. El-Deeb, and I. M. El-Shahat, "Evaluation of bed cover properties produced from double fabric based on honeycomb," *J. Text.*, vol. 2015, pp. 1–7, 2015.
- [13] A. A. E. Abo Khozym, Radwan, G. Abd El Hamied, Asser, N. A. H. Abd El Wahab, and M. M. M. El Sheikh, "Comparative study of the aesthetic properties of (knitted and weaving) jacquard fabrics used in mattress fabrics," *J. Arts Appl. Sci.*, vol. 9, no. 3, pp. 21–35, 2022.
- [14] E. H. Shirazi and M. Abdel Gawad, "Improvement of the properties of multi-layered fabrics used in the production of mattresses to achieve the best functional performance," *Int. Des. J.*, vol. 7, no. 4, pp. 117–125, 2017.
- [15] J. Liang, H. Cong, Z. Gao, A. Zhang, and Z. Dong, "Computer-aided design of weft-knitted two-side jacquard fabric," *Int. J. Cloth. Sci. Technol.*, vol. 33, no. 1, pp. 122–136, 2021.
- [16] H. Gong and B. Ozgen, "Fabric structures: Woven, knitted, or nonwoven," in *Engineering of high-performance textiles*. Cambridge, England: Woodhead Publishing, 2018, pp. 107–131.
- [17] X. Zhang and P. Ma, "Application of knitting structure textiles in medical areas," *Autex Res. J.*, vol. 18, no. 2, pp. 181–191, 2018.
- [18] S. A. Abbasi, A. Marmaralı, and G. Ertekin, "Thermal comfort properties of weft knitted quilted fabrics," *Int. J. Cloth. Sci. Technol.*, vol. 32, no. 6, pp. 837–847, 2020.
- [19] D. J. Spencer, *Knitting technology: a comprehensive handbook and practical guide*, 3rd ed. Cambridge, England: Woodhead Publishing, 2001.
- [20] B. Haex, *Back and bed: ergonomic aspects of sleeping*. Boca Raton, USA: CRC press, 2004.

- [21] Z. Önder, S. Üstüntağ, N. Paşayev, and H. G. Türksoy, "Process optimization of pad-dry-fixation and foam coating methods for flame retardant mattress fabrics," *Tekst. Muhendis*, vol. 28, no. 123, pp. 199–207, 2021.
- [22] Z. Vlaović, N. Klarić, and D. Domljan, "Investigating the impact of long-term use on mattress firmness and sleep quality-preliminary results," *Appl. Sci.*, vol. 14, no. 21, pp. 1–14, 2024.
- [23] S. Terliksiz, F. Kalaoğlu, and S. H. Eryürük, "Analysis of thermal comfort properties of jacquard knitted mattress ticking fabrics," *Int. J. Cloth. Sci. Technol.*, vol. 28, no. 1, pp. 105–114, 2016.
- [24] S. Kaplan and H. Tokgoz, "Objective and subjective evaluations of quilted mattress ticking fabrics for their thermal comfort performances," *Int. J. Cloth. Sci. Technol.*, vol. 35, no. 4, pp. 648–664, 2023.
- [25] L. Onal and M. Yildirim, "Comfort properties of functional three-dimensional knitted spacer fabrics for home-textile applications," *Text. Res. J.*, vol. 82, no. 17, pp. 1751–1764, 2012.
- [26] C. Atkinson, *False twist textured yarns: Principles, processing and applications*. Cambridge, England: Woodhead Publishing, 2012.
- [27] S. Akter, M. A. Motalb, and M. Helali, "Effect of different crimp method of jute fibre on strength and elongation properties of jute yarn and woven fabric," *Fibres Text.*, vol. 29, pp. 78–85, 2022.
- [28] J. W. Hearle, "The 20th-century revolution in textile machines and processes. Part 2: textured yarns and other technologies," *Ind. Archaeol. Rev.*, vol. 36, no. 1, pp. 32–47, 2014.
- [29] J. Luo, F. Wang, and B. Xu, "Factors affecting crimp configuration of PTT/PET bi-component filaments," *Text. Res. J.*, vol. 81, no. 5, pp. 538–544, 2011.
- [30] S. P. Rwei, Y. T. Lin, and Y. Y. Su, "Study of self-crimp polyester fibers," *Polym. Eng. Sci.*, vol. 45, no. 6, pp. 838–845, 2005.
- [31] G. Xiang, H. Hua, Q. Gao, J. Guo, X. Zhang, and X. Wang, "Fabrication and properties of self-crimp side-by-side bicomponent filaments composed of polyethylene terephthalates with different intrinsic viscosity," *Fibres Text. East.*

- Eur., vol. 151, no. 2, pp. 68-74, 2022.
- [32] S. Zhu, X. Meng, X. Yan, and S. Chen, "Evidence for bicomponent fibers: a review," *e-Polym.*, vol. 21, no. 1, pp. 636–653, 2021.
- [33] K. P. Vlakna, "Crimped polypropylene yarns," *Kovine, Zlitine, Tehnol.*, vol. 33, no. 6, pp. 523–526, 1999.
- [34] T. Matsuo, "Polypropylene fibers crimped by asymmetrical quenching," *J. Text. Mach. Soc. Jpn*, vol. 23, no. 2, pp. 29–34, 1977.
- [35] T. Karthik and R. Rathinamoorthy, "Sustainable synthetic fibre production," in *Sustainable fibres and textiles*. Cambridge, England: Woodhead Publishing, 2017, ch. 8, pp. 191–240.
- [36] R. S. Blackburn, *Biodegradable and sustainable fibres*. Cambridge, England: Woodhead publishing, 2006, pp. 191–218.
- [37] L. Shao, Y. Xi, and Y. Weng, "Recent advances in PLA-based antibacterial food packaging and its applications," *Molecules*, vol. 27, no. 18, pp. 1–24, 2022.
- [38] Y. Yang *et al.*, "Poly(lactic acid) fibers, yarns and fabrics: Manufacturing, properties and applications," *Text. Res. J.*, vol. 91, no. 13–14, pp. 1641–1669, 2021.
- [39] S. Xu, J. Chen, B. Wang, and Y. Yang, "Sustainable and hydrolysis-free dyeing process for polylactic acid using nonaqueous medium," *ACS Sustainable Chem. Eng.*, vol. 3, no. 6, pp. 1039–1046, 2015.
- [40] D. W. Farrington, J. Lunt, S. Davies, and R. Blackburn, "Poly (lactic acid) fibers," in *Biodegradable and sustainable fibres*. Cambridge, England: Woodhead Publishing, 2005, pp. 191–219.
- [41] M. L. Di Lorenzo and R. Androsch, *Industrial applications of poly (lactic acid)*.Cham, Switzerland: Springer, 2018.
- [42] N. F. Zaaba and M. Jaafar, "A review on degradation mechanisms of polylactic acid: Hydrolytic, photodegradative, microbial, and enzymatic degradation," *Polym. Eng. Sci.*, vol. 60, no. 9, pp. 2061–2075, 2020.
- [43] J. Leenslag and A. Pennings, "High-strength poly (l-lactide) fibres by a dryspinning/hot-drawing process," *Polymer*, vol. 28, no. 10, pp. 1695–1702, 1987.

- [44] I. Horáček and V. Kalíšek, "Polylactide. I. Continuous dry spinning-hot drawing preparation of fibers," *J. Appl. Polym. Sci.*, vol. 54, no. 11, pp. 1751–1757, 1994.
- [45] I. Horáček and V. Kalíšek, "Polylactide. III. Fiber preparation by spinning in precipitant vapor," *J. Appl. Polym. Sci.*, vol. 54, no. 11, pp. 1767–1771, 1994.
- [46] A. M. Manich, R. Miguel, M. J. S. Silva, J. Lucas, M. Martí, and D. Cayuela, "Effect of processing and wearing on viscoelastic modeling of polylactide/wool and polyester/wool woven fabrics subjected to bursting," *Text. Res. J.*, vol. 84, no. 18, pp. 1961–1975, 2014.
- [47] S. Chattopadhyay and R. Guruprasad, "Blending of cotton and poly (lactic acid) fiber: Combined optimization of blend ratio and yarn twist using mixture-process design," *J. Nat. Fibers*, vol. 18, no. 5, pp. 631–643, 2021.
- [48] A. Jabbar, M. Tausif, H. R. Tahir, A. Basit, M. R. A. Bhatti, and G. Abbas, "Polylactic acid/lyocell fibre as an eco-friendly alternative to polyethylene terephthalate/cotton fibre blended yarns and knitted fabrics," *J. Text. Inst.*, vol. 111, no. 1, pp. 129–138, 2020.
- [49] R. Guruprasad, G. Krishna Prasad, G. Prabu, S. Raj, and P. Patil, "Low-stress mechanical properties and fabric hand of cotton and polylactic acid fibre blended knitted fabrics," *Indian J. Fibre Text. Res.*, vol. 43, no. 3, pp. 381–384, 2018.
- [50] M. Maqsood and G. Seide, "Development of biobased socks from sustainable polymer and statistical modeling of their thermo-physiological properties," *J. Clean. Prod.*, vol. 197, pp. 170–177, 2018.
- [51] M. Maqsood and G. Seide, "Statistical modeling of thermal properties of biobased compostable gloves developed from sustainable polymer," *Fibers Polym.*, vol. 19, pp. 1094–1101, 2018.
- [52] R. Guruprasad, M. Vivekanandan, A. Arputharaj, S. Saxena, and S. Chattopadhyay, "Development of cotton-rich/polylactic acid fiber blend knitted fabrics for sports textiles," *J. Ind. Text.*, vol. 45, no. 3, pp. 405–415, 2015.
- [53] N. Pimenta, P. Chaves, L. Fernandes, and D. Freitas, "Motion detection in an intelligent textile mattress cover," in 8th International Symposium on Ambient

- Intelligence (ISAmI 2017), Porto, Portugal, 2017, pp. 47–54.
- [54] P. Meier, O. Ferhi, and M. Prochaska, "Behavior recognition through an intelligent mattress cover," in 2024 IEEE 13th Global Conference on Consumer Electronics (GCCE), Kitakyushu, Japan, 2024, pp. 965–967.
- [55] S. Peng, K. Xu, X. Jiang, and W. Chen, "Flexible electrodes based smart mattress for non-contact cardiac signals measurement," in 42nd Annual International Conference of the IEEE Engineering in Medicine & Biology Society (EMBC), Montréal, Québec, Canada, 2020, pp. 4059–4062.
- [56] B. Babušiak, M. Šmondrk, L. Balogová, and M. Gála, "Mattress topper with textile ECG electrodes," *Fibres Text.*, vol. 3, pp. 25–28, 2020.
- [57] G. Cay and K. Mankodiya, "SleepSmart: smart mattress integrated with etextiles and IoT functions for sleep apnea management," in 2020 IEEE International Conference on Pervasive Computing and Communications Workshops (PerCom Workshops), Austin, Texas, USA, 2020, pp. 1–2.
- [58] S. Z. Assefa, M. Diaz-Abad, E. M. Wickwire, and S. M. Scharf, "The Functions of Sleep," *AIMS Neurosci.*, vol. 2, no. 3, pp. 155–171, 2015.
- [59] J. A. Rowley and M. S. Badr, "Normal sleep," in *Essentials of Sleep Medicine*. Cham, Switzerland: Humana Press, 2022, pp. 3–19.
- [60] A. K. Patel, V. Reddy, K. R. Shumway, and J. F. Araujo, "Physiology, sleep stages," in *StatPearls [Internet]*. Treasure Island, USA: StatPearls Publishing, 2024.
- [61] J. W. Antony, L. Piloto, M. Wang, P. Pacheco, K. A. Norman, and K. A. Paller, "Sleep spindle refractoriness segregates periods of memory reactivation," *Curr. Biol.*, vol. 28, no. 11, pp. 1736–1743, 2018.
- [62] J. W. Antony, M. Schönauer, B. P. Staresina, and S. A. Cairney, "Sleep spindles and memory reprocessing," *Trends Neurosci.*, vol. 42, no. 1, pp. 1–3, 2019.
- [63] M. H. Gandhi and P. D. Emmady, "Physiology, k complex," in *StatPearls* [Internet]. Treasure Island, USA: StatPearls Publishing, 2023.
- [64] B. Zolovska and J. Shatkin, "Key differences in pediatric versus adult sleep," in *Encyclopedia of Sleep*. Amsterdam, Netherlands: Academic Press, 2013, pp.

- 573-578.
- [65] N. A. Collop, R. E. Salas, M. Delayo, and C. Gamaldo, "Normal sleep and circadian processes," *Crit. Care Clin.*, vol. 24, no. 3, pp. 449–460, 2008.
- [66] M. H. Kryger, T. Roth, and W. C. Dement, *Principles and Practice of Sleep Medicine*. Philadelphia, USA: Saunders, 2010.
- [67] C. J. Amlaner, R. Greene, M. Hanson, G. G. Nichols, and C. Thibodeau, *Sleep, sleep disorders, and biological rhythms*. Colorado Springs, USA: BSCS, 2003.
- [68] V. K. Somers, M. E. Dyken, A. L. Mark, and F. M. Abboud, "Sympathetic-nerve activity during sleep in normal subjects," *N. Engl. J. Med.*, vol. 328, no. 5, pp. 303–307, 1993.
- [69] P. L. Madsen *et al.*, "Cerebral O₂ metabolism and cerebral blood flow in humans during deep and rapid-eye-movement sleep," *J. Appl. Physiol.*, vol. 70, no. 6, pp. 2597–2601, 1991.
- [70] J. L. Broussard and S. Klein, "Insufficient sleep and obesity: Cause or consequence," *Obesity*, vol. 30, no. 10, pp. 1914–1916, 2022.
- [71] A. V. Nedeltcheva, J. M. Kilkus, J. Imperial, D. A. Schoeller, and P. D. Penev, "Insufficient sleep undermines dietary efforts to reduce adiposity," *Ann. Intern. Med.*, vol. 153, no. 7, pp. 435–441, 2010.
- [72] K. Sullivan and C. Ordiah, "Association of mildly insufficient sleep with symptoms of anxiety and depression," *Neurol. Psychiatry Brain Res.*, vol. 30, pp. 1–4, 2018.
- [73] V. K. Chattu, M. D. Manzar, S. Kumary, D. Burman, D. W. Spence, and S. R. Pandi-Perumal, "The global problem of insufficient sleep and its serious public health implications," *Healthcare*, vol. 7, no. 1, pp. 1–16, 2019.
- [74] G. A. Kerkhof, "Epidemiology of sleep and sleep disorders in The Netherlands," *Sleep Med.*, vol. 30, pp. 229–239, 2017.
- [75] D. Léger, B. Poursain, D. Neubauer, and M. Uchiyama, "An international survey of sleeping problems in the general population," *Curr. Med. Res. Opin.*, vol. 24, no. 1, pp. 307–317, 2008.
- [76] V. K. Chattu, S. M. Sakhamuri, R. Kumar, D. W. Spence, A. S. BaHammam,

- and S. R. Pandi-Perumal, "Insufficient Sleep Syndrome: Is it time to classify it as a major noncommunicable disease?," *Sleep Sci.*, vol. 11, no. 2, pp. 56–64, 2018.
- [77] J. L. Paterson, A. C. Reynolds, and D. Dawson, "Sleep schedule regularity is associated with sleep duration in older australian adults: implications for improving the sleep health and wellbeing of our aging population," *Clin. Gerontol.*, vol. 41, no. 2, pp. 113–122, 2018.
- [78] B. Shang *et al.*, "Nonpharmacological interventions to improve sleep in nursing home residents: A systematic review," *Geriatr. Nurs.*, vol. 40, no. 4, pp. 405–416, 2019.
- [79] K. Peuhkuri, N. Sihvola, and R. Korpela, "Diet promotes sleep duration and quality," *Nutr. Res.*, vol. 32, no. 5, pp. 309–319, 2012.
- [80] Y. Takano, S. Iwano, S. Aoki, N. Nakano, and Y. Sakano, "A systematic review of the effect of sleep interventions on presenteeism," *Biopsychosoc. Med.*, vol. 15, pp. 1–10, 2021.
- [81] D. Driot *et al.*, "Non-drug and drug alternatives to benzodiazepines for insomnia in primary care: Study among GPs and pharmacies in a Southwest region of France," *Therapies*, vol. 74, no. 5, pp. 537–546, 2019.
- [82] J. Yang *et al.*, "Mindfulness-based movement intervention to improve sleep quality: A meta-analysis and moderator analysis of randomized clinical trials," *Int. J. Environ. Res. Public Health*, vol. 19, no. 16, pp. 1–18, 2022.
- [83] J. V. Rundo and R. Downey III, "Polysomnography," in *Handbook of clinical neurology*, vol. 160. Amsterdam, Netherlands: Elsevier, 2019, pp. 381–392.
- [84] Q. Pan, D. Brulin, and E. Campo, "Current status and future challenges of sleep monitoring systems: systematic review," *JMIR Biomed. Eng.*, vol. 5, no. 1, pp. 1–28, 2020.
- [85] S. Kwon, H. Kim, and W.-H. Yeo, "Recent advances in wearable sensors and portable electronics for sleep monitoring," *Iscience*, vol. 24, no. 5, pp. 1–16, 2021.
- [86] E. Debellemaniere et al., "Performance of an ambulatory dry-EEG device for

- auditory closed-loop stimulation of sleep slow oscillations in the home environment," *Front. Hum. Neurosci.*, vol. 12, pp. 1–15, 2018.
- [87] S. Haghayegh, S. Khoshnevis, M. H. Smolensky, K. R. Diller, and R. J. Castriotta, "Accuracy of wristband Fitbit models in assessing sleep: systematic review and meta-analysis," *J. Med. Internet Res.*, vol. 21, no. 11, pp. 1–17, 2019.
- [88] S. Haghayegh, S. Khoshnevis, M. H. Smolensky, and K. R. Diller, "Accuracy of PurePulse photoplethysmography technology of Fitbit Charge 2 for assessment of heart rate during sleep," *Chronobiol. Int.*, vol. 36, no. 7, pp. 927–933, 2019.
- [89] L. Chang *et al.*, "SleepGuard: Capturing rich sleep information using smartwatch sensing data," *Proc. ACM Interact. Mob. Wearable Ubiquitous Technol.*, vol. 2, no. 3, pp. 1–34, 2018.
- [90] X. Liu, J. Cao, S. Tang, and J. Wen, "Wi-sleep: Contactless sleep monitoring via wifi signals," in *2014 IEEE Real-Time Systems Symposium*, Rome, Italy, 2014, pp. 346–355.
- [91] H. Hong, L. Zhang, C. Gu, Y. Li, G. Zhou, and X. Zhu, "Noncontact sleep stage estimation using a CW Doppler radar," *IEEE J. Emerg. Sel. Top. Circuits Syst.*, vol. 8, no. 2, pp. 260–270, 2018.
- [92] Y. Ren, C. Wang, J. Yang, and Y. Chen, "Fine-grained sleep monitoring: Hearing your breathing with smartphones," in *2015 IEEE Conference on Computer Communications*, Hong Kong, China, 2015, pp. 1194–1202.
- [93] T. Hao, G. Xing, and G. Zhou, "iSleep: unobtrusive sleep quality monitoring using smartphones," in *Proceedings of the 11th ACM Conference on Embedded Networked Sensor Systems*, Rome, Italy, 2013, pp. 1–14.
- [94] Z. Chen *et al.*, "Unobtrusive sleep monitoring using smartphones," in *7th International Conference on Pervasive Computing Technologies for Healthcare*, Venice, Italy, 2013, pp. 145–152.
- [95] J. M. Kortelainen, M. Van Gils, and J. Pärkkä, "Multichannel bed pressure sensor for sleep monitoring," in *2012 Computing in Cardiology*, Krakow, Poland, 2012, pp. 313–316.

- [96] R. van Dijk, W. Liang, B. Zhang, and J. Hu, "Development and evaluation of a non-obtrusive patient monitoring system with smart patient beds," in *Distributed, Ambient and Pervasive Interactions: 5th International Conference, DAPI 2017*, Vancouver, BC, Canada, 2017, pp. 482–490.
- [97] V. Verhaert, "Ergonomic analysis of integrated bed measurements: towards smart sleep systems," Ph.D. dissertation, Dept. Mech. Eng., KU Leuven, Belgium, 2011.
- [98] S. Nazaré, R. D. Davis, and K. Butler, "Assessment of factors affecting fire performance of mattresses: a review," *Fire Sci. Rev.*, vol. 1, pp. 1–27, 2012.
- [99] L. Ren *et al.*, "Effect of mattress bedding layer structure on pressure relief performance and subjective lying comfort," *J. Tissue Viability*, vol. 32, no. 1, pp. 9–19, 2023.
- [100] M. Matusiak, "Study of quilted fabrics used in outdoor clothing," *Tekstilec*, vol. 60, no. 4, pp. 302–309, 2017.
- [101] A. G. Temesgen and O. Sahu, "Comparative study on the mechanical properties of weft knitted and warp fabric reinforced composites," *J. Mod. Mater.*, vol. 9, no. 1, pp. 21–25, 2022.
- [102] P. Zheng, G. Jiang, and H. Cong, "Design method of circular weft-knitted jacquard fabric based on jacquard module," *Autex Res. J.*, vol. 22, no. 2, pp. 217–224, 2021.
- [103] Z. Guo, M. Eriksson, H. de la Motte, and E. Adolfsson, "Circular recycling of polyester textile waste using a sustainable catalyst," *J. Clean. Prod.*, vol. 283, pp. 1–8, 2021.
- [104] H. Sugiyama, "Synthetic fibers having down/feather-like characteristics and suitable for wadding," USA Patent 4364996 Patent Appl. 4364996, 1982.
- [105] R. Gong and X. Chen, "Technical yarns," in *Handbook of technical textiles*. Cambridge, England: Woodhead Publishing, 2016, pp. 43–62.
- [106] L. Mckeen, "Renewable resource and biodegradable polymers," in *The effect of sterilization on plastics and elastomers*, vol. 10, 3rd ed. Norwich, USA: William Andrew, 2012, pp. 305–317.

- [107] L. Xiao, B. Wang, G. Yang, and M. Gauthier, "Poly (lactic acid)-based biomaterials: synthesis, modification and applications," in *Biomedical science*, engineering and technology, vol. 11. Rijeka, Croatia: InTechOpen, 2012, pp. 247–282.
- [108] B. Das, A. Das, V. K. Kothari, R. Fanguiero, and M. Araújo, "Moisture transmission through textiles. Part I: Processes involved in moisture transmission and the factors at play," *Autex Res. J.*, vol. 7, no. 2, pp. 100–110, 2007.
- [109] D. Uttam and Ramratan, "Thermophysiological clothing comfort," *J. Text. Eng. Fash. Technol.*, vol. 7, no. 3, pp. 98–103, 2021.
- [110] D. Vlad and L.-I. Cioca, "Research regarding the influence of raw material and woven fabric geometry on the air permeability of mattress," *Procedia Eng.*, vol. 181, pp. 324–329, 2017.
- [111] S. Terliksiz, F. Kalaoglu, and S. H. Eryuruk, "Moisture transport properties of double jersey mattress ticking fabrics," *Tekst. Muhendis*, vol. 19, no. 85, pp. 14–19, 2012.
- [112] A. Wan, G. Jiang, and H. Cong, "Effect of activated carbon from coffee residue on the properties of weft-knitted polyester mattress fabric," *J. Text. Eng. Fash. Technol.*, vol. 4, no. 3, pp. 239–243, 2018.
- [113] B. Sapancı, S. Üstüntağ, and C. Güneşoğlu, "Development of thermo-regulating mattress fabrics by application microcapsules containing n-hexadecane/n-octadecane coated with gum arabic/gelatin," *J. Text. Inst.*, pp. 1–11, 2024.
- [114] Standard Test Method for Linear Density of Yarn (Yarn Number) by the Skein Method, ASTM D1907-01, 2017.
- [115] Standard Test Method for Tensile Properties of Yarns by the Single-Strand Method, ASTM D2256/D2256M-21, 2021.
- [116] Standard Test Methods for Mass Per Unit Area (Weight) of Fabric, ASTM D3776-09, 2009.
- [117] Standard Test Method for Thickness of Textile Materials, ASTM D1777-96, 2019.

- [118] Standard Specification for Tolerances for Knitted Fabrics, ASTM D3887-96, 2017.
- [119] T. Horváth, T. J. Szabó, and K. Marossy, "Synthesis of polylactic acid (PLA) by polycondensation method," *Int. J. Eng. Manag. Sci.*, vol. 5, no. 2, pp. 286–293, 2020.
- [120] H.-C. Kim, D.-Y. Kim, J.-E. Lee, and K. Park, "Improvement of mechanical properties and surface finish of 3d-printed polylactic acid parts by constrained remelting," *Adv. Mater. Lett.*, vol. 8, pp. 1199–1203, 2017.
- [121] *Textiles Standard atmospheres for conditioning and testing*, ISO 139:2005, 2005.
- [122] T. J. Kang and J. Y. Lee, "Filament crimp in three dimensions measured by image analysis and fractal geometry," *Text. Res. J.*, vol. 71, no. 2, pp. 112–116, 2001.
- [123] B. Ma *et al.*, "Effect of poly (lactic acid) crystallization on its mechanical and heat resistance performances," *Polymer*, vol. 212, pp. 1–9, 2021.
- [124] C. Liu, C. Xie, and X. Liu, "Properties of yak wool in comparison to cashmere and camel hairs," *J. Nat. Fibers*, vol. 15, no. 2, pp. 162–173, 2018.
- [125] S. Sarkeshick, H. Tavanai, M. Zarrebini, and M. Morshed, "An investigation on the effects of heat-setting process on the properties of polypropylene bulked continuous filament yarns," *J. Text. Inst.*, vol. 100, no. 2, pp. 128–134, 2009.
- [126] A. S. Vaughan and D. C. Bassett, "Crystallization and morphology," in Comprehensive Polymer Science and Supplements vol. 2. Amsterdam, Netherlands: Pergamon, 1989, pp. 415–457.
- [127] W. Li, Y. Yang, X. Xi, and J. Feng, "Hydrophilic modification of polylactic acid fiber and the usage of natural dye for multi-levered improvement of the fabric staining depth and the stability effect," *Langmuir*, vol. 40, pp. 3859–3872, 2024.
- [128] M. Zorah *et al.*, "Improvement thermomechanical properties of polylactic acid via titania nanofillers reinforcement," *J. Adv. Res. Fluid Mech. Therm. Sci.*, vol. 70, no. 1, pp. 97–111, 2020.
- [129] A. Chakraborty, P. Ghalsasi, and P. Radha, "Green engineering: Poly (lactic acid)

- composite materials fortified with surface-modified nanocellulose from borassus flabellifer leaves," *Biomass Convers. Biorefin.*, pp. 1–18, 2024.
- [130] J. Yu, P. Ji, K. Chen, H. Ji, F. Tang, and R. Chen, "Structure and performance changes of high-modulus and low-shrinkage poly (ethylene terephthalate) industrial fibers under different heat treatment conditions," *Text. Res. J.*, vol. 92, no. 11–12, pp. 2019–2030, 2022.
- [131] S. Saeidlou, M. A. Huneault, H. Li, and C. B. Park, "Poly (lactic acid) crystallization," *Prog. Polym. Sci.*, vol. 37, no. 12, pp. 1657–1677, 2012.
- [132] Textiles Domestic washing and drying procedures for textile testing, ISO 6330:2021, 2021.
- [133] H. Hu, M. Cai, P. Hong, Y. Li, L. Luo, and H. Wu, "Research on body pressure distribution of mattress for different genders," in *Advances in Ergonomics in Design: Proceedings of the AHFE 2019 International Conference on Ergonomics in Design*, Washington DC, USA, 2019, pp. 502–513.
- [134] Standard Test Method for Pilling Resistance and Other Related Surface Changes of Textile Fabrics: Martindale Tester, ASTM D4970/D4970M, 2022.
- [135] Standard Test Method for Abrasion Resistance of Textile Fabrics (Martindale Abrasion Tester Method), ASTM D4966-22, 2022.
- [136] F. Teng, L. Tu, X. Wang, H. Shen, and W. Xue, "Ultralight air-filled hollow yarn fabrics for efficient thermal insulation and its heat and mass transfer mechanism," *Compos. Part A: Appl. Sci. Manuf.*, vol. 185, pp. 1–11, 2024.
- [137] J. E. Song and S. Lee, "Application and evaluation knitted electrodes for body signal measurement using adhesive intermediate electrode," *Fash. Text.*, vol. 11, no. 1, pp. 1–15, 2024.
- [138] C. C. Vu and J. Kim, "Simultaneous sensing of touch and pressure by using highly elastic e-fabrics," *Appl. Sci.*, vol. 10, no. 3, pp. 1–12, 2020.
- [139] D. Matsouka, S. Vassiliadis, S. Mitilineos, N. Stathopoulos, and E. Siores, "Three-dimensional weft-knitted textile fabrics-based capacitors," *J. Text. Inst.*, vol. 109, no. 1, pp. 98–105, 2018.
- [140] W. Bolton, Engineering science. Abingdon, Oxfordshire, UK: Routledge, 2007,

- p. 244.
- [141] J. Aniulis, B. Kryszak, M. Grzymajło, G. Dudzik, K. Abramski, and K. Szustakiewicz, "Characterisation and manufacturing methods of material extrusion 3D printing composites filaments based on polylactide and nanohydroxyapatite," *Addit. Manuf.*, vol. 94, pp. 1–17, 2024.
- [142] S. Li, T. Chen, and X. Xiao, "Periodically inlaid carbon fiber bundles in the surface of honeycomb woven fabric for fabrication of normal pressure sensor," *J. Mater. Sci.*, vol. 55, pp. 6551–6565, 2020.
- [143] C. Gumus *et al.*, "Textile-based pressure sensor arrays: A novel scalable manufacturing technique," *Micro Nano Eng.*, vol. 15, pp. 1–9, 2022.
- [144] X. Guo, Y. Huang, X. Cai, C. Liu, and P. Liu, "Capacitive wearable tactile sensor based on smart textile substrate with carbon black/silicone rubber composite dielectric," *Meas. Sci. Technol.*, vol. 27, no. 4, pp. 1–9, 2016.
- [145] L. Kato Tech Co. "KES-FB3-A Compression Tester." https://english.keskato.co.jp/contents/katotech-catalog-kesfb3a-en-41.pdf (accessed 02 Dec, 2024).